



# Design and functional validation of pain modulators: crosstalk between **TRAAK** and **TRPV1**

**Magdalena Nikolaeva Koleva**

**Industrial Doctoral Thesis**

Director: Dr. Gregorio Fernández Ballester  
Codirectora: Dra. Isabel Devesa Giner

Programa de Doctorado en Biología Molecular y Celular

ELCHE, 2021

Instituto de Investigación, Desarrollo e Innovación  
en Biotecnología Sanitaria de Elche (IDiBE)

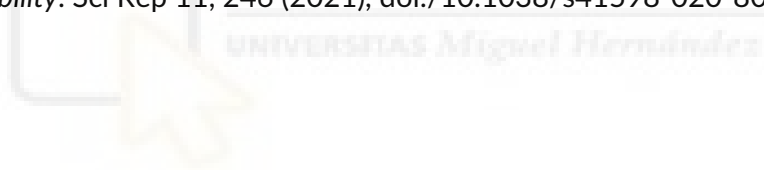
AntalGenics SL.

UNIVERSIDAD MIGUEL HERNÁNDEZ DE ELCHE



La presente tesis doctoral titulada “Design and functional validation of pain modulators: crosstalk between TRAAK and TRPV1” realizada por Dña. Magdalena Nikolaeva Koleva se presenta en formato por compendio de artículos previamente publicados, cuyas referencias son las indicadas a continuación:

Nikolaeva-Koleva, M., Butron, L., González-Rodríguez, S. et al. *A capsaicinoid-based soft drug, AG1529, for attenuating TRPV1-mediated histaminergic and inflammatory sensory neuron excitability*. Sci Rep 11, 246 (2021), doi:/10.1038/s41598-020-80725-z







Dr. Gregorio Fernández Ballester, Catedrático de la Universidad Miguel Hernández de Elche,

**CERTIFICA** que el trabajo de investigación que lleva por título “Design and functional validation of pain modulators: crosstalk between TRAAK and TRPV1”, presentado por Dña. Magdalena Nikolaeva Koleva para optar al grado de Doctora, ha sido realizado bajo su dirección en el Instituto de Investigación, Desarrollo e Innovación en Biotecnología Sanitaria de la Universidad Miguel Hernández de Elche. Considerando que la presente tesis se halla concluida, **AUTORIZA** su presentación para que pueda ser juzgada por el tribunal correspondiente.

Y para que así conste a los efectos oportunos, se expide el presente escrito.

Fdo: Dr. Gregorio Fernández Ballester

Catedrático de Universidad Miguel Hernández de Elche

Elche, octubre 2021





**Dra. Isabel Devesa Giner**, Profesora asociada de la Universidad Miguel Hernández de Elche,

**CERTIFICA** que el trabajo de investigación que lleva por título “Design and functional validation of pain modulators: crosstalk between TRAAK and TRPV1”, presentado por Dña. Magdalena Nikolaeva Koleva para optar al grado de Doctora, ha sido realizado bajo su co-dirección en Antalgenics S.L., empresa spin-off de la Universidad Miguel Hernández de Elche. Considerando que la presente tesis se halla concluida, **AUTORIZA** su presentación para que pueda ser juzgada por el tribunal correspondiente.

Y para que así conste a los efectos oportunos, se expide el presente escrito.

Fdo: Dra. Isabel Devesa Giner

Profesora asociada de la Universidad Miguel Hernández de Elche

Elche, octubre 2021





**Dra. Asia Fernández Carvajal**, Catedrática y Coordinadora del Programa de Doctorado en Biología Molecular y Celular del Instituto de Investigación, Desarrollo e Innovación en Biotecnología Sanitaria de Elche (IDiBE) de la Universidad Miguel Hernández de Elche.

**DA SU CONFORMIDAD** para el depósito y la defensa de la tesis doctoral titulada: “Design and functional validation of pain modulators: crosstalk between TRAAK and TRPV1”, presentada por Dña. Magdalena Nikolaeva Koleva, mediante el procedimiento excepcional derivado de la crisis sanitaria por COVID-19.

Y para que así conste a los efectos oportunos, se expide el presente documento

Fdo: Dra. Asia Fernández Carvajal

Coordinadora de la CAPD de Biología Molecular y Celular

Universidad Miguel Hernández

Elche, octubre 2021



La presente tesis doctoral ha sido cofinanciada por la Agencia Española de Investigación para las ayudas de Doctorados Industriales del Ministerio de Economía, Industria y Competitividad con Referencia **DI-16-08303** y título “Diseño y evaluación funcional de nuevos moduladores del canal iónico TRAAK para el tratamiento del dolor crónico”.



# INDEX

INDEX OF ABBREVIATIONS .....	14
INDEX OF FIGURES AND TABLES .....	15
SUMMARY .....	16
<b>1. INTRODUCTION</b> .....	<b>19</b>
1.- PAIN .....	21
2.- NOCICEPTION.....	22
3.- ION CHANNELS KEY ROLE IN CELL EXCITABILITY .....	25
3.1. Shaping cell excitability .....	26
3.2. Two-pore domain K <sup>+</sup> (K <sub>2</sub> P) channels.....	27
3.2.1. TREK channels subfamily.....	28
3.2.1.1. Expression and localization .....	28
3.2.1.2. Thermosensibility .....	29
3.2.1.3. Fatty acids regulation.....	29
3.2.1.4. pH regulation.....	30
3.2.1.5. Functional regulation partners.....	30
3.2.2. TRAAK.....	32
3.2.2.1. Gating and mechanosensitivity.....	33
3.2.2.2. Pharmacology.....	36
3.2.2.2.1. TRAAK lipidic modulation .....	36
3.2.2.2.2. TRAAK targeted by activators .....	37
3.2.2.2.3. TRAAK targeted by inhibitors.....	40
3.3. TRP channels family.....	41
3.3.1. TRPV1 channel.....	42
3.3.1.1. Expression .....	43
3.3.1.2. Structure .....	43
3.3.1.3. Polymodality.....	45
3.3.1.4. TRPV1 lipidic modulation .....	46
3.3.1.5. TRPV1 analgesic targeting.....	47
4.- TREATING CHRONIC PAIN .....	48
<b>2. OBJECTIVES</b> .....	<b>51</b>
<b>3. MATERIAL AND METHODS</b> .....	<b>55</b>
1.- BINDING SITES DEFINITION .....	57
1.1. Molecular docking assays.....	57
1.2. Exploring new TRAAK binding sites .....	58
2.- VIRTUAL SCREENING .....	59
2.1. Virtual screening assays .....	59
2.2. Virtual screening libraries.....	60
2.3. Structure-activity relationship (SAR) .....	61
3.- C-TERMINAL DOMAIN RECONSTRUCTION .....	61
3.1. YASARA automatic homology model based on manual alignment .....	61
3.2. YASARA manual homology and <i>ab initio</i> model.....	62
3.3. YASARA automatic homology model .....	63
3.4. YASARA Z-score .....	63
3.5. Online 3D structure prediction tools.....	65
3.6. Secondary structure prediction.....	65
4.- PUTATIVE PROTEIC INTERACTING PARTNERS .....	65
5.- CHEMICAL COMPOUNDS .....	66

---

6.- CELL CULTURE .....	67
6.1. Plasmid amplification .....	67
6.2. Stable cell line Hek 293LTV .....	68
6.3. TRAAK recombinant expression in Hek 293LTV cells.....	68
6.4. Primary culture of DRG nociceptors .....	69
7.- ELECTROPHYSIOLOGY .....	70
7.1. Patch-clamp recordings from recombinant cells .....	70
7.1.1. TRAAK recordings.....	70
7.1.2. TRP recordings.....	71
7.2. Patch-clamp recordings on DRG neurons .....	73
7.2.1. TRAAK recordings.....	73
7.2.2. TRP recordings.....	73
7.3. Microelectrode array measurements .....	74
7.4. Statistical analysis.....	74
<b>4. RESULTS .....</b>	<b>77</b>
1.- TRAAK BINDING SITES DEFINITION.....	79
1.1. TRAAK global blind docking.....	79
1.2. Exploring new binding sites.....	81
2.- VIRTUAL SCREENING.....	84
3.- TRAAK C-TERMINAL DOMAIN RECONSTRUCTION.....	94
3.1. YASARA automatic homology model based on manual alignment.....	94
3.2. YASARA manual homology and <i>ab initio</i> model .....	96
3.3. YASARA automatic homology model .....	99
3.4. Online 3D structure predictions .....	100
3.5. Secondary structure prediction .....	101
4.- TRAAK PUTATIVE PROTEIC INTERACTING PARTNERS.....	104
5.- <i>IN VITRO</i> COMPOUNDS TESTING.....	106
5.1. TRAAK electrophysiological behaviour in recombinant cells .....	106
5.2. <i>In vitro</i> testing of VS selected compounds .....	109
5.3. Compounds pharmacological characterisation on recombinant cells.....	113
5.4. Compounds effect on DRG sensory neurons .....	117
6.- STRUCTURE ACTIVITY RELATIONSHIPS (SAR) .....	122
6.1. Astemizol .....	122
6.2. Terfenadine .....	129
7.- EXPLORING AG1529 EFFECT ON TRP CHANNELS.....	134
7.1. AG1529 inhibitory activity on recombinant hTRPV1 channel .....	134
7.2. AG1529 modestly inhibits other thermoTRPs.....	138
7.3. AG1529 inhibitory effect on capsaicin-evoked neuronal firing .....	140
7.4. AG1529 shares the vanilloid TRPV1 binding site.....	141
<b>5. DISCUSSION .....</b>	<b>143</b>
<b>6. CONCLUSIONS .....</b>	<b>153</b>
<b>7. BIBLIOGRAPHY .....</b>	<b>157</b>
<b>8. AGRADECIMIENTOS .....</b>	<b>171</b>
<b>9. ANNEX.....</b>	<b>173</b>

---

## INDEX OF ABBREVIATIONS

---

<b>AA</b>	Arachidonic acid
<b>AP</b>	Action potential
<b>ASIC</b>	Acid sensing ion channel
<b>CGRP</b>	Calcitonin gene-related peptide
<b>CNS</b>	Central nervous system
<b>DRG</b>	Dorsal root ganglia
<b>FBS</b>	Fetal bovine serum
<b>K<sub>2</sub>P</b>	Potassium two-pore domain channel
<b>NGF</b>	Nerve growth factor
<b>PIP<sub>2</sub></b>	Phosphatidylinositol-4,5-bisphosphate
<b>PLC</b>	Phospholipase C
<b>PNS</b>	Peripheral nervous system
<b>P/S</b>	Penicillin/Streptomycin
<b>PUFA</b>	Polyunsaturated fatty acids
<b>SD</b>	Standard deviation
<b>SEM</b>	Standard error mean
<b>SF</b>	Selectivity filter
<b>SP</b>	Substance P
<b>TG</b>	Trigeminal ganglia
<b>TRAAK</b>	Twik-related arachidonic acid-activated potassium channel
<b>TRP</b>	Transient receptor potential channel
<b>V<sub>m</sub></b>	Cell resting membrane potential
<b>VS</b>	Virtual screening

---

---

INDEX OF FIGURES AND TABLES

Figure 1 - page 24	Figure 23 - page 98	Figure 45 - page 123
Figure 2 - page 24	Figure 24 - page 98	Figure 46 - page 124
Figure 3 - page 28	Figure 25 - page 99	Figure 47 - page 124
Figure 4 - page 33	Figure 26 - page 100	Figure 48 - page 125
Figure 5 - page 35	Figure 27 - page 101	Figure 49 - page 126
Figure 6 - page 39	Figure 28 - page 102	Figure 50 - page 127
Figure 7 - page 41	Figure 29 - page 103	Figure 51 - page 128
Figure 8 - page 42	Figure 30 - page 105	Figure 52 - page 130
Figure 9 - page 45	Figure 31 - page 107	Figure 53 - page 131
Figure 10 - page 60	Figure 32 - page 108	Figure 54 - page 132
Figure 11 - page 62	Figure 33 - page 109	Figure 55 - page 132
Figure 12 - page 63	Figure 34 - page 110	Figure 56 - page 133
Figure 13 - page 78	Figure 35 - page 112	Figure 57 - page 135
Figure 14 - page 80	Figure 36 - page 113	Figure 58 - page 136
Figure 15 - page 81	Figure 37 - page 114	Figure 59 - page 137
Figure 16 - page 81	Figure 38 - page 115	Figure 60 - page 138
Figure 17 - page 82	Figure 39 - page 116	Figure 61 - page 139
Figure 18 - page 83	Figure 40 - page 118	Figure 62 - page 139
Figure 19 - page 94	Figure 41 - page 118	Figure 63 - page 140
Figure 20 - page 95	Figure 42 - page 120	Figure 64 - page 141
Figure 21 - page 96	Figure 43 - page 121	Figure 65 - page 142
Figure 22 - page 97	Figure 44 - page 123	
<hr/>		
Table 1 - page 23	Table 6 - page 88	Table 11 - page 93
Table 2 - page 66	Table 7 - page 89	Table 12 - page 99
Table 3 - page 85	Table 8 - page 90	Table 13 - page 110
Table 4 - page 86	Table 9 - page 91	Table 14 - page 111
Table 5 - page 87	Table 10 - page 92	

---

## SUMMARY

Multiple pathologies elapse in presence of chronic pain. Up to 20% of EU population suffers from chronic pain, thus the related social and economic burden is very high. Currently, pain treatments do exist, although their efficacy is limited and their prolonged use leads to important side effects. Ion channels modulation has constituted a target to treat pain since a long time. Recently, the poorly explored K<sub>2</sub>P channels family has gained importance in pain modulation. Noteworthy, TRAAK presence in sensory neurons, together with its co-localization with thermoTRPs, opens a leeway to address pain in an innovative way. In the present work, the identification and functional validation of TRAAK selective modulators or double modulators of TRAAK and TRPV1, constituted the main goal.

Virtual screening assays of numerous ligand libraries enabled the identification of TRAAK putative modulators. Topoisomerase I antagonist irinotecan showed TRAAK mediated current increase in a time-sustained, reversible and dose-dependent manner. Irinotecan increased action potential hyperpolarization state in a neuropathic pain model of rat DRG neurons, induced by taxol. Histamine receptor 1 antagonists astemizol and terfenadine decreased basal TRAAK current in a dose-dependent and reversible manner. Terfenadine produced depolarization induced neuronal firing in primary DRG neurons. AG1529 exerted no effect on TRAAK current but caused TRPV1 antagonism. It preferentially and reversibly blocked capsaicin-induced TRPV1 current and marginally affected acid pH-elicited channel current. It had no effect on voltage- or heat-induced TRPV1 gating. It showed cross-reactivity with TRPM8 and TRPA1. *In silico* docking model located AG1529 on capsaicin binding pocket and the shift of its EC<sub>50</sub> to higher value supported the hypothesis of capsaicin-competitive antagonism of AG1529. The compound was also able to block capsaicin-induced neuronal firing.

Despite there are lot of unknowns which must be explored, this work sat up the funds of a new way to modulate chronic pain.

## RESUMEN

Múltiples patologías transcurren en presencia de dolor crónico. Hasta un 20% de la población europea sufre de dolor crónico, por lo que la carga social y económica relacionada con este es muy elevada. En la actualidad sí existen tratamientos para el dolor a pesar de que su eficacia es limitada y su uso prolongado conlleva a la aparición de importantes efectos secundarios. La modulación de canales iónicos ha constituido desde hace mucho tiempo una diana para tratar el dolor. Recientemente, la escasamente explorada familia de canales iónicos K<sub>2</sub>P ha ido ganando importancia en la modulación del dolor. Cabe mencionar que la presencia de TRAAK en neuronas sensoriales, junto con su colocalización con thermoTRPs, abre una vía innovadora de tratar el dolor. El principal objetivo del presente trabajo es la identificación y validación funcional de moduladores selectivos de TRAAK o moduladores dobles de TRAAK y TRPV1.

Los ensayos de cribado virtual de numerosas librerías de ligandos permitieron la identificación de moduladores putativos de TRAAK. El antagonista de la topoisomerasa I irinotecan, mostró un incremento sostenido en el tiempo, reversible y dosis dependiente de las corrientes mediadas por TRAAK. Irinotecan aumentó la hiperpolarización de los potenciales de acción en un modelo neuropático de neuronas sensoriales de los ganglios de la raíz dorsal inducido por taxol. Los antagonistas del receptor de histamina 1, astemizol y terfenadin, disminuyeron la corriente basal mediada por TRAAK de forma reversible y dosis dependiente. Terfenadin causó el disparo de potenciales de acción a través de despolarización del potencial de membrana de las neuronas sensoriales de los ganglios de la raíz dorsal. AG1529 no tuvo efecto sobre la corriente de TRAAK, pero causó antagonismo sobre TRPV1. De forma preferente y reversible bloqueó la corriente de TRPV1 inducida por capsaicina y afectó marginalmente la corriente del canal inducida por pH ácido. No tuvo efecto sobre la apertura de TRPV1 provocada por voltaje o temperatura alta. Mostró reactividad cruzada sobre TRPM8 y TRPA1. El modelo *in silico* de acoplamiento molecular localizó AG1529 en el bolsillo de unión de capsaicina. El desplazamiento de la EC<sub>50</sub> de capsaicina hacia mayores valores apoya la hipótesis de antagonismo de AG1529 competitivo con capsaicina. El compuesto fue capaz de bloquear el disparo de potenciales de acción neuronales inducidos por capsaicina.

A pesar de las muchas incógnitas que deben ser exploradas en mayor detalle, este trabajo establece las bases de una nueva forma de modular el dolor crónico.



# INTRODUCTION





## 1. PAIN

Organisms sense their environment and process the incoming sensory information in order to respond to the external world. During a life-threatening situation our organism is warned through our sensory circuitry. In this context, **pain** stands as a life-protecting mechanism that can save our lives. According to the **IASP** or International Association for the Study of Pain, it is defined as an unpleasant sensory and emotional experience associated with actual or potential tissue damage, or described in terms of such damage [1]. It is described as an emotional experience because based on the context, memory, emotion, social and other issues, each patient builds up its own pain experience with a high level of subjectivity [2]. Although pain is crucial for a fast response against potential hazardous situation, its extended effect has a physiological impact in terms of prolonged stress, delayed healing or the development of chronic pain. It also presents a financial and a quality-of-life impact as it causes depression, anxiety, sleeplessness and also impairs social relationships. Pain can be classified as follows:

- **Nociceptive**: represents the normal response to noxious injury of diverse tissues [3]. Depending on the insulted tissue it is divided into:
  - **Somatic**: often well localized affecting musculoskeletal or cutaneous areas. It can be superficial or deep.
  - **Visceral**: usually referred, vague and not clearly defined. It arises from hollow organs or smooth muscle.
- **Neuropathic**: stands for the pain initiated by a primary lesion or dysfunction on the somatosensory nervous system and leads to long-term changes in pain pathway structures and the processing of sensory information [4]. There can be pain amplification without stimulation and increased sensitivity to painful or nonpainful stimuli producing hyperalgesia or allodynia, respectively. Neuropathic pain can be peripheral or central depending on the level of injury of the somatosensory nervous system.
- **Inflammatory**: arises due to activation and sensitization of the nociceptive pain pathway by the release of inflammatory mediators in a specific tissue [5].

- **Unclassified pain disorders:** their underlying mechanisms are still poorly understood. They include cancer, migraine, primary headache and fibromyalgia [6, 7].

Although pain and **itch** are distinct sensations, they both rely on the nervous system whose sensory subdivisions interact [8]. This reason makes itch worthwhile to be mentioned. Similar to pain, itch is a survival-enhancing mechanism that produces an irritating sensation and brings attention to the affected area.

Pain can be also classified depending on the time of duration as:

- **Acute:** it is related with direct tissue damage and normally lasts less than 6 months.
- **Chronic:** it persists after tissue healing is complete or beyond the course of an acute disease, normally more than 6 months.

## 2. NOCICEPTION

Pain should be distinguished from the term **nociception** which is the neural process that encodes noxious stimuli and describes how pain becomes a conscious experience. Painful stimuli are converted into nerve impulses by **nociceptors**. Nociception and nociceptor were first defined in 1903 and 1906, respectively, by Charles Scott Sherrington [9, 10], terms that state pain is a specific sensation with its own sensory machinery. Accordingly, neurons are the primary and fundamental unit that constitutes brain and the whole nervous system. Nociceptors are a highly specialized subset of primary sensory neurons that respond only to pain stimuli. Their cell bodies are localized in the **dorsal root ganglia** (DRG) or **trigeminal ganglia** (TG) located in the spinal cord or the trigeminal equivalent in the brainstem, respectively. They normally project to tissues like skin, muscle and viscera. They are organized based on the type of stimuli they respond to, which can be chemical, mechanical or thermal. They are also classified depending on their diameter and the degree of myelination which determines their conduction velocity (Table 1). The majority of large myelinated (**A $\beta$** ) afferents are mechanoreceptors which respond to touch and hair movement [11]. Nociceptors are divided into two major classes, medium sized myelinated afferents (**A $\delta$** ) responsible for the fast well localised sharp pain transmission and small sized unmyelinated **C** fibres which conduct slow poorly localised dull pain. A $\delta$  fibres are responsible for the fast

withdraw of the affected body part from the stimulus. In turn, A $\delta$  fibres are subdivided into type I which respond to mechanical and chemical stimuli and type II which reply to heat induced pain [12]. Type I A $\delta$  fibres have higher heat threshold compared to type II fibers. Finally, C fibres which are classified as polymodal, because of their response to mechanical, thermal and chemical stimuli, are also subdivided into two groups. The peptidergic C fibres express calcitonin gene-related peptide (CGRP) and substance P (SP) while the non-peptidergic bind primarily to isolectin B4 (IB4+) [13]. Nevertheless, not all C fibres are nociceptive, some are in charge of itch transduction, the so called pruriceptors [14].

**Table 1. Classification of primary afferents.**

Classification	Diameter	Myelin	Velocity	Sensory function
A $\beta$	Large (6-12 $\mu$ m)	Yes	>35 m/s	Touch/Hair movement
I A $\delta$	Medium (1-5 $\mu$ m)	Thin	5-35 m/s	Fast mechanical/chemical pain
II A $\delta$				Fast heat pain
Peptidergic C	Small (0.2-1.5 $\mu$ m)	No	<2 m/s	Slow pain
Non-peptidergic C				

Pain nociception is constituted by four phases: (i) transduction, (ii) transmission, (iii) modulation and (iv) perception. **Transduction** stands for the process during which ion channels are modulated by acute noxious stimuli generating an ion flow either by their opening (Na<sup>+</sup> or Ca<sup>2+</sup> channels) or closing (K<sup>+</sup> channels). Ion channel modulation triggers an action potential through the depolarization of the cell membrane (Figure 1). Many ion channels are linked to G-protein receptors and in many cases chemical stimuli act on these last modifying indirectly channel activity through intracellular signalling pathways. After transducing the noxious stimulus at the periphery its **transmission** to the central nervous system (CNS) should be produced. This occurs as a conduction of action potentials through A $\delta$  and C-fibres, which are primary order neurons, into the dorsal horn of the spinal cord forming synapses with interneurons or second order neurons. During this first synapse the **modulation** and integration of the sensory information takes place. The dorsal horn plays an important role in this process. It is divided into laminae in which primary afferents end in a well-ordered way depending on the fibre type (Figure 2). Laminae I and II are the most superficial and constitute the dorsal horn site which receives the major part of nociceptive afferent input. A $\delta$  nociceptors end in laminae I while C fibres mainly in laminae II, peptidergic C-fibres occupy the outer part and non-peptidergic C-fibres its central zone. A $\beta$  non nociceptive afferents terminate in deeper laminae III and V [15-17]. The neural impulses then travel through projection neurons or

third order neurons and ascend to the brain following two types of spinothalamic tracts, the neospinothalamic tract which carries the fast sharp acute pain inputs and the paleospinothalamic tract responsible for the slow dull chronic pain transmission. These tracts project to the limbic system, reticular formation, hypothalamus, thalamus and finally to the somatosensory cortex, for interpretation also known as **perception**. This last step stands for the conscious awareness of pain and the specific sensory experience of individuals where many genetic and socio-cultural factors can influence pain perception.

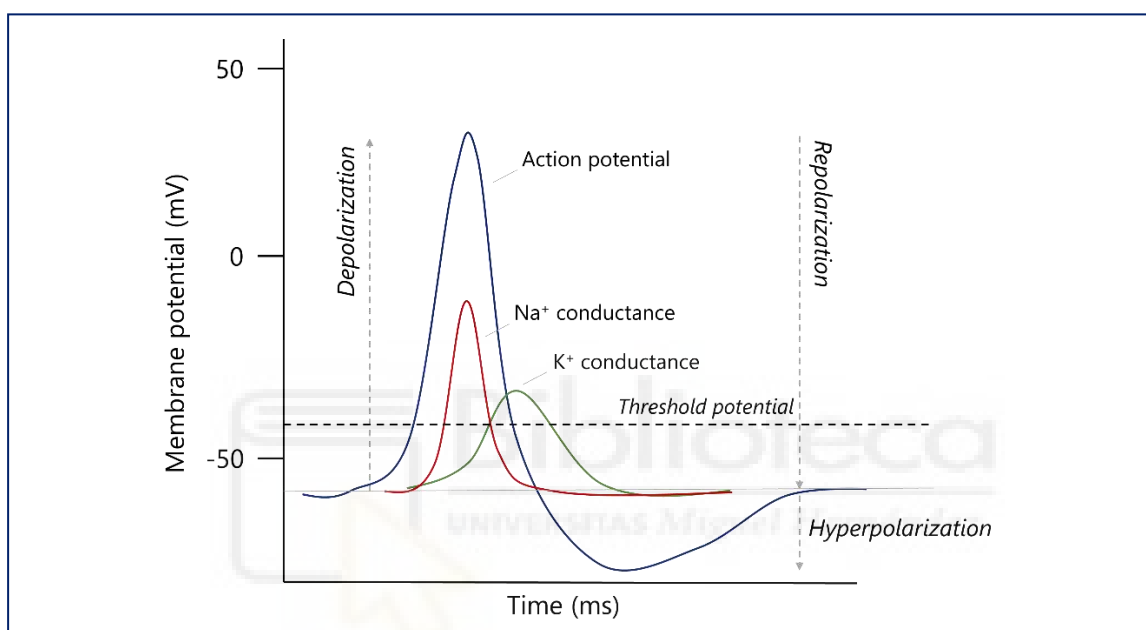


**Figure 1. The action potential.** Opening of  $\text{Na}^+$  ion channels produces a  $\text{Na}^+$  influx which depolarizes cell membrane. If threshold potential is reached, an action potential is triggered. With the opening of  $\text{K}^+$  ion channels  $\text{K}^+$  ions get out of the cell repolarizing cell membrane and even hyperpolarizing it. Once  $\text{K}^+$  and  $\text{Na}^+$  ion channels are closed, cell membrane potential returns to its resting potential. Adapted from Bezanilla F. 2006 [18].

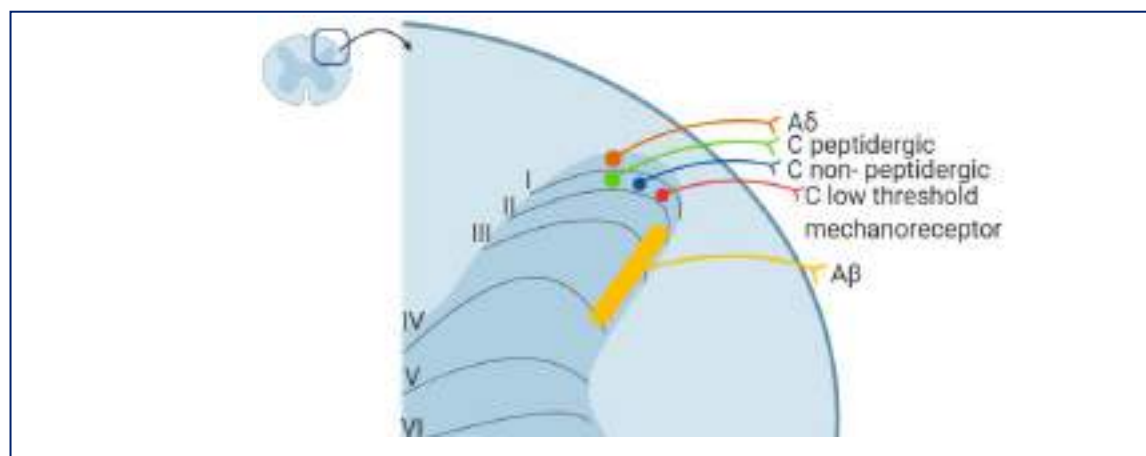


**Figure 2. Laminae division of spinal cord dorsal horn.** Somatotopic arrangement of primary afferents endings into the grey matter of the spinal cord. Primary afferents activated by noxious cutaneous stimuli mainly innervate laminae I and II while mechanoreceptors carrying touch signals project to deeper laminae III and IV. Adapted from Todd AJ et al, 2010 [16].

Environmental noxious chemicals detection is important, but organisms are also capable of detecting endogenous irritants normally produced during injury and/or inflammation. Beside of activating nociceptor terminals, endogenously generated factors can produce a **peripheral sensitisation** enhancing excitability of these terminals, lowering their response threshold and increasing the response to a given stimulus. Two resulting phenomena arise from this, **hyperalgesia**, an extremely painful reaction to a not so painful stimuli and **allodynia** where non-painful stimuli are perceived as painful. Apart from the peripheral terminals of activated nociceptors, non-neural cells as immune cells, fibroblasts and keratinocytes release inflammatory mediators such as SP, CGRP, adenosine triphosphate (ATP), protons, histamine, bradykinin, serotonin, nerve growth factor (NGF) and a lot more [19, 20].

### 3. ION CHANNELS KEY ROLE IN CELL EXCITABILITY

A wide array of ion channels populates nociceptors termini and transduces sensory inputs, depolarizing nociceptors and propagating the initiated electrical signals upstream to the brain. Among these, transient receptor potential (TRP) channels, acid-sensing ion channels (ASIC), potassium two-pore domain (K<sub>2</sub>P) channels, ATP-gated (P<sub>2</sub>X) receptors and voltage-gated potassium (K<sub>v</sub>), sodium (Na<sub>v</sub>) and calcium (Ca<sub>v</sub>) channels are the principal determinants of action potential generation and propagation in sensory nerves [21].

Chemical and electrostatic gradients have a great relevance on excitable cells like nociceptors. Its generation and dissipation actively depends on the ion channels and transport proteins present in the cell. Chemical gradients are regulated by the opening or closing of ion channels which are protein complexes that constitute aqueous pores in the cell membrane enabling passive diffusion of a given ion. The Na<sup>+</sup>/K<sup>+</sup> ATPase constantly acts to maintain a K<sup>+</sup> high but Na<sup>+</sup> low concentration in the cytoplasm. The net ion flux stops when a balance between the chemical and electrostatic gradients is reached. The voltage for a specific ion, at which this equilibrium is reached, is determined by the **Nernst equation** (1) [22], where  $E_x$  is the Nernst equilibrium potential for an ion,  $R$  is the Gas constant ( $1.987 \text{ cal K}^{-1} \text{ mol}^{-1}$ ),  $T$  is the temperature in Kelvin,  $z$  is the charge of the ion,  $F$  is the Faraday's constant ( $9.648 \times 10^4 \text{ }^\circ\text{C mol}^{-1}$ ) and  $[X]_o$  and  $[X]_i$  are the external and internal concentrations of the ion X, respectively.

$$(1) \quad E_x = \frac{RT}{zF} \cdot \ln \frac{[X]_o}{[X]_i}$$

The cell resting membrane potential ( $V_m$ ) depends on the sodium, potassium, calcium and chloride concentrations inside and outside the cell and the relative permeability of the membrane to each one of the ions. This permeability is dynamic and in turn depends on the amount of a specific subset of ion channels present in a cell and their opened or closed state at a given time. It is described by the **Goldman-Hodgkin-Katz equation** (2) [23], where  $P$  is the permeability of the membrane to a specific ion.

$$(2) \quad V_m = \frac{RT}{F} \cdot \ln \frac{P_x[X]_o + P_y[Y]_o}{P_x[X]_i + P_y[Y]_i}$$

The  $V_m$  of sensory neurons ranges between -45 and -75 mV, which is closer to the equilibrium potential of potassium than sodium because cell membranes are more densely populated by  $K^+$  channels.

### 3.1. Shaping cell excitability

The detection of noxious stimuli at nociceptors terminals starts with the opening of nociceptive ion channels such as ASICs and especially **TRPs** [24]. TRPV1 [25] is of great importance in nociception and will be detailed further on. The activation of this last family leads to an influx of  $Na^+$  and  $Ca^{2+}$  ions through the cell membrane, depolarizing it. If the depolarization is sufficient  $Na_v$  channels activate, allowing more  $Na^+$  ions to enter the cell and further depolarizing the membrane until reaching a threshold that triggers an action potential (AP) firing. Beside  $Na_v$  channels,  $K_v$  channels are also activated by the membrane depolarization, although with slower kinetics.  $K^+$  channels conduct  $K^+$  ions outside the cell, arresting the AP and contributing to the membrane potential repolarization. An appreciable fact is that only few subtypes of  $Na_v$  channels, but a plethora of  $K^+$  channels are expressed in neurons. The dynamic regulation of  $K^+$  channels expression and activity hence opens up a leeway through which neurons tune many excitability features. Leak  $K^+$  current is an outstanding determinant of neuronal  $V_m$ . The enhancement of  $K^+$  leak channels hyperpolarizes cells and reduces the AP firing frequency [26]. On the contrary, halting their constitutive conductance, depolarizes cells increasing neuronal excitability [27]. This means that leak  $K^+$  currents and thus the activity of  $K^+$  leak channels establish the magnitude of a stimulus required to fire an AP and also its spike shape, frequency and intensity [28, 29]. The  $K^+$  leak currents relevance for excitable membrane role has been noted since 1940s [30] but the proteins mediating

them were first detected almost 60 years later [31], the so called **two-pore domain K<sup>+</sup> channels (K<sub>2</sub>P)**.

### 3.2. Two-pore domain K<sup>+</sup> (K<sub>2</sub>P) channels

Four distinct families house almost 80 different types of K<sup>+</sup> channels [32] which have been classified into: voltage-gated (K<sub>v</sub>), inward rectifiers (K<sub>ir</sub>), calcium activated (K<sub>Ca</sub>) and two-pore domain (K<sub>2</sub>P) potassium channels. Although with different transmembrane structure they present a single aqueous K<sup>+</sup> selective pore. The permeation pathway is lined by four P-loop copies with the amino acid sequence signature Gly-Tyr-Gly which configures the selectivity filter [33]. Although the majority of potassium channels are formed by four subunits, each one with one P-loop, the first K<sup>+</sup> leak channel identified in a high organism, *Drosophila melanogaster*, contained two subunits with two P-loops each [34]. A fusion of two of the four subunits forming canonical K<sup>+</sup> channels into a single protein chain is observed giving rise to the typical architecture of the K<sub>2</sub>P channels family.

Currently 15 KCNK K<sub>2</sub>P encoding genes (Figure 3 A) are identified in humans [35] and classified into six subfamilies: **TRESK** (spinal cord located), **TWIK** (weak inward rectifiers), **TASK** (acid-inhibited), **TALK** (alkalinisation-activated), **THIK** (halothane-inhibited), and **TREK** (lipid and mechanosensitive) potassium channels. K<sub>2</sub>P channels present rather low sequence homology by about 20% with the exception of THIK, TASK and TREK subfamilies. K<sub>2</sub>P structural distribution is constituted by four transmembrane domains (TM1-TM4), two re-entrant pore forming loops (P1, P2), a N and C terminal cytosolic domains and an extracellular cap-domain (E1, E2) positioned just above the outer pore formed by the continuity of TM1 into the extracellular part and connected to P1, bifurcating the K<sup>+</sup> permeation pathway (Figure 3 B). It creates the so called extracellular ion pathways which are molecular dimension tunnel-like entrances which actually prevent direct ion flow between the extracellular region and the mouth of the pore. This last motif is thought to hinder interactions between the K<sup>+</sup> pore and peptide toxins to which K<sub>2</sub>P channels are insensitive, contrary to the rest of K<sup>+</sup> channels [36]. Because of the presence of two P-loops per subunit, K<sub>2</sub>P channels are normally assembled as dimers [37, 38], homodimers and sometimes heterodimers [39, 40] especially in the TREK subfamily [41] where all members heterodimerize between them diversifying even more the functionality of these channel types. The first crystal structures of K<sub>2</sub>P channels were reported in 2012 and corroborated K2P1 (TWIK-1) [42] and K2P4 (TRAAK) [43] orchestrate as dimers. These were followed by the publication of K2P10 (TREK-2) [44] and K2P2 (TREK-1) [45] structures.

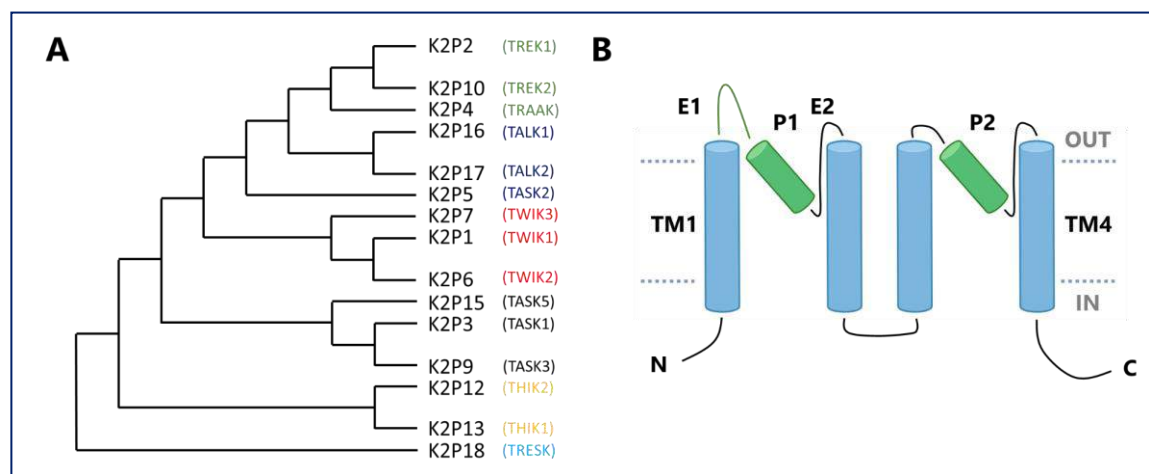


**Figure 3. K<sub>2</sub>P channels family.** 15 K<sub>2</sub>P channel subunits are identified in humans. **A)** Relatedness between protein subunits is represented in the phylogenetic tree. **B)** Cartoon showing the membrane architecture of K<sub>2</sub>P channels with four transmembrane domains (TM1-TM4), two pore forming loops (P1, P2), an N and C terminal cytosolic domains and a cap-domain (TM1-P1 connecting extracellular loop, E1). Adapted from Plant L.D. 2012 [27].

Although it was ignored until recently, K<sub>2</sub>P channels show gating response to voltage even though they lack a conventional voltage sensor [46]. Nevertheless, this voltage dependence seems rather unimportant as its effect is quite weak in channels activated by other pathways like membrane tension, lipids or acidification.

### 3.2.1. TREK channels subfamily

TWIK-1, from tandem of P-domains in a weak inward-rectifying K<sup>+</sup> channel 1, was the first K<sub>2</sub>P channel identified in humans in 1996 by Lesage *et al* [47]. This was followed by the identification of the first member of the TREK subfamily, TREK-1 or TWIK-related K<sup>+</sup> channel 1 in 1996 by Fink *et al* [48]. The resting members of the TREK subfamily, TRAAK from TWIK-related arachidonic acid activated K<sup>+</sup> channel was described in 1998, again by Fink's group [49], and finally TREK-2 or TWIK-related K<sup>+</sup> channel 2 found in 2000 by Bang *et al* [50] and Lesage *et al* [51]. They have been described as mechanosensors being activated by membrane stretch [43, 52-55]

#### 3.2.1.1. Expression and localization

TRAAK and TREK-1 channels are widely expressed in the CNS [56] being actually first cloned from brain and cerebellum, although other K<sub>2</sub>P channels like TWIK-1, TASK-1 and TASK-3 are also expressed in the CNS. TREK-1 and TREK-2 are expressed in embryonic and immature mouse brain in high level, while in adult CNS TREK-1 is found in cortex, striatum, hypothalamus, hippocampus and amygdala [57, 58]. TREK-2 expression

is found in hippocampus, striatum and olfactory bulb [59]. Expression of both channels is also substantive in cortical astrocytes [60, 61]. TRAAK main adult area of expression is the cortex and spinal cord. The TREK subfamily has also been identified in the **peripheral nervous system** (PNS), being the main contributors of the membrane potential maintenance in **DRG** neurons [62]. They localize in large and small diameter neurons of DRG and TG. Different groups have reported distinct relative expression levels in somatosensory neurons of these TREK channels subfamily [63]. This expression contrast could mirror species expression differences and heterogeneity of studied nociceptors and is also supported by the detection of functionally active variants [64-66].

#### 3.2.1.2. Thermosensibility

TRAAK, TREK-1 and TREK-2 have been identified as **thermotransducers**, their activity increases sharply from 37°C to 43°C where it plums increasing the excitability of nociceptors at noxious temperatures [67, 68]. However, they are also active at cold temperatures, for instance TREK-1 activity increases from 22°C to 42°C, while TRAAK function, from 17°C to 42°C. This suggests TRAAK and TREK-1 as fine tuners of nociceptors temperature excitation [69]. Studies which co-localize TRAAK and TREK-1 with some thermoTRPs [70], the thermosensors by excellence [71], support the idea of thermosensation modulation by the TREK subfamily members. TREK channels also modulate **thermal hyperalgesia** in inflammation and **cold allodynia** in neuropathic pain after treatment with oxaliplatin. It is described that oxaliplatin lowers the expression of diverse potassium channels including the TREK subfamily, promoting peripheral nerve excitability. This is backed up by the *kcnk2* and *kcnk4* knockout mice which present altered cold and heat responses [72, 73].

#### 3.2.1.3. Fatty acids regulation

TREK channels subfamily is activated by **polyunsaturated fatty acids** (PUFA) in a reversible manner, representing **arachidonic acid** (AA) the greatest example [49, 74]. The permeation of these channels is being increased 5- to 20-fold in presence of PUFA. Functional evidences support a direct effect of PUFA on channels, linked to structural specificity. Indeed, in the presence of cyclo-oxygenase and lipoxygenase inhibitors, the potency of AA on TREK subfamily is unchanged showing an independency between AA effect and its metabolism. Also, the observed effect is conserved in excised patch-clamp configuration, where cell machinery and metabolism is no longer present [50]. This fact is not observed during the activation by lysophospholipids with hydrophobic acyl chains and

---

polar heads indicating that the effect is not directly exerted over the channel. Neither saturated fatty acids nor PUFA derivatives with substitutions by hydroxyl or methyl esters of the carboxyl group exhibit no effect on TREK channels subfamily [49].

**Phosphatidylinositol-4,5-bisphosphate** (PIP<sub>2</sub>) an acidic membrane phospholipid is the most abundant phosphoinositol in the inner leaflet of the membrane. It has been shown to be involved in the interaction between TREK-1 C-terminal and the plasma membrane activating the channel [75-77]. This was corroborated by the fact that hydrolysis of PIP<sub>2</sub> by phospholipase C (PLC) inhibits TREK-1 probably by the unbinding of its C-terminal from the membrane [78].

#### 3.2.1.4. pH regulation

**Internal acidification** converts low-activity TREK channels into high-activity ones, insensitive to other stimuli like AA, phosphorylation or membrane stretch. Glutamic acid 306 (E306) localized in the C-terminal region was identified through alanine scanning as the intracellular proton sensor in TREK-1 [79]. E306 is located in a cluster of positively charged residues which interact with the membrane enabling the essential interaction C-terminal-membrane to achieve opening of TREK-1. The mutation E306A transforms the channel into constitutively active.

TREK channels subfamily is also sensitive to **extracellular pH** variations. TREK-1 is inhibited by acidification while TREK-2 is activated by it [80, 81]. The extracellular proton (pH<sub>o</sub>) sensor is a conserved histidine residue on several K<sub>2</sub>P members, H126 in TREK-1 and H151 on TREK-2, located on the TM1-P1 loop. Although pH sensor localisation, the opposed responses of these channels are related to differences on P2-TM4 extracellular loop which designates attraction or repulsion between the protonated side chain of the pH sensing histidines and the positively or negatively charged closely located residues. No information regarding TRAAK pH regulation exists.

#### 3.2.1.5. Functional interaction partners

TRAAK is not regulated by **protein kinase A** (PKA) nor **protein kinase C** (PKC) phosphorylation of residues on the cytoplasmic C-terminal, after stimulation of Gs or Gq coupled receptors [82], contrary to TREK-1 and TREK-2 [51]. For TREK-1 a possible interaction between two phosphorylation sites is suggested. Indeed, phosphorylation of serine 333 (S333) by PKA is needed for following phosphorylation of S300 by PKA or PKC [83]. It has been shown that MGLuR2 and MGLuR4 Gi coupled receptors stimulation

reduces PKA activity and increases TREK current. Contrary, other receptors coupled to Gs and Gq like serotonin 5HT<sub>4</sub>sR and 5HT<sub>2b</sub>R receptors, muscarinic M<sub>3</sub>R, angiotensin IIR and glutamate MGlur1 and 5 receptors inhibit TREK channels [84-86]. Another important enzyme which catalyzes hydrolysis of membrane phospholipids is phospholipase D (PLD). PLD<sub>2</sub>, but not PLD<sub>1</sub>, potentiates through direct interaction and phosphatidic acid production TREK-1 and TREK-2, but not TRAAK [87].

Immunoprecipitation and mass spectrometry analysis established **A-kinase anchoring protein** (AKAP150) gets PKA, PKC and other synaptic protein containing PDZ domains in close interaction with TREK-1 [88]. AKAP150 binds to the region comprised between residues V258 and R311 [88]. AKAP150 also binds to TREK-2 but not to TRAAK. When associated with AKAP150, TREK-1 turns completely activated and is no longer sensitive to AA, acidic pH or membrane stretch.

Another association partner of TREK-1 and TREK-2 is **microtubule-associated protein 2** (MAP2). MAP2 binds between residues 335 and 360 of the C-terminal of TREK-1 which contains positively charged residues essential for the binding [89]. Accordingly, MAP2 binds to TREK-2 but not TRAAK because these residues are not conserved in this last channel. The effect of MAP2 is the increase of channel density at the lipidic membrane rather than inducing any change in channel gating properties. Thus MAP2 and AKAP150 present different binding sites which allow both proteins to interact simultaneously and show an additive effect over TREK-1 [89].

**β-subunit of catomer protein complex 1** (β-COP1) was identified as a direct interacting protein of TREK-1 through its N-terminal [90]. Interestingly, β-COP1 also interacts with TREK-2 despite the low conservation of the N-terminal. COP1 participates in the formation of Golgi vesicles involved in transport of membrane proteins. For some K<sub>2</sub>P channels such as TASK-1 and TASK-3, the interaction with β-COP1 has been seen to retain channels in the endoplasmatic reticulum decreasing their surface expression. For TREK-1 it is observed the contrary, surface expression and current density are increased [91, 92]. It is not clear if β-COP1 has any effect on TRAAK.

Finally, **neurotensin receptor 3** (NTSR3) which participates in intracellular protein trafficking directly binds to TREK-1 in the Golgi network. This interaction normally enhances TREK-1 trafficking to the cell membrane, although a post translational maturation process on the N-terminal domain of NTSR3 produces a 44 amino acids

peptide which also binds TREK-1 but triggers its endocytosis [93]. No data relating TRAAK and NTSR3 was found.

### 3.2.2. TRAAK

As mentioned previously, TRAAK or **TWIK-related arachidonic-acid activated potassium channel** structure was first obtained in 2012 by Brohawn *et al* [43] while its gating mechanism was further explored later in 2014 by the same group [55]. If the structure of the channel is observed from a transmembrane view, the transmembrane region spans 35 Å in height and TM2 and TM3 extend 10 Å more into the cytoplasmatic side. The cap-domain unprecedented in other ion channels and conserved through the K<sub>2</sub>P family extends 35 Å into the extracellular side (Figure 4 A). When observed from cytoplasmatic view, the channel has a rhomboidal shape with dimensions of 75 Å x 50 Å (Figure 4 B). The helices TM2 and TM4 are the pore-lining and cross the membrane in an oblique manner, while TM1 and TM3 run almost perpendicular to the lipid membrane (Figure 4 A). The extracellular cap domain presents the characteristics previously explained generally for all K<sub>2</sub>P channels.



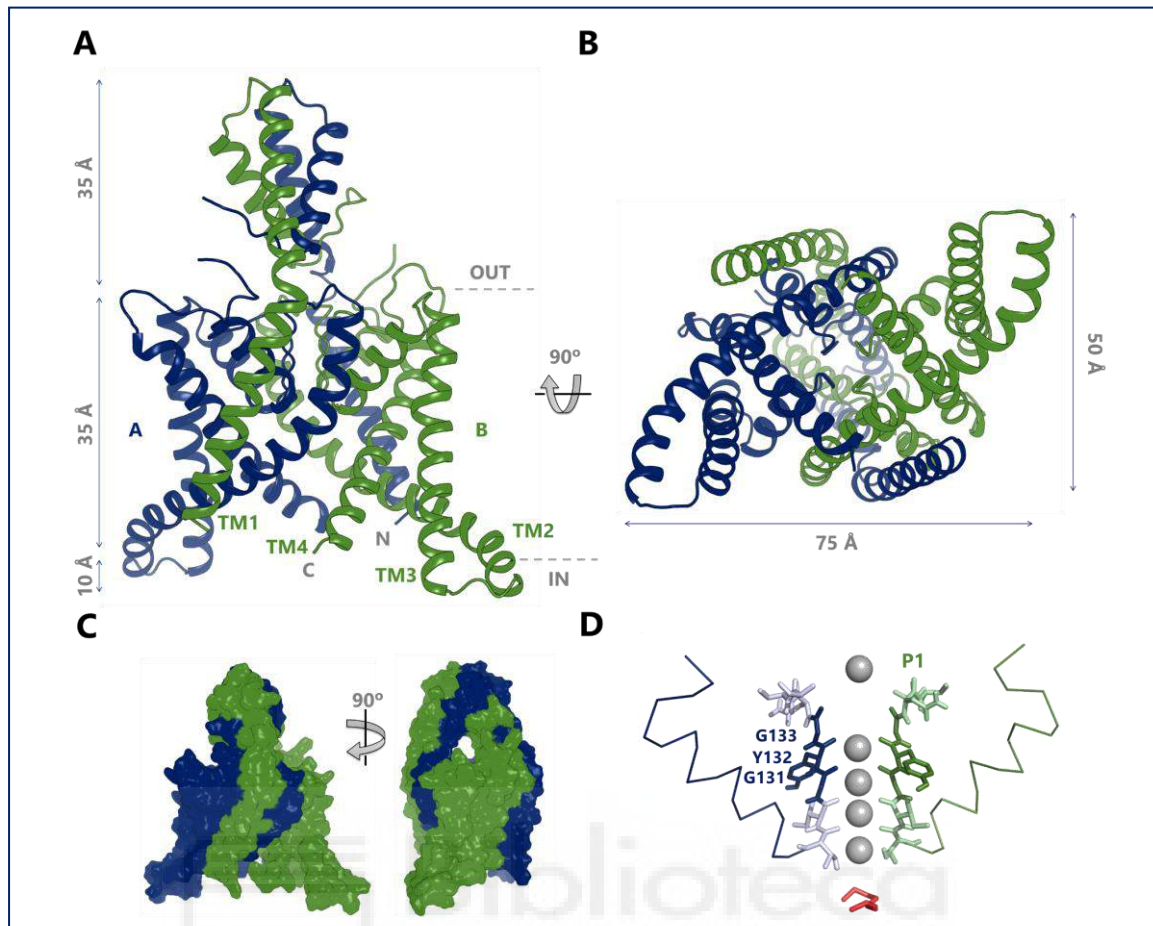


**Figure 4. TRAAK crystallographic structure. General characteristics.** TRAAK in non-conductive conformation observed from transmembrane (A), cytoplasmic (B) view and represented as cartoon. Subunit A is shown in blue while subunit B in green. Transmembrane helices (TM) 1-4 from subunit B are labelled. Approximate position of the lipid bilayer is shown in gray dashed lines. Approximate extensions of each region are shown. C) The same conformation of TRAAK represented as surface to note the bifurcated pore by the presence of the extracellular cap-domain. D) Selectivity filter represented by two of the four P-loops with the typical amino acid sequence signature Gly-Tyr-Gly of potassium ion channels. The pore of the channel in non-conductive conformation is occupied by four potassium ions (in gray) and another one present on the side facing the extracellular compartment. An acyl chain (in red) is occupying the location theoretically of another potassium ion; this probably clogs the pore and gives rise to this non-conductive state of the channel.

### 3.2.2.1. Gating and mechanosensitivity

Similar to other  $K_2P$  members the selectivity filter (SF) of TRAAK is formed by **four P-loops** arranged in pair for each channel subunit and contrary to the rest of  $K^+$  channels which present one P-loop per subunit. SF of the majority of  $K^+$  channels present the **canonical sequence** TxGYGDx (being x a hydrophobic amino acid) and TRAAK's one does not go far from that, being TIGYGNV (Figure 4 D). The central cavity under the SF is wide open and does not present any steric hindrance to ion flow.

In the last reported structure of TRAAK with 2.5 Å resolution and RCSB ID 4WFF (non-conducting state) the channel is asymmetrical because of the position which the TM4 helix adopts in each subunit. TM4A is "up" indicating that TM4A is packed tightly

against TM2B through hydrophobic residues creating a continuous surface that faces the membrane and seals the channel cavity against lipids entry. On the other side TM4B is “down” crossing the membrane without sealing the lateral fenestration exposing the channel cavity to the lipid bilayer through a 5 Å-wide opening between channel subunits (Figure 5 B, upper panel). The oscillation of the helix has as a central hinge point G268, a K<sup>+</sup> channels conserved residue (Figure 5 A). The presence of an electron density corresponding to a ten-carbon acyl chain detected in the crystallographic structure, beneath the SF is thought to be able to reach the cavity (Figure 4 D), extending from this intramembrane lateral opening of the channel, event also observed in other K<sub>2</sub>P related structures like TWIK-1 [42].

In the conductive state (RCSB ID 4WFE) both TM4A and TM4B remain in the “up” conformation sealing any intramembrane opening (Figure 5 B, lower panel). This state was obtained in presence of the TRAAK activator trichloroethanol [94] and the acyl chain density in the cavity under the SF was no longer observed, instead an ion occupied the site. The lipids are also absent in TREK-2 structure blocked by fluoxetine which actually occupies the central cavity entrance [44]. Hypothetically, a TM4 down-positioned where TRAAK structure is **blocked by a lipid is the non-conductive conformation** of the channel. **A TM4 up-oriented produces a conductive** TRAAK state, although, depending on the sort of lipid present in the bilayer, there is a difference in channel conductivity. Indeed, unbranched diphytanoyl acyl chains render lower current levels while branched ones higher. This means that branched lipids are unfavoured when entering the cavity under the SF in order to block ion permeation [55].

The assumption that TRAAK conductivity depends on the arrangement of both TM4 helices is also corroborated by the cysteine double mutant TRAAK (I159C, R284C) which formed a disulphide bridge stabilizing the conductive conformation of the channel [55]. The switch from one state to the other occurs not only due to the movement of TM4 alone but it can be coupled to additional conformational changes. For instance, the cytoplasmatic TM2-TM3 linker rotates 10-15° towards TM4 but only when it is in “up” configuration, otherwise they would sterically clash. This TM2-TM3 linker rotation actually stabilizes the conductive channel. Another change between conductive and non-conductive state is the TM4 extracellular end displacement from the channel conduction axis. These structural changes between both states of the channel can explain its mechanosensitivity which is directly mediated by the lipid bilayer [54].

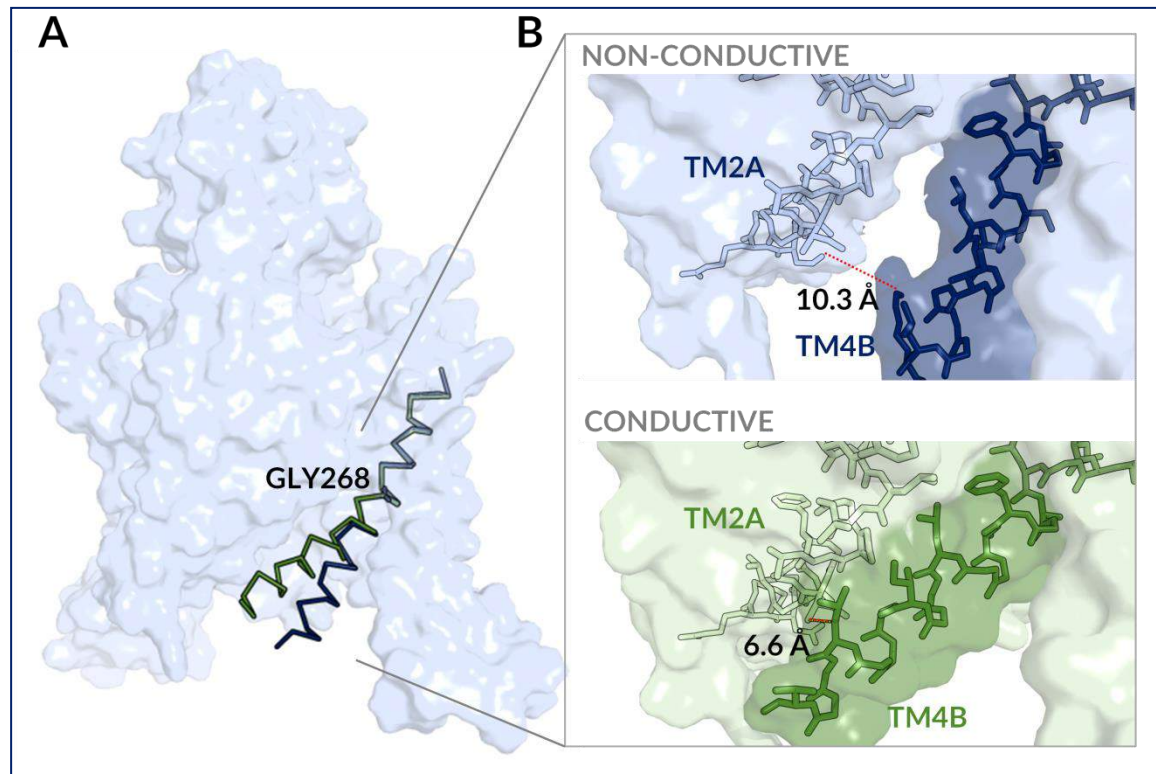


**Figure 5. Structural details of conductive and non-conductive states of TRAAK.** **A)** General overview of TM4B helix (present as ribbon) position in conductive (green) and non-conductive (blue) states of the channel. Helix oscillation centres in G268 as hinge point. **B)** Zoom on TM4B on its interface with TM2A which depicts the presence of a lateral fenestration to the lipid bilayer and a higher distance (red dashed line - 10.3 Å) between both helix in non-conductive state (upper panel) compared to conductive state (lower panel) where this lateral opening is not patent.

The transmembrane **proximal C-terminal domain** (pCt) also plays an important role in channel activity. Actually, it exerts a direct control on TRAAK current amplitude even in absence of stimuli modifying channel properties like open probability and mean open time. pCt has opposite effects on TRAAK and TREK-1, inhibiting the first and activating the last [95]. pCt-SF coupling through TM4 has been suggested [42, 44] and evidenced by the mutation by three glycine residues in the TM4/pCt junction whose flexibility decouples pCt from SF decreasing channel sensitivity to the modulatory effect of pCt [95]. There are also several evidences supporting the idea that pCt interacts directly with the cell membrane. Accordingly, internal acidification acts on TREK-1 E306 decreasing its negative charge thus increasing pCt interaction with the negatively charged phospholipids of the cell membrane stimulating channel activity [79]. Contrary, S333 phosphorylation introduces negative charges into pCt thus decreasing its interaction with the membrane and also channel activity. The negatively charged phospholipid of the membrane which binds to pCt could be PIP<sub>2</sub>. It activates TRAAK [77] and has a dual effect on TREK-1 [76] which suggest that both channels have different affinity to PIP<sub>2</sub>. In this regard, TREK-1 has three positively charged residues R329, R330 and R331 which

are not conserved in TRAAK (Q288, R289, A230) which grants different affinity of both channels to PIP<sub>2</sub>. Swapping both sequences turns TRAAK more sensitive to PIP<sub>2</sub> and also increases its current amplitude. Nevertheless, pCt may not be the only PIP<sub>2</sub> binding site and actually TM1-TM2-TM4 and TM2-P2 subunit junctions could be engaged [45]. In that sense, PIP<sub>2</sub> pulls pCt and TM4 exerting a force that maintains TM4/SF in down conformation in basal conditions in the case of TREK-1 whose “down state” is suggested to be the active one contrary to TRAAK [44].

Expansion of protein cross-sectional area is favoured by membrane tension and is matched with an energy difference needed to promote force activation. The conformational changes that suffers TRAAK from non-conductive to conductive state make its shape more cylindrical which has energetic consequences. This shape matches better the plane of a membrane while a more wedge-shaped channel, in non-conductive state, forces a curvature in the membrane which obviously has an energy penalty [96]. As a consequence, a cylindrical shaped channel is energetically favoured when an increase in membrane tension is produced.

### 3.2.2.2. Pharmacology

TREK subfamily is modulated by diverse chemical stimuli [97-99] such as fatty acids, anaesthetics and diverse drugs. For instance, arachidonic acid is the main lipidic TRAAK modulator [49]. Anaesthetics like chloroform, halothane, isoflurane [100, 101]; anaesthetic gases like nitrous oxide, xenon and cyclopropane [102] and local anaesthetics like bupivacaine and lidocaine [103, 104] have demonstrated a modulatory action over TREK channels subfamily. Also, drugs like riluzole which is a neuroprotective agent employed in amyotrophic lateral sclerosis to protect motoneurons, paroxetine and fluoxetine, a serotonin reuptake inhibitors [45, 88, 105-107] and neurotransmitters-activated second messengers pathways [74, 75, 108] are worth mentioning. A more detailed TRAAK pharmacology view is presented below.

#### 3.2.2.2.1. TRAAK lipidic modulation

AA modulates ion channels and neuronal function by diverse mechanisms. It is able to bind directly to membrane proteins on both sides of the cellular membrane or insert between membrane lipids altering the mechanical properties of the bilayer. It activates PKC pathway and regulates gene transcription [109]. It stimulates channel affinity changes for membrane PIP<sub>2</sub> and finally, its metabolism produces lipid mediators involved in nociceptor inflammatory sensitization [110]. As mentioned previously, TRAAK

is activated by **PUFA** like AA, docosahexanoic acid and eicosapentanoic acid (EPA) [49], and by the anionic amphipath **trinitrophenol** by direct channel binding [53]. It has also been demonstrated that distinct phospholipids activate TRAAK and TREK-1 channels. **Lysophosphatidylcholine** (C18:1), **platelet-activating factor** (PAF, C16:0) and **lyso-PAF** stimulate both channels in a comparable manner. Contrary, no effect on TRAAK nor TREK-1 is exerted by phosphatidylcholine with two acyl chains (C18:0 and C18:1) and lysophosphatidic acid without head group, neither saturated fatty acids like myristate (C14:0), palmitate (C16:0), stearate (C18:0) or arachidate (C20:0). It seems that rather than charge it is the size of the head group which contributes positively to the stimulation of both channels. Indeed, **lysophosphatidylinositol** and **lysophosphatidylserine** are both negatively charged while lysophosphatidylcholine and **lysophosphatidylethanolamine** present neutral charge. In contrast, lysophosphatidylserine and lysophosphatidylethanolamine with smaller head groups are weakly effective while lysophosphatidylinositol and lysophosphatidylcholine which present larger head groups strongly activate both channels. Also, short length acyl chained lysophosphatidylcholine (C6:0 – C10:0) are weakly effective in comparison to long chained ones (C14:0 – C18:0) which strongly activate both channels [111] (Figure 6).

#### 3.2.2.2.2. TRAAK targeted by activators

The vast majority of **opioid** analgesic drugs like morphine modulate nociception affecting mostly  **$\mu$ -opioid receptors** [112] which gets evident from the fact that no analgesic or side effects of morphine are present in  $\mu$ -opioid receptors knock-out mice [113]. This is actually why it becomes so difficult to separate beneficial from side effects of opioids. Nevertheless, it has been demonstrated that TREK-1 acts downstream of  $\mu$ -opioid receptors and shows strong analgesic effects when activated without exhibiting opioid-like adverse effects [114] such as cognitive impairment, insomnia, respiratory depression and dependence [115, 116]. From mutagenesis assays it becomes clear that morphine leads to a reduction in PKA activity and thus stimulates TREK-1 reducing the phosphorylation of S333 in the C-terminal domain of the channel which in turn hyperpolarizes neuronal cells in the pain pathway [114]. Nevertheless, the role of TRAAK and TREK-2 in opioid analgesia has not been studied so far.

The involvement of TREK channels subfamily in analgesia is demonstrated by the use of **riluzole** (Figure 6) to prevent sensory and motor deficits induced by **oxaliplatin** neurophatic effects which limit drastically its clinical use as anticancer agent [117, 118]. Oxaliplatin treatment down-regulates TRAAK and TREK-1 channels in nociceptors and

TRAAK and TREK-1 knock-out mice show an increased sensory perception which mimics wild-type mice treated with oxaliplatin [72]. Riluzole seems to activate TRAAK, TREK-1 [119] and TREK-2 [73] reversing the negative effects of oxaliplatin without affecting its anticancer capacity [120]. It has been effectively used in diverse pain models [121, 122]. TRAAK activation by riluzole is fast, stable and reversible, while TREK-1 activation is transient followed by  $K^+$  current decrease [119]. This double effect on TREK-1 has been related with the capability of riluzole to increase intracellular cAMP activating PKA resulting in TREK-1 inhibition.

**Fenamates** [123] are non-steroidal **anti-inflammatory agents** which are potent activators of  $K^+$  currents in rabbit corneal epithelium [124]. They showed to exert an effect on TRAAK, TREK-1 and TREK-2. In particular, flufenamic, niflumic and mefenamic acid effect was assessed (**Figure 6**). Flufenamic and niflumic acid showed a comparable effect, higher than the one exerted by mefenamic acid [125].

Daniel Minor's group used a yeast-based screen to test more than 100.000 small molecules and developed a dihydroacridine carbazole-based analogue compound **ML67-33** as a fast and reversible activator of TRAAK, TREK-1 and TREK-2, but not other  $K_2P$  channels [126] (**Figure 6**). The compound activates TREK-1 in outside-out and inside-out configuration. Activation of the C-type gate, which can be stabilized by mutations in P1 pore helix G137I [127] or the M4 transmembrane helix W275S [128] and make the channel resistant to ML67-33, suggests this compound acts directly on the C-type gate components and does not require any cytosolic factors. Indeed, C-terminal coupling loss does not affect ML67-33 activation. Activation takes place through a novel mechanism which does not involve C-terminal, contrary to previously reported activators like chloroform and arachidonic acid [74, 129], and inhibitors such as fluoxetine [44, 78].

The fenamic acid derivative **BL-1249** (5,6,7,8-tetrahydro-naphthalen-1-yl)-[2-(1H-tetrazol-5-yl)-phenyl]-amine is a selective potent TREK channels activator when applied extracellularly [44, 130], although its  $EC_{50}$  is 10-fold higher for TRAAK [131] (**Figure 6**). Its effect has shown to reverse the TREK-1 genetic mutation implicated in right ventricular outflow tract tachycardia [132]. It activates TREK channels stimulating the SF C-type gate but also multiple transmembrane domains contribute to BL-1249 effect, such as M2/M3 interface and in particular F185 and L147 for TREK-1. Moreover, C-terminal tail is important for BL-1249 stimulation although its role mediating selectivity action between the TREK channels is limited [131].

All these data lead to the design need and urge of new modulators for TREK channels subfamily and in particular for TRAAK which still remains poorly druggable.

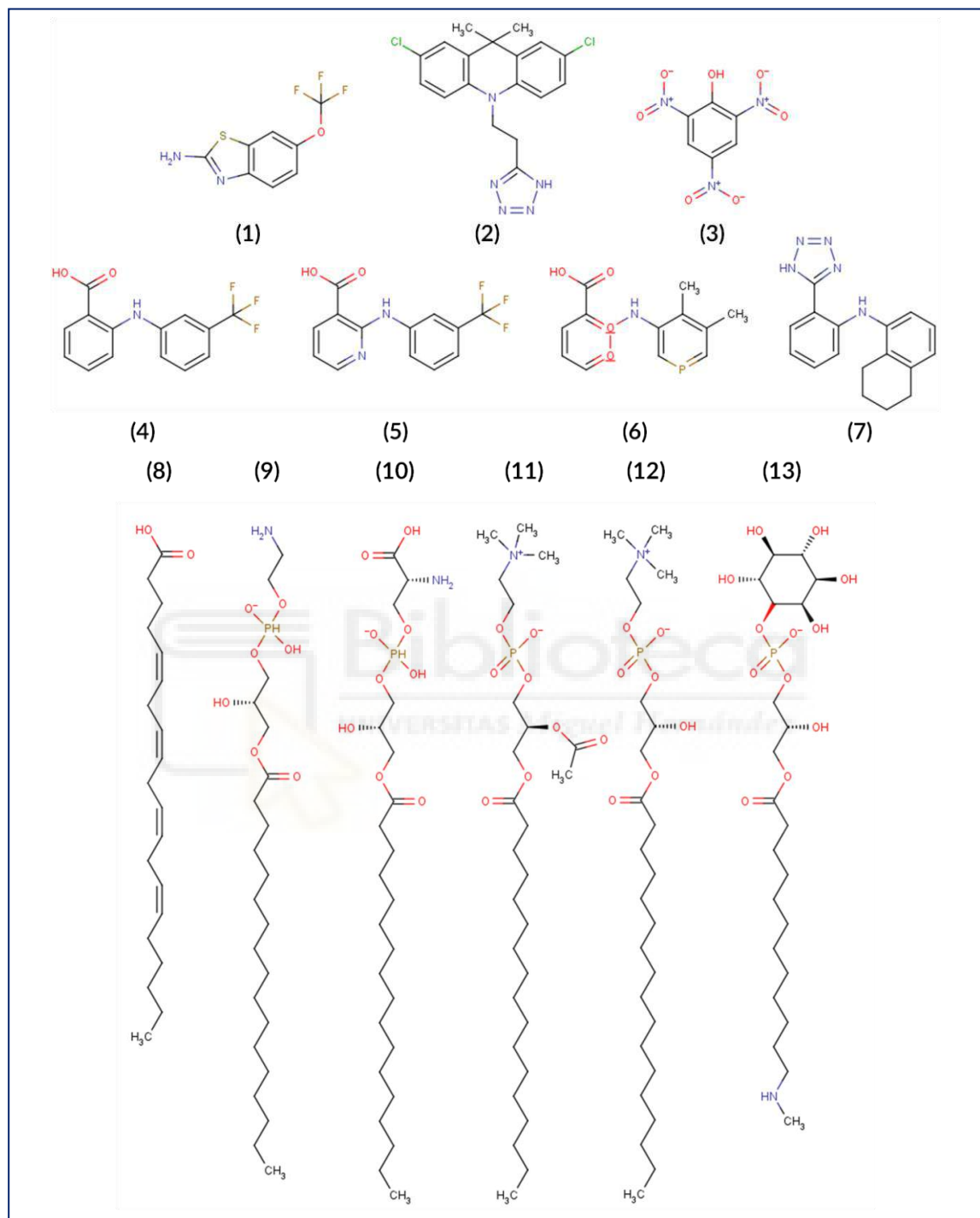


**Figure 6. Chemical structure of TRAAK activators.** Chemical structure of TRAAK activators is depicted as wireframe. (1) riluzole, (2) ML67-33, (3) trinitrophenol, (4) flufenamic acid, (5) niflumic acid, (6) mefenamic acid, (7) BL-1249, (8) AA, (9) LPE, (10) LPS, (11) PAF, (12) LPC, (13) LPI.

### 3.2.2.2.3. TRAAK targeted by inhibitors

The neuroprotective agent **sipatrigine** (Figure 7), a substituted pyrimidine derived from lamotrigine was first developed to antagonize Na<sup>+</sup> [133] and low-voltage-activated Ca<sup>2+</sup> [134] channels. Nevertheless, it showed a much more potent antagonistic effect on TRAAK and TREK-1 [106] proving evidence of the role of TREK channels in neuroprotection.

**TKDC** (N-(4-chlorophenyl)-N-(2-(3,4-dihydroquinolin-2-(1H)-yl)-2-oxoethyl) methanesulfonamide) is an inhibitor of all three members of TREK subfamily, targeting the extracellular cap of these channels [135] (Figure 7). TKDC inhibitory effect on TRAAK is more than 10-fold lower than the inhibition it exerts on TREK-1. TKDC binds between extracellular helices E1 and E2 moving this last against the SF and enhancing its interaction with the pore region blocking the extracellular ion pathway, thus unveiling a novel binding site, merely explored. Mutagenesis studies suggest Q76, I80 and L102 are the key residues for TKDC binding in TREK-1. In TRAAK on the contrary, these residues are substituted by A35, E38 and V42, respectively and are possibly the responsible for the lower TKDC effect on this member. An exclusion of the sulfonil group of TKDC (**28NH**, Figure 7) resulted in a higher inhibitory effect on TRAAK, almost 7-fold change, while conserving the IC<sub>50</sub> range values prior found for TKDC on TREK-1 and TREK-2. Docking models suggest that ionic interactions between E38 and the sulfonil group of TKDC might affect its binding to TRAAK. TKDC was tested on mice and a 10-day chronic treatment with low dose of TKDC showed that the compound is able to induce antidepressant-like effect [135].

**Tetramethrin** is a pyrethroid insecticide which causes sensory alterations like paraesthesias, transient pain and burning when applied dermally (Figure 7). Tetramethrin showed an inhibitory effect on TRAAK, TREK-1 and TREK-2 channels when tested on DRG sensory neurons producing a depolarization-induced neuronal firing. It also activates TRPV1 and TRPA1 nociceptive channels which co-localize with K<sub>2</sub>P channels [70, 136].

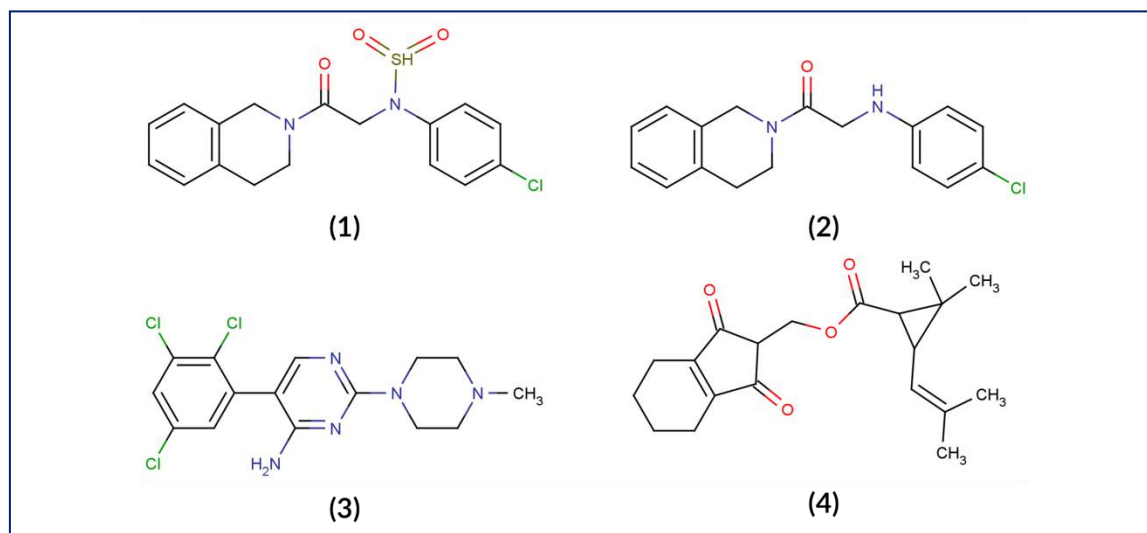


**Figure 7. Chemical structure of TRAAK inhibitors.** Chemical structure of TRAAK inhibitors is depicted as wireframe. (1) TKDC, (2) 28NH, (3) sipatrigine, (4) tetramethrin.

### 3.3. TRP channels family

As previously mentioned, besides  $K_2P$ , TRP channels are of great importance for sensory inputs transduction in nociceptors, especially TRPV1, TRPA1 and TRPM8, all members of the so called thermoTRPs. TRP channels are  $Ca^{2+}$  and  $Na^+$  permeable channels first discovered in *Drosophila* mutant with visual defects and transient instead of sustained photoreceptor potential [137]. The mammalian homologs were identified in 1995 and have been proposed for second messenger and store-operated  $Ca^{2+}$  entry conduction channels [138, 139]. They participate in the intracellular homeostasis of  $Ca^{2+}$  and  $Mg^{2+}$ . There are seven subfamilies of TRP channels: **TRPC** (canonical), **TRPV** (vanilloid), **TRPA** (ankyrin), **TRPM** (melastatin), **TRPP** (polycystin), **TRPML** (mucolipin) and **TRPN** (*Drosophila* NOMPC) expressed only in fish, flies and worms (Figure 8 A). The classification of the TRP superfamily is based on differences in their amino acid sequences and topological structure instead of their function [140, 141].

Briefly, the structure of TRP channels is represented by six transmembrane helices (TM1 - TM6) and a pore-forming loop between TM5 and TM6. Both N- and C-terminal domains are located in the cytosol and vary on the functional motifs and the number of amino acids between different subfamilies. N-terminal of TRPA, TRPV, TRPN and TRPC subfamilies is characterized by the presence of between 4 and 30 tandem copies of **ankyrin repeat domains** which participate in protein-protein interaction. TRPC, TRPV and TRPM subfamilies contain a conserved **TRP box** located in the C-terminal just below the last transmembrane domain lodging hydrophobic residues (Figure 8 B) [142].

TRP channels are modulated by a variety of chemical and physical stimuli including lipid messengers, serine/threonine/tyrosine kinases, exogenous ligands such as capsaicin and allyl isothiocyanate, endogenous molecules like DAG, eicosanoids and inorganic ions as  $\text{Ca}^{2+}$ ,  $\text{Mg}^{2+}$  and  $\text{H}^+$  [143-145]. Physical stimuli represent temperature, mechanical stimuli and voltage [146-148]. The **heterogeneity of modulators** for this family makes these channels essential components of diverse sensory processes like hearing, taste, vision, thermal sensation and as already stated, pain. Indeed, the diverse expression of these nociceptive ion channels is what defines the functional properties of nociceptors [149-152].

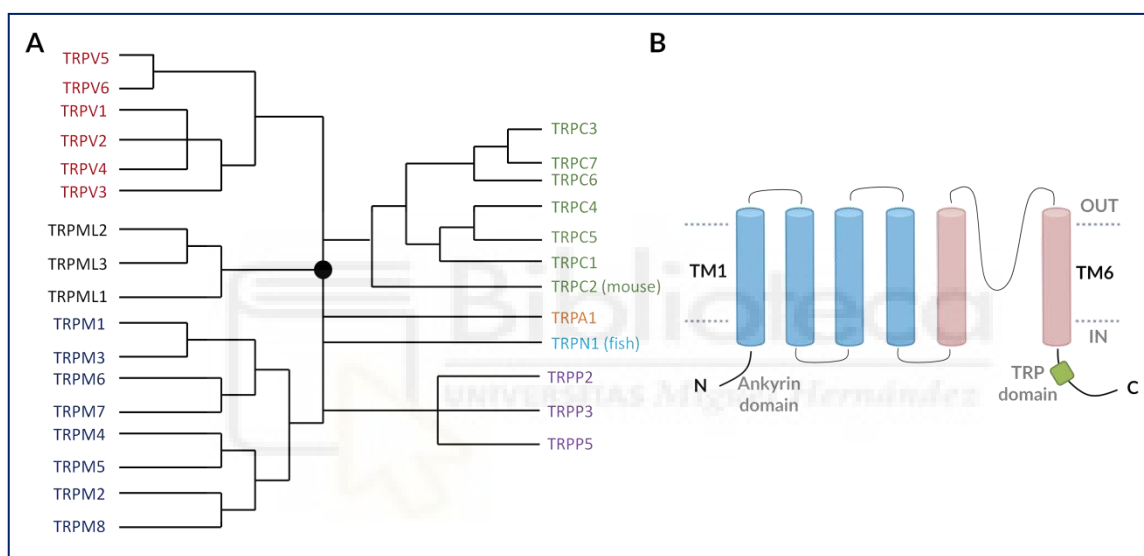


**Figure 8. TRP channels family.** **A)** 29 TRP channels are identified. Relationship level between protein subunits is represented in the phylogenetic tree adapted from Montell C. et al, 2002 [141]. **B)** Cartoon showing the membrane architecture of TRP channels with six transmembrane domains (TM1-TM6), a pore-forming loop between TM5 and TM6, N- and C-terminal cytosolic domains with tandem copies of ankyrin repeat domains and TRP box, respectively.

### 3.3.1. TRPV1 channel

**TRPV1** is one of the six members of the TRPV subfamily involved in noxious sensation and highly expressed in small and medium sized DRG neurons [25]. Its structure follows the pattern of the rest of TRP channels, with 839 amino acids comprising six TM domains, six ankyrin repeat domains in its N-terminal and a large C-terminal domain with a coiled coil domain and a calmodulin binding site [153]. Different splicing variants of TRPV1 have been described resulting in the loss of distinct number of amino acids and shorter molecular structures [154]. TRPV1 is a **polymodal channel** which senses physical stimuli like noxious heat temperatures [155], acidic pH (lower than 5.9) [156] and

mechanical stimuli. It is activated by a diversity of ligands being the best known activator capsaicin a vanilloid pungent substance found in chilli peppers [157], but it is also activated by endovanilloids like leukotriene B4 [158], cannabinoids as cannabidiol [159], toxins as resiniferatoxin (RTX) [160], and inhibited by molecules like capsazepine [161], BCTC [162], nicotine [163] and acetylsalicylic acid [164].

### 3.3.1.1. Expression

TRPV1 is widely expressed along human body. It can be found in **non-neuronal** and **neuronal tissues** including central and peripheral nervous system. Examples of expression in non-neuronal tissues are kidney, cardiac muscle, respiratory system and liver [165-168]. Its expression in the PNS is elevated in DRG and TG neurons. In skin it is found in cutaneous sensory nerve fibers and non-neuronal cells like mast cells, keratinocytes, the infundibulum of hair follicles, sebocytes and sweat glands [169].

### 3.3.1.2. Structure

TRPV1 molecular structure in resting state (RCSB ID: 3J5P) was first resolved in 2013 by Cheng *et al* [170] by 3D cryomicroscopy with a resolution of 3.4 Å including the cytoplasmic domains although with lower resolution of 4.8 Å. TRPV1 has a tetrameric architecture where subunits are arranged in a four-fold symmetry around a central ion permeation pathway (**Figure 9 A**). As other TRP channels, each TRPV1 subunit consists of six transmembrane  $\alpha$  helices spanning the lipid bilayer. Between TM5 and TM6 locates a reentrant loop which together with TM5 and TM6 constitutes the pore. Only four out of six ankyrin repeat domains (ARD) at the N-terminus were identified. They are followed by a linker motif conserved in TRPV subfamily which connects ARD with the pre-TM1 helix. The TRP signature domain, a 23-25 amino acids long region, was also determined as an interfacial helix following TM6 (**Figure 9 B**). It interacts with the TM4-TM5 linker which runs parallel to the membrane, and with the pre-TM1 helix through hydrogen bonding and salt bridges, affecting pore conformation and subunits assembly [142]. The TM1-TM4 domain presents an aromatic hydrophobic cluster, packing tightly and providing rigidity to the domain. Thus it serves as a stationary anchor upon which TM4-TM5 linker moves facilitating channel gating [171]. The outer region of the pore is wide open. The regions of the pore loop proximal to TM5 and TM6 constitute a binding site for spider toxins. By the center of the pore path the selectivity filter  $^{643}\text{GMGD}^{646}$  is found. Continuing down the pore, a constriction site between TM6 helices appears. A hydrophobic seal formed by

residue I679 of the four TM6 helices which are in close proximity conforms the lower gate.

More recently in 2016, TRPV1 structure was captured in lipid nanodiscs in three configurations with improved resolution (2.9 – 3.4 Å). Apo, in resting state unbound to any ligand (RCSB ID: 5IRZ), with the highly potent agonist molecule **RTX**, located in the capsaicin binding site (RCSB ID: 5IRX), and with the inhibitor molecule capsazepine located in the same binding pocket (RCSB ID: 5ISO) [172]. RTX fits precisely into the capsaicin binding pocket establishing hydrogen bonds and hydrophobic interactions with key residues involved in capsaicin binding. RTX forms hydrogen bonds with T550, S512 and R557 and it is stabilized by its hydrophobic interactions with residues L515, V518, M547 and I573 as capsaicin does. RTX, equally to capsaicin, brings closer residues R557 and E570 through hydrogen bonding **pulling the S4-S5** linker from the central axis provoking a conformational change in the channel which opens its lower gate [173]. Capsazepine by the contrary, also interacts with some of the mentioned key residues but does not facilitate the R557-E570 interaction. It competes for the binding to this hydrophobic pocket, stabilizing the channel in its resting state. In the same vanilloid-binding pocket a phosphatidylinositol lipid density in the apo structure was found. This supports the idea that the TRP domain adjacent to TM6 is implicated in the regulation PIP<sub>2</sub> exerts on diverse TRP families [174]. It also rejects the idea that a region containing eight positively charged residues on the C-terminal of TRPV1 are the responsible for PIP<sub>2</sub> binding and inhibitory effect [175].

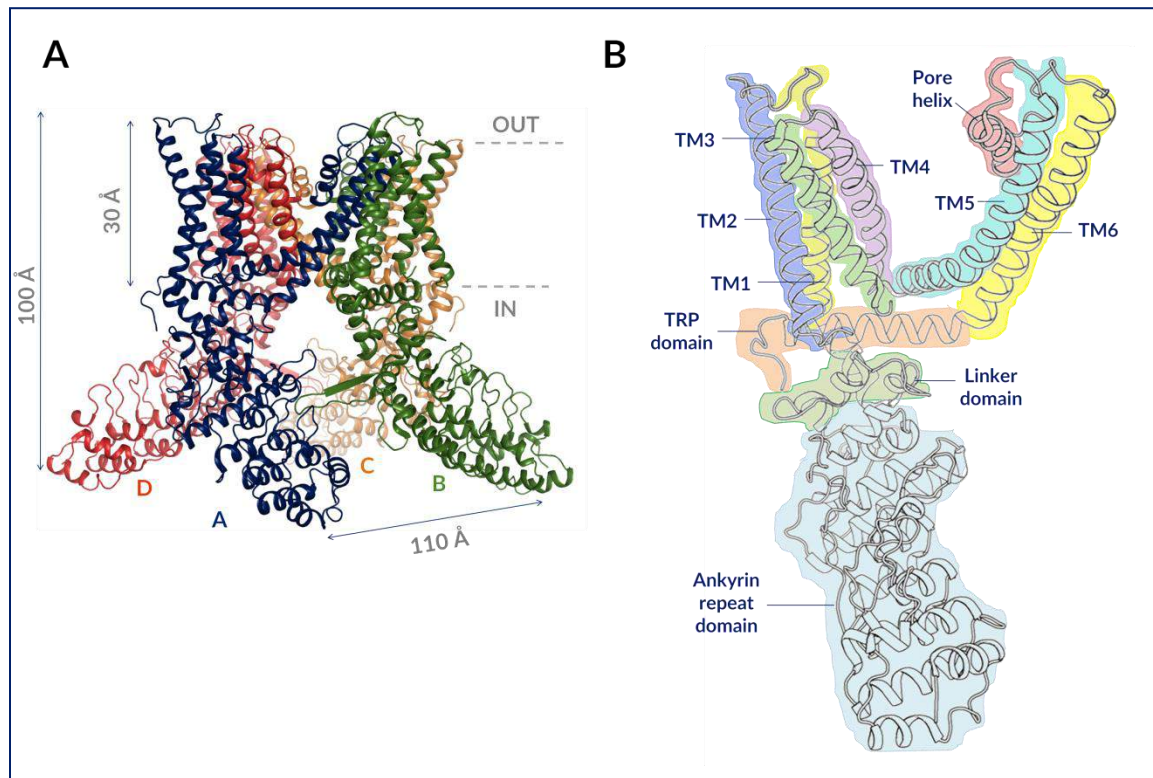


**Figure 9. TRPV1 molecular structure. General characteristics.** A) Tetrameric channel architecture represented as cartoon and where each subunit is depicted in different colour. The span of the transmembrane domain is 30 Å while the whole channel vertical and horizontal lengths are 100 Å and 110 Å, respectively. B) One subunit is represented in detail so different domains can be appreciated. The ankyrin repeat domain is found on the N-terminus, followed by a pre-TM1 linker domain. Then TM1 helix spans the lipid bilayer and connects through a loop to TM2 which is followed by TM3 and TM4 connecting to TM5. Between TM5 and TM6 the pore loop and helix are found. After TM6 TRP domain appears and connects with the cytoplasmic C-terminus not shown on the figure.

### 3.3.1.3. Polymodality

**ThermoTRPs** are gated by temperature changes, in the case of TRPV1 it is stimulated by temperatures  $>43^{\circ}\text{C}$  [157]. It is still unclear how exactly TRPV1 senses these temperature changes. It seems that the protein itself is heat-sensitive since it can be activated by high temperatures being reconstituted in liposomes [176]. Another possibility is that thermoTRPs respond to a mechanical force through the membrane curvature changes induced by temperature [148].

**Protons** evoked currents in primary afferent neurons are carried principally by ASIC and TRPV1 channels. TRPV1 is opened by protons only if extracellular pH decreases below 6 [157]. A mild acidosis, between 6 and 7 sensitizes the channel to other stimuli. Indeed, TRPV1 temperature activation threshold decreases in acidic environments [156]. These different effects of acidic pH on the channel are possible because they are mediated by different amino acid residues. E600 on the extracellular side of TM5 causes a proton induced sensitization, while V538 in the TM3-TM4 linker, T633 in the pore helix

and E648 between TM6 and SF are responsible for the direct channel activation [177-179].

**Voltage** dependence appears clear in current-voltage relations derived from voltage steps from -100 to +40 mV in TRPV1 transfected HEK293 cells exhibiting prominent outward rectification [157].

### 3.3.1.4. TRPV1 lipidic modulation

Endogenous **lipids** from various metabolic pathways including cyclooxygenase (COX), lipoxygenase (LOX) and cytochrome P450 (CYP) can regulate TRP channel activity in sensory neurons which highlights their important role in controlling pain perception in the nervous system. A good example is PIP<sub>2</sub> whose effect on TREK nociceptive ion channels was previously discussed. Besides that, all thermoTRPs are subjected to regulation through direct binding as the case of TRPV1 and TRPA1 or by indirect mechanism involving interacting partners whose activity depends on PIP<sub>2</sub> binding. Although extensively debated, PIP<sub>2</sub> effect on TRPV1 and TRPA1 seems to provoke channel activation and a subsequent desensitization [180, 181]. Another example is **AA** which enhances TRPV1 activity in the same way as it does with other nociceptive ion channels like ASIC. AA potentiates TRPV1 in a dose dependent manner although TRPV1 currents do not fully recover to their basal level after the end of AA application [182]. AA binding site on TRPV1 still remains unknown. As previously discussed, AA metabolism produces diverse mediators which sensitize or directly activate nociceptive ion channels. Such is the case of 12-HETE (hydroxyeicosatetraenoic acid) produced through LOX metabolism of AA which activates TRPV1 [183]. Also leucotriene B4 and hepoxilin A3 have been identified as TRPV1 activators on sensory neurons [184]. COX and LOX metabolites from the precursors EPA and DHA like resolving E1 and D2 have been shown to inhibit TRPV1 [185]. Diverse lipids are able to interact directly with the capsaicin binding site. Such is the case of retinoids with a catechol or vanillyl-like moieties, which serve as reactive groups for the binding to the capsaicin pocket [186]. Another region identified as a lipid binding site is the C-terminal of TRPV1, although the exact residues involved in it are unknown. It is suspected that lysophosphatidic acid (LPA) binds to this C-terminal region [187]. There are still a lot of uncertainties related to the exact lipid binding sites present in TRPV1 [188].

### 3.3.1.5. TRPV1 analgesic targeting

TRPV1 targeted analgesic molecules have centred in two ways of TRPV1 modulation. First, **agonists** that lead to channel opening and following **desensitization** have been developed. An example is capsaicin [189, 190] and molecules with a vanillyl moiety. Nevertheless these compounds present an important clinical limitation, as they produce excitation of TRPV1 expressing sensory C-afferents, giving rise to a notorious burning sensation which usually reduces patient adherence to the treatment [191]. Another property of capsaicin which limits its application is its high lipophilicity increasing its accumulation on skin when used for long periods of time, causing erythema reactions and increasing the risk of skin carcinogenesis in the presence of tumour promoters like sunlight [192, 193]. Some of the strategies used to decrease these side effects centre on delimiting the area of exposure to the substance as it happens with topical patches [194]. The development of weak agonists which cause a strong desensitization or photoswitchable agonists that activate only when irradiated with a particular wavelength constitute other options [195, 196].

On the other hand, numerous **antagonists** of TRPV1 have been developed [197, 198]. Some of them have entered phase I and phase II clinical trials but they have not advanced beyond due to considerable side effects. The most important is the interference with the physiological role of TRPV1 and the hyperthermic risk due to systemic absorption of the compounds and their effect on the CNS [199]. Some antagonists when used during long periods of time also promote tumour development [200]. Thus, the need for novel therapeutic strategies becomes patent.

### 4. TREATING CHRONIC PAIN

As chronic pain is present in multiple pathologies and can affect up to 20% of EU population [201], existing analgesic therapies must be improved. Currently, the majority of pain treatments, from minor to major potency, rely on peripheral analgesics such as paracetamol, the salicylate aspirin and nonsteroidal anti-inflammatory drugs (NSAIDs) like ibuprofen, naproxen, ketoprofen, meloxicam and others. Weak central opioids are also an option, like codeine, and strong central opioids like morphine [202]. Nevertheless, treating chronic pain usually requires prolonged use of analgesics leading to important secondary effects including dependence, depression and death in the case of an overdose by morphine [203].

Thus, the design and development of new therapeutic drugs to treat chronic pain is of vital importance. Different types of pain have been identified and increasing evidences support the idea that potassium channels play an important role in all of them. Among the defined pain types, TREK channels subfamily has recently demonstrated to be closely involved in neuropathic pain release caused by chemotherapeutic agents.

Neurotoxic chemotherapeutic agents used in cancer treatments cause peripheral neuropathies, which are painful and dose-limiting side effects. Up to 85% of patients are affected and report paresthesias on hands and feet [204, 205]. Examples of chemotherapeutic drugs that produce sensory neuropathy belong to the group of taxans, alkaloids (paclitaxel) and platinum drugs (oxaliplatin, cisplatin) [206]. Neuropathic pain can be identified by changes in AP firing patterns, inflammation, axonal transport dysfunction and others [207]. Increased spontaneous firing causes hyperexcitability of DRG sensory neurons and involves voltage-gated sodium channels and potassium channels [208, 209]. In physiological conditions  $K_2P$  channels generate leak currents which hyperpolarize and stabilize neurons at a potential below their firing threshold [210]. Disrupting this constitutive conductance results in cell depolarization and increased excitability. There is no specific FDA-approved treatment for sensory neuropathy although opioid and anti-inflammatory therapies could be considered.

Leak potassium channels have demonstrated to be involved in peripheral neuropathy. Indeed, TREK-2 has been targeted by the activator riluzole in order to abolish the neuropathic side effects of oxaliplatin [120]. Also, TREK-1 modulation by MiR-183-5p has shown to alleviate neuropathic pain [211].

Paclitaxel (brand name Taxol) is a microtubule-binding cancer agent used in solid tumours, which produces hyperexcitability in DRG sensory neurons [206] similar to oxaliplatin and thus could be also counteracted by leak potassium channel activators.

Other types of pain such as inflammation-mediated pain are also suitable to be targeted by potassium channels. It is characterized by sensitization or activation of nociceptors by inflammatory agents like cytokines, chemokines, acidity, etc. K<sub>2</sub>P channels family constitute a good target to treat inflammatory pain as they are inhibited by inflammation molecular components like prostaglandin E2 and acidification [210, 212] causing neuronal hyperexcitability. Sensitization or activation of pro-algesic channels from the TRP family along with K<sub>2</sub>P channels inhibition causes sensory neuron hyperexcitability as already mentioned. Co-localization of both channel families in sensory neurons could open an unexplored way to treat pain, through drug dual action, inhibiting TRP family and activating K<sub>2</sub>P one.





# OBJECTIVES



Biblioteca  
UNIVERSITAS Miguel Hernández





In order to provide heterogeneity of possible chronic pain treatments and explore new molecular targets [27, 97-99, 210] poorly investigated by the time, the main objective of this thesis is the **design, pharmacological characterization and validation of new regulatory molecules of the TRAAK channel activity.**

The specific objectives of this project are the following:

- 1- ***In silico* molecular modelling and identification** of susceptible sites for TRAAK activity modulation.
- 2- TRAAK modulators ***in silico* design and identification.**
- 3- **Functional evaluation** of *in silico* designed putative TRAAK modulators.
- 4- ***In vitro* pharmacological characterisation** of selected hit modulators.





# MATERIAL AND METHODS





## 1. BINDING SITES DEFINITION

### 1.1. Molecular docking assays

Human TRAAK crystal structure in resting state (RCSB ID code: 4WFF) with 2.5 Å resolution and rat TRPV1 crystal structure in open (3.3 Å resolution, RCSB ID code: 5IRZ) and closed (3.3 Å resolution, RCSB ID code: 3J5P) states were obtained from the Research Collaboratory for Structural Bioinformatics (RCSB) Protein Data Bank (PDB) (<https://www.rcsb.org>). AA, EPA, sipatrigine, riluzole, capsaicin and capsazepine structures with PubChem ID 444899, 446284, 60803, 5070, 1548943 and 2733484, respectively, were obtained from the National Centre for Biotechnology Information (NCBI) PubChem database (<https://www.ncbi.nlm.nih.gov/pccompound>). The structure of AG1529 was drawn and transformed into 3D structure with Marvin Sketch from ChemAxon (<https://chemaxon.com/>). TRAAK global blind docking assay was performed in order to determine possible binding sites present in the transmembrane and extracellular domains of TRAAK. Docking procedure was accomplished with AutoDock 4 [213] implemented in YASARA [214] in which a total of 500 docking runs were set. TRPV1 global blind docking was set with 800 docking runs. Ligands were treated as completely flexible, and these were clustered around the putative binding sites. The Assisted Model Binding with Energy Refinement (AMBER03) [215] force field was used in the performance of simulated annealing optimization of the complexes, moving the structure to a nearby stable energy minimum. Docking results were analysed with a homemade Python script which highlights those residues interacting with the ligand most frequently. It provides the interaction frequency and the mean  $\pm$  SD of the interaction energy for each residue. A cluster represents a number of single runs where ligands occupy interaction sites which differ in less than 5 Å RMSD (Root Mean Square Deviation). More positive energies mean more favourable interaction, a convention accepted in physics to which YASARA sticks. To further explore the best binding site for each TRPV1 ligand, a focalized docking assay with a total of 150 flexible dockings was performed in a limited area of 22:30:25 Å (x:y:z) around the capsaicin binding site centered in the global docking conformation that adopted each molecule in this particular site. Figures were drawn with open source PyMol from PyMOL Molecular Graphics System, Version 1.8 Schrödinger, LLC (<http://www.pymol.org>).

### 1.2. Exploring new TRAAK binding sites

To explore new putative binding sites on TRAAK we used TREK-2 crystal structure in complex with the blocker norfluoxetine (RCSB ID code: 4XDK) [44] located on the intracellular opening of the pore and TREK-1 crystal structure in complex with the agonist ML-402 (RCSB ID code: 6CQ9) [45] revealing a new cryptic binding site near the SF. A sequence alignment between the crystallized regions of these two channels with TRAAK was used to compare residues identity between both couples of channels in the respective binding sites. As the sequence alignments revealed key residues were conserved, a structural alignment with YASARA Mustang method [216] was carried out in order to transfer the corresponding ligands to the TRAAK structure. An energy minimization was then performed on the two resulting TRAAK structures so that any steric clashes between side chains of TRAAK residues with the corresponding ligand could be removed.

New antagonists binding site was described in the extracellular domain of TRAAK [135]. Given that no crystal structure complex of TRAAK and neither the antagonists TKDC nor 28NH was reported from that description, a focalized docking assay was performed in order to reproduce the interaction between TRAAK and these ligands which localize in the same binding pocket. TKDC chemical structure was drawn and 3D cleaned using Marvin Sketch from ChemAxon (<https://chemaxon.com/products/marvin>). Focalized docking centred in between E1 and E2 from contrary subunits was performed using the same methodology as in the previous section although flexibility was given to key residues L87(A), E90(A), E64(B), L65(B) and V68(B). A total of 200 runs were performed, treating ligand as completely flexible.

## 2. VIRTUAL SCREENING

### 2.1. Virtual screening assays

Virtual screening (VS) assays were performed with AutoDock 4 [213] (<https://autodock.scripps.edu/resources/adt>) remotely on a node cluster (Scientific Computation Cluster, UMH). Docking preparation of ligands and receptor was achieved with AutoDockTools and AutoDock 4. A grid box (search space) with dimensions in the xyz axis specified on Figure 10, was set with a spacing of 0.375 Å and centred on 4 putative binding sites determined during the TRAAK binding sites definition step. Grid maps or grid-based potential energies files of the receptor were pre-calculated for each atom type present in the library of ligands to be docked. A grid map is a three-dimensional mesh of regularly spaced points enclosing the receptor where each point is the sum of the pairwise potential interaction energy of a probe atom with each atom of the macromolecule. Electrostatics and desolvation maps were also calculated. Receptor and ligands were transformed from pdb and mol2 formats to pdbqt format supported by AutoDock. Pdbqt stands for pdb plus “q” (charge) and “t” (autodock\_type). For each ligand AutoDock performs 50 independent docking runs, all of them starting with the same initial conditions. Docking assay output consisted in a dlq file for each docked ligand from which the free energy of binding in the largest cluster was extracted. From the 50 independent docking runs, all those that presented a RMSD (Root Mean Square Deviation) lower than 0.5 Å were clustered together. Ligands were then sorted by interaction energy being the lowest the best.

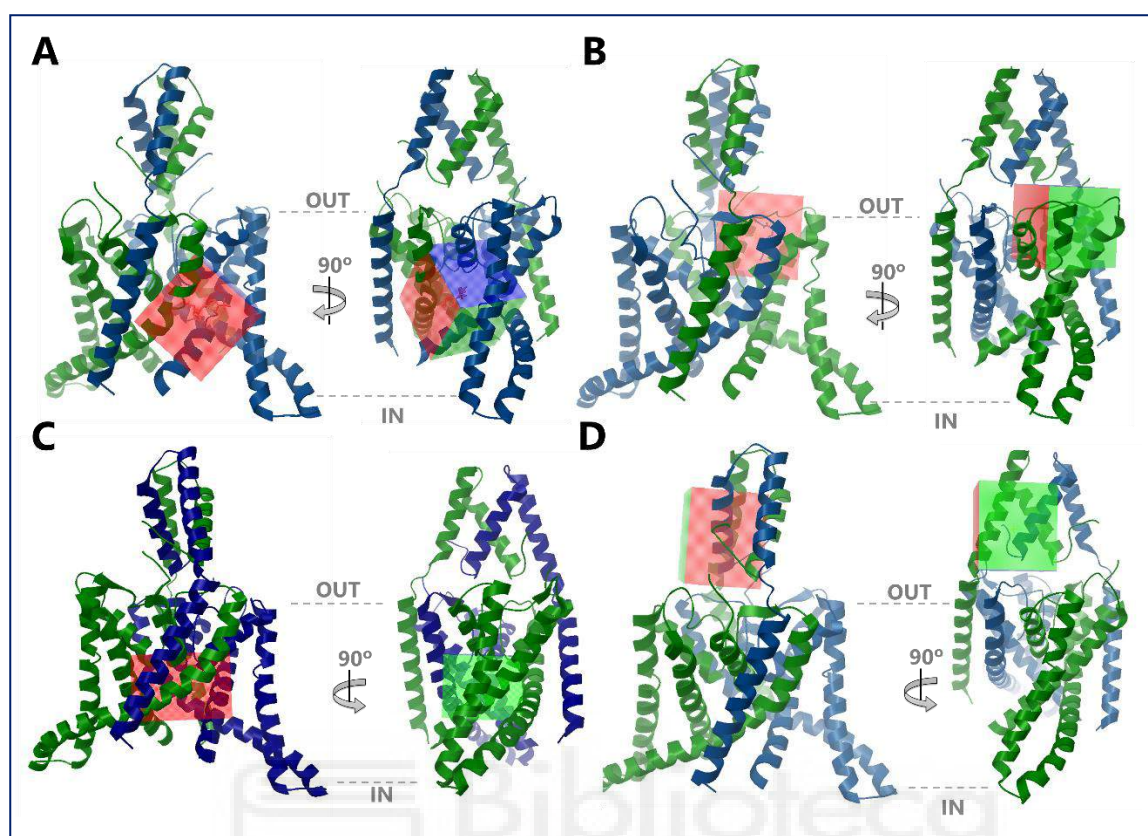


Figure 10. TRAAK VS explored binding sites. TREK-2 norfluoxetine (A), TREK-1 ML-402 (B) TRAAK decane (C) and TRAAK TKDC (D) corresponding binding sites with dimensions 50x50x50 Å (A and B) 50x60x40 Å (C) and 50x45x55 Å (D).

A consensus docking was performed re-evaluating AutoDock constructed dlj files with two other scoring algorithms, DSX a knowledge-based scoring function [217] and X-Score [218]. Final punctuation (3) of each ligand is shown as a summatory of the score of each function normalized to the corresponding score of the control ligand, thus control ligand has always the score of 3.

$$(3) \quad Final_{score} = \left( \frac{AutoDock_{Ligand}}{AutoDock_{control}} \right) + \left( \frac{DSX_{Ligand}}{DSX_{control}} \right) + \left( \frac{Xscore_{Ligand}}{Xscore_{control}} \right)$$

## 2.2. Virtual screening libraries

The chemical libraries used to perform the VS assays contain lipids, FDA approved drugs, natural compounds and peptides. The majority of libraries were downloaded from ZINC database (<https://www.zinc.docking.org>) [219]. This is the case of Prestwick, FDA-approved drugs library, ActiveBiopharma, AfroDB and NubbeNaturals, all three containing natural compounds. A lipid library was obtained from LipidMAPS (<https://www.lipidmaps.org>) [220] and a library of di and tri peptides with different

terminal protections (N-terminal amidation and C-terminal acetylation) was home constructed using PyMOL and Python. In tables, protection is denoted by “1”, thus if both terminals of an alanine dipeptide are protected, the nomenclature would be “AA\_11”.

### 2.3. Structure-activity relationship (SAR)

Affinity and specificity of tested hit compounds were improved by structure-activity relationship (SAR) study. New molecules were constructed using MarvinSketch from ChemAxon (<https://chemaxon.com/products/marvin>). Chemical group substitution was made manually and unsystematically. All ligands were 3D cleaned and saved as mol2 format. Molecular weight, logP, hydrogen bond donors (HBD) and acceptors (HBA) were calculated also with MarvinSketch (*Calculations > Elemental analysis /Protonation /Others*). Ligand docking of molecules of each round was performed with Autodock 4 as previously explained on section 2.1 from Material & Methods in order to obtain the interaction energy in the binding pocket of interest.

## 3. C-TERMINAL DOMAIN RECONSTRUCTION

4WFE and 4WFF crystal structures represent a dimer comprising residues 2-260 of each monomer, thus 133 residues from the C-terminal are missing on both crystal structures. C-terminal reconstruction was performed through homology modelling following distinct procedures. Although there are other K<sub>2</sub>P channels (RCSB ID codes: 4TWK, 4BW5, 3UKM) whose structures have been determined, they are also missing their C-terminal domains due to its high mobility, preventing the possibility to perform a homology model with these crystals.

### 3.1. YASARA automatic homology model based on manual alignment

A peptidic sequence alignment using BlastP (protein-protein alignment) against the PDB repository was performed with the 133 residues long C-terminal TRAAK sequence, with default settings. The only matches corresponded to a 17 amino acids long C-terminal proximal region from mutant TRAAK channels, but which actually are not present in the corresponding crystal structures. BlastP [221, 222] search settings were changed in order to decrease its restrictiveness. Search of short queries was enabled, alignments with high E-value were taken as biologically significant (expected threshold = 20), the seed size which permits alignment initiation was decreased (word size = 2) and gap costs to extend the alignment were also decreased (gap costs: existence = 6,

extension = 2). Three new results comprising longer part of the C-terminal sequence were obtained, although with quite low scores. The best one corresponding to structure with RCSB ID code 1Q15 was used in a homology modelling assay with YASARA. The structure 1Q15 was modified erasing the part not in agreement with the sequence aligned with TRAAK C-terminal corresponding to our template (135-237). A fasta file with the sequence alignment between query (TRAAK C-terminal) and subject (1Q15) was created and provided to YASARA. The model was built manually through the programme interface (*Options > Experiment*). Provided material for the experiment was checked to fulfil the requirements of YASARA which can be found in YASARA manual, section “Build a homology model”. Finally, an energy minimization was carried out executing the available macro script “*md\_run.mcr*” until reaching equilibrium. Model scores are depicted before and after energy minimization.

### 3.2. YASARA manual homology and *ab initio* model

Another strategy used in C-terminal reconstruction consisted in searching protein alignments using as query shorter segments from the TRAAK C-terminal sequence. Alignments were performed with the following regions: 261-293; 294-321; 322-356 and 357-393. Gap costs were modified as follows: Existence = 7, extension = 2. The best alignment of each region was saved as fasta file and each corresponding template structure was shortened to the part observed in the alignment. Homology modelling was performed as previously exposed. TRAAK C-terminal sequence was not entirely covered by the four obtained models (Figure 11), thus *ab initio*-like modelling on the segments not contemplated by the models was performed. Homology models were loaded in YASARA and fused sequentially minimizing the energy of the resulting model (*Simulation > Define simulation cell > Around all atoms > Simulation > Cell boundaries > Periodic > Run macro “md\_run.mcr” > Stop when equilibrium is reached*). The resulting PDB file and sequence in fasta format were saved. Alignment between TRAAK C-terminal and the segmented model was used for the *ab initio*-like modelling (Figure 12).

>TRAAKC					
	260	270	280	290	300
TTIGNWLRVV	SRRT	RAEMGG	LTAQAASWTG	TVTARVTQRA	GPAAPPPEKE
	310	320	330	340	350
QPLLPPPPCP	AQPLGRPRSP	SPPEKAQPPS	PPTASALDYP	SENLA	FIDES
	360	370	380	390	
SDTQSERGCP	LPRAPRGRRR	PNPPRKPVRP	RGPRPRDKG	VPV	

**Figure 11. TRAAK C-terminal sequence coverage by the four short homology models.** Uncovered regions are depicted in yellow and each homology model appears in distinct colour (red, cyan, green, purple).

```

>TRAAKC
SRRTAEMGGLTAQAASWTGTVTARVTQRAGPAAPPPEKEQPLLPPPPCPAQPLGRPRSFS
PPEKAQPPSPPTASALDYPSENLAFIDESSDTQSERGCPLPRAPRGRRRPNPPRKPVRPRGPRPRDKGVPV

>SegmentedModel
-----LTAQAASWTGTVTARVTQRAGPA-PPPEKEQPLLPPP-----
PPEKAQPPSPPTASALDYPSENLAFIDESSDTQSERGCPLPRAPRGRRRPNPPRKPVRPRGPRPRDK-----

```

**Figure 12.** YASARA format alignment between TRAAK C-terminal sequence and the short segmented homology model needed to construct the *ab initio*-like C-terminal structure model.

### 3.3. YASARA automatic homology model

TRAAK C-terminal model construction was also tried automatically with YASARA starting only with the C-terminal sequence in fasta format and executing the assay as follows: *Options> Choose experiment> Homology modelling> Select fasta*. The target sequence was blasted against UniRef90 using PSI-BLAST [223] in order to build a position-specific scoring matrix (PSSM) and then using this profile PDB was searched for potential templates. Target secondary structure prediction and sequence profiling were also obtained on this step. Templates sequence profiles were obtained as target's or from YASARA's more accurate PSSP database (**P**rofiles from **S**equence- and **S**tructurally related **P**roteins). Target-template alignment was obtained using SSALN (alignment algorithm using structure-dependent substitution matrices and gap penalties learned from structurally aligned protein pairs) scoring matrices [224]. An alignment score was given to each template and structural quality was checked according to WHAT-CHECK [225] from PDBFinder2 database [226]. More extended explanation of the steps followed by YASARA during an automatic homology modelling can be found on its User Manual.

In the model quality diagram, a depression in quality was observed in comparison with the first region of the segmented homology model constructed before, thus a swap in that region increased overall model quality.

### 3.4. YASARA Z-score

YASARA scores the homology models by a Z-score also known as standard score. It represents a validation not based on quantum chemistry but on a comparison with a gold standard of a reference structure and more specifically, on general aspects of protein structure codified in knowledge-based energies. Nevertheless, these energies depend on the size and shape of the protein, so they must be normalized in order to obtain estimates of the expected average energy and standard deviation. Thereby, obtaining a Z-score

means calculating how many standard deviations a given structure is away from the average of a gold standard and it can be expressed as the following equation, where  $x$  is a raw value,  $\mu$  is the average value of a gold standard population and  $\sigma$  is the standard deviation of this population.

$$(4) \quad Z = \frac{x - \mu}{\sigma}$$

Z-score comprises the following values: <-5 - disgusting; <-4 - terrible; <-3 - bad; <-2 - poor; <-1 - satisfactory; <0 - good; >0 - optimal. The elements taken in consideration in the structure scoring were dihedrals, where normality of dihedral angles according to the force field was checked and 1D and 3D packing which stand for the normality of 1D and 3D distance-dependent packing interactions in the YASARA2 force field [227], respectively. Dihedrals or also torsion angles in a polypeptide chain describe the rotation of the polypeptide backbone around bonds between N-C $\alpha$  ( $\varphi$ ) and C $\alpha$ -C ( $\psi$ ). Protein torsion angles of a given protein structure are normally plotted in a Ramachandran plot which provides a convenient way of visualizing its distribution. Dihedrals Z-score in YASARA, similar to Ramachandran plot serves as an indicator of the quality of 3D structure because torsion angles control protein folding and actually, if we were able to predict the Ramachandran angles for a particular protein, we would be able to predict its fold. The final model quality is a weighted sum of each parameter as follows:

$$\text{Overall model quality} = 0.145 * \text{Dihedrals} + 0.390 * \text{1D packing} + 0.465 * \text{3D packing}$$

### 3.5. Online 3D structure prediction tools

A variety of online servers are available for protein structure prediction. Between them, the ones used for TRAAK C-terminal structure prediction were SWISS MODEL (<https://swissmodel.expasy.org/interactive>) [228, 229], PS-v2 Protein Structure Prediction Server (<http://ps2.life.nctu.edu.tw>) [230, 231], Phyre2 (<http://www.sbg.bio.ic.ac.uk/~phyre2/html/page.cgi?id=index>) [232], I-TASSER (<https://zhanglab.ccmb.med.umich.edu/I-TASSER/>) [233] and Galaxy Homomer (<https://bio.tools/galaxyhomomer>) [234].

### 3.6. Secondary structure prediction

Secondary structure prediction of TRAAK C-terminal was carried out using two online servers, CFFSP (<https://www.biogem.org/tool/chou-fasman/>) [235, 236] and GOR (<http://cib.cf.ocha.ac.jp/bitool/GOR/>) [237]. Entire TRAAK sequence was used in order to check if predictions would match with already crystallized TRAAK regions.

## 4. PUTATIVE PROTEIC INTERACTING PARTNERS

The high number of proline residues in the C-terminal domain of TRAAK is indicative of a possible presence of SH3 target regions. The online tool PrediAdan [238] contains 84 SH3 domain structures (<http://adan-embl.ibmc.umh.es/asp/phosphoprotein/phosphoproteinlist-prediadan.asp>). The ability of a residue to fit in a position of a ligand can be evaluated through position specific scoring matrices (PSSM). PSSM are built by individual mutagenesis and its energetic evaluation of each position of SH3 domains ligands, previously transformed to poly-Ala, to the 20 natural amino acids. Position by position scan was performed with FoldX [239]. Thus, this tool allows to perform estimates, given a base sequence, if any region of it can act as a ligand of any of the 84 SH3 domains and therefore if TRAAK interacts with the protein that contains a given SH3 domain. 7 fragments from the C-terminal domain were evaluated against the 84 SH3 domains available in the server. Due to the different length of each ligand, the obtained energy was normalized per residue.

## 5. CHEMICAL COMPOUNDS

All chemical compounds used in this work are summarized in Table 2. Arachidonic acid, menthol, AITC and terfenadine stock solutions were prepared in 100% ethanol, amiloride in distilled water and the rest of compounds in 100% DMSO. Astemizol was stored at 4°C, the rest of compounds at -20°C. Arachidonic acid stock solution was gassed with nitrogen in order to prevent it from oxidation during storage.

**Table 2. Chemical compounds.** Compounds name, synthesis name, reference and work concentrations are specified.

Compound name	Synthesis name	Reference	Work concentration
Arachidonic acid (AA)	<i>cis,cis,cis,cis</i> -5,8,11,14-Eicosatetraenoic acid	10931, Sigma Aldrich	10, 25, 50, 100 µM
Capsaicin	8-Methyl-N-vanillyl-trans-6-nonenamide	M2028, Sigma Aldrich	1 nM – 20 µM
Capsazepine	N-[2-(4-Chlorophenyl)ethyl]-1,3,4,5-tetrahydro-7,8-dihydroxy-2H-2-benzazepine-2-carbothioamide	C191, Sigma Aldrich	10 µM
BCTC	N-(4-tertiarybutylphenyl)-4-(3-chloropyridin-2-yl)tetrahydropyrazine-1(2H)-carbox-amide	SML0355, Sigma Aldrich	1 nM
Menthol	2-Isopropyl-5-methylcyclohexanol	M2772, Sigma Aldrich	100 µM
AMTB	N-(3-aminopropyl)-2-N-(2-thienylmethyl)benzamide hydrochloride	SML0103, Sigma Aldrich	10 µM
AITC	Allylisotiocyanate	377430, Sigma Aldrich	60 µM
HC030031	1,2,3,6-Tetrahydro-1,3-dimethyl-N-[4-(1-methylethyl)phenyl]-2,6-dioxo-7H-purine-7-acetamide	H4415, Sigma Aldrich	10 µM
AG1529	2-((4-hydroxy-2-iodo-5-methoxybenzyl)amino)-2-oxoethyl dodecanoate	Medalchemistry	100 nM – 30 µM
Sipatrigine	2-(4-Methyl-1-piperazinyl)-5-(2,3,5-trichlorophenyl)-4-pyrimidinamine	4044, Tocris	10 µM
Irinotecan	(S)-4,11-diethyl-3,4,12,14-tetrahydro-4-hydroxy-3,14-dioxo-1H-pyrano[3',4':6,7]indolizino[1,2-b]quinolin-9-yl ester	I1406, Sigma Aldrich	1, 10, 50, 100 µM
Astemizole	1-(4-Fluorobenzyl)-2-(1-[4-methoxyphenethyl]piperidin-4-yl)aminobenzimidazole	A2861, Sigma Aldrich	10 µM
Terfenadine	α-[4-(1,1-Dimethylethyl)phenyl]-4-	T9652, Sigma Aldrich	10 µM

---

	(hydroxydiphenylmethyl)-1-piperidinebutanol		
TEA	Tetraethylammonium	T2265, Sigma Aldrich	2 mM
Amiloride	N-Amidino-3,5-diamino-6-chloropyrazinecarboxamide	A7410, Sigma Aldrich	50 $\mu$ M

---

## 6. CELL CULTURE

### 6.1. Plasmid amplification

pCMV6-Entry mammalian vector with C-terminal Myc- DDK Tag expressing human TRAAK channel was obtained from OriGene (Ref. RC213846) (Figure 13). Plasmid amplification was carried out on competent C41 *E. coli* bacteria. These were incubated with 1.7%  $\beta$ -mercaptoethanol (Ref 63690, Fluca) during 10 minutes in ice in order to permeabilize their membrane. 100 ng of plasmid were added to 90  $\mu$ L competent bacteria culture and incubated 30 minutes in ice, followed by a thermal shock of 45 seconds at 42°C and 2 minutes in ice. 900  $\mu$ L of liquid Luria-Bertani (LB) media was then added and incubated during 1 hour at 37°C. 200  $\mu$ L of bacteria suspension was seeded on solid LB media petri dishes with kanamicin (25  $\mu$ g/ $\mu$ L) as resistance antibiotic. An isolated colony was picked and grown in 50 mL liquid LB media with kanamicin during 1 day at 37°C. Plasmid purification was performed using E.Z.N.A Plasmid midi kit (Ref. D6904-03, Omega Biotek) following manufacturer's instructions. Purified plasmid was quantified using NanoDrop spectrophotometer taking in consideration that 260/280 nm and 260/230 nm ratios must be between 1.8 and 2.0. Lower ratios indicate possible proteic or kit fenolic compounds contaminations.

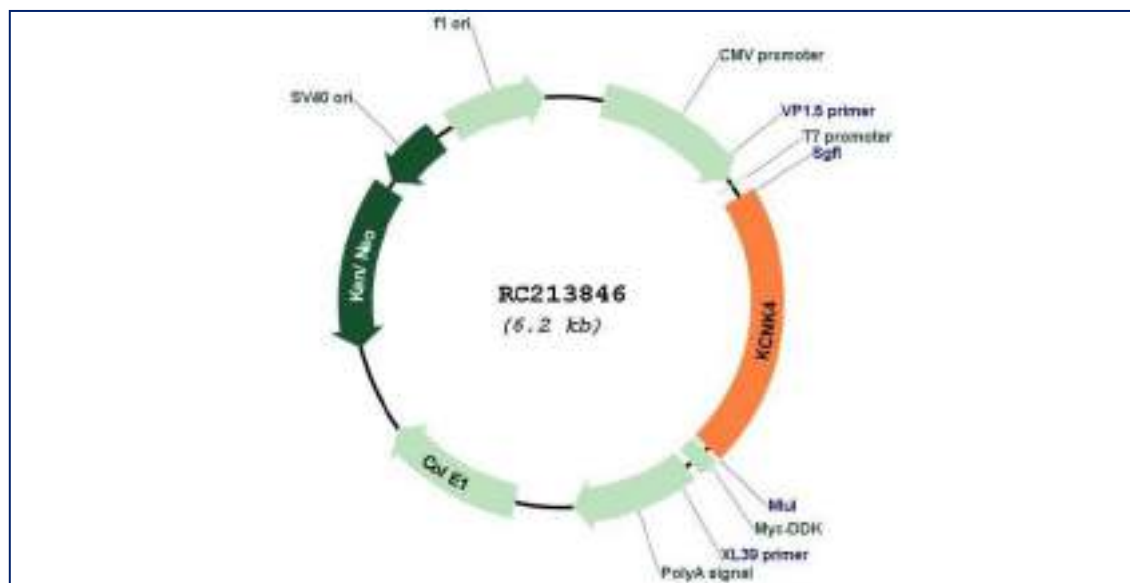


**Figure 13. Circular map for RC213846.** Plasmid vector type pCMV6-Entry map expressing human gene KCNK4 encoding TRAAK ion channel, followed by a Myc-DDK tag, under a cytomegalovirus promoter and containing kanamycin and neomycin antibiotic resistance genes.

## 6.2. Stable cell line Hek 293LTV

Human Embryonic Kidney cells (Hek) 293LTV were grown for maintenance on a T25cm<sup>2</sup> flask until 90% confluence in supplemented medium (DMEM medium with 2 mM Glutamax (Ref. 31331, Gibco), 1% penicillin/streptomycin (P/S) (Ref. 15140, Gibco), 10% fetal bovine serum (FBS) (Ref. 10500, Sigma Aldrich) and 0.8% essential amino acids (Ref. 11140, Gibco)). Cells were dissociated with a 3 min incubation of 1 mL Trypsin-EDTA 0.05% (Ref. 25200, Gibco) followed by enzyme inactivation with 5 mL complete medium. All cell culture procedure was performed in a laminar flow cabinet (Model Telstar AV-100). Culture was maintained on 37°C, 5% CO<sub>2</sub> in a ThermoScientific incubator.

## 6.3. TRAAK recombinant expression in Hek 293LTV cells

Hek 293LTV cells at 60% confluence were transiently co-transfected with hTRAAK and YFP encoding plasmids using Lipofectamine 3000 (Ref. L3000, Invitrogen) following manufacturer instructions. The total amount of plasmid DNA used in T25cm<sup>2</sup> flask transfection was 4.5 µg in a relation of 2:1 (hTRAAK:YFP). 48h post transfection cells were trypsinized and seeded with a confluence of 20.000 cells/well on a 12 mm glass coverslip treated with poly-L-lysine solution (Ref. P4707, Sigma Aldrich). All experiments were performed after 24-48h cell seeding.

#### 6.4. Primary culture of DRG nociceptors

All procedures were approved by the Institutional Animal and Ethical Committee of the University Miguel Hernández de Elche (UMH), in accordance with the guidelines of the Economic European Community, the National Institutes of Health, and the Committee for Research and Ethical Issues of the International Association for the Study of Pain. Animals were kept in a controlled environment (21– 23°C, 12 h light/dark cycle), and had food and water available *ad libitum*. Neonatal Wistar rats were purchased from UMH in house bred stock (originally from Harlan Laboratories). Neonatal DRGs from Wistar rats (3–5 days-old) were isolated and digested with 0.25% (w/v) collagenase (type IA, Ref. C9891, Sigma Aldrich) in DMEM GlutaMax with 1% (v/v) P/S solution for 1 h (37°C, 5% CO<sub>2</sub>, ThermoScientific incubator) [240, 241] and then mechanically dissociated. Single cell suspension was passed through a 100 µm cell strainer and washed with DMEM GlutaMax with 10% (v/v) FBS and 1% (v/v) P/S. Cells were seeded on 12 mm glass coverslip treated with poly-L-lysine (Ref. P9155, Sigma Aldrich) and laminin (Ref. 2020, Sigma Aldrich) (5 µg/mL) in DMEM GlutaMax with 10% (v/v) FBS and 1% (v/v) P/S, supplemented with mouse 2.5S NGF 50 ng/mL (Ref. G5141, Sigma Aldrich) and 1.25 µg/mL cytosine arabinoside (Ref. C1768, Sigma Aldrich). All experiments were performed 48 h after cell seeding. All cell culture procedures were performed in a laminar flow cabinet (Model Telstar AV- 100).

To induce a neuropathic pain *in vitro* model, neurons were cultured on 12 mm glass coverslips for 5 days and then were treated with 10 µM taxol for 24 hours. Patch clamp registers were performed on day 8. IB4+ and IB4- neurons were distinguished by IB4-alexa 568 (Molecular Probes, Invitrogen) labelling (10µg/mL in external solution during 10 min followed by 10 min wash). Antibody fluorescence was visualized with ET545 excitation filter and ET605 emission filter.

## 7. ELECTROPHYSIOLOGY

### 7.1. Patch-clamp recordings from recombinant cells

Whole-cell patch-clamp recordings were conducted using an EPC-10 amplifier (HEKA Elektronik) with Patchmaster software. Patch pipettes, prepared from thin-wall borosilicate capillary glass tubing, were pulled with a horizontal flaming/brown Micropipette puller Model P-97 from Sutter Instrument to a final resistance of 2-8 M $\Omega$  when filled with internal solution. Recordings were acquired at 10 kHz and low-pass filtered at 3 kHz. Recordings with leak currents >200pA or series resistance >20M $\Omega$  were discarded. All measurements were performed at room temperature except heat-evoked TRPV1 activity recordings.

#### 7.1.1. TRAAK recordings

Intracellular pipette solution to record TRAAK currents contained (in mM): 150 KCl, 5 EGTA, 3 MgCl<sub>2</sub> and 10 HEPES, pH 7.4 adjusted with KOH. Extracellular physiological solution contained (in mM): 150 NaCl, 5 KCl, 1 CaCl<sub>2</sub>, 3 MgCl<sub>2</sub> and 10 HEPES, pH 7.4 adjusted with NaOH.

Cells were maintained at a holding potential of -70 mV. Voltage dependence was studied in a voltage step protocol from -120 mV to 120 mV using 100 ms steps. Conductance was calculated with equation:

$$(5) \quad G = \frac{J}{V - V_r}$$

where G is channel conductance, J is the current density (nA/pF), V<sub>r</sub> (mV) is the reversal potential and V (mV) is the applied voltage.

AA was applied at 10  $\mu$ M to check TRAAK expression in transfected cells with exception of AA dose-response experiments where it was assessed at 10, 25, and 50  $\mu$ M. Current was registered by voltage ramps from -120 to +120 mV with a duration of 500 ms and in 10 mV increments and interpulse of 500 ms, or stepping from -120 to +120 mV with a duration of 100 ms in increments of 10 mV and interpulse of 3 s. Compounds were tested over the basal TRAAK current. The protocol consisted in the application of 10  $\mu$ M AA followed by a variable washout period until current reached basal level. Each tested substance was applied during 1 min followed by a washing period. Percentage of activation or blockage is expressed relative to basal current. Time to reach maximum current amplitude was measured only when AA was applied or in combination with a

blocker compound. Protocol consisted in two AA pulses with a washout period in between for control experiments, or the application of AA along with a blocker during the second pulse. Time to reach maximum current amplitude was normalized to first AA peak.

Expression magnitude of other Hek potassium channels was studied by 2 mM TEA blocker application alone or in presence of AA, in mock and TRAAK transfected cells. Cells were perfused with the substances 1 min before each register.

### 7.1.2. TRP recordings

Intracellular pipette solution to record TRP currents contained (in mM): 150 NaCl, 3 MgCl<sub>2</sub>, 5 EGTA and 10 HEPES, pH 7.2 adjusted with CsOH. Extracellular physiological solution contained (in mM): 150 NaCl, 6 CsCl, 1 MgCl<sub>2</sub>, 1.5 CaCl<sub>2</sub>, 10 glucose and 10 HEPES, pH 7.4 adjusted with NaOH. For extracellular acidic solution (pH = 5.5) 10 mM HEPES was substituted with 10 mM MES remaining the rest of components equal to the physiological solution and adjusting to pH 5.5 with HCl.

In voltage-clamp recordings, cells were maintained at a constant potential to evaluate distinct modulators. Total currents were always normalized to the first current peak evoked by a stimulus.

For capsaicin dose-response relationships (from 1 nM to 20 μM), responses were normalized with respect to that evoked in the absence of the channel blocker. Capsaicin dose-response curves were fitted to the Michaelis-Menten Isotherm:

$$(6) \quad \frac{I}{I_{max}} = \frac{1}{\left(\frac{1+[capsaicin]}{EC_{50}}\right)^{nH}}$$

where EC<sub>50</sub> denotes the concentration of capsaicin needed to activate half of the maximal response, and nH denotes the Hill coefficient, which is an estimation of the number of vanilloid binding sites. Dose-response curves for blockade activity were fitted to the Michaelis-Menten Isotherm:

$$(7) \quad \frac{I}{I_{max}} = \frac{1}{\left(\frac{1+[blocker]}{IC_{50}}\right)^{nH}}$$

where IC<sub>50</sub> denotes the concentration of channel blocker that inhibits half of the response obtained in its absence (I<sub>max</sub>). Experimental data were fitted to the Hill equation with a nonlinear least-square regression algorithm with the Prism7 software package.

Reversibility of AG1529 effect was assessed in a two pulses 500 nM capsaicin protocol (P1, P2) separated by 90 s wash. 1  $\mu$ M AG1529 was applied 30 s before and during P1 (AG1529 treated cells). TRPV1 desensitization was monitored only by the application of two capsaicin pulses (control cells). Ratios P2/P1 between control and AG1529 treated cells were compared.

1  $\mu$ M AG1529 effect on TRPV1 voltage dependence was studied in a voltage step protocol from -120 mV to 120 mV using 100 ms steps of 20 mV from a holding potential at 0 mV. Leak currents were not subtracted. Conductance was calculated with equation (5).

Heat-elicited TRPV1 currents were evoked by increasing external bath temperature to 43°C with a heatable perfusion cannula PH01 programmed with the temperature controller TC02 from Multi Channel Systems MCS GmbH. Ionic currents were recorded with a voltage ramp protocol from -120 mV to 120 mV in 300 ms. The protocol to evaluate TRPV1 heat-evoked gating inhibition by AG1529 consisted in: (i) record the ionic activity of the channel at 37°C using the voltage ramp protocol (basal activity); (ii) increase the external bath temperature up to 43°C and record the channel activity using the voltage ramp protocol (P1); (iii) decrease the temperature until 37°C and perfuse AG1529 (10  $\mu$ M), capsazepine (10  $\mu$ M) or BCTC (1 nM) for 30 s; and, (iv) rise the temperature to 43°C and record the ionic currents with the voltage ramp protocol (P2). The mean P2/P1 ratio for control was used for normalizing the ionic current at 120 mV for all treatments.

To monitor AG1529 effect on pH-evoked TRPV1 currents, ASIC channels activated by acidic pH present in Hek 293LTV cell line were blocked with 50  $\mu$ M amiloride [242]. Currents were evoked at -60 mV with a pulse of external solution at pH 5.5. The activity of 10  $\mu$ M AG1529 was compared to that of capsazepine at 10  $\mu$ M and BCTC at 1 nM.

AG1529 effect on TRPM8 and TRPA1 was studied in the same way as on TRPV1. Protocols consisted in the application of two pulses (P1, P2) of the corresponding channel agonist (100  $\mu$ M menthol for TRPM8 or 60  $\mu$ M AITC for TRPA1). AG1529 at 10  $\mu$ M was applied 30 s before and during P2 (AG1529 treated cells). Channel desensitization was monitored by the application of the two pulses of the corresponding channel agonist (control cells). P2/P1 ratio of AG1529 treated cells was compared with P2/P1 ratio of control cells.

## 7.2. Patch-clamp recordings on DRG neurons

Whole-cell patch-clamp recordings on sensory DRG neurons from neonatal Wistar rats were conducted using an EPC-10 amplifier (HEKA Elektronik) with Patchmaster software. Patch pipettes prepared from thin-wall borosilicate capillary glass tubing were pulled with a horizontal flaming/brown Micropipette puller Model P-97 from Sutter Instrument to a final resistance of 2-8 M $\Omega$  when filled with internal solution. Recordings were acquired at 10 kHz and low-pass filtered at 3 kHz. Recordings with leak currents >200pA or series resistance >20M $\Omega$  were discarded. Intracellular pipette solution contained (in mM): 4 NaCl, 126 K gluconate, 0.02 CaCl<sub>2</sub>, 1 MgSO<sub>4</sub>, 5 HEPES, 15 glucose, 3 ATP, 0.1 GTP and 5 EGTA, pH 7.2 adjusted with KOH. Extracellular solution contained (in mM): 140 NaCl, 4 KCl, 2 CaCl<sub>2</sub>, 2 MgCl<sub>2</sub>, 10 HEPES, 5 glucose and 20 mannitol, pH 7.4 adjusted with NaOH. Neurons were voltage-clamped at -70 mV.

### 7.2.1. TRAAK recordings

DRG neurons of small diameter were maintained at a membrane potential of -70 mV. Neuronal firing was stimulated by the injection of current which depolarized cells in 40 mV from the holding potential, in two occasions and separated by 2 minutes. 1 minute before second current ramp, cells were perfused with test compounds (irinotecan, astemizol or terfenadine at 25  $\mu$ M) or control (AA at 10  $\mu$ M). Basal neuronal response to the two depolarizing ramps was monitored without applying any substance. Number of action potentials during first and second ramp, and also 30 s before second ramp were monitored. Voltage difference during hyperpolarization state of action potentials between first ramp and depolarization induced firing zone before second ramp was measured only for registers in presence of terfenadine.

In the taxol induced neuropathic pain *in vitro* model of rat DRG neurons, cells were maintained at their natural resting membrane potential. Cells were perfused with 10  $\mu$ M AA or irinotecan during 1 minute before registering a 10 ms 10 pA current steps protocol until reaching 300 pA.

### 7.2.2. TRPV1 recordings

Current-clamp recordings of APs generated by the application of two pulses of 500 nM capsaicin in a time interval of 5 min and a 1 min perfusion of 1  $\mu$ M AG1529 before the second capsaicin pulse, during the injection of a constant depolarizing current that maintained the membrane potential at -70 mV were used to calculate P2/P1 ratio of

AP generation. Voltage-gated DRG neuron currents were evoked by stepping from  $-50$  to  $55$  mV for  $10$  ms with  $5$  mV increments with  $2$  s interpulse intervals. Inward and outward current densities (nA/pF) were obtained by dividing the peak inward and outward current, respectively, by the cell capacitance. AG1529 ( $1$   $\mu$ M) was perfused during  $2$  min before recording the step protocol.

### 7.3. Microelectrode array measurements

Recordings were performed using multiple electrode planar arrays of 60-electrode thin MEA chips. Electrodes present a  $30$   $\mu$ m diameter and  $200$   $\mu$ m inter-electrode spacing with an integrated reference electrode (Multichannel Systems GmbH) [241]. The electrical activity of primary sensory neurons was recorded by the MEA1060 System (Multi Channel Systems GmbH) and MC\_Rack software version 4.3.0. Measurement of neuronal firing activity was performed by the application of two  $30$  s long  $40$  mM KCl pulses, separated by a washing period of  $9$  min with external physiological solution as the one used for patch-clamp recordings on DRG neurons.  $90$  s before and during second KCl pulse, control ( $10$   $\mu$ M AA) and tested compounds (irinotecan, astemizol or terfenadine at  $25$   $\mu$ M) were perfused. Protocol for control of basal KCl response consisted in a  $10.5$  min washing period with no compound application before second KCl pulse. Solutions were applied using a continuous perfusion system ( $2$  mL/min). All measurements were performed at  $\sim 34.5^\circ\text{C}$  using Multichannel Systems Temperature Controller.

Data were analyzed using MC\_RACK spike sorter with a sample rate of  $25\text{kHz}$  and Butterworth high-pass  $2^{\text{nd}}$  order filter applied with  $200$  Hz cutoff. An evoked spike was defined when the amplitude of the neuronal electrical activity was established by automatic threshold estimation at  $-4.0$   $\mu$ V standard deviation. Electrodes not displaying electrical activity in the first KCl pulse were discarded. Mean spike frequency for both KCl pulses were then extracted. Ratio P2/P1 of mean spike frequency was calculated and normalized to basal KCl response in order to compare different conditions. Number of spikes produced during the  $90$  s compounds application was also extracted.

### 7.4. Statistical analysis

All data are expressed as mean  $\pm$  SEM. The number of replicates is indicated on figure legends or on the bar graphs where each dot represents one replicate. Data was statistically analyzed using paired or unpaired Students' t-test or One-Way ANOVA. Paired One-Way ANOVA was used only for irinotecan test on taxol induced neuropathic pain *in vitro* model. Statistical analysis is denoted on figure legends. P-value for all analysis

was set at 0.05 and if group difference is statistically significant p-value appears depicted on the corresponding graph. F (DFn, DFd) and p-value are reported on figure legend for each One-Way ANOVA.





# RESULTS



Biblioteca  
UNIVERSITAS Miguel Hernández





## 1. TRAAK BINDING SITES DEFINITION

### 1.1. TRAAK global blind docking

Global blind docking experiments with TRAAK crystal structure 4WFF and 500 runs per assay were performed using AA, EPA, riluzole and sipatrigine as ligands. These assays intended to explore possible binding sites inside transmembrane and extracellular domains of TRAAK channel and gave rise to the following results. The 500 runs with AA showed 173 clusters representing putative binding sites with interaction energies between 8.18 and 2.07 kcal/mol. EPA runs were clustered in 182 groups with interacting energies between 8.21 and 1.95 kcal/mol. Riluzole was represented in 36 clusters with energies ranging from 7.81 to 5.13 kcal/mol and finally sipatrigine runs were grouped in 37 clusters with energies from 14.37 to 9.32 kcal/mol. Best key interacting residues are depicted on bar plots on [Figure 14](#). It shows the mean  $\pm$  SD of residue interacting energy and the number of runs in which a given residue appears. Most representative clusters of those runs are shown on TRAAK structures of [Figure 14](#). Residues T129, I154, G158, L161, T238, L269 and L276 conform a pocket just below the intracellular opening of the pore. Residues L95, G97, G98, A99, D100, A113, N134, V135, A136, R138, E221, D222 and W223 shape a binding site located on the extracellular lateral opening of the pore involving regions from the extracellular cap domain and the extracellular loops connecting transmembrane helices while A92, D93 and P101 displace this binding site to the central extracellular axis of the pore. AA best putative binding sites are shown on [Figure 14](#) as surface representation and presented a mean  $\pm$  SD interaction energy from a given number of runs (n) as follows: [1]:  $6.84 \pm 0.66$  (18); [2]:  $5.38 \pm 0.66$  (7); [3]:  $5.61 \pm 0.66$  (12). Following the same nomenclature for EPA best interaction sites were [1]:  $6.96 \pm 0.60$  (23); [2]:  $6.08 \pm 0.80$  (17), for riluzole, [1]:  $7.30 \pm 0.31$  (58); [2]:  $7.47 \pm 0.36$  (13) and for sipatrigine, [1]:  $13.10 \pm 0.69$  (136); [2]:  $12.20 \pm 0.52$  (104). Thus, blind global docking experiments can be used to estimate or predict putative binding sites through individual solution clustering statistics. Some binding site predicted by the blind docking assay could have biologic relevance although it has not been discovered experimentally.

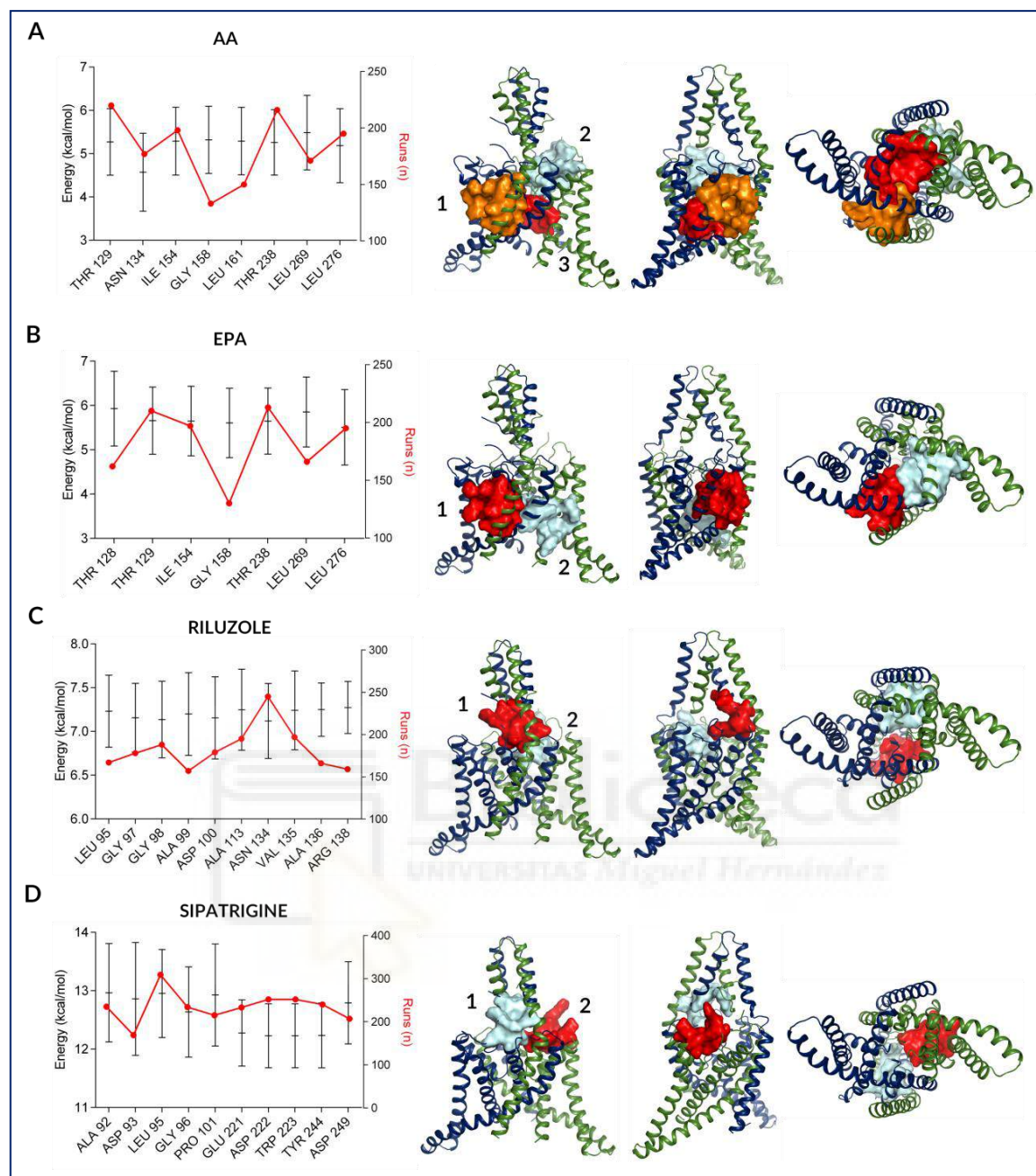


**Figure 14. TRAAK global blind docking results.** Bar graphs represent the mean  $\pm$  SD of interacting energy and the number of runs in which best key interacting residues appear from experiments with AA (A), EPA (B), riluzole (C) and sipatrigine (D). Most representative clusters of those runs for each ligand are represented on TRAAK cartoon 3D structures by surface illustration. Second cartoon representation is rotated 45° in the vertical axis to any side with respect to the first representation, while the third suffers a 45° rotation in the horizontal axis and represents an intracellular view of the channel. Different cluster sites representation is depicted in different colour and enumerated. AA best putative binding sites show mean  $\pm$  SD interaction energy from a given number of runs (n) as follows: 1 -  $6.84 \pm 0.66$  (18); 2 -  $5.38 \pm 0.66$  (7); 3 -  $5.61 \pm 0.66$  (12). Following the same nomenclature for EPA best interaction sites are 1 -  $6.96 \pm 0.60$  (23); 2 -  $6.08 \pm 0.80$  (17), for riluzole, 1 -  $7.30 \pm 0.31$  (58); 2 -  $7.47 \pm 0.36$  (13) and for sipatrigine, 1 -  $13.10 \pm 0.69$  (136); 2 -  $12.20 \pm 0.52$  (104).

## 1.2. Exploring new binding sites

Structure based protein sequence alignment between TRAAK 4WFF and TREK-2 4XDK crystal structures is shown in Figure 15. Coincidence between both sequences is highlighted in red. Norfluoxetine binding site location is underlined on the sequence alignment, all residues match on both structures except I214 and V278 on TREK-2 (corresponding to L151 and I233, respectively, on TRAAK) which suffered a conservative mutation.

```

4xdk: 95  ---SRKWTV VAIFVVVVVY IVTGGIVFRA LEQPFESSQK NTIALEKAEF LRDFVVCVSPQ ELKTLIQNAL DADNAGVSPI
4wff: 28  ----RSTTL LALLALVLLY LVSGALVFRA LEQPHQQQAQ RELGEVREKF LRAMPVSDQ ELGLLIKVA DALGGADPE

4xdk: 172 GEGSH--MDL GSAPFFAGTV ITTIGYGHIA PSTEGGKIFC ILYAIFGIFL FGFLLAGIGD QLGTFGKSI -----
4wff: 107 TQSSHSAMD L GSAPFFSCTI ITTIGYGNVA LRTDAGRLFC IFYALVGIFL FGIILLACVD RLGSLSRHSI GHEIAIFLKW

4xdk: 240  -----VI STILFILAGC IVFVTIPAVI FKYIEGNTAL ESIYFVVVTL VVVGFGDFVA GGNAGINREM YKPLVWFMI L
4wff: 187 HVPPPELVRVL SAMLFLIGC LLFVLTPTFV FCMEDWSKL EAIYFVIVTL VVVGFGDYVA GADPRGDEPA YQPLVWFMI L

4xdk: 312 VGLAYFAAVL SMIGDMLRVL SKETKE
4wff: 267 LGLAYFASVL TTIGNMLR

```

Figure 15. TREK-2 (4XDK) and TRAAK (4WFF) protein sequence alignment. Sequence match is highlighted in red. Norfluoxetine binding site is marked by lines. Not matching residues from norfluoxetine binding site between both structures are pointed by an arrow.

Figure 16 shows the structure based protein sequence alignment between TRAAK 4WFF and TREK-1 6CQ9 structures in order to check ML402 binding site environment translated to TRAAK structure. Key residues of ML402 binding site appear underlined on the sequence alignment. Residues G261 and V273 on TREK-1 (corresponding to A244 and L260, respectively on TRAAK) suffer a conservative mutation, while K271 (TREK-1) suffers a non-conservative mutation being replaced by Q258 on TRAAK.

```

6cq9: 35  SDAINVMKW KTVSTIFLVV VLYLIIGATV FRALQSPQEI SQRRTIVIQR EKFLRAHPCV SDCELDLILQ QIVAAINAGI
4wff: 29  .....8 TLLALLALV LLYLVSGALV FRALQSPHEQ QAQRELGEVR EKFLRAHPCV SDCELDGLIK EVADALGGGA

6cq9: 115 IPLGASSNQV SHNDLGSFPF FAGTVITTIQ FGNISPRTEG GRIFCIITAL LGIPLFGILL AGVQQLSTI FKGELARVED
4wff: 100 D.....H SAMDLGSAPF FSGVITTTIG YGNVALHEDA GRIFCIITAL VGIPLFGIIL AGVQDREGSS LNHGIGHHA

6cq9: 195 TPIKWNVQST KIRIISTLIIF ILPGCVLFA LPAVIFKHIE GWSALDAIYF VVITLTTIGF GDYVAGGSDI KYLDFYKPVV
4wff: 182 IFL....PDE LVKVLAMLF LLIGCLLFLV TPTFVFCYME DWSKLEAIYF VIVVLTTVGF GDYVAGADPR .....YQRLV

6cq9: 275 WFWILVGLAY FAAVLSMIGD WLRVIAEKTK EAVGEPHAAH AE
4wff: 262 WFWILLGLAY FAS.....

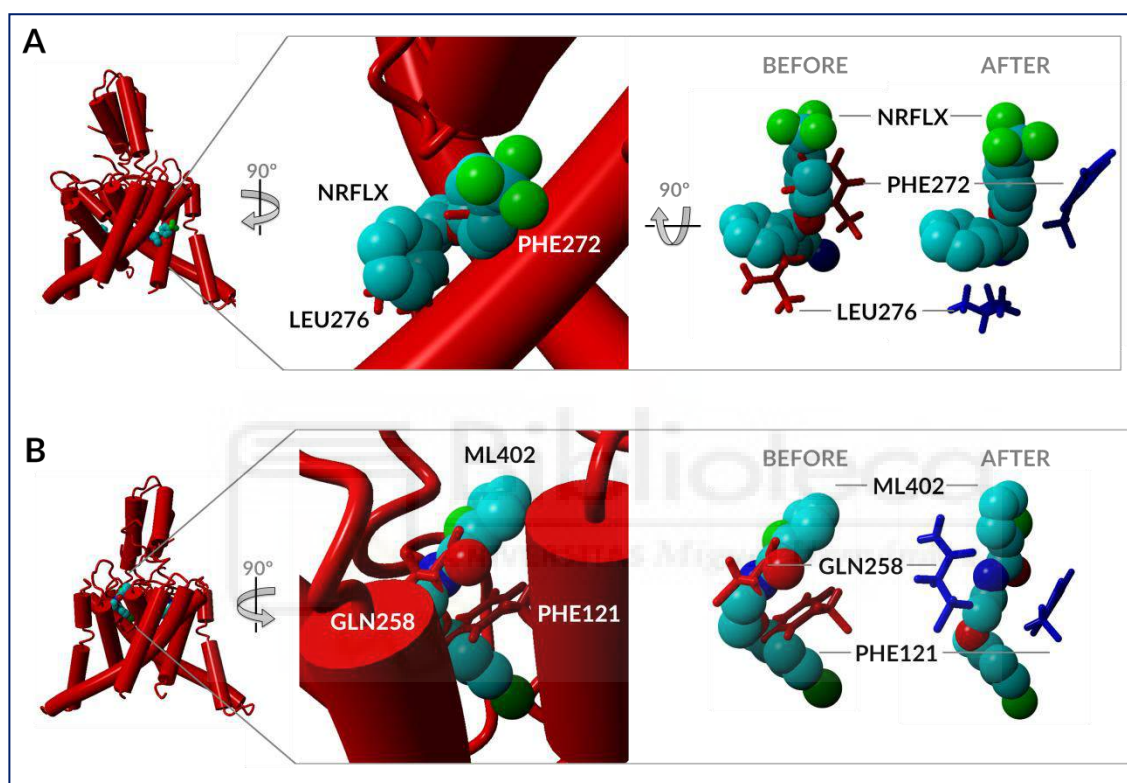
```

Figure 16. TREK-1 (6CQ9) and TRAAK (4WFF) protein sequence alignment. Sequence match is highlighted in red. ML402 binding site is marked by lines. Not matching residues from ML402 binding site between both structures are pointed by an arrow.

After structure alignment between TRAAK and TREK-2-norfluoxetine complex (or TREK-1-ML402 complex) the ligands were transferred to TRAAK structure to build two different models: TRAAK-norfluoxetine and TRAAK-ML402 complexes. Corresponding binding sites were explored for possible sterical clashes between ligands and residues

## RESULTS

from TRAAK channel. F272, L276 and F121, Q258 pairs were sterically hindered by norfluoxetine and ML402, respectively, as shows Figure 17 in red. After energy minimization performed with YASARA, these clashes were relaxed adapting TRAAK structure to embrace both ligands, moving side chains of both residue pairs to new more favourable positions while the backbone was kept fixed, as shown on Figure 17 in blue. These final TRAAK structures were used in further virtual screening experiments.



**Figure 17.** Norfluoxetine (A) and ML402 (B) binding sites location on TRAAK. Sterical clashes with key binding residues can be observed in red in the inset right panel. After energy minimization clashes were fixed and are shown in blue.

The focalized docking experiment used to reproduce the binding of TKDC to a cryptic binding site in the extracellular cap domain of TRAAK between E1 and E2 rendered as result a very similar interaction pose of TKDC to the one shown by Luo *et al* [136]. TKDC accommodates between E1 and E2 forming hydrophobic interactions with residues L65, V87 and A94 while hydrogen bonding with E90 and D93 give specificity to the interaction (Figure 18 inset). The represented pose of the ligand on Figure 18 makes reference to the most populated cluster (23 in total) of individual runs (30/200 runs) and the most energetically favoured with an interaction energy of  $6.47 \pm 1.05$  kcal/mol. Receptor and ligand resulting from this docking assay was used to further explore this binding site in search of new modulators.

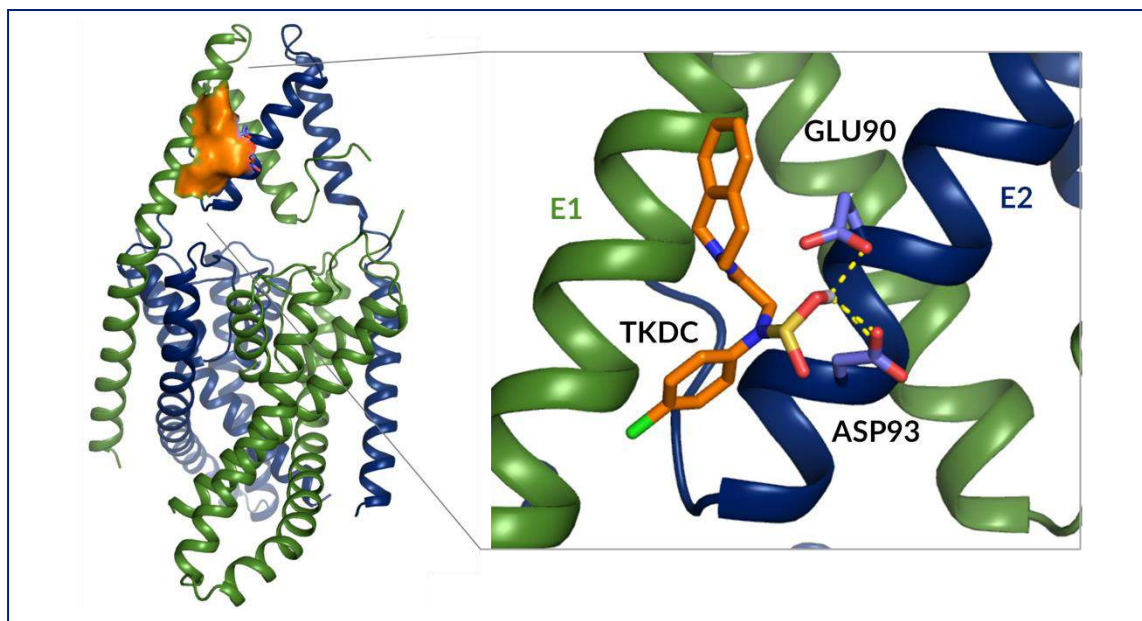


**Figure 18.** TKDC binding site location on TRAAK extracellular cap domain. TKDC is located between E1 and E2 of the extracellular cap domain of TRAAK. Apart from hydrophobic interactions with residues L65, V68 and A94, TKDC forms hydrogen bonds with E90 and D93.

Sipatrigine and riluzole most representative binding sites determined by the blind docking experiments partially overlap with TKDC binding site, locating between the extracellular cap and transmembrane domain. AA and EPA most representative interaction sites also suffer partial overlap either with the decane crystal, on the intracellular pore opening, with norfluoxetine or with ML402 binding site. Thus, for the virtual screening assays, explored binding sites corresponded to the decane crystal, norfluoxetine and ML402 binding sites transferred to TRAAK structure and TKDC interaction site (Figure 10).

### 2. VIRTUAL SCREENING

The virtual chemical libraries ActiveBiopharma (containing 1293 molecules), AfroDB (501), FDA approved (2691), NubbeNaturals (409), Prestwick (1649), LipidMaps (fatty acids) (4354) and Dipeptides (1600), were docked against each of the four TRAAK binding sites defined in the previous section (norfluoxetine, ML402, TKDC and decane). AutoDock ligand poses were evaluated by Xscore, DSX and AutoDock score functions in order to decrease possible false positive or negative results.

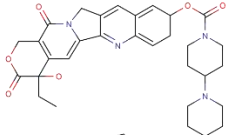
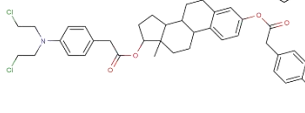
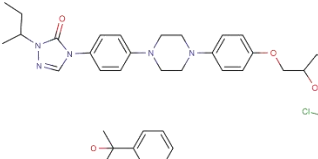
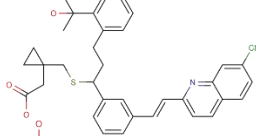
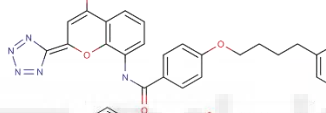
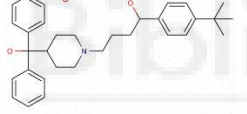
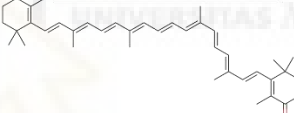
The equivalent norfluoxetine binding site on TRAAK top 40 consensus docking results are shown on [Table 3](#). A summatory of normalized individual scores of each ligand with respect to the control ligand (norfluoxetine molecule) is shown as final ranking punctuation. Molecules receiving better score than control ligand were considered as potential TRAAK modulators. The number of molecules selected following these criteria and the percentage with respect to the total amount of molecules were: ActiveBiopharma: 644 (50%); AfroDB: 249 (50%); FDA approved: 1029 (62%); NubbeNaturals: 122 (30%); Prestwick: 594 (36%); LipidMaps: 1098 (25%); Dipeptides: 6 (0.4%). 70% of the top 40 hits belong to FDA approved or Prestwick libraries which house ligands already approved as drugs ([Table 4](#)). All of them are characterized by a high molecular weight (near or more than 500 g/mol), high hydrophobicity ( $\log P > 5$ , except irinotecan) and structures divided in two bulky parts connected by an acyl chain of different length.

**Table 3. Consensus norfluoxetine binding site virtual screening results.** Xscore, DSX and AutoDock scores are shown separately for each ligand. For DSX and AutoDock the lower the score is, the better the ligand-receptor interaction energy is. For Xscore, the higher the score is, the better the binding energy is. Final score ( $\Sigma_{\text{norm}}$ ) represents the summatory of the normalized individual scores of each ligand with respect to the control ligand. The final score of the control ligand is always 3 (not shown). Best 40 ligands in terms of  $\Sigma_{\text{norm}}$  are shown.

Norfluoxetine binding site					
Library	Name	Xscore	DSXscore	Autodock	$\Sigma_{\text{norm}}$
Prestwick	ZINC01612996	7.95	-159.20	-12.63	4.59
FDAApproved	ZINC08101102	8.33	-167.00	-11.83	4.45
FDAApproved	ZINC03830974	7.81	-159.86	-12.74	4.41
FDAApproved	ZINC03831151	8.92	-146.67	-12.39	4.40
Prestwick	ZINC22001688	7.97	-146.40	-12.13	4.38
Prestwick	ZINC03812892	8.36	-147.79	-11.39	4.36
FDAApproved	ZINC03812892	8.51	-146.24	-12.09	4.30
FDAApproved	ZINC03830369	9.40	-100.55	-14.61	4.26
AfroDB	ZINC95485964_2	8.02	-133.01	-12.76	4.25
Prestwick	ZINC04213094	7.18	-142.35	-12.33	4.24
ActiveBiopharma	ZINC13986815	7.57	-155.66	-12.52	4.24
FDAApproved	ZINC08101070	7.98	-153.11	-11.53	4.22
FDAApproved	ZINC08101101	8.33	-142.07	-11.82	4.19
Prestwick	ZINC22034135	7.43	-153.14	-10.70	4.19
NubbeNaturals	ZINC84154140	7.03	-150.91	-13.66	4.19
FDAApproved	ZINC04213094	7.21	-153.98	-12.06	4.17
FDAApproved	ZINC03831150	8.67	-125.46	-12.48	4.15
AfroDB	ZINC95486256	6.86	-129.28	-13.78	4.15
FDAApproved	ZINC03831511	8.36	-146.33	-11.03	4.15
AfroDB	ZINC95486025	7.84	-132.94	-12.11	4.15
FDAApproved	ZINC08101100	8.63	-134.33	-11.70	4.15
AfroDB	ZINC95485981	7.81	-122.28	-13.12	4.14
NubbeNaturals	ZINC03984030	8.61	-127.63	-13.15	4.13
FDAApproved	ZINC03830973	7.77	-145.36	-11.74	4.13
FDAApproved	ZINC03831459	8.38	-132.44	-12.06	4.13
FDAApproved	ZINC08101077	8.53	-120.39	-12.86	4.12
Prestwick	ZINC00601274	7.48	-147.09	-10.62	4.12
FDAApproved	ZINC03831231	7.90	-127.45	-13.00	4.12
FDAApproved	ZINC03830746	7.48	-147.64	-11.78	4.12
Prestwick	ZINC01482077	7.81	-140.78	-10.56	4.10
FDAApproved	ZINC08101103	8.52	-138.31	-11.03	4.09
ActiveBiopharma	ZINC14210869	7.9	-147.9	-11.45	4.09
Prestwick	ZINC01655706	7.81	-146.63	-9.99	4.09
LipidMaps	LMFA08020185	7.76	-134.12	-11.47	4.09
ActiveBiopharma	ZINC19362713	7.6	-159.55	-10.81	4.09
LipidMaps	LMFA13010056	7.01	-155.88	-10.52	4.08
FDAApproved	ZINC03831457	8.31	-124.57	-12.27	4.06
Prestwick	ZINC03831511	8.39	-131.22	-10.42	4.06
Prestwick	ZINC22034381	7.68	-140.26	-10.48	4.06
AfroDB	ZINC95486263	7.98	-121.98	-12.07	4.04

## RESULTS

**Table 4. Characteristics of top 7 hits obtained on norfluoxetine binding site.** Common name, chemical structure, final docking score, molecular weight (MW), logP value, hydrogen bond donors (HBD) and acceptors (HBA) are summarized for each ligand. Violations of Lipinski Rule of 5 are marked in reddish colour.

Name	Common name	Structure	$\Sigma_{\text{norm}}$	MW	LogP	HBD	HBA
ZINC01612996	Irinotecan		4.59	586.68	4.09	2	8
ZINC08101102	Estradiol mustard		4.45	788.68	9.41	0	4
ZINC03830974	Itrazole		4.41	705.64	5.57	0	12
ZINC03831151	Montelukast		4.40	586.19	8.94	1	5
ZINC22001688	Pranlukast		4.38	481.51	6.63	1	7
ZINC03812892	Terfenadine		4.36	471.68	6.44	3	2
ZINC03830369	Orobronze		4.26	564.85	10.96	0	2

On Table 5 are shown the equivalent ML402 binding site on TRAAK top 40 consensus docking results. ML402 binding site locates completely inside TRAAK transmembrane domain near the selectivity filter. It presents no clear aperture to intra or extracellular media. A summatory of normalized individual scores of each ligand with respect to the control ligand (ML402 molecule) is shown as final ranking punctuation. Molecules receiving better score than control ligand were considered as potential TRAAK modulators. The number of molecules selected following these criteria and the percentage with respect to the total amount of molecules were: ActiveBiopharma: 985 (76%); AfroDB: 345 (69%); FDA approved: 1791 (67%); NubbeNaturals: 229 (56%); Prestwick: 636 (39%); LipidMaps: 2051 (47%); Dipeptides: 150 (9%). 75% of the top 40 hits belong to FDA approved or Prestwick libraries which house ligands already approved as drugs (Table 6). Molecular weight of top 7 hits is, as in the case of norfluoxetine binding site, high (near 500 g/mol). There are very hydrophobic and very hydrophilic

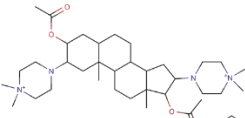
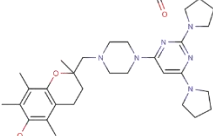
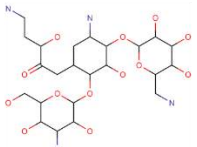
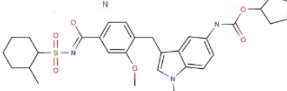
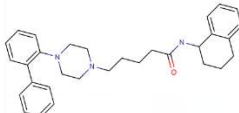
ligands. In contrast to best norfluoxetine binding site hits, ML402 site hits are compact, with spherical or cylindrical surface.

**Table 5. Consensus ML402 binding site virtual screening results.** Xscore, DSX and AutoDock scores are shown separately for each ligand. For DSX and AutoDock the lower the score is, the better the ligand-receptor interaction energy is. For Xscore, the higher the score is, the better the binding energy is. Final score ( $\Sigma_{\text{norm}}$ ) represents the summatory of the normalized individual scores of each ligand with respect to the control ligand. The final score of the control ligand is always 3 (not shown). Best 40 ligands in terms of  $\Sigma_{\text{norm}}$  are shown.

ML402 binding site					
Library	Name	Xscore	DSXscore	Autodock	$\Sigma_{\text{norm}}$
FDA_approved	ZINC03831339	8.41	-158.77	-16.47	5.42
ActiveBiopharma	ZINC27519725	8.12	-180.00	-14.48	5.23
FDA_approved	ZINC08101060	6.77	-130.83	-19.46	5.16
FDA_approved	ZINC00896717	8.80	-148.27	-14.85	5.15
ActiveBiopharma	ZINC14975987	8.68	-170.36	-13.62	5.10
FDA_approved	ZINC08101137	6.78	-154.76	-15.47	4.98
FDA_approved	ZINC03830925	8.18	-143.11	-14.52	4.94
FDA_approved	ZINC14593244	8.68	-146.60	-13.05	4.88
FDA_approved	ZINC03831506	8.16	-143.82	-13.94	4.87
FDA_approved	ZINC03831605	8.76	-124.09	-15.17	4.87
FDA_approved	ZINC03830384	8.09	-132.58	-15.12	4.86
FDA_approved	ZINC03831340	8.13	-127.34	-15.45	4.84
LipidMaps	LMFA08020174	8.00	-167.57	-11.48	4.84
FDA_approved	ZINC03830383	8.11	-139.06	-14.24	4.84
FDA_approved	ZINC08101132	6.56	-107.40	-19.52	4.84
FDA_approved	ZINC03830386	8.16	-131.19	-14.93	4.83
FDA_approved	ZINC03830923	8.11	-133.60	-14.68	4.83
FDA_approved	ZINC03830924	8.21	-143.77	-13.42	4.82
ActiveBiopharma	ZINC03810247	8.28	-162.39	-12.57	4.81
FDA_approved	ZINC03812892	9.04	-139.63	-12.68	4.81
LipidMaps	LMFA08020206	8.23	-154.77	-12.22	4.80
FDA_approved	ZINC03831454	8.48	-139.21	-13.35	4.79
FDA_approved	ZINC00538180	8.11	-159.96	-11.61	4.79
AfroDB	ZINC95485965	8.78	-120.25	-16.13	4.78
FDA_approved	ZINC08101057	6.78	-95.84	-19.94	4.78
FDA_approved	ZINC03831458	8.64	-138.32	-13.09	4.78
FDA_approved	ZINC03831511	9.04	-132.97	-13.06	4.77
AfroDB	ZINC77257204	8.23	-134.17	-15.34	4.76
FDA_approved	ZINC03831340	8.19	-128.19	-14.62	4.76
FDA_approved	ZINC03830385	8.17	-137.00	-13.70	4.76
ActiveBiopharma	ZINC27519725	8.15	-159.49	-12.56	4.75
FDA_approved	ZINC08101106	8.26	-146.60	-12.54	4.75
LipidMaps	LMFA08020185	8.28	-151.00	-12.04	4.74
FDA_approved	ZINC08101133	6.65	-137.22	-15.53	4.74
FDA_approved	ZINC00896452	8.47	-138.49	-13.01	4.74
FDA_approved	ZINC14593247	8.54	-147.16	-12.00	4.74
LipidMaps	LMFA08020204	8.07	-154.47	-11.87	4.73
FDA_approved	ZINC08101100	9.30	-135.05	-12.18	4.73
Prestwick	ZINC04245720	8.01	-176.76	-10.75	4.72

## RESULTS

**Table 6. Characteristics of top 7 hits obtained on ML402 binding site.** Common name, chemical structure, final docking score, molecular weight (MW), logP value, hydrogen bond donors (HBD) and acceptors (HBA) are summarized for each ligand. Violations of Lipinski Rule of 5 are marked in reddish colour.

Name	Common name	Structure	$\Sigma_{\text{norm}}$	MW	LogP	HBD	HBA
ZINC03831339	Pipecuronium		5.42	602.91	3.63	0	4
ZINC27519725			5.23	520.70	4.21	1	8
ZINC08101060	Amikacin		5.16	585.62	-8.42	12	17
ZINC00896717	Accolate		5.15	575.69	6.27	1	7
ZINC14975987			5.10	481.68	6.23	1	3
ZINC08101137	Kanamycin		4.98	484.50	-7.29	11	15
ZINC03830925	Idarubicin		4.94	497.51	1.02	5	9

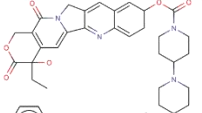
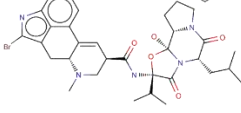
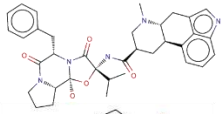
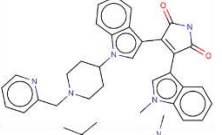
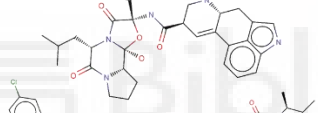
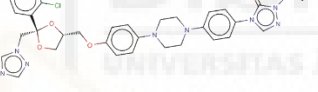
On Table 7 are shown the equivalent decane binding site of TRAAK top 40 consensus docking results. Decane molecule was used as control ligand. Given the large size of the pocket constituted just below the intracellular pore opening of TRAAK, almost 80% of ligands of each library screened virtually, received a better interaction energy compared to control. Large compounds were favoured in this interaction and actually top hits shown on Table 8 present a molecular weight higher than 500 Da. Dipeptides did not received good scores, again due to their size. The majority of top hits did not violate other Lipinski's Rule of 5 parameters, except molecular weight.

**Table 7. Consensus decane binding site virtual screening results.** Xscore, DSX and AutoDock scores are shown separately for each ligand. For DSX and AutoDock the lower the score is, the better the ligand-receptor interaction energy is. For Xscore, the higher the score is, the better the binding energy is. Final score ( $\Sigma_{\text{norm}}$ ) represents the summatory of the normalized individual scores of each ligand with respect to the control ligand. The final score of the control ligand is always 3 (not shown). Best 40 ligands in terms of  $\Sigma_{\text{norm}}$  are shown.

Decane binding site					
Library	Name	Xscore	DSXscore	Autodock	$\Sigma_{\text{norm}}$
Prestwick	ZINC08143921	8.40	-129.44	-9.71	6.90
Prestwick	ZINC01612996	7.23	-146.22	-9.56	6.89
Prestwick	ZINC03995608	7.47	-141.73	-8.75	6.60
Prestwick	ZINC03995616	7.60	-134.66	-8.69	6.49
ActiveBiopharma	ZINC01494900	7.47	-129.98	-9.19	6.46
Prestwick	ZINC04245686	7.31	-152.08	-7.93	6.46
Prestwick	ZINC03830974	7.07	-150.51	-8.05	6.43
AfroDB	ZINC95486223	7.36	-127.47	-9.48	6.37
ActiveBiopharma	ZINC22001688	7.28	-139.81	-8.30	6.33
ActiveBiopharma	ZINC13831229	7.49	-135.65	-8.25	6.29
AfroDB	ZINC95486263	7.31	-129.16	-9.09	6.27
ActiveBiopharma	ZINC27519725	7.11	-145.94	-7.81	6.26
Prestwick	ZINC04245662	7.48	-131.76	-8.21	6.26
Prestwick	ZINC22001688	7.42	-127.66	-8.40	6.25
Prestwick	ZINC03830975	7.08	-132.62	-8.32	6.23
AfroDB	ZINC95486188	8.66	-126.40	-8.17	6.22
ActiveBiopharma	ZINC19796084	7.08	-144.43	-7.75	6.21
Prestwick	ZINC00601274	6.76	-149.65	-7.56	6.20
Prestwick	ZINC08143556	6.71	-153.59	-7.37	6.19
ActiveBiopharma	ZINC40951976	7.17	-129.82	-8.43	6.18
ActiveBiopharma	ZINC00601274	6.81	-150.16	-7.43	6.17
ActiveBiopharma	ZINC03810247	7.30	-151.70	-6.99	6.12
Prestwick	ZINC03978005	7.43	-134.34	-7.80	6.16
Prestwick	ZINC22034381	7.39	-127.46	-8.04	6.12
AfroDB	ZINC95486025	7.06	-132.16	-8.53	6.11
ActiveBiopharma	ZINC00598509	7.39	-127.35	-8.09	6.07
Prestwick	ZINC03830973	7.06	-143.83	-7.26	6.06
Prestwick	ZINC03830976	7.04	-132.25	-7.76	6.04
AfroDB	ZINC95486207	6.94	-126.99	-8.62	6.03
AfroDB	ZINC95486210	6.99	-135.76	-8.09	6.03
AfroDB	ZINC95486333	7.66	-119.19	-8.54	6.01
ActiveBiopharma	ZINC14975990	7.49	-125.40	-7.83	5.98
ActiveBiopharma	ZINC03784334	7.09	-131.73	-7.70	5.98
Prestwick	ZINC19796084	7.10	-137.76	-7.25	5.97
AfroDB	ZINC95486212	7.11	-124.91	-8.42	5.97
AfroDB	ZINC95486111	7.94	-125.35	-7.85	5.96
AfroDB	ZINC95486198	7.43	-111.24	-8.91	5.95
Prestwick	ZINC04245638	7.19	-114.07	-8.28	5.95
Prestwick	ZINC03812892	7.55	-114.42	-7.97	5.92
NubbeNaturals	ZINC43552595	7.29	-117.16	-7.55	5.87

## RESULTS

**Table 8. Characteristics of top 7 hits obtained on decane binding site.** Common name, chemical structure, final docking score, molecular weight (MW), logP value, hydrogen bond donors (HBD) and acceptors (HBA) are summarized for each ligand. Violations of Lipinski Rule of 5 are marked in reddish colour.

Name	Common name	Structure	$\Sigma_{\text{norm}}$	MW	LogP	HBD	HBA
ZINC08143921			6.90	664.89	6.37	2	6
ZINC01612996	Irinotecan		6.89	586.68	4.09	2	8
ZINC03995608	Bromocriptine		6.60	654.61	3.19	3	6
ZINC03995616	Ergoloid		6.49	611.74	2.72	3	6
ZINC01494900	Enzastaurin		6.467	515.62	4.93	1	4
ZINC04245686	Ergocryptine		6.46	575.71	2.43	3	6
ZINC03830974	Itrazole		6.43	705.64	5.57	0	12

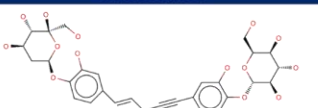
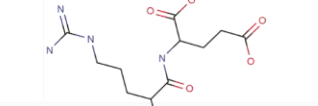
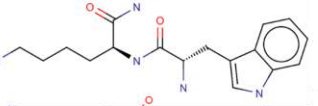
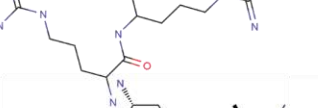
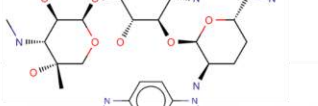
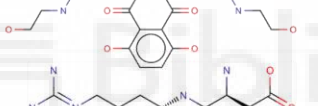
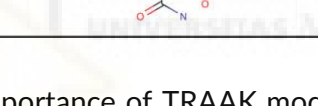
The fourth explored binding site was the TKDC one, which is probably the most size limited. Space between cap-helices is restricted although it could be the most easily accessible binding site due to its localisation on the extracellular domain of TRAAK. Several dipeptides mimic quite well TKDC molecule and present a similar molecular weight. On Table 9 are shown top 40 consensus docking results on the equivalent TKDC binding site on TRAAK. TKDC molecule was used as control ligand. All top hit compounds were very water soluble and showed large number of chemical groups which act as hydrogen bond donors or acceptors (Table 10).

**Table 9. Consensus TKDC binding site virtual screening results.** Xscore, DSX and AutoDock scores are shown separately for each ligand. For DSX and AutoDock the lower the score is, the better the ligand-receptor interaction energy is. For Xscore, the higher the score is, the better the binding energy is. Final score ( $\Sigma_{\text{norm}}$ ) represents the summatory of the normalized individual scores of each ligand with respect to the control ligand. The final score of the control ligand is always 3 (not shown). Best 40 ligands in terms of  $\Sigma_{\text{norm}}$  are shown.

TKDC binding site					
Library	name	Xscore	DSXscore	Autodock	$\Sigma_{\text{norm}}$
AfroDB	ZINC95486256	8.45	-162.77	-12.03	5.85
Dipeptides	RE_10L	8.18	-143.11	-10.46	5.78
Dipeptides	WK_10L	8.68	-146.60	-10.27	5.67
Dipeptides	RR_10L	8.16	-143.82	-10.16	5.61
Prestwick	ZINC08143541	8.18	-143.11	-10.9	5.61
Prestwick	ZINC03794794	8.68	-146.60	-10.72	5.52
Dipeptides	DR_10L	8.76	-124.09	-9.97	5.51
Dipeptides	KE_10L	7.22	-128.66	-9.9	5.47
AfroDB	ZINC95486006	8.46	-161.70	-11.21	5.45
Prestwick	ZINC19363537	8.16	-143.82	-10.48	5.39
Dipeptides	RW_10L	7.62	-131.07	-9.73	5.38
Dipeptides	HR_10L	7.83	-130.99	-9.67	5.34
Prestwick	ZINC19632618	8.76	-124.09	-10.37	5.34
AfroDB	ZINC95486212	6.77	-130.83	-10.94	5.32
Dipeptides	RR_00L	7.43	-136.00	-9.62	5.31
AfroDB	ZINC95486188	8.80	-148.27	-10.92	5.31
AfroDB	ZINC95486007	6.78	-154.76	-10.9	5.30
AfroDB	ZINC77257204	8.18	-143.11	-10.82	5.26
Dipeptides	QR_10L	7.47	-132.01	-9.48	5.24
Dipeptides	NR_10L	7.42	-127.10	-9.41	5.20
AfroDB	ZINC95486207	8.68	-146.60	-10.69	5.20
Prestwick	ZINC18098320	7.22	-128.66	-10.09	5.19
Dipeptides	RE_00L	7.13	-128.88	-9.39	5.19
Dipeptides	FK_10L	7.81	-129.48	-9.36	5.17
Dipeptides	WR_10L	7.43	-143.38	-9.36	5.17
Dipeptides	YR_10L	7.28	-125.83	-9.36	5.17
AfroDB	ZINC95486354	8.16	-143.82	-10.58	5.14
Prestwick	ZINC22034381	7.62	-131.07	-9.98	5.14
AfroDB	ZINC95486005	8.76	-124.09	-10.55	5.13
Dipeptides	WK_00L	7.66	-115.54	-9.28	5.13
Dipeptides	DK_10L	8.06	-127.75	-9.24	5.10
Dipeptides	RD_10L	7.69	-118.64	-9.23	5.10
Dipeptides	KD_10L	8.19	-128.19	-9.19	5.08
AfroDB	ZINC95486207	8.09	-132.58	-10.43	5.07
Dipeptides	RK_00L	8.17	-137.00	-9.17	5.07
AfroDB	ZINC95486263	8.13	-127.34	-10.37	5.04
Dipeptides	YK_10L	7.66	-115.54	-9.12	5.04
Dipeptides	KR_10L	6.65	-121.22	-9.1	5.03
Dipeptides	WS_10L	8.47	-119.49	-9.1	5.03
Prestwick	ZINC21981303	7.83	-130.99	-9.75	5.02
Prestwick	ZINC04245617	7.43	-136.00	-9.74	5.01
Dipeptides	RP_10L	8.54	-109.16	-9.07	5.01

## RESULTS

**Table 10. Characteristics of top 7 hits obtained on TKDC binding site.** Common name, chemical structure, final docking score, molecular weight (MW), logP value, hydrogen bond donors (HBD) and acceptors (HBA) are summarized for each ligand. Violations of Lipinski Rule of 5 are marked in reddish colour.

Name	Common name	Structure	$\Sigma_{\text{norm}}$	MW	LogP	HBD	HBA
ZINC95486256			5.85	606.58	-1.74	10	14
RE_10L			5.78	302.17	-3.24	6	8
WK_10L			5.67	329.19	0.09	5	5
RR_10L			5.61	314.22	-2.87	6	8
ZINC08143541	Gentamicin		5.61	477.60	-3.33	8	12
ZINC03794794	Mitoxantrone		5.52	444.49	-0.14	8	10
DR_10L			5.51	288.15	-3.53	6	8

Finally, given the importance of TRAAK modulation by fatty acids, a library of 39 capsaicin soft drugs was virtually screened against norfluoxetine, ML402 and TKDC binding sites. New capsaicin soft drugs development is currently being under study for the treatment of skin disorders targeting TRPV1. They are designed to undergo deactivation by the hydrolyzing activity of esterases found on skin, resulting in a fatty acid and a vanilloid head group. Decane binding site was not explored given that it overlaps with norfluoxetine's one. Table 11 summarizes consensus docking results against each binding site. Better results were obtained for norfluoxetine and ML402 binding sites when ligand score was compared to control score.

**Table 11. Capsaicinoids library consensus docking results on norfluoxetine, ML402 and TKDC binding sites.** Final score ( $\Sigma_{\text{norm}}$ ) represents the summatory of the normalized individual scores of each ligand with respect to the control ligand for AutoDock, DSX and Xscore functions. The final score of the control ligand is always 3. Results for the entire library are shown.

Norfluoxetine		ML402		TKDC		
name	$\Sigma_{\text{norm}}$	name	$\Sigma_{\text{norm}}$	name	$\Sigma_{\text{norm}}$	
NRFL	3.00	ML402	3.00	TKDC	3.00	
AG1566	AG61	3.87	FS106	4.26	AG46	3.38
AG1567	AG60	3.68	FS114	4.21	AG16	3.22
AG1564	FS87	3.38	AG22	4.14	AG9	3.18
AG1560	FS125	3.36	FS101	4.10	FS122	3.13
AG1530	AG46	3.35	FS85	4.02	AG60	3.07
AG1551	AG18	3.35	AG61	4.02	FS87	3.05
AG1554	FS72	3.34	FS117	3.93	FS97	2.93
AG1550	AG1C	3.32	FS72	3.86	AG49	2.89
AG1557	FS106	3.31	AG16	3.82	AG1D	2.89
AG1528	FS117	3.28	AG46	3.81	AG20	2.88
AG1555	AG22	3.27	FS105	3.79	AG14	2.87
AG1548	FS84	3.20	FS102	3.79	AG1A	2.86
AG1529	AG26	3.19	FS87	3.78	AG13	2.85
	AG32	3.19	AG26	3.77	AG1B	2.85
AG1565	FS102	3.16	FS110	3.73	AG43	2.85
AG1543	AG9	3.12	AG33	3.66	FS126	2.84
AG1563	AG16	3.09	AG60	3.65	AG52	2.83
AG1527	FS115	3.03	FS97	3.50	AG47	2.81
	AG33	2.97	AG14	3.46	FS84	2.81
AG1547	AG14	2.95	AG18	3.43	FS96	2.78
AG1534	FS96	2.93	AG1B	3.41	AG32	2.74
AG1542	FS122	2.93	FS96	3.39	AG18	2.73
AG1544	AG1A	2.92	FS115	3.38	FS117	2.73
AG1541	FS82	2.90	FS111	3.37	FS82	2.72
AG1537	AG49	2.88	AG20	3.34	AG61	2.62
AG1539	AG1D	2.86	AG1C	3.34	FS102	2.58
AG1538	AG47	2.85	AG32	3.33	FS115	2.51
AG1561	FS126	2.85	FS122	3.24	FS125	2.50
AG1558	FS111	2.84	FS82	3.17	AG26	2.49
AG1545	AG13	2.81	FS84	3.16	FS111	2.42
AG1535	AG52	2.80	AG43	3.13	FS85	2.39
AG1552	FS110	2.80	AG47	3.12	AG1C	2.38
AG1540	AG20	2.79	AG1D	3.10	FS106	2.35
AG1551	AG1B	2.77	AG13	3.08	FS101	2.24
AG1559	FS105	2.76	AG1A	3.05	AG22	2.22
AG1553	FS101	2.72	AG49	3.02	FS114	2.16
AG1549	FS97	2.71	AG9	3.00	AG33	2.16
AG1556	FS85	2.70	AG52	2.84	FS72	2.14
AG1536	AG43	2.69	FS126	2.08	FS105	1.98
AG1562	FS114	2.66	FS125	1.49	FS110	1.27

Although a large variety of molecules belonging to different chemical libraries have been screened against each TRAAK putative binding site, the ones selected for *in vitro* testing correspond to the Prestwick library of already approved drugs and the capsaicinoid AG1529 with a C12:0 fatty acid tail which showed a better interaction energy than control molecule for both norfluoxetine and ML402 binding sites. Prestwick selected compounds corresponded to physical availability even though they are present in the top 40 ligands of any or few of the virtual screening binding sites. Finally, virtual screening resulted in the election of 9 compounds to be assessed *in vitro*, irinotecan, terfenadine, pranlukast, astemizol, pimozone, lidoflazine, gliquidone, tribenoside and AG1529.

### 3. TRAAK C-TERMINAL DOMAIN RECONSTRUCTION

#### 3.1. YASARA automatic homology model based on manual alignment

Reconstruction of TRAAK C-terminal domain, whose amino acid sequence is highlighted in green on Figure 19, was targeted by homology modelling. Search of homologous structures was carried out by looking for a proper protein sequence alignment or Blast against NCBI PDB database. The only match with default settings corresponded to a 17 amino acids long C-terminal proximal region from mutant TRAAK channel which was actually not present in the corresponding crystal structure.

>hTRAAK				
10	20	30	40	50
MRSTLLALL	ALVLLYLVS	ALVFRALEQP	HEQQAQRELG	EVREKFLRAH
60	70	80	90	100
PCVSDQELGL	LIKEVADALG	GGADPETNST	SNSSHSAWDL	GSAFFFFSGTI
110	120	130	140	150
ITTIGYGNVA	LRTDAGRLFC	IFYALVGIPL	FGILLAGVGD	RLGSSLRHGI
160	170	180	190	200
GHIEAIFLKW	HVPPELVRVL	SAMLFLLIGC	LLFVLTPTFV	FCYMEDWSKL
210	220	230	240	250
EAIYFVIVTL	TTVGFGDYVA	GADPRQDSPA	YQPLVWFWIL	LGLAYFASVL
260	270	280	290	300
TTIGNWLRVV	SRRTRAEMGG	LTAQAASWTG	TVTARVTQRA	GPAAPPPEKE
310	320	330	340	350
QPLPPPPCP	AQPLGRPRSP	SPPEKAQPPS	PPTASALDYP	SENLAFIDES
360	370	380	390	
SDTQSERGCP	LPRAPRGRRR	PNPPRKVVRP	RGPGRPRDKG	VPV

**Figure 19. Human TRAAK channel monomer sequence.** Sequence covered by existing crystal structures of TRAAK is shown in black while the 133 residues long C-terminal domain whose structure has not been resolved yet is marked in green.

To extend the search, alignment parameters were changed as already stated in section 3.1. 3 matches with different TRAAK C-terminal regions were obtained. Alignments are shown and ranked on Figure 20. The best one with score of 26.4

corresponds to *Carbapenam Synthetase Chain A* with ID 1Q15, being the only structure out of the 3 matches actually available. Homology modelling was performed with YASARA as explained in section 3.1. Results are shown on Figure 21. Model item (dihedrals, 1D packing, 3D packing and overall) scoring is expressed in Z-Score before and after energy minimization. Model 3D structure after energy minimization is depicted as well. Its colouring goes along with model quality where blue stands for a perfect score and yellow for worse. Model quality per residue is also shown and secondary structure adoption of the sequence is shown as blue cylinder or red arrow representing an  $\alpha$ -helix of  $\beta$ -sheet, respectively. The majority of residues are comprised between 0 and -2 in terms of quality per residue. The model is in extended configuration with short  $\alpha$ -helix on the C-terminal proximal region and two short  $\beta$ -sheets by the middle of the structure forming an anti-parallel  $\beta$ -laminae. Although dihedrals normality score is “good” 1D, 3D and the overall scoring of the model are “poor”.

Chain A, Carbapenam Synthetase						
Sequence ID: <a href="#">1Q15_A</a> Length: 503 Number of Matches: 1						
Score	Expect	Method	Identities	Positives	Gaps	
26.4 bits(69)	3.1	Composition-based stats.	31/110(28%)	45/110(40%)	12/110(10%)	
Query 17	SWTGTVTARVTQRAGPAAPPPEKEQPLPPPPCPAQLGRPRSPSPEKAQPPSPPTASA	76				
Sbjct 135	AVMTNSLKLVTAAEGEGALWFE-EEALV---C--QSLMRADTYTPVKNAQRLKPGAVHV	187				
Query 77	LDYPSENLAFIGDESSDTQ--SERGCPLPRAPRGR---RRPMPRPKPVPRP	121				
Sbjct 188	LTHDSEGYSFVESRTLTPASNQLLALPRELLALIDRYLNAPLEDLAPR	237				

Chain B, Structure Of Tra1 Subunit Within The Chromatin Modifying Complex Saga						
Sequence ID: <a href="#">5OEJ_B</a> Length: 3825 Number of Matches: 1						
Score	Expect	Method	Identities	Positives	Gaps	
26.1 bits(68)	5.1	Composition-based stats.	21/67(31%)	30/67(44%)	8/67(11%)	
Query 14	QAASWTGTVTARVTQRAGPAAPPPEKEQPLPPPPCPAQLGRPRSPSP--EKAQ--PP	69				
Sbjct 3217	QTRTETSGTTAESDKK--PSIPP--KEEQGSPQSRPATTQASPAQSQENGESSQKHPP	3272				
Query 70	SPPTASA 76					
Sbjct 3273	EIPTDTS 3279					

Chain A, Cryo-em Structure Of The Rabbit Voltage-gated Calcium Channel Cav1.1 Complex At 4.2 Angstrom						
Sequence ID: <a href="#">3JBR_A</a> Length: 1873 Number of Matches: 1						
Score	Expect	Method	Identities	Positives	Gaps	
25.5 bits(66)	7.2	Composition-based stats.	19/68(28%)	25/68(36%)	4/68(5%)	
Query 48	PCPAQLGRPRSPSPEKAQPPSPPTASALDYPSENLAFIGDESSDTQSERGCPLPRAPRG	107				
Sbjct 1717	PCAGKLNQQLVQPGMPINQAPPAPCQPSTDPPEPGRQRTSLTGSLLQDE--APQRRSSEG	1774				
Query 108	R--RRPNP 113					
Sbjct 1775	STPRRPAP 1782					

**Figure 20. Protein sequence alignments with TRAAK C-terminal domain and personalized filter.** 3 matches between distinct parts of TRAAK C-terminal domain are shown classified by matching score from better to worst.



**Figure 21.** Homology modelling of TRAAK C-terminal domain using as target structure 1Q15. Model item scoring is expressed in Z-Score before and after energy minimization. Dihedrals, 1D packing, 3D packing and overall score are shown. Model 3D structure after energy minimization is depicted as well as model quality per residue. Model colouring goes along with model quality where blue stands for a perfect score and yellow for terrible. Secondary structure adoption of the sequence is shown as blue cylinder or red arrow representing an  $\alpha$ -helix of  $\beta$ -sheet, respectively.

### 3.2. YASARA manual homology and *ab initio* model

Given the low score of the automatic homology model based on manual alignment model, another strategy to build TRAAK C-terminal model was adopted. Searching for sequence alignments with shorter TRAAK C-terminal regions in agree with the new alignment adjustment parameters mentioned in section 3.2 of Materials & Methods was carried out. Sequence alignments with the four TRAAK C-terminal regions shown on Figure 11 in red, cyan, green and purple correspond to alignments on Figure 22 2A, 2B, 2C and 2D respectively. Respective homology-built models from these alignments can be inspected on Figure 23. 2A and 2D models have “optimal” overall score while 2B and 2C “satisfactory”. The only “bad” region in quality per residue, in all four models corresponds to the proximal PPSPP sequence in model 2B. One secondary folding region was identified, an  $\alpha$ -helix, covering almost the entire 2A model. As shown on Figure 11, coverage of TRAAK C-terminal domain sequence by the constructed four short homology models is not complete. *Ab initio* modelling was performed on those parts not encompassed by the homology models forming a final model shown on Figure 24. The overall scoring of the final model is “satisfactory” although its 1D packing is “poor”. The score of model 1 (Figure 21) is being improved in this second model (Figure 24).

Chain A, Crystal Structure Of Ms6564 From Mycobacterium Smegmatis							
Sequence ID: <a href="#">4JKZ_A</a> Length: 194 Number of Matches: 1							
Score	Expect	Method	Identities	Positives	Gaps		
24.9 bits(57)	18	Compositional matrix adjust.	12/23(52%)	15/23(65%)	0/23(0%)		2A
Query	11	LTAQAASHVTGTVARVTQAGPA	33				
		+TA ASW GT+ A +T R G A					
Sbjct	87	VTADLASWAGTLAAALTTRRGHA	109				
Chain A, Solution Structure Of Tandem Sh3 Domain Of Sorbin And Sh3 Domain- Containing Protein 1							
Sequence ID: <a href="#">2MOX_A</a> Length: 143 Number of Matches: 1							
Score	Expect	Method	Identities	Positives	Gaps		
23.5 bits(53)	40	Compositional matrix adjust.	14/35(40%)	18/35(51%)	1/35(2%)		2B
Query	62	PPEKAQPPSPPTASALDYPSENLAFIGESSDTQSE	96				
		P EKAQP L+Y E +A + + DTQ E					
Sbjct	65	PAEKAQPKKLTVPQVLEY-GEAIKFNFGDTQVE	98				
Chain A, Crystal Structure Of Oxidation Intermediate (20 Min) Of Nadh- Cytochrome B5 Reductase From Pig Liver							
Sequence ID: <a href="#">3W2E_A</a> Length: 271 Number of Matches: 2							
Score	Expect	Method	Identities	Positives	Gaps		
26.5 bits(55)	2.0		10/17(59%)	11/17(64%)	5/17(29%)		2C
Query	2	PPPEKEQPLL---PPP	14				
		PPPE E+PL PPP					
Sbjct	233	PPPE-EEPLVLMCGPPP	248				
Chain A, Crystal Structure Of A3vp1 Of Agill OF STREPTOCOCCUS MUTANS							
Sequence ID: <a href="#">3IPK_A</a> Length: 497 Number of Matches: 2							
Score	Expect	Method	Identities	Positives	Gaps		
22.1 bits(49)	12	Composition-based stats.	10/33(30%)	15/33(45%)	2/33(6%)		2D
Query	1	RGCLPRAPRRRRPNPPRPVVRPRGGRPRDK	33				
		R +P+ + +P PP KP P P +K					
Sbjct	439	RAVWPKVTK--EKPTPPVKPTAPTPTYETEK	469				

**Figure 22. Protein sequence alignments with four TRAAK C-terminal domain regions.** Panels 2A-D show the best sequence alignment match found for each C-terminal domain regions depicted in figure 11: 2A) L11-A33 matches with V87-A109 from 4JKZ; 2B) P62-E96 matches with P65-E98 from 2MOX; 2C) P2-P14 matches with P233-P248 from 3W2E; 2D) R1-K33 matches with R439-K469 from 3IPK. Searches were done with BLASTp against PDB database.

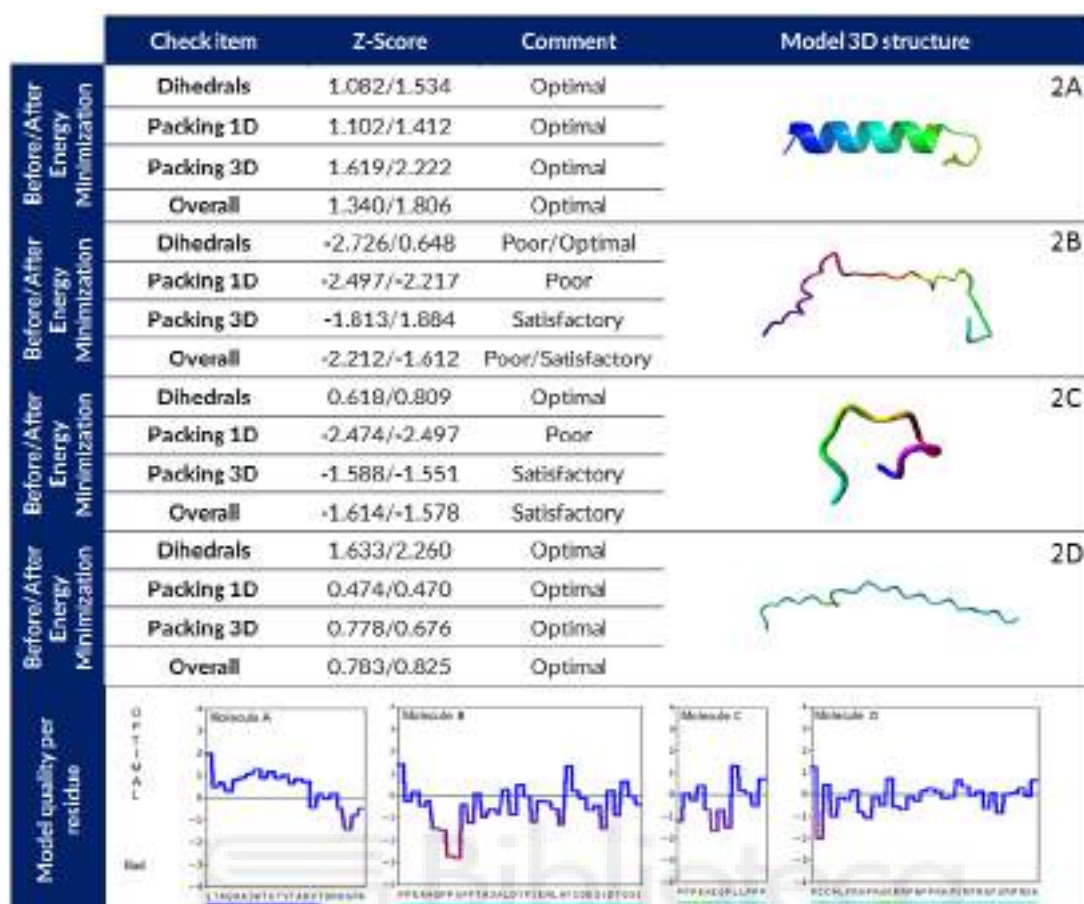


Figure 23. Homology modelling of four TRAAK C-terminal domain regions. Target structures used to build all the models are the one shown on Figure 22. Model item scoring is expressed in Z-Score before and after energy minimization. Dihedrals, 1D packing, 3D packing and overall score are shown. Model 3D structure after energy minimization is depicted as well as model quality per residue. Model colouring goes along with model quality where blue stands for a perfect score and yellow for terrible. Secondary structure adoption of the sequence is shown as blue cylinder representing an  $\alpha$ -helix.



Figure 24. TRAAK C-terminal domain model combining homology and *ab initio* modelling. Model item scoring is expressed in Z-Score before and after energy minimization. Dihedrals, 1D packing, 3D packing and overall score are shown. Model 3D structure after energy minimization is depicted as well as model quality per residue. Model colouring goes along with model quality where blue stands for a perfect score and yellow for terrible. Secondary structure adoption of the sequence is shown as blue cylinder representing an  $\alpha$ -helix.

### 3.3. YASARA automatic homology model

Finally, TRAAK C-terminal domain reconstruction was targeted through automatic homology modelling by YASARA. During template search only two structure matches were found, summarized in Table 12. Structure 3IOX corresponds to an adhesion protein localized on the surface of *S. mutans* and structure 4Q6Z to a lipoproteic regulator of protein 1B related to penicillin binding from *E. coli*. In accordance to the total score, 3IOX shows a better cover percentage of TRAAK sequence, a better alignment score and better E-value. Three different models from this target and one from 4Q6Z were constructed as shown on Figure 25. The best one has an overall Z-score of -0.177, covers 3IOX structure between residues 16-115 and is formed by two short  $\alpha$ -helix, one on the proximal end and one by the middle of the structure while the rest of the model remains as disordered folding. Observing the model quality per residue of the best 3IOX model on Figure 26, apparently substituting the proximal end by model 2A shown on Figure 23 it could be improved. After this substitution the model was improved to “optimal” with a score of 0.090 instead of -0.177.

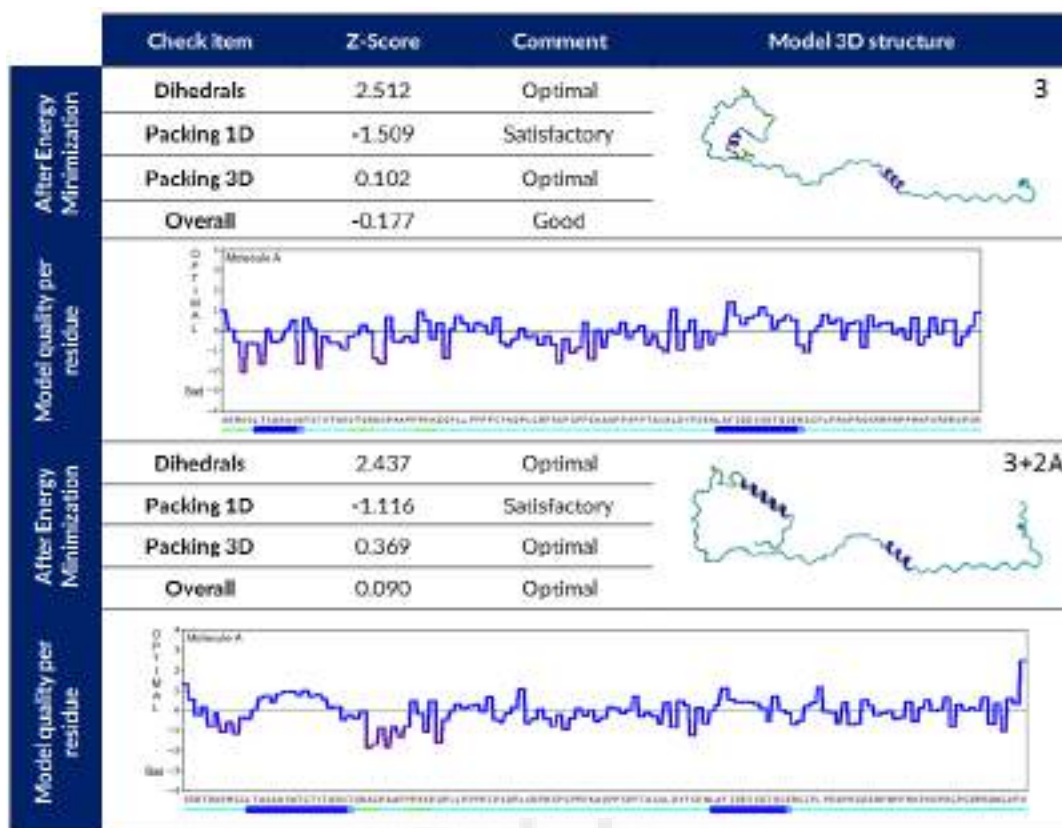
**Table 12.**

Target structure matches found by sequence alignment with TRAAK C-terminal sequence during YASARA automatic homology modelling assay.

Template	Total score	BLAST E-value	Align Score	Cover	ID	Resolution	Information
1	8.49	0.014	37	41%	3IOX-A	1.80Å	Crystal structure of A3vp1 of AgIII of <i>S. mutans</i>
2	5.85	0.25	32	38%	4Q6Z-A	2.80Å	Lpob C-terminal domain from <i>E. coli</i>

Rank	Z-score	Model ID	Residues	Comment	Structure
1	-0.177	3IOX-A03	16-115	Good	
2	-1.014	3IOX-A01	16-115	Satisfactory	
3	-1.408	3IOX-A02	16-127	Satisfactory	
4	-2.862	4Q6Z-A	17-133	Poor	

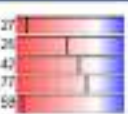
**Figure 25. TRAAK C-terminal domain automated homology models.** Models are ranked according to overall Z-score. Model 3D structure after energy minimization is depicted. Blue cylinder represents an  $\alpha$ -helix while red arrow a  $\beta$ -sheet.



**Figure 26. Final TRAAK C-terminal domain automated homology models.** Automated model (3) is correct (good overall score) but it was improved (optimal overall score) swapping 2A model with the corresponding region from model 3 (3+2A). Model item scoring is expressed in Z-Score after energy minimization. Dihedrals, 1D packing, 3D packing and overall score are shown. Model 3D structure is depicted as well as model quality per residue. Secondary structure adoption of the sequence is shown as blue cylinder representing an  $\alpha$ -helix.

### 3.4. Online 3D structure predictions

Modelling of TRAAK C-terminal domain was also attempted using online 3D structure prediction platforms mentioned before. The overall result obtained from all these platforms predicted C-terminal domain remains in unfolded configuration. The scores provided by all the online tools were poor. Figure 27 summarizes the most important characteristics of only some models, given that some of the used online prediction servers were not able to make any structure prediction based on the query.

Platform	Score	Match structure	Protein	Coverage	Structure
SWISS MODEL	OMEAN -5.27 CA -2.26 All Atoms -1.42 Solvation -0.77 Torsion -5.58	1UM1	MeCP2	32%	
					
Ps-v2	Underrange	1MV3_A	BIN1	22%	
I-TASSER	-3.30 (-5 to 2)	2NBI	Pleuralin 1	25%	
Galaxy Homomer	-0.570 (-5 to >0)	No info	No info	No info	

**Figure 27. 3D structure prediction servers results for TRAAK C-terminal domain modelling.** Summary of the most important data provided by online prediction platforms about TRAAK C-terminal domain reconstructed homology models. Overall score provided by these platforms comprises different ranges as specified. Broadly, target sequence coverage in all models was poor. 3D model structures in general remain unfolded, being small regions recognized as  $\alpha$ -helices or  $\beta$ -sheets.

### 3.5. Secondary structure prediction

Secondary structure prediction servers were employed in order to obtain general information about TRAAK C-terminal domain secondary structure and to check matches with the 3D structure prediction from online servers and manual reconstructions. CFFSP prediction is shown in Figure 28 and GOR's in Figure 29. Both predicted transmembrane domains were conformed by  $\alpha$ -helices while C-terminal region spanning from residue 260 to 393 mainly adopted a random coil conformation.





#### 4. TRAAK PUTATIVE PROTEIC INTERACTING PARTNERS

The evaluation of 7 TRAAK C-terminal domain fragments against the 84 SH3 ADAN database domains gave rise to 5880 possible ligand-SH3 complexes whose interaction energy comprises values from 111.4 kcal/mol (worst) to -21.3 kcal/mol (best). Mainly two regions from TRAAK 260-393 sequence group the major part of SH3 targets as it can be observed on [Figure 30](#). These regions comprise residues 290-314 and 355-386 being this last the most energetically favoured. Some SH3 domains target multiple TRAAK regions with small difference in binding energy. Examples could be domains from proteins with PDB ID 2P4R and 2OI3. Ligand recognition and sequence complementarity between SH3 domain and a fragment from TRAAK C-terminal does not necessarily indicate that both proteins interact. It could be that the biological environment of both is not coincident. That is why best results were filtered by cellular localization and function of the protein corresponding to a SH3 domain. Solutions in which proteins present a localization distinct from TRAAK's one or any function which in any case could modulate TRAAK function, were discarded. Such is the case of solutions 1OEB, 1W70 related with immune response or 1SSH and 2DRM which are found in unicellular organisms. Best putative TRAAK interacting partner proteins are depicted on [Figure 30](#). These proteins correspond to tyrosine kinases (2DIX- interferon inducible double stranded RNA dependant protein kinase activator A (PACT); 1BBZ, 2OI3, 2O88, 1BO2 - ABL tyrosine kinase), ubiquitinases (2P4R, 2BZ8 -ubiquitin protein ligase), oxidases (1OV3 - NADPH oxidase) and cytoskeletal remodellers (2O9V - cytoskeletal remodelling and cell adhesion).

Through computational techniques, TRAAK-protein interacting partners could be predicted, even though a reliable C-terminal structure model was not achieved. This is feasible with only the availability of TRAAK sequence and the recompilation of previous studies of SH3 domains interaction.

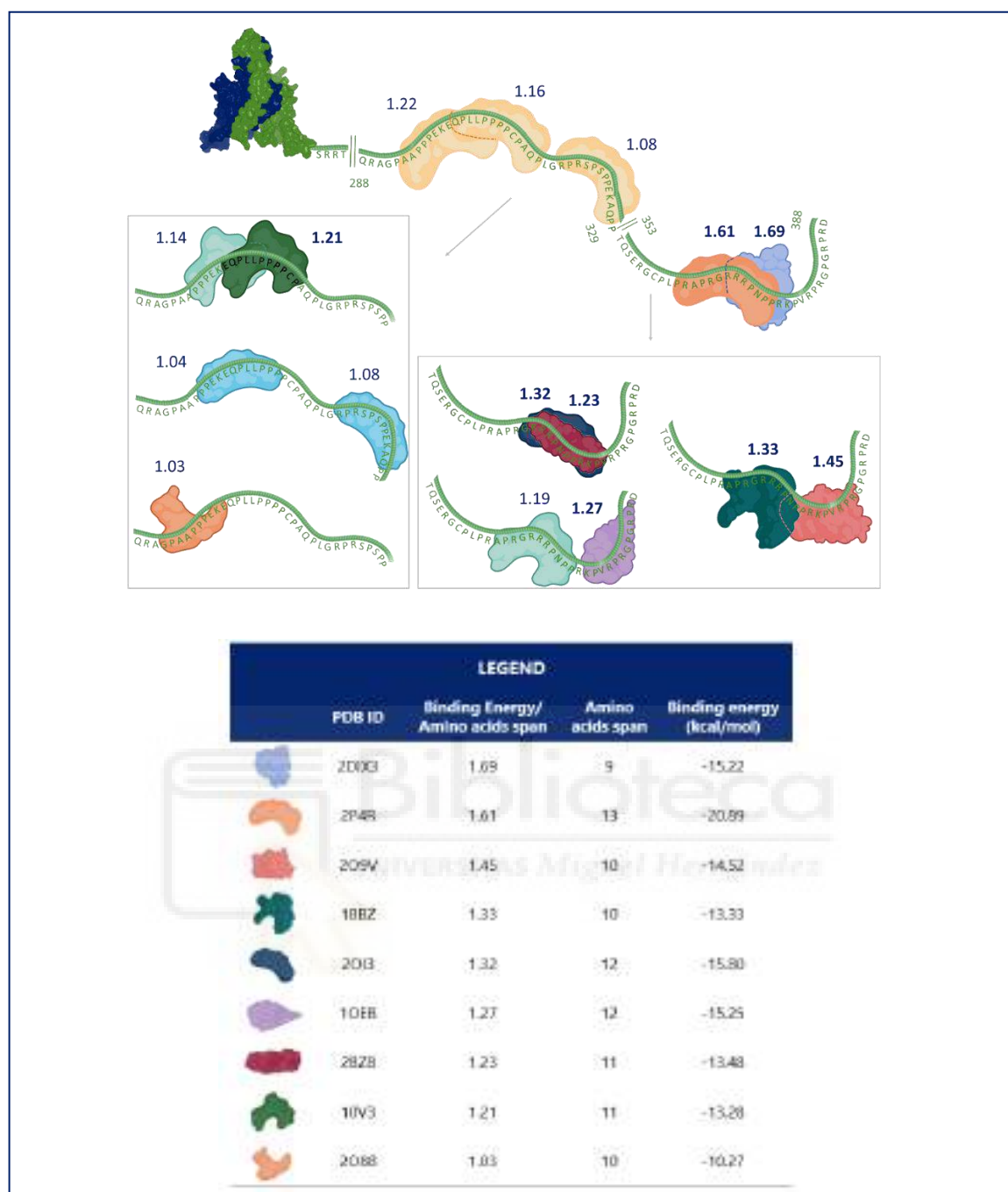


**Figure 30. TRAAK putative proteic interacting partners through SH3 domains.** TRAAK C-terminal sequence corresponding to residues 288-329 and 355-388 is shown as green strand. Distinct proteins containing SH3 domains are represented with diverse colour and shape surfaces on TRAAK sequence with which they interact. For proteins interacting in more than one region, the best in terms of energy is shown in darker colour (e.g. 2P4R, 20I3, 10V3). Normalized absolute binding energy according to the number of interacting amino acids is annotated in blue above each protein (the best ones appear in bold). The PDB ID of each protein, its total binding energy in kcal/mol, the number of amino acids it interacts with and the normalized absolute binding energy can be seen in the legend.

## 5. IN VITRO COMPOUNDS TESTING

### 5.1. TRAAK electrophysiological behaviour in recombinant cells

In order to determine if transiently co-transfected Hek 293LTV cells with hTRAAK and a fluorescent protein (YFP) could be used as a model to test VS selected compounds, it was necessary to check if TRAAK current was electrophysiologically detectable in these cells. Current was registered with voltage-clamped patch clamp in whole-cell mode stepping from -120 to +120 mV in 10 mV increases, during 300 ms and at a holding potential of -70 mV or by a ramp protocol from -120 to +120 mV as shown on [Figure 31](#). In non-transfected (mock) cells current amplitude at +120 mV was quite small (200 pA). In TRAAK expressing cells, outward, instantaneous and non-inactivating current up to 2 nA was detected, while almost no inward current was observed [49] ([Figure 31 A](#)). The application of arachidonic acid (AA) at different concentrations increased the outward current noticeably ([Figure 31 A](#)). An increase in inward current was also observed, although the ratio inward/outward current was very small. Perfusion of cells with 10  $\mu\text{M}$  AA increased 2-fold the basal TRAAK current at positive potentials, at 25  $\mu\text{M}$  more than 4-fold and at 50  $\mu\text{M}$ , almost 6-fold ([Figure 31 B](#)). At this last concentration, the registered outward current was so high that in more cases cells suffered and the seal was time unsustainable. Current density (pA/pF) obtained after instillation of 10  $\mu\text{M}$  AA pronounced the outward rectifying behaviour of the channel in the studied conditions ([Figure 31 C](#)). In the  $G/G_{\text{max}}$  - voltage relationship can be observed that at 7 mV almost 50% of the channels are in open state and at 50 mV nearly maximal conductance is reached ([Figure 31 D](#)).

Hek 293LTV cells express endogenous voltage dependant  $\text{K}^+$  channels [243]. In order to check the presence and amplitude of  $\text{K}_v$  currents in TRAAK Hek 293LTV transfected cells and if they could obstruct TRAAK current registers and compounds test, whole cell currents from TRAAK expressing cells were registered. [Figure 32](#) shows currents recorded with the specified step and ramp protocols in basal conditions, after instillation of the classical  $\text{K}^+$  channel blocker tetraethylammonium (TEA) at 2 mM, 10  $\mu\text{M}$  AA or 2 mM TEA plus 10  $\mu\text{M}$  AA. TEA provoked a light decrease of basal current at positive potentials (40-80 mV) which was statistically insignificant. When cells were stimulated with AA, TEA produced even lower current blockage, demonstrating endogenous  $\text{K}_v$  currents presence should not affect compounds test. Aiming to decrease possible effect interference between channel types, it was decided to perform experiments at potentials higher than 80 mV ([Figure 32 B](#)).

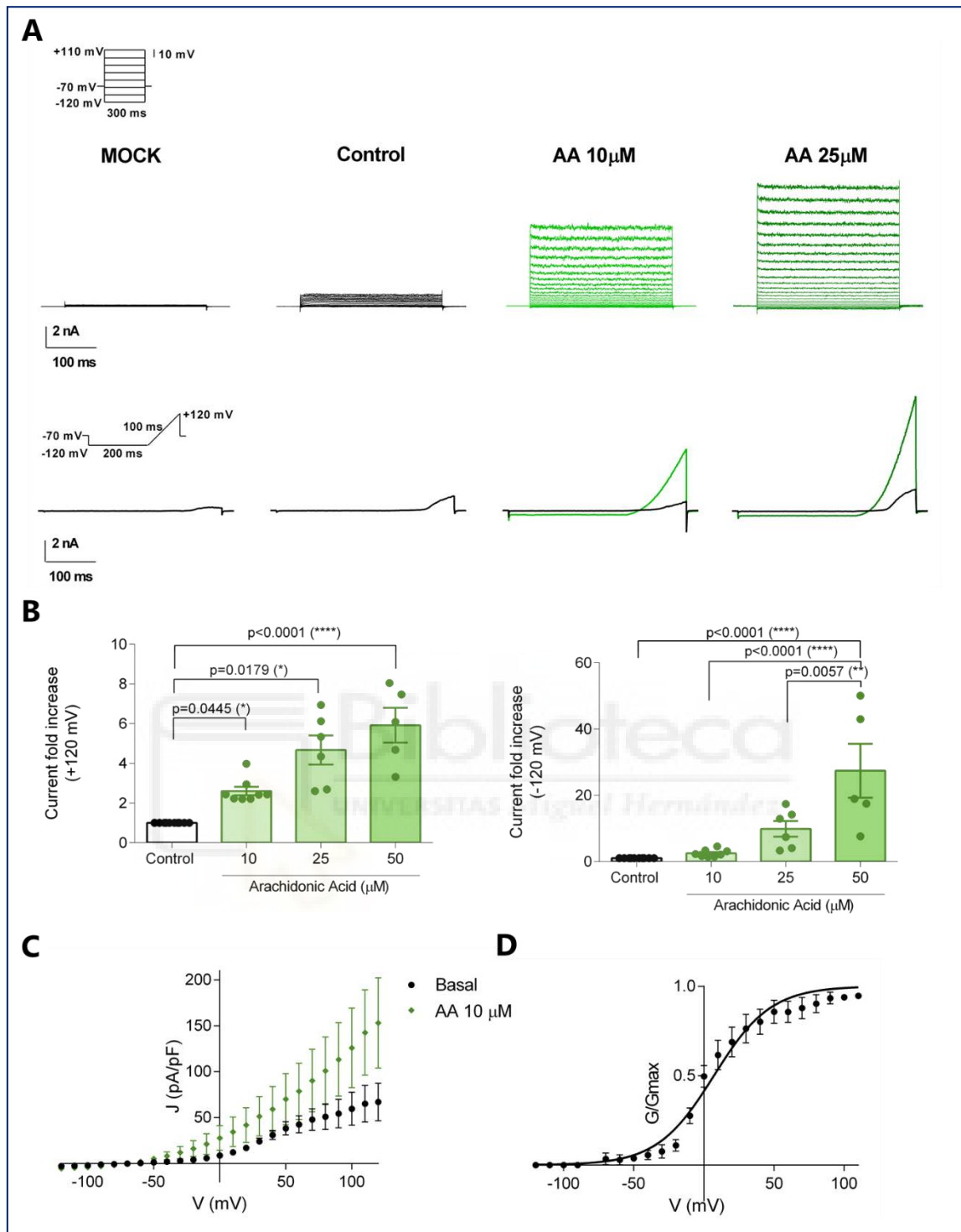


**Figure 31. TRAAK electrophysiological behaviour in recombinant cells. A)** Representative current registers obtained with the depicted steps and ramp protocols in mock and TRAAK expressing cells (black traces) and after stimulation with arachidonic acid (green traces). **B)** Arachidonic acid dose response relationships from TRAAK current registered at +120 (left panel) and -120 mV (right panel). Statistical analysis consisted in One-Way ANOVA with Bonferroni post-hoc test ( $F(3,25)=24.81$ ,  $p<0.0001$  – left panel;  $F(3,25)=14.72$ ,  $p<0.0001$  – right panel). Statistical significance was set at  $p<0.05$ . **C)** Current density (pA/pF) from basal TRAAK current and after stimulation with 10 μM arachidonic acid (n=8). **D)** G/Gmax - voltage relationship of TRAAK current (n=8). Data was fitted to a Boltzmann sigmoidal with constraints (bottom = 0 and top = 1).  $V_{50} = 7.08 \pm 1.82$  mV and slope =  $20.22 \pm 1.67$ . All data is expressed as mean  $\pm$  SEM.

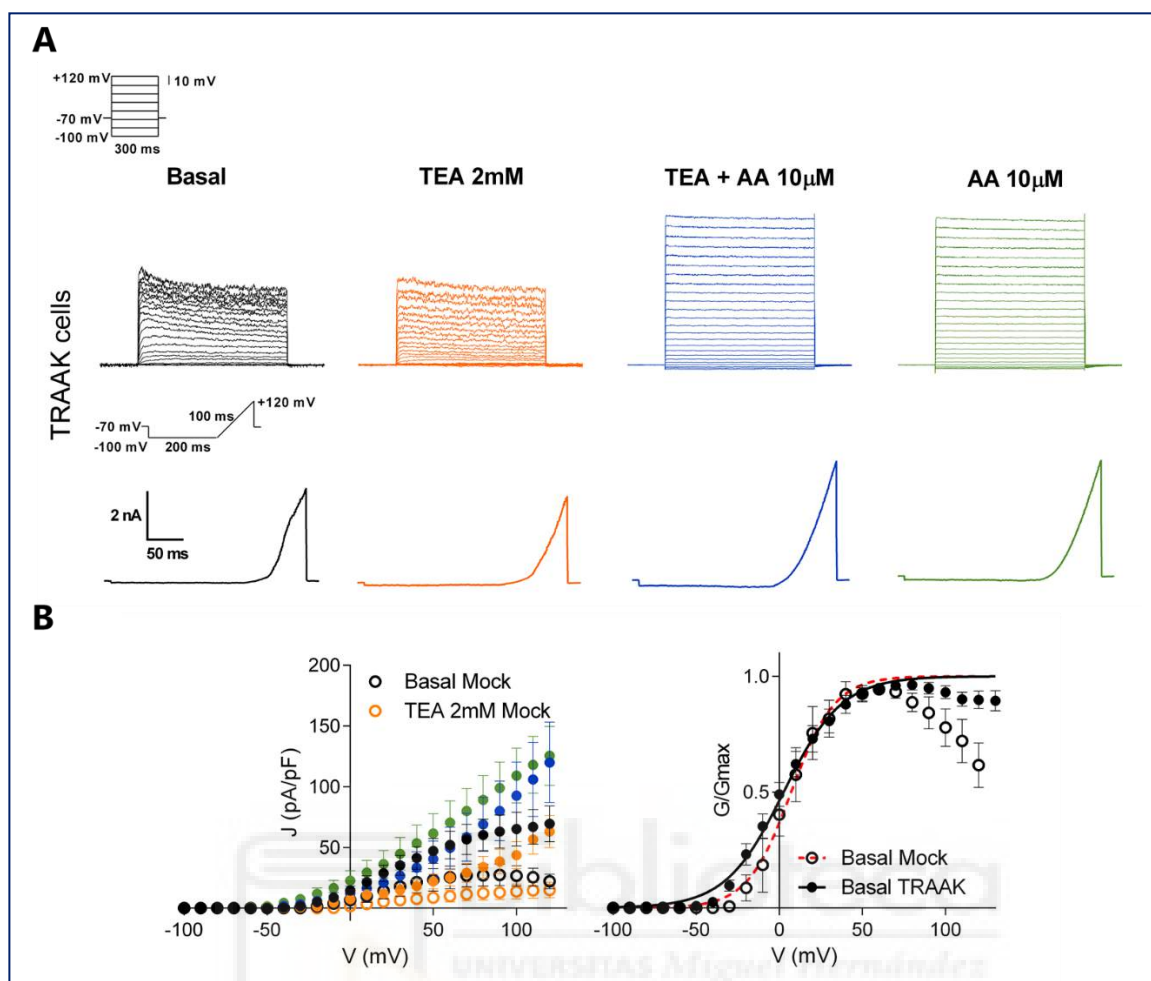


**Figure 32. Non-TRAAK  $K^+$  current registered in recombinant cells.** **A)** Representative current registers obtained with the depicted steps and ramp protocols in TRAAK transfected cells. TRAAK basal current registers are shown in black, current after application during 1 min of 2 mM TEA in orange, 2 mM TEA plus 10  $\mu$ M arachidonic acid in blue and 10  $\mu$ M arachidonic acid in green. Current density (pA/pF) from previous conditions and from mock cells (left panel), and  $G/G_{max}$ -voltage relationship from mock and TRAAK expressing cells (right panel) are shown in **B)** ( $n=6$ ). Data from  $G/G_{max}$ -voltage relationships was fitted to a Boltzmann sigmoidal with constrains (bottom = 0 and top =1). Data is expressed as mean  $\pm$  SEM.

The capacity to block TRAAK current in transiently transfected cells was explored using 10  $\mu$ M sipatrigine, a neuroprotective agent known to inhibit TREK-1 and TRAAK channels [106]. Sipatrigine demonstrated to effectively inhibit TRAAK current, up to 50% in some cells, although the mean blockage was  $22.1 \pm 0.7\%$  as shown on Figure 33. Its effect was more pronounced at positive potentials.

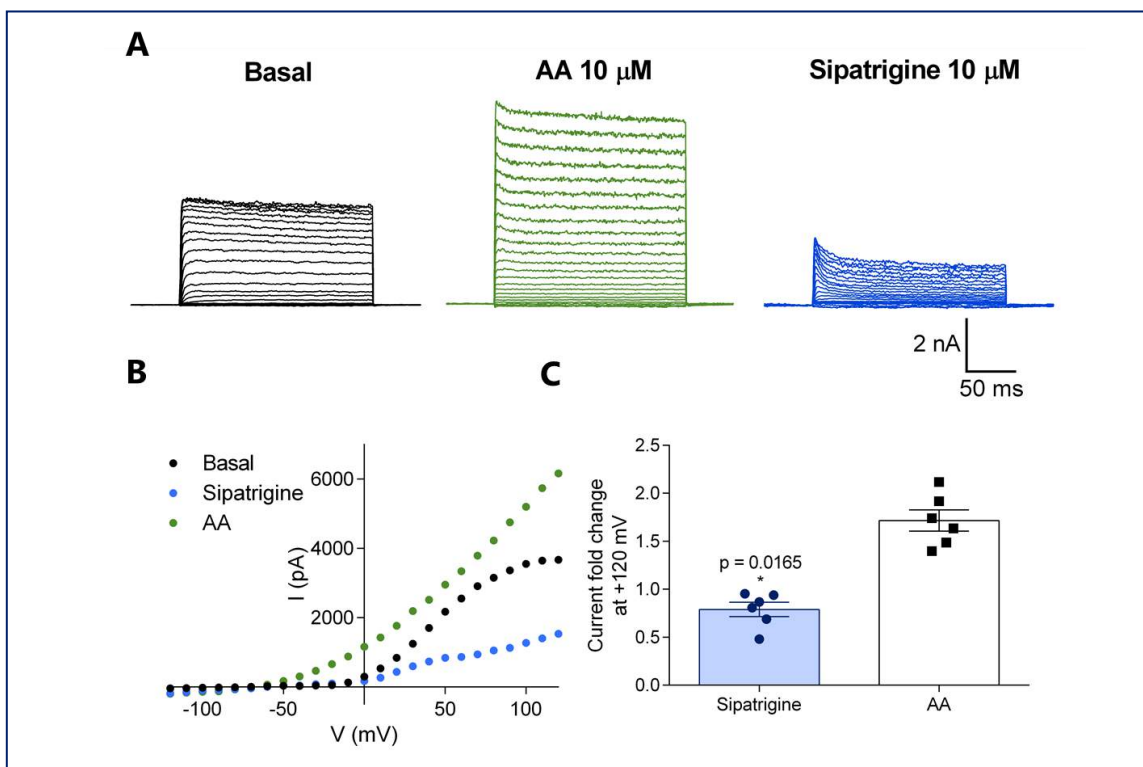


**Figure 33. Sipatrigine inhibitory effect on TRAAK currents.** **A)** Representative basal TRAAK current (black traces), after application of 10  $\mu\text{M}$  AA (green traces) and 10  $\mu\text{M}$  sipatrigine (blue traces) during 1 min. **B)** Representative IV relationship of TRAAK current from **A)** conditions. **C)** Current fold change at +120 mV for sipatrigine and AA compared to basal current. Sipatrigine effect was statistically compared to basal current using an unpaired Students' t-test. Statistical significance was set at  $p < 0.05$ . Data is expressed as mean  $\pm$  SEM.

## 5.2. *In vitro* testing of VS selected compounds

Hit molecules selected by virtual screening were tested on transiently transfected Hek 293LTV cells with hTRAAK. The expressed channel was observed to conduct much more outward current when cell suffered depolarization than inward current when hyperpolarized, a typical behaviour of outward rectifier  $\text{K}^+$  channels [48, 244]. Registered current was non-inactivating and reversed at a value near  $\text{K}^+$  equilibrium (Figure 31 A, C). In whole cell configuration channel activity was potentiated by arachidonic acid (Figure 31 A, B). This effect was completely reversible at low concentrations (Figure 35 C). Registered current was almost insensitive to classical  $\text{K}^+$  channel blockers like TEA at 2 mM (Figure 32) [244]. A light decrease in current was observed at positive potentials from 40 to 80 mV which was statistically insignificant and could be blamed to Hek cells endogenous expression of  $\text{K}_v$  channels [243]. Capacity to block registered current was explored by the instillation of sipatrigine, a TRAAK and TREK-1 blocker [106], which effectively decreased whole cell current at 10  $\mu\text{M}$  (Figure 33). All these data suggest that

## RESULTS

hTRAAK channel is effectively expressed during Hek cells transient transfection making the study system acceptable for VS hit compounds testing.

Virtual screening hit compounds from Prestwick library were perfused only on cells which first responded to AA in order to guarantee TRAAK expression. Effect of the 8 selected compounds from Prestwick chemical library tested at 10  $\mu$ M is shown on Figure 34. Pranlukast, lidoflazine, gliquidone and tribenoside exerted no significant effect on TRAAK current. Terfenadine, astemizol and pimozide seemed to block TRAAK and only irinotecan enhanced channel current (Table 13). Irinotecan, astemizol and terfenadine were selected to further characterize their effect.

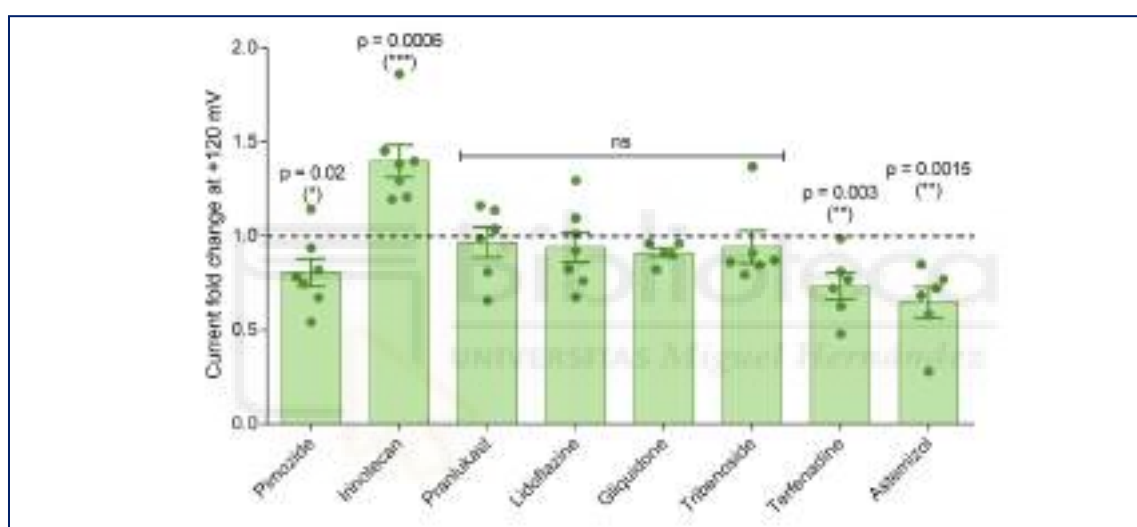


**Figure 34. Prestwick VS selected candidates' effect on TRAAK.** Current fold change at +120 mV of compounds compared to basal TRAAK current. Data was statistically analysed using an unpaired Students' t-test. Statistical significance was set at  $p < 0.05$ . Data is expressed as mean  $\pm$  SEM.

**Table 13. Prestwick VS selected candidates' effect on TRAAK.**

Compound	Current fold change at +120 mV	SEM	Comment
Irinotecan	1.40	0.09	Agonist
Astemizol	0.65	0.08	Antagonist
Terfenadine	0.73	0.07	Antagonist
Pimozide	0.81	0.07	Antagonist
Pranlukast	0.96	0.08	No effect
Lidoflazine	0.94	0.08	No effect
Gliquidone	0.91	0.03	No effect
Tribenoside	0.94	0.09	No effect

A group of ADME properties of the 8 *in vitro* tested compounds were studied in order to figure out if there is any specific physico-chemical characteristic which helps

distinguish between active and inactive molecules (Table 14). In bold are shown those properties which concur in the active molecules and differ from the inactive ones. For instance, all compounds that showed any effect on TRAAK have a net positive charge of +1, polar desolvation around -50 kcal/mol, tPSA (topological polar surface area) [245] around 45 Å<sup>2</sup> and an ilogP (3D physics-based octanol/water partition coefficient) [246] between -6.5 and -9. Curiously, if we analyse TRAAK contact potential (Figure 35), norfluoxetine (Site A) and ML402 (Site B) binding pockets show a negatively charged surface favouring binding of positively charged molecules. Pranlukast has a negative charge which would not allow it to enter the pocket, while gliquidone and tribenoside have no charge which could result in the decay of any possible effect. Pranlukast and gliquidone show a tPSA value of 130 Å<sup>2</sup> which indicates both are quite bad cell permeators. Lidoflazine shows a very negative polar desolvation value which means it prompts to precipitate. Its ilogP value is also highly negative meaning that the compound is highly hydrophilic. This could difficult its binding to a buried protein pocket. Generally, the ESOL values [247] of all the tested compounds state they are poorly soluble.

**Table 14. Prestwick VS selected candidates' ADME properties.** Molecular weight – MW (g/mol); Octanol/water partition coefficient – LogP; Charge; Polar desolvation (free energy); tPSA – topological polar surface area (Å<sup>2</sup>); ilogP – implicit octanol/water partition coefficient; ESOL – aqueous solubility.

Compound	MW	LogP	Charge	Polar-desolv	tPSA	ilogP	ESOL
Astemizol	459.58	5.58	<b>1</b>	<b>-51.93</b>	<b>43.52</b>	<b>-8.45</b>	-6.38
Terfenadine	472.68	6.60	<b>1</b>	<b>-46.43</b>	<b>44.90</b>	<b>-6.06</b>	-6.70
Pimozide	462.55	6.01	<b>1</b>	<b>-51.66</b>	<b>42.23</b>	<b>-8.98</b>	-7.09
Irinotecan	587.69	3.97	<b>1</b>	<b>-53.16</b>	113.71	<b>-6.57</b>	-6.37
Pranlukast	481.50	4.84	-1	-40.96	130.09	-4.53	-4.86
Gliquidone	527.63	5.32	0	-17.31	130.26	1.64	-5.87
Lidoflazine	493.63	6.13	2	-129.14	37.98	-26.73	-6.43
Tribenoside	478.58	4.50	0	-13.10	66.38	2.40	-4.76

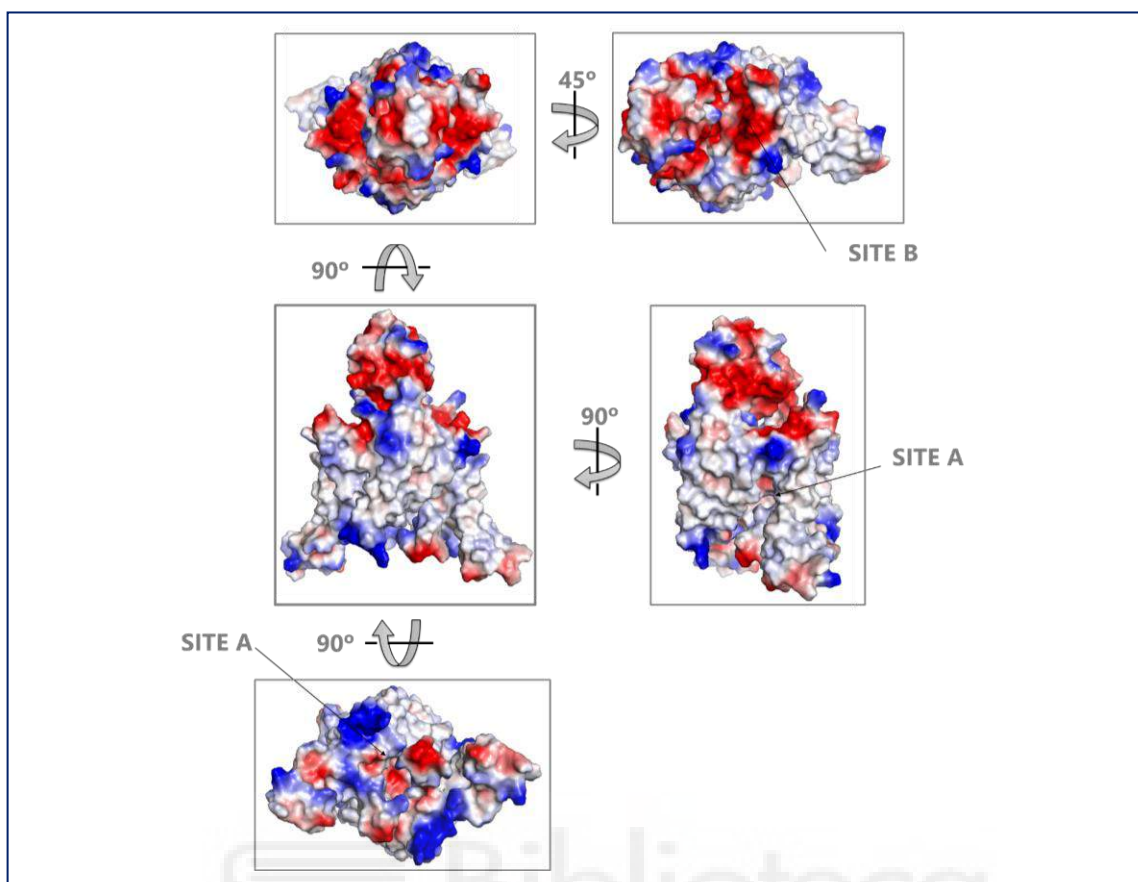


**Figure 35. TAAK contact potential.** Red and blue colours denote negative and positive charge, respectively. Site A points to the norfluoxetine binding pocket and Site B to ML402's one. Both central panels represent TAAK from a transmembrane view, lower panel, from an intracellular view and both upper panels from an extracellular view.

AG1529 (AG26) was selected from the capsaicinoids library screened virtually on TAAK given that it shown a better interaction energy than control for norfluoxetine and ML402 binding sites and because it has a C12 fatty acid tail which mimicking effect of other fatty acids could activate TAAK. The perfusion during 1 min of 5  $\mu$ M AG1529 on TAAK expressing Hek 293LTV cells did not exerted any change in basal TAAK current, as it can be seen on Figure 36.

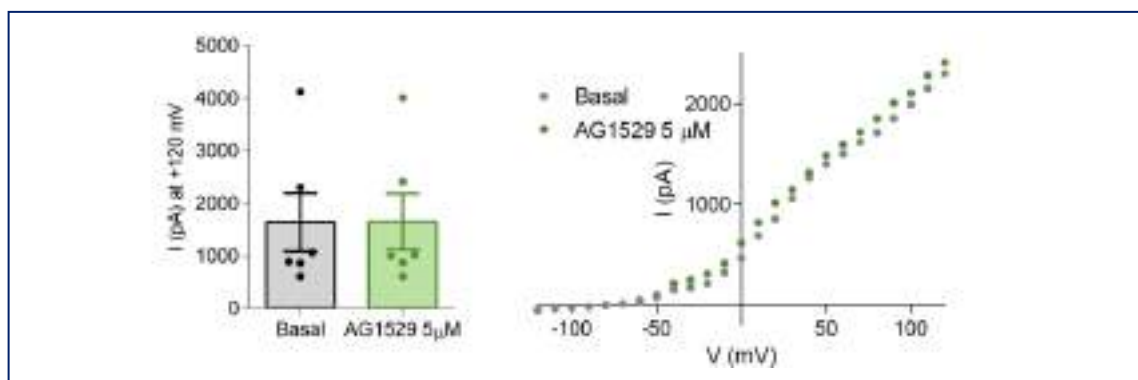


**Figure 36. AG1529 (AG26) effect on TRAAK.** Bar graph represents change in TRAAK current (pA) at +120 mV in basal state and after application of 5  $\mu\text{M}$  AG1529 during 1 min. Representative IV relationship of current from -120 mV to +120 mV in basal condition and after perfusion of 5  $\mu\text{M}$  AG1529 during 1 min. Data was statistically analysed using a paired Students' t-test. Statistical significance was set at  $p < 0.05$ . No statistically significant difference was observed. Data is expressed as mean  $\pm$  SEM.

### 5.3. Compounds pharmacological characterisation on recombinant cells

Irinotecan effect was assessed on recombinantly expressed hTRAAK. Figure 37 A shows the current density-voltage relationships from -120 to +120 mV in basal conditions and after application of 10  $\mu\text{M}$  irinotecan or AA. An increase in outward current can be noted after application of 10  $\mu\text{M}$  irinotecan, similar to AA. Contrary to AA, irinotecan provokes a 1.5-times increase in inward current with respect to basal current after washout (Figure 37 B). Irinotecan activates reversibly TRAAK as suggested by the recovery of basal current (Figure 37 C). Maximal current after instillation of irinotecan is reached slower compared to AA (Figure 37 D). Irinotecan was tested at 1, 10 and 100  $\mu\text{M}$ . No effect was detected at 1  $\mu\text{M}$  while 100  $\mu\text{M}$  produced a 5-fold current increase at +120 mV (Figure 37 E, F). At this last concentration activation was irreversible.

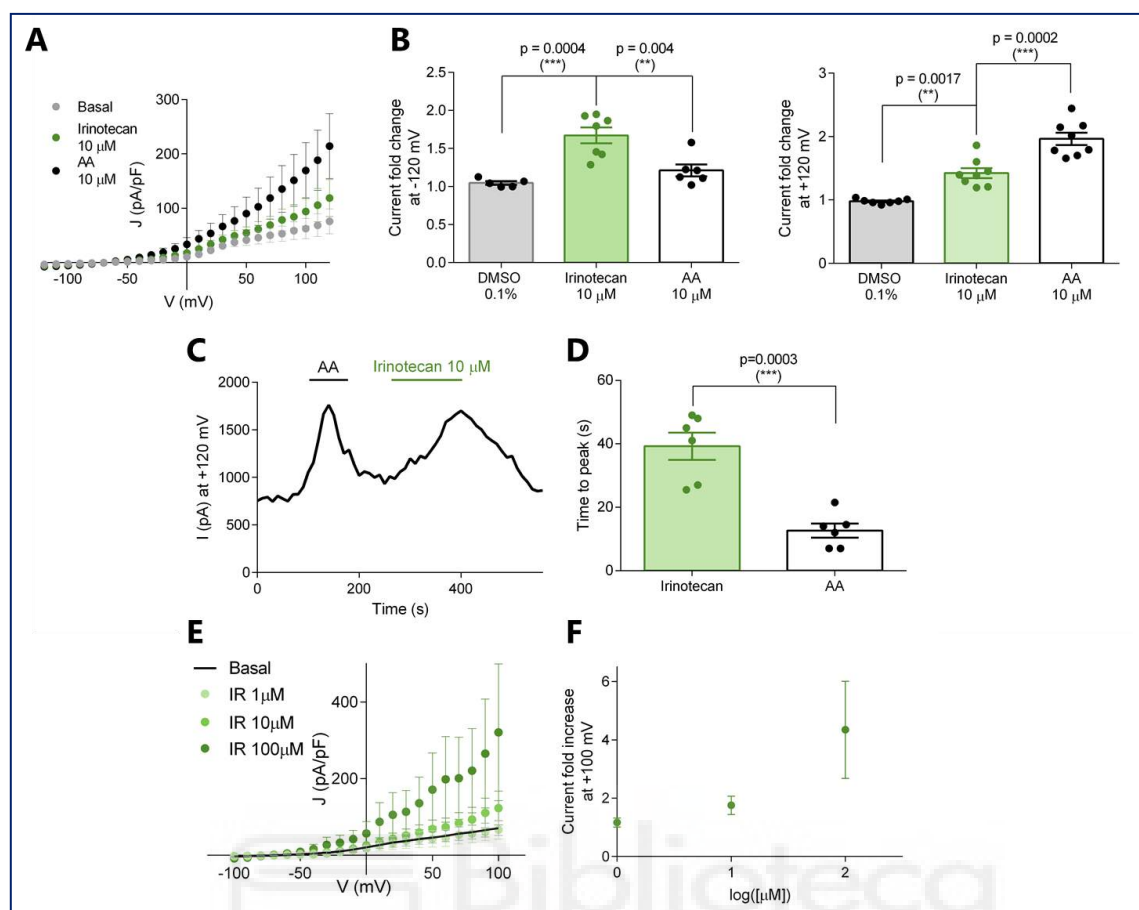


**Figure 37. Irinotecan effect characterisation on TRAAK transiently transfected cells.** **A)** Current densities of cells expressing TRAAK in basal condition (grey), after application of 10  $\mu\text{M}$  irinotecan (green) or 10  $\mu\text{M}$  AA (black) ( $n=6$ ). **B)** Current fold change at -120 mV (left) and +120 mV (right). Data is normalized with respect to basal current. Data was statistically analysed using One-Way ANOVA with Bonferroni's post hoc test ( $F(2,15)=14.93$ ,  $p=0.0003$  – left panel;  $F(2,20)=41.27$ ,  $p<0.0001$  – right panel). Statistical significance was set at  $p<0.05$ . **C)** Course time of current variation at +120 mV after instillation of 10  $\mu\text{M}$  AA or 10  $\mu\text{M}$  irinotecan. **D)** Time to reach maximal current peak after application of 10  $\mu\text{M}$  AA or 10  $\mu\text{M}$  irinotecan. Data was statistically analysed using unpaired Students' t-test. Statistical significance was set at  $p<0.05$ . **E)** Current densities of TRAAK expressing cells after perfusion with 1, 10 and 100  $\mu\text{M}$  irinotecan ( $n=11$ ). Black line shows basal current. **F)** Current fold increase at +100 mV after instillation of 1, 10 and 100  $\mu\text{M}$  irinotecan. P-value for statistical significance is shown on panel. Data is expressed as mean  $\pm$  SEM.

Astemizol effect was tested on hTRAAK transiently transfected Hek 293LTV cells at 10  $\mu\text{M}$  (Figure 38). This compound shows an inhibitory effect on basal TRAAK current mainly at positive potentials ( $35 \pm 8\%$ ) but also at negative ones to some extent ( $15 \pm 6\%$ ) (Figure 38 A, B). Its effect is reversible as shown on the time course of current registered at +120 mV (Figure 38 C). Dose-response curve from 100 nM to 100  $\mu\text{M}$  reveals no inhibition is produced at 1  $\mu\text{M}$ . Maximal inhibition corresponded to nearly 50% of basal TRAAK current reached at 100  $\mu\text{M}$ . No higher concentrations were explored due to solubility issues (Figure 38 D). Astemizol effect was also explored when co-applied with AA. No change in maximal peak current was observed (Figure 38 E). A shift to major

values of time, to reach maximum current, was noted during co-application of astemizol and AA, both at 10  $\mu\text{M}$ . AA effect took twice more time to reach maximum values when co-applied with astemizol (Figure 38 E, F).

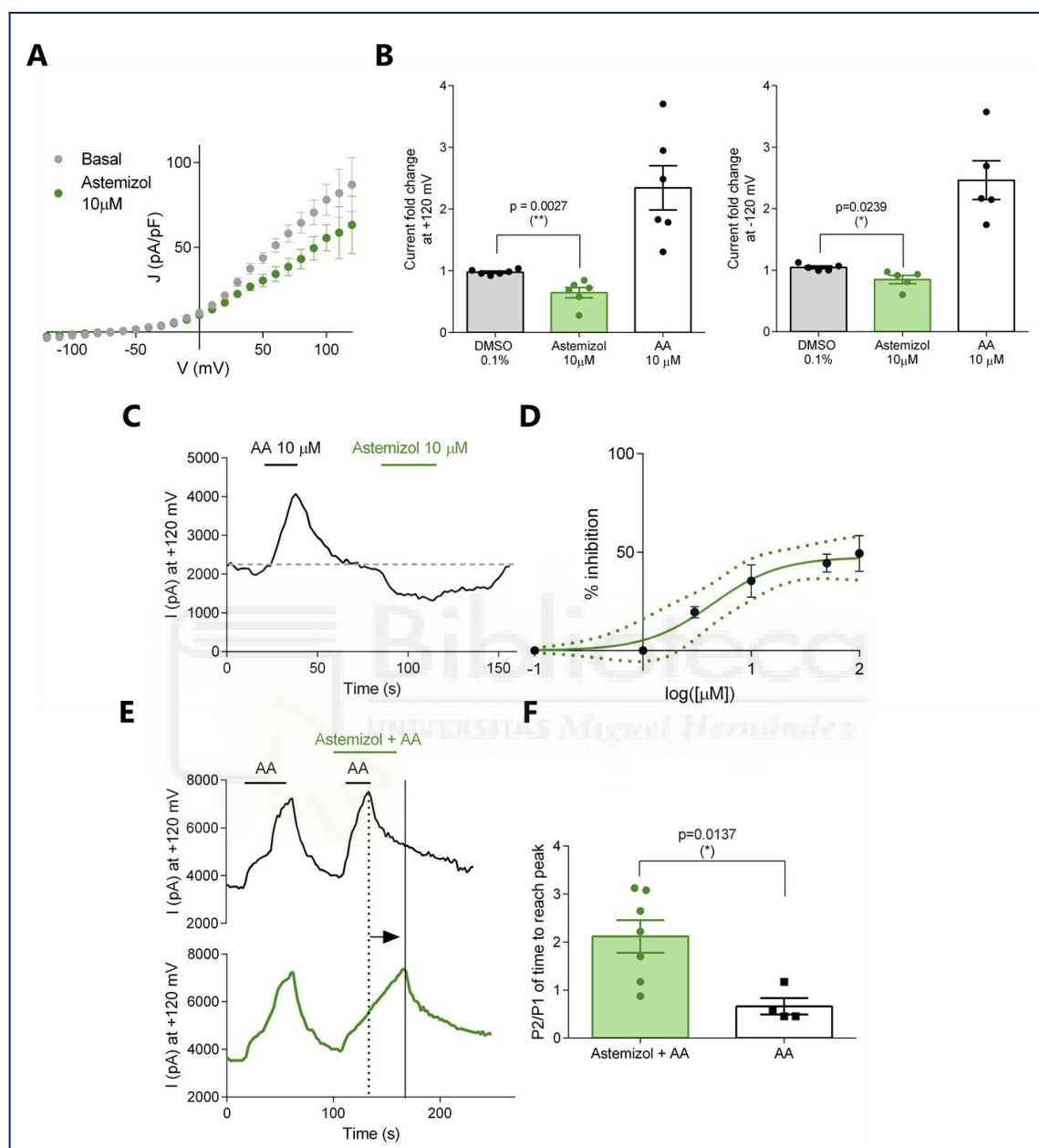


**Figure 38. Astemizol effect characterisation on TRAAK transiently transfected cells. A)** Current densities of cells expressing TRAAK in basal condition (grey) and after application of 10  $\mu\text{M}$  astemizol (green) ( $n=6$ ). **B)** Current fold change at +120 mV (left) and -120 mV (right). Data is normalized with respect to basal current. **C)** Course time of current variation at +120 mV after instillation of 10  $\mu\text{M}$  AA or 10  $\mu\text{M}$  astemizol. Grey dashed line denotes basal current. **D)** Astemizol dose-response curve from 100 nM to 100  $\mu\text{M}$  with 95% confidence interval (dotted lines) ( $n=21$ ). **E)** Course time of current variation at +120 mV after application of 10  $\mu\text{M}$  AA in two consecutive pulses (black trace) or co-application of 10  $\mu\text{M}$  AA and 10  $\mu\text{M}$  astemizol during second pulse (green trace). Time to reach maximal current peak is increased during co-application of astemizol during second AA pulse (dotted vertical line). **F)** Ratio of time to reach maximal current peak between first and second AA application or astemizol co-application during second AA pulse. All data was statistically analysed using unpaired Students' t-test. Statistical significance was set at  $p < 0.05$ . P-value for statistical significance is denoted on panel. Data is expressed as mean  $\pm$  SEM.

## RESULTS

Effect of terfenadine was tested on hTRAAK recombinantly expressed on Hek 293LTV cells at 10  $\mu\text{M}$ . Terfenadine inhibited TRAAK current only at positive potentials ( $27 \pm 7\%$ ) (Figure 39 A, B). Figure 39 C shows terfenadine effect is reversible as basal current is recovered after compound washout. Terfenadine dose-response relationship was explored from 100 nM to 100  $\mu\text{M}$ . Maximum inhibition ( $80 \pm 3\%$ ) was reached at 100  $\mu\text{M}$ .  $\text{IC}_{50}$  calculated fitting a Boltzmann sigmoidal corresponds to  $23.4 \pm 1.2 \mu\text{M}$  (Figure 39 D). Higher concentrations of terfenadine could not be explored due to solubility troubles. Co-application of terfenadine and AA at 10  $\mu\text{M}$  produced a shift to higher values of time needed to reach maximal current peak. No changes in current peak amplitude were observed (Figure 39 E, F).

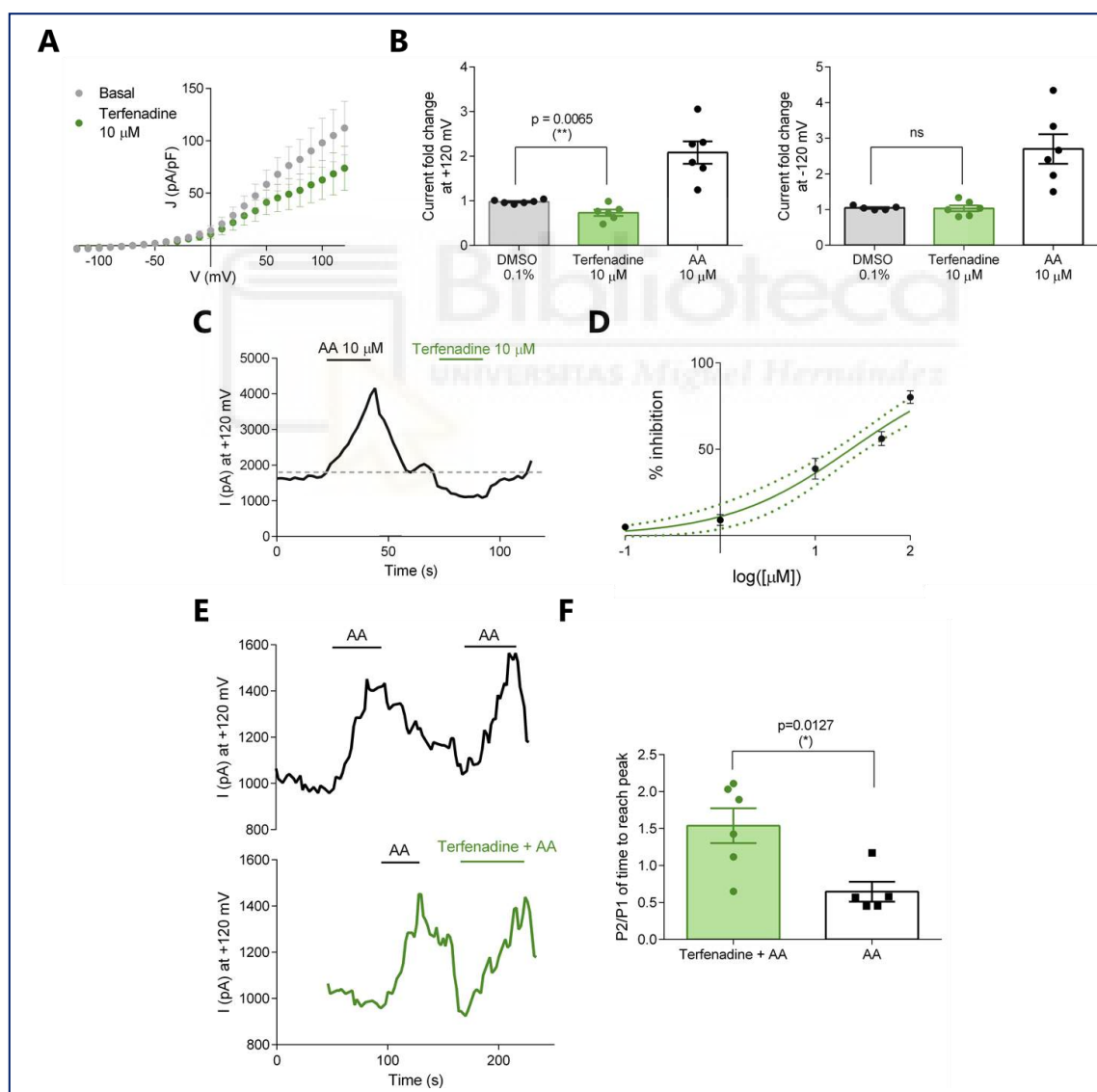


**Figure 39. Terfenadine effect characterisation on TRAAK transiently transfected cells. A)** Current densities of cells expressing TRAAK in basal condition (grey) and after application of 10  $\mu\text{M}$  terfenadine (green) ( $n=7$ ). **B)** Current fold change at +120 mV (left) and -120 mV (right). Data is normalized with respect to basal

current. **C)** Course time of current variation at +120 mV after instillation of 10  $\mu$ M AA or 10  $\mu$ M terfenadine (grey dashed lines denotes basal current). **D)** Terfenadine dose-response curve from 100 nM to 100  $\mu$ M with 95% confidence interval (dotted lines) (n=25). **E)** Course time of current variation at +120 mV after application of 10  $\mu$ M AA in two consecutive pulses (black trace) or co-application of 10  $\mu$ M AA and 10  $\mu$ M terfenadine during second pulse (green trace). Time to reach maximal current peak is increased during co-application of terfenadine during second AA pulse. **F)** Ratio of time to reach maximal current peak between first and second AA application or terfenadine co-application during second AA pulse. All data was statistically analysed using unpaired Students' t-test. Statistical significance was set at  $p < 0.05$ . P-value for statistical significance is shown on panel. Data is expressed as mean  $\pm$  SEM.

#### 5.4. Compounds effect on DRG sensory neurons

Effect of irinotecan, astemizol and terfenadine was studied on neonatal rat DRG neurons. Compounds were evaluated with a protocol of 2 min separated current ramp pulses lasting 5 s and starting from the holding potential to a resulting potential of 40 mV increment. The representative registers for each compound are depicted on [Figure 40 A](#). Perfusion of terfenadine before the second ramp pulse clearly induced AP firing at almost holding potential (in 9 out of 11 cells). A change in AP firing threshold to less depolarized values was observed for cells perfused with terfenadine. Neither a significant AP firing frequency nor AP duration change was observed for any of the substances ([Figure 40 B](#)).

Analysing action potential waveform from first ramp (P1) and the interval previous to the second ramp (Pre P2) during which terfenadine was applied ([Figure 41](#)), a clear change in AP hyperpolarization state was observed. Hyperpolarization in Pre P2 action potentials was much lower compared to P1 action potentials reinforcing the hypothesis of  $K_2P$  channels blockage.

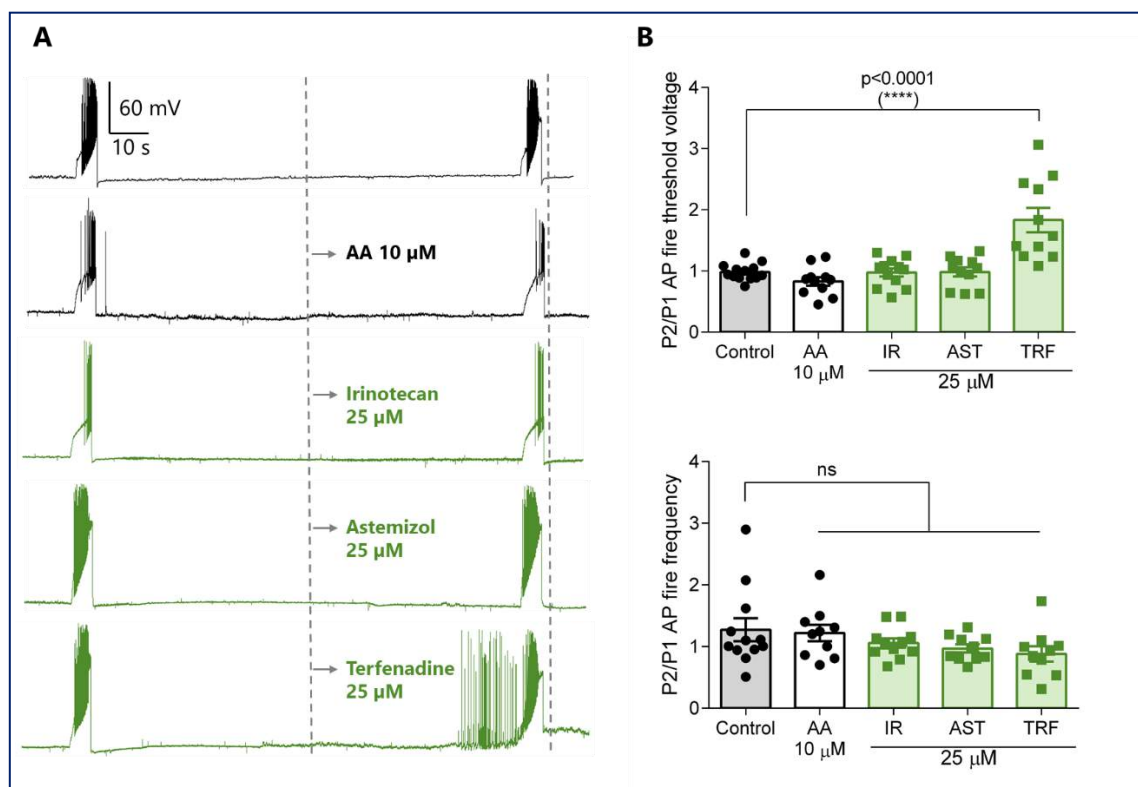


**Figure 40. Hit compounds effect on DRG neurons studied by patch-clamp.** A) Representative current-clamped registers of DRG neurons action potential firing. Cells were stimulated by two current ramp pulses from holding potential to an increase by 40 mV from it. Cells were perfused with 10  $\mu\text{M}$  AA or 25  $\mu\text{M}$  irinotecan, astemizol or terfenadine 1 min before and during second current ramp pulse. B) Ratio of AP fire threshold voltage between first and second voltage pulse (upper panel) and ratio of AP firing frequency between both pulses (lower panel) ( $n=11$  – AA, astemizol and terfenadine; 12 – irinotecan; 13 – control). Data was statistically analysed using One-Way ANOVA with Bonferroni post hoc test ( $F(4, 53) = 14.99, p < 0.0001$ ). Statistical significance was set at  $p < 0.05$ . P-values for statistical difference are denoted on panels. All data is shown as mean  $\pm$  SEM.

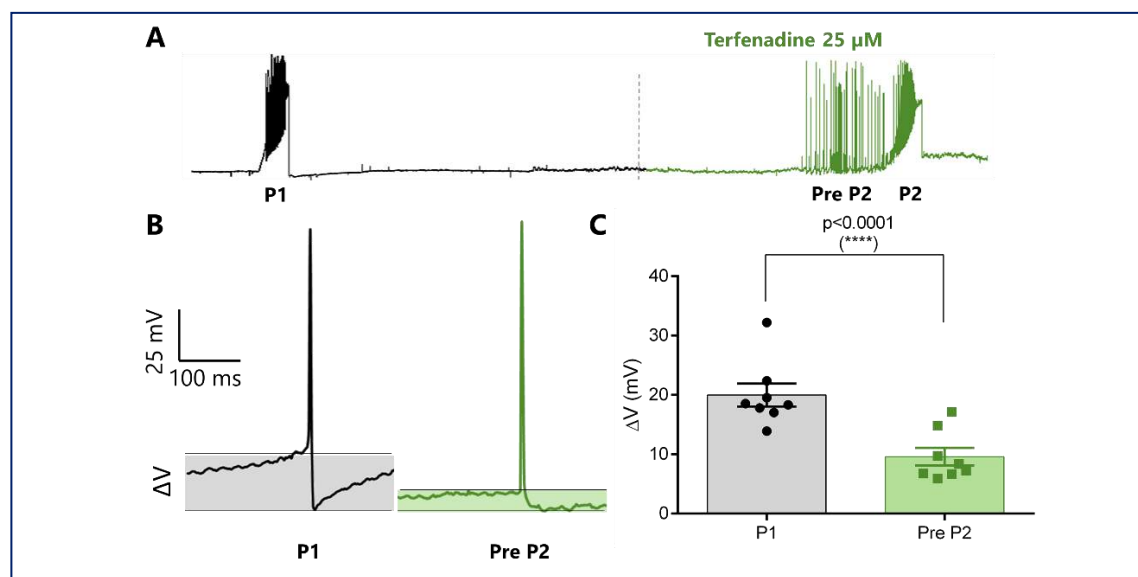


**Figure 41. Change in AP hyperpolarization state after neuron treatment with 25  $\mu\text{M}$  terfenadine.** A) Representative current-clamped register of DRG neurons action potential firing where cell was stimulated by two current ramp pulses from holding potential to an increase by 40 mV from it. Cell was perfused with 25

---

$\mu$ M terfenadine 1 min before and during second voltage ramp pulse. **B)** Representative action potentials from pulse 1 (P1) and previous to pulse 2 (Pre P2). Highlighted region focuses on the difference in voltage ( $\Delta V$ ) between resting potential voltage and hyperpolarization state voltage. **C)** Column graph showing  $\Delta V$  (mV) for P1 and Pre P2. Data was statistically analysed using paired Students' t-test. Statistical significance was set at  $p < 0.05$ . P-value for statistical difference is denoted on panel. Data is shown as mean  $\pm$  SEM.

To study the effect of the selected compounds on more complex system, multielectrode array (MEA) cultured with neonatal rat DRG neurons was used. Two 40 mM KCl pulses of 30 s (P1 and P2) separated by 10.5 min were used to evoke the firing of neuronal action potentials. 1.5 min before the second KCl pulse, cells were perfused with 10  $\mu$ M AA, terfenadine, astemizol or irinotecan at 25  $\mu$ M (Figure 42 A). Mean spike frequency ratio between P2 and P1 calculated for each condition showed that the application of 10  $\mu$ M arachidonic acid inhibits action potential firing. The application of 25  $\mu$ M astemizol or terfenadine exerted no clear effect on action potential firing, while perfusion with 25  $\mu$ M irinotecan stimulated firing during P2 (Figure 42 B). The number of spikes evoked during the application of each compound was higher in the case of irinotecan (Figure 42 C).

To further characterize irinotecan, its effect was tested on a neuropathic pain *in vitro* model of adult rat DRG neurons treated with 10  $\mu$ M taxol during 24 hours. In IB4+ and IB4- untreated neurons, irinotecan did not induce any change in cell resting membrane potential contrary to AA which hyperpolarized cells (Figure 43 A and B - left panels). However, in IB4- neurons treated with taxol, irinotecan hyperpolarized resting membrane potential of neurons contrary to AA application (Figure 43 A - right panel). AA perfusion halted completely AP firing stimulated by current injection in 10 pA steps up to 300 pA (data not shown). In IB4- neurons, taxol treatment produces a decrease in AP hyperpolarization state (Figure 43, C - basal), effect not observed in IB4+ neurons. In IB4- neurons, irinotecan was able to reverse taxol effect on the AP hyperpolarization state (Figure 43, C - right panel).

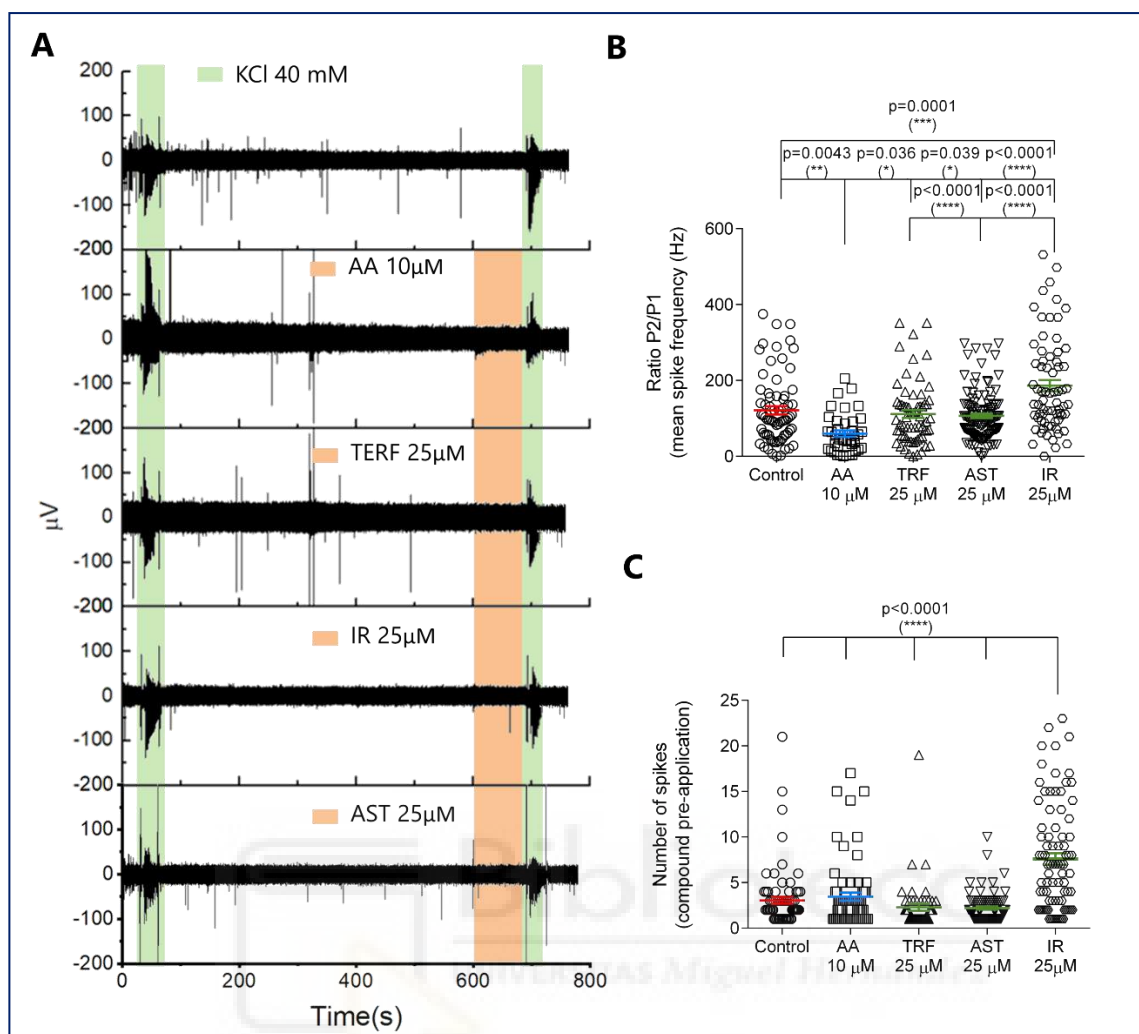


**Figure 42. Hit compounds effect on DRG neurons studied by MEA. A)** Representative MEA recordings showing KCl-evoked action potential firing. Green and orange highlighted regions stand for time laps of 40 mM KCl (20 s) and compound (90 s) application, respectively. Compound perfusion continued during second KCl pulse. **B)** Normalized KCl-induced firing (P2/P1) for control (O), in presence of agonists arachidonic acid at 10 μM (□) and irinotecan at 25 μM (○) and in presence of antagonists terfenadine (Δ) and astemizol (∇), both at 25 μM. **C)** Number of action potentials fired during compounds application before second KCl pulse. Outliers were removed (ROUT (Q=1%). Data was analysed using One-Way ANOVA with Bonferroni's post hoc test ( $F(4, 350) = 15.74, p < 0.0001$ ). P-values for statistical difference are denoted on panels. All data is expressed as mean ± SEM.

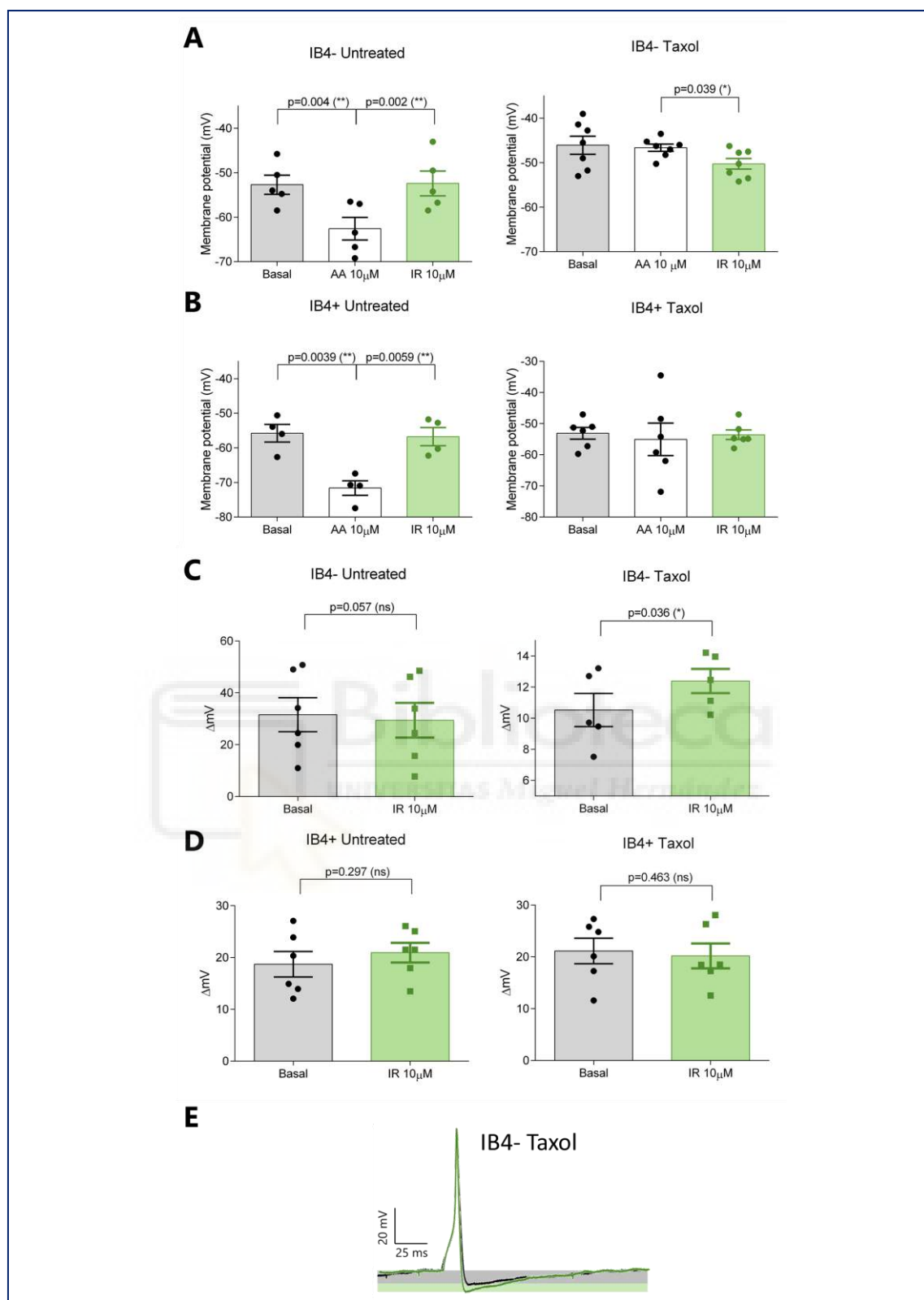


**Figure 43. Irinotecan increases action potential hyperpolarization state in taxol treated IB4- DRG neurons and hyperpolarizes cell resting membrane potential.** Cell membrane potential of IB4- (untreated A-left panel; taxol treated A-right panel) and IB4+ (untreated B-left panel; taxol treated B-right panel) neurons, after application of 10  $\mu$ M AA (white bars) or irinotecan (green bars) during 1 minute. Data was statistically analysed using paired One-Way ANOVA with Bonferroni post-hoc test ( $F(1.529, 6.118) = 52.83, p = 0.002$  - IB4- untreated;  $F(1.514, 9.085) = 3.980, p = 0.065$  - IB4- taxol;  $F(1.249, 3.746) = 29.73, p = 0.006$  - IB4+ untreated;  $F(1.154, 5.772) = 0.2022, p = 0.7036$  - IB4+ taxol). Difference between resting membrane

potential and peak potential reached during action potential hyperpolarization state for IB4<sup>-</sup> (untreated C – left panel; taxol treated – C right panel) and IB4<sup>+</sup> (untreated D – left panel; taxol treated – D right panel) neurons perfused with 10  $\mu$ M irinotecan. Data was analysed using paired Students' t-test. P-value for statistical difference is depicted on each panel. All data is shown as mean  $\pm$  SEM. E) Representative change in hyperpolarization state of an action potential of IB4<sup>-</sup> neuron treated with taxol and perfused with 10  $\mu$ M irinotecan, compared to basal value.

## 6. STRUCTURE ACTIVITY RELATIONSHIPS (SAR)

Structure activity relationship (SAR) was used for hit optimization. The three-dimensional space determined as a putative astemizol and terfenadine binding pocket was further explored in order to determine its key residues and chemical properties. This pocket is a combination of the decane's one (on the intracellular opening of the pore) and norfluoxetine's one (on a lateral fenestration in the transmembrane domain, near to the intracellular compartment). This information was used to introduce favourable structural modifications in both ligands and improve their affinity and specificity against TRAAK.

### 6.1. Astemizol

Astemizol modification started with the fluorine group removal (Figure 44, 1), an enlargement of the link between the piperidine and benzimidazole rings (Figure 44, 2) and the modification of the anisole ring to larger groups (Figure 44, 3-10) in order to improve hydrophobic interactions in the cavity under the intracellular opening of the pore (Figure 51 A, B). According to the binding energy and visual inspection the best substituents are #6 and #7 with energy of -11.86 and -12.32 kcal/mol, respectively. They correspond to larger R-groups that fill the cavity under the pore. Different modifications were done using as base molecules both substituents, #6 (Figure 45) and #7 (Figure 46). The one with lowest interaction energy, -15.10 kcal/mol, was #76 which incorporates three alkyl groups linked to the naphthalene which further improve hydrophobicity. The absence of the ether group from the anisole ring enhances ligand affinity (Figure 47). The presence of an alkyl, amino or alcohol group at naphthalene position alpha did not introduce a difference in binding energy (Figure 47, 761 – 763). The fluorine group removal lowered additionally the interaction energy (Figure 44, 1 and Figure 48, 7633).

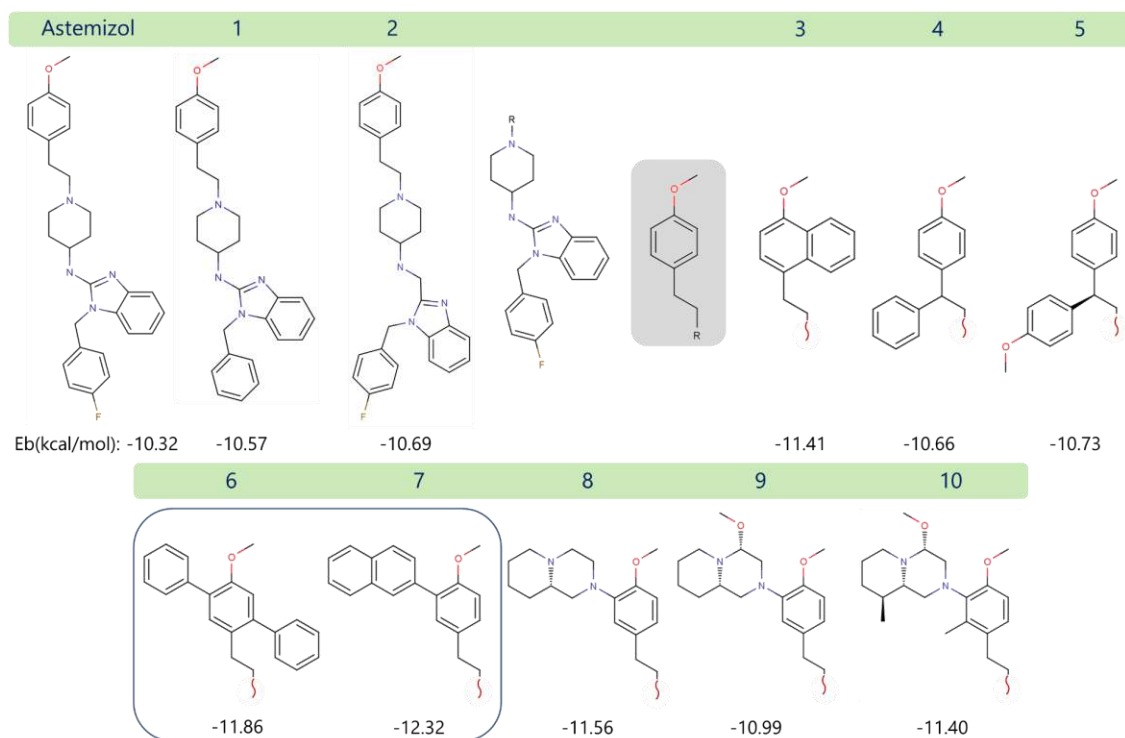


**Figure 44. Astemizol SAR improvement, round 1.** The starting point molecule is highlighted in grey and the base molecule is the one on the left of starting point molecule and receives no numeration. Distinct substituents carry an R#. Interaction energy in kcal/mol is shown under each molecule. The best substituents in terms of energy are marked by a blue rectangle and are normally used as base molecules in further rounds. R-group #7 is the best one with a binding energy of -12.32 kcal/mol followed by #6 with -11.86 kcal/mol. The main base molecule in this round represents the benzimidazole and piperidine rings from astemizol.

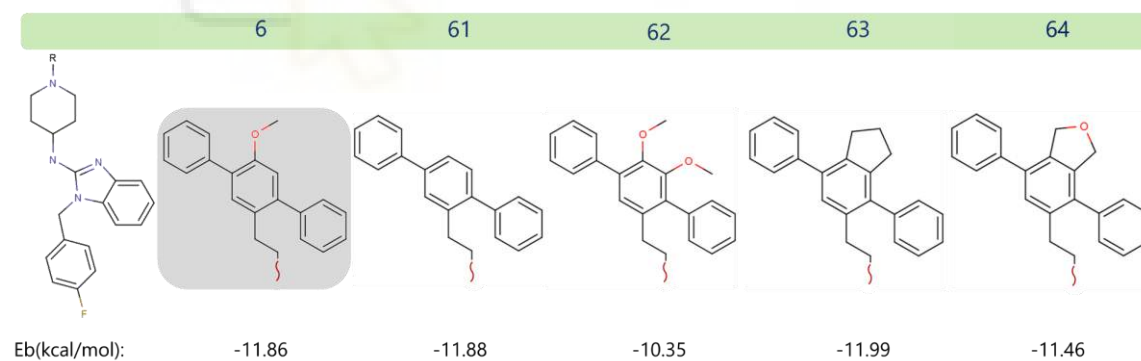


**Figure 45. Astemizol SAR improvement, round 2.** The starting point molecule, #6 from round 1 is highlighted in grey. Interaction energy in kcal/mol is shown under each molecule.

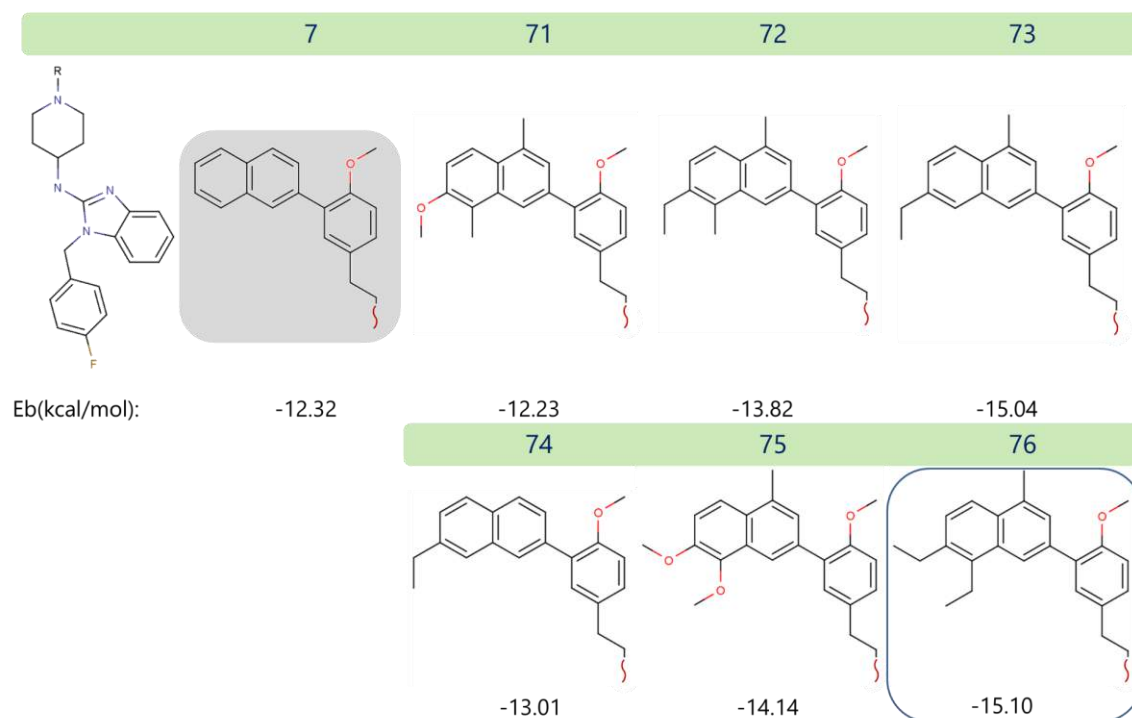


**Figure 46. Astemizol SAR improvement, round 2.** The starting point molecule, #7 from round 1 is highlighted in grey. Interaction energy in kcal/mol is shown under each molecule. The best substituents in terms of energy are marked by a blue rectangle and are normally used as base molecules in further rounds, in this case R-group #76 with binding energy of -15.10 kcal/mol.

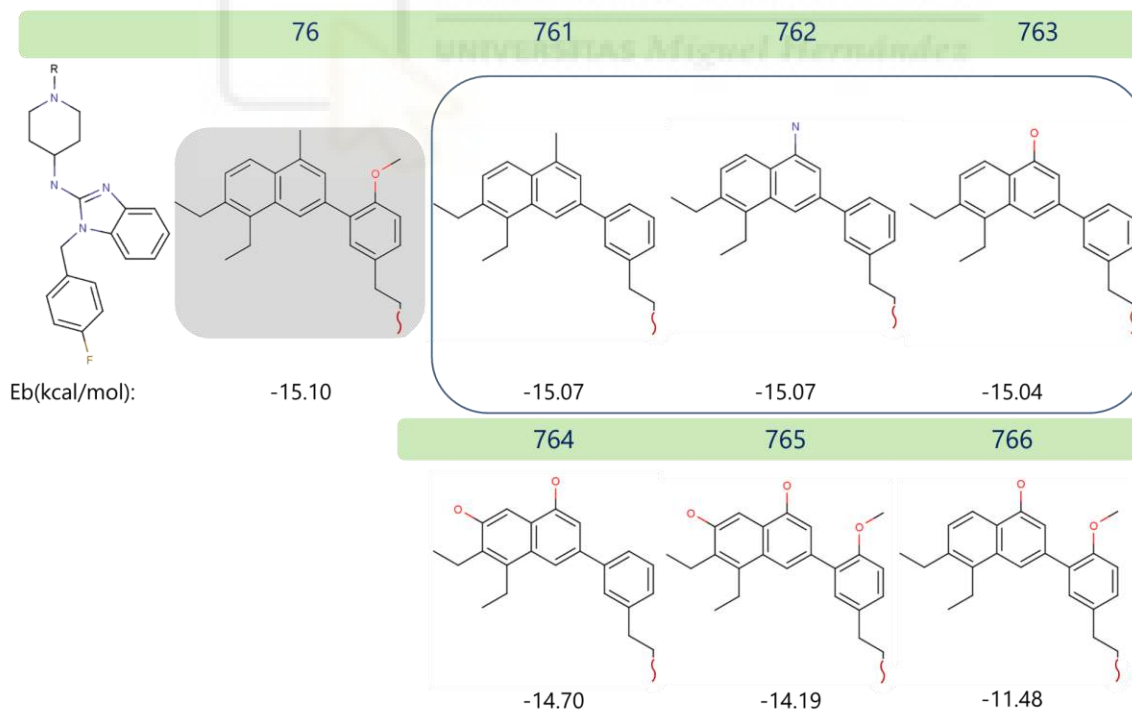


**Figure 47. Astemizol SAR improvement, round 3.** The starting point molecule, #76 from round 2 is highlighted in grey. Interaction energy in kcal/mol is shown under each molecule. The best substituents in terms of energy are marked by a blue rectangle and are normally used as base molecules in further rounds. R-groups #761, #762 and #763 are the best, although they do not represent an improvement compared to the previous round best R-group, #76.

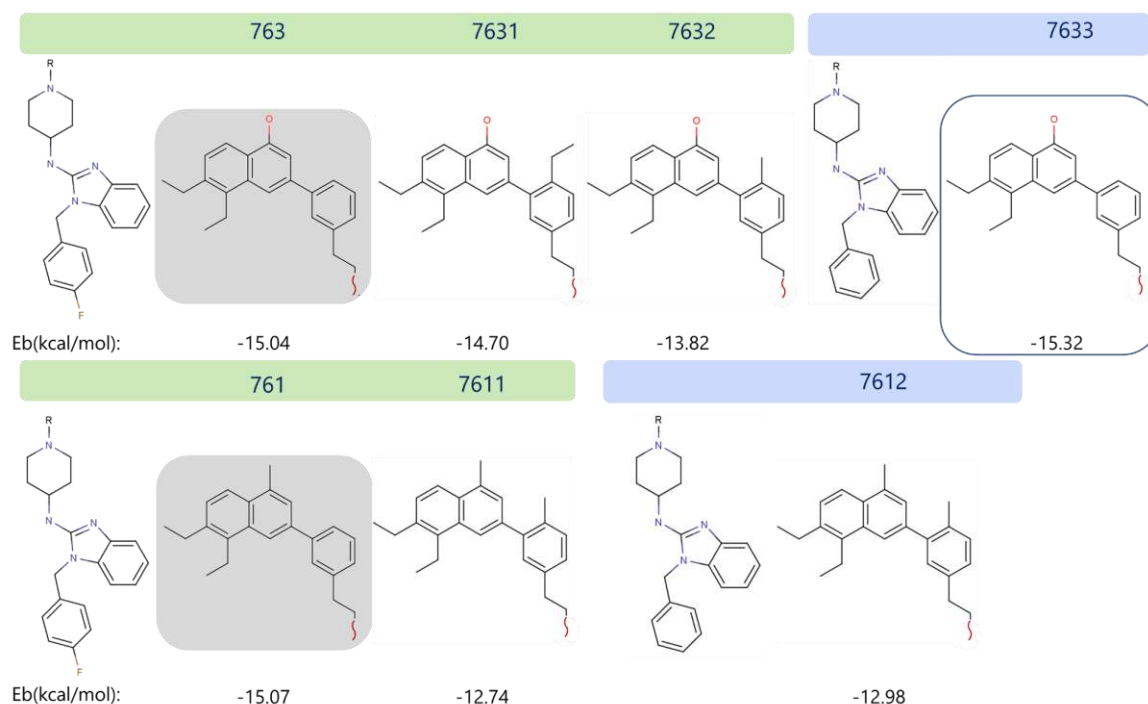


**Figure 48. Astemizol SAR improvement, round 4.** The starting point molecules, #761 and #763 from round 3 are highlighted in grey. Interaction energy in kcal/mol is shown under each molecule. Different groups are depicted in distinct colours. The best substituents in terms of energy are marked by a blue rectangle and are normally used as base molecules in further rounds. The absence of fluorine group attached to the benzene ring of the base molecule, together with substituent # 7633 or #763, improve the interaction energy.

Modifications in the benzimidazole ring were performed in order to enhance reactivity with the cysteine 206 residue (Figure 49). The hypothesis working towards was to modify covalently C206. Although this mechanism has not been described for none of the TREK channels subfamily it has been widely explored during TRPA1 activation [248]. The best candidates were #76331 and #76332 with a ketone group linked to the benzimidazole ring. Finally, in order to improve hydrogen bonds formation with threonine residues located on the intracellular end of P1 and P2, another alcohol group was added to R-group #7633 (Figure 50). The interaction energy of the resulting ligand was -16.07 kcal/mol. From a molecular point of view, given that the binding site is located on the lateral fenestration of TRAAK, in between the lipid bilayer (Figure 51 A), the lipophilicity of the molecule would ease the interaction through that channel region. Hydrophobic interactions with key residues L151a, F272a, L276a, I154b, P155b, F157b and L269b (a and b in the residues numbering stands for chain A and B, respectively) are stimulated with ligand #763321, contrary to astemizol (Figure 51 B, C). Hydrogen bonds formation between naphthalene alcohol groups and residues T129a and T238b are found in few docking poses where distances between reacting groups vary from 2.7 to 3.8 Å. Distance between C206a and the ketone group from the benzimidazole group also vary but in the

## RESULTS

most populated cluster is 3.3 Å. Nevertheless, ligand #763321 violates twice the Rule of 5 of Lipinski [249]. Its molecular weight is 640.34 g/mol with 3 hydrogen bond donors (HBD) and 7 acceptors (HBA), logP of 7.82 and logD of 5.19. It has a molecular weight higher than 500 g/mol and a logP higher than 5.6. This means that the compound would be extremely hydrophobic, its bioaccumulation probably would be high, as well as its toxicity. If topically applied, the molecule could cross the skin and accumulate there given its low solubility, balking its transport and excretion.

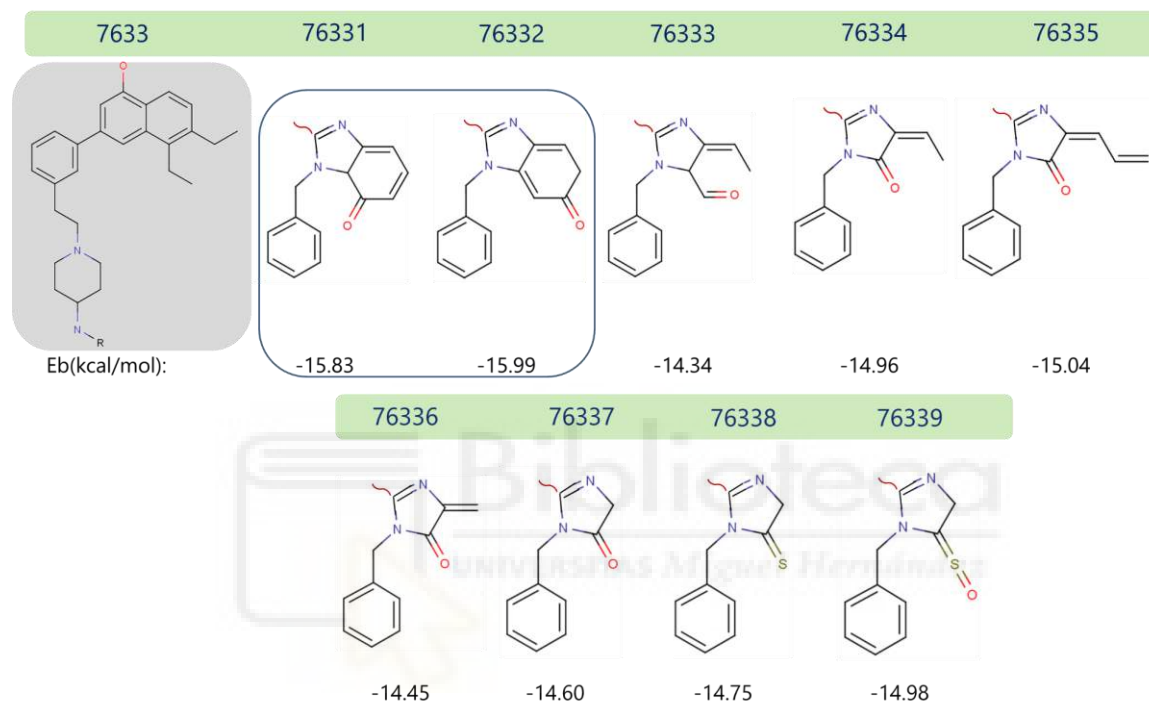


**Figure 49. Astemizol SAR improvement, round 5.** The base molecule, #7633 from round 4 is highlighted in grey. Interaction energy in kcal/mol is shown under each molecule. The best substituents in terms of energy are marked by a blue rectangle and are normally used as base molecules in further rounds. The base molecule in this round represents the piperidine and benzene rings from astemizol linked to substituent #7633. Best substituents from this round are #76331 and #76332 with binding energy of -15.83 and -15.99 kcal/mol, respectively.

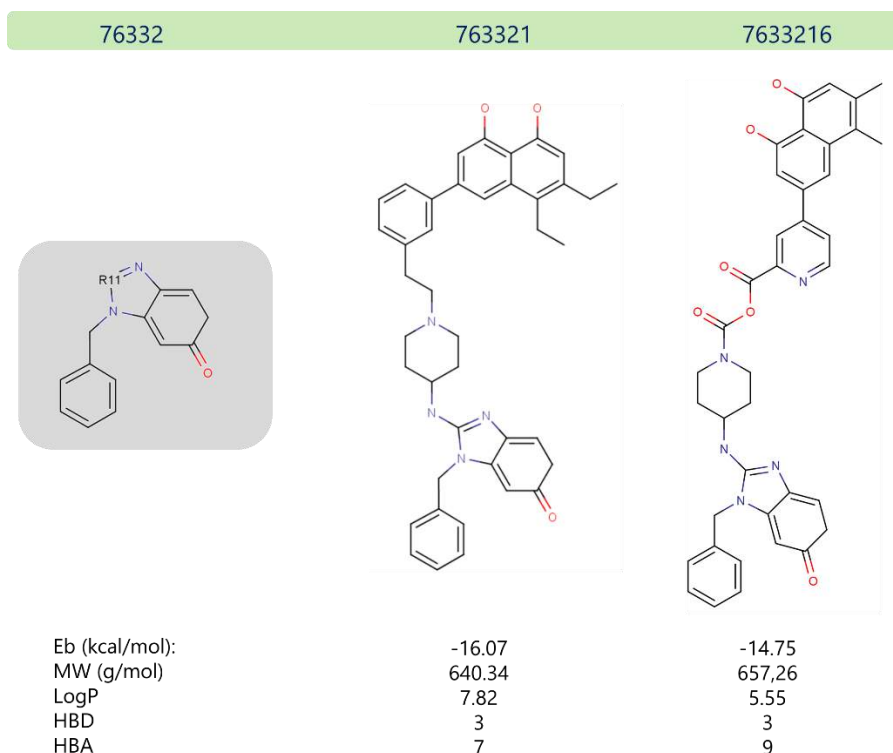


**Figure 50. Astemizol SAR improvement, round 6 and 7.** The base molecule, #76332 from round 5 is highlighted in grey. Interaction energy in kcal/mol, molecular weight in g/mol, logP, hydrogen bond donors (HBD) and hydrogen bond acceptors (HBA) are shown under each molecule. Molecule #7633216 was developed from molecule #763321 as base.

Given that substance hydrophobicity range is key in drug discovery and the violation of this Lipinski parameter is quite pronounced for molecule #763321, light changes of its molecular structure were performed. The introduction of amine groups in the link between the piperidine and the former anisole ring transformed into a pyridine, were contemplated. Also, the transformation of the naphthalene ethyl groups to methyl ones. Finally, the introduction of an ester group between the pyridine and piperidine rings reduces logP parameter and transforms the molecule into esterase hydrolysable which could reduce its accumulation and toxicity in topical applications (Figure 50). From all these changes, the best one in terms of binding energy and reduction in logP proved to be the hydrolyzable ester group. Although its molecular weight resulted in a slight increase compared to ligand #763321, 657.26 g/mol, its logP was reduced to 5.55. It presented 3 HBD and 9 HBA. Its interaction energy was weakened to -14.75 kcal/mol compared to the -16.07 kcal/mol of ligand #763321. This should not be a problem as there is still a considerable improve of binding energy compared to astemizol (-10.32 kcal/mol). Also, the expected equilibrium constant of molecule #763321 should be 1.7 pM while the one of ligand #7633216, 15 pM, compared to the theoretical 27 nM of

## RESULTS

astemizol. These values were obtained applying the equation (8) that correlates the free Gibbs energy ( $G$ ) and the equilibrium constant ( $K_{eq}$ ) of a reaction ( $R = 1.987 \frac{\text{cal}}{\text{mol.K}}$ ).

$$(8) \quad \Delta G = -RT \ln K_{eq}$$

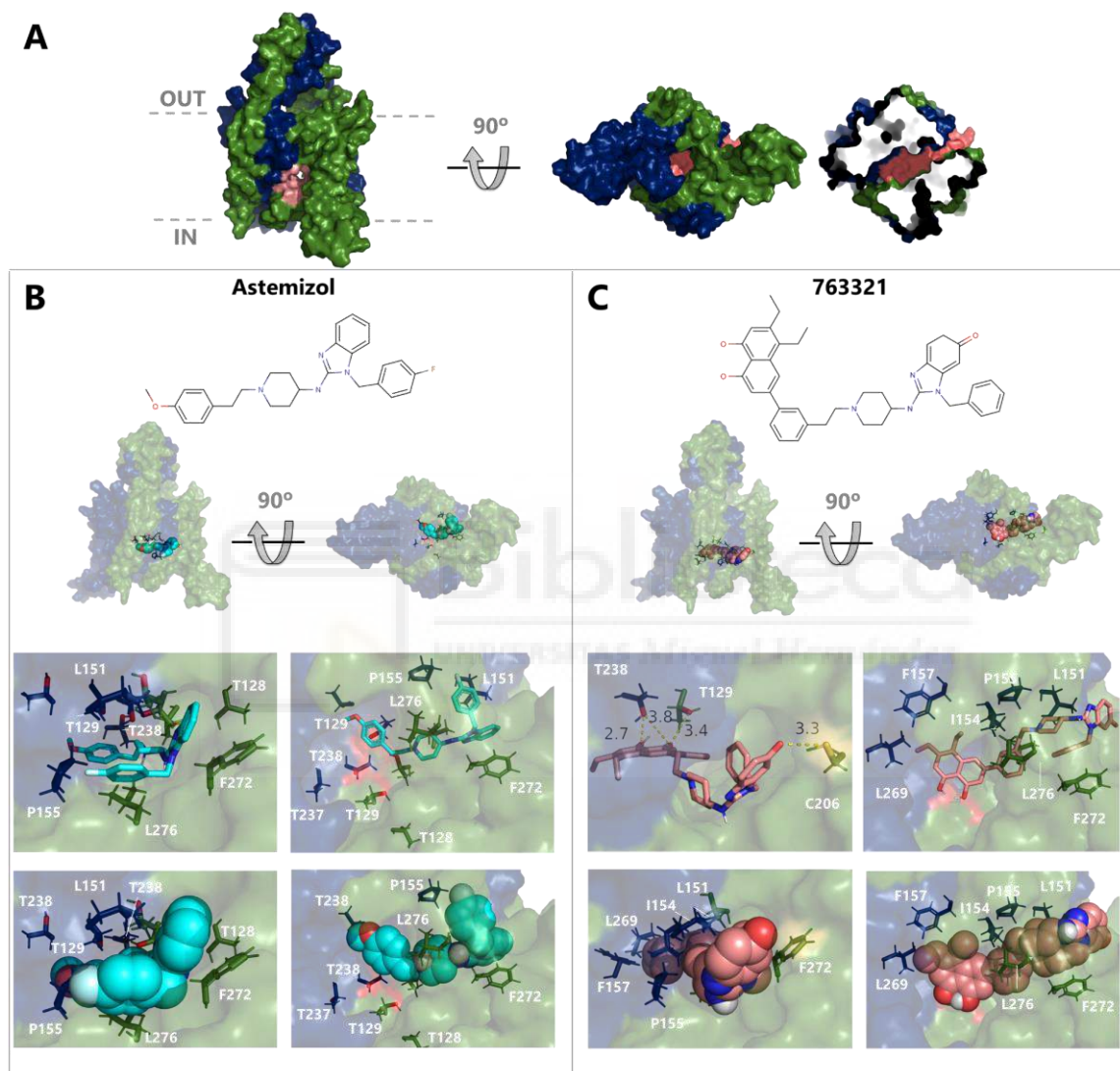


**Figure 51. Astemizol SAR improvement, comparison.** **A)** Astemizol binding site is represented as salmon surface on TRAAK crystal structure. TRAAK chain A is shown in green while chain B in blue. **B)** Astemizol inserts under TRAAK intracellular pore opening through a lateral fenestration. Transmembrane view of astemizol putative active site is shown on the left column and an intracellular view on the right one. Astemizol is shown as sticks or as spheres for a better spatial occupancy understanding. The benzimidazole and fluorobenzene rings occupy the opening of the lateral TRAAK fenestration. Hydrophobic interactions with residues F272a (a stands for chain A), L276a, L151b (b stands for chain B) and P155b are key and shape the pocket opening. The piperidine and anisole rings orient to the inside of the intracellular pore opening pocket. **C)** Transmembrane view of 763321 in the putative astemizol binding site is shown on the left column and an intracellular view on the right one. 763321 was designed to occupy the same binding site as astemizol but increasing its affinity and specificity for this given region. Astemizol anisole ring was substituted by a larger group (naphthalene) optimizing the hydrophobic interactions in the huge pocket under the intracellular pore opening with residues I154b, F157b and L269b. The alcohol groups linked to the naphthalene form hydrogen

bonds with T129a and T238b anchoring the ligand to the pore entrance and clogging it. The proximity of the cetone group on the benzimidazole ring to C206a could modify covalently the cysteine residue.

## 6.2. Terfenadine

The putative binding site of terfenadine is the same as astemizol. Both benzene groups linked to the piperidine ring of terfenadine position on the lateral membrane opening of TRAAK. The resting benzene group linked to the piperidine ring through an acyl chain occupies the intracellular cavity under the pore. This last corresponds to the main part of the molecule subjected to study. Hydrophobic interactions in general and hydrogen bonding with threonine residues located in the intracellular opening of the pore were intended to be improved. Best substituents from the first round were #5 and #7 with interaction energy of -11.32 and -11.15 kcal/mol, respectively (Figure 52). Round 2 substituents based on molecule #5 or #7 are depicted on Figure 53 and 54, respectively. R-groups #51 and #501 showed a binding energy of -12.37 and -12.39 kcal/mol respectively. Alcohol group from R-group #501 formed a hydrogen bond with residue T237. Molecule #75 was the best substituent based on #7 with energy of -11.51 kcal/mol (Figure 54). It was further improved in a third round, being molecule #753 with interaction energy of -13.75 kcal/mol the best one (Figure 55). Given the extreme hydrophobicity of molecule #753 which presented a logP value of 9.57, two amine groups were introduced in the acyl chain linking the piperidine with the naphtalene ring. A great decrease in interaction energy was observed in all the resulting candidates (Figure 56) while logP value was improved slightly. LogP value of molecule #7531 with the best energy from this round is 6.82, a value which still violates Lipinski Rule of 5.

In summary, best candidates from terfenadine based improvement correspond to molecule #501 with molecular weight of 535.37 g/mol, logP of 5.61, 3 HBD and 5 HBA and molecule #51 with molecular weight of 519.37 g/mol, logP of 6.09, 2 HBD and 4 HAB. Although the improvement in binding energy is not as high as in the case of astemizol there is still an improve in two orders of magnitude (theoretical equilibrium constant of terfenadine and molecule #501 are 34.5 nM and 0.8 nM, respectively).

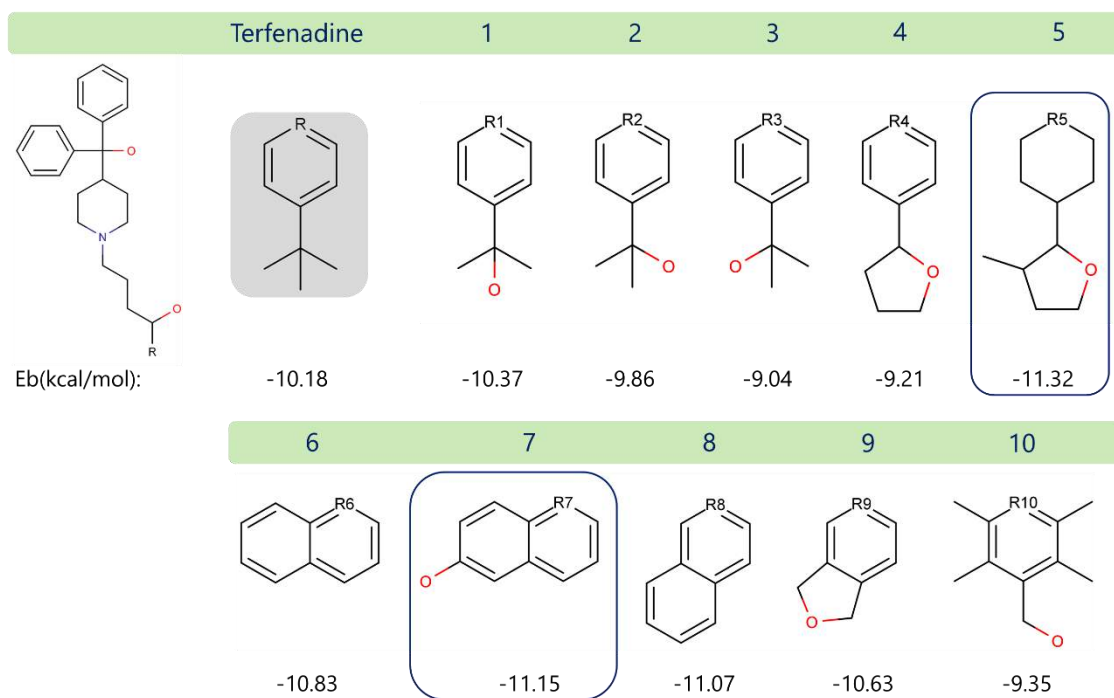


**Figure 52. Terfenadine SAR improvement, round 1.** The starting point molecule is highlighted in grey and base molecule appears on the left from it without numeration. Distinct substituents carry an R#. Interaction energy in kcal/mol is shown under each molecule. The best substituents in terms of energy are marked by a blue rectangle and are normally used as base molecules in further rounds. R-group #5 and #7 are the best one with a binding energy of  $-11.32$  and  $-11.15$  kcal/mol, respectively.

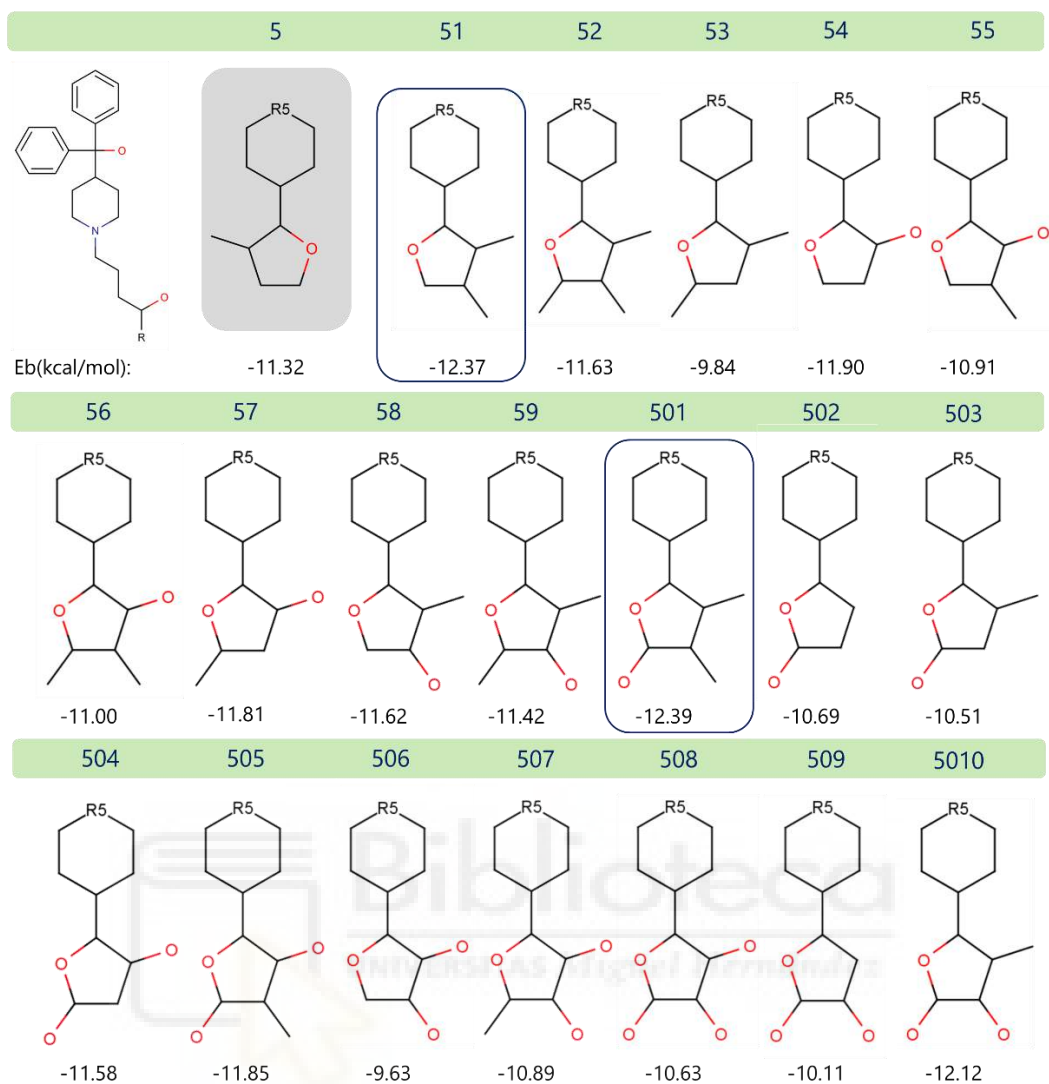


**Figure 53. Terfenadine SAR improvement, round 2.** The starting point molecule, #5 from round 1 is highlighted in grey. Interaction energy in kcal/mol is shown under each molecule. The best substituents in terms of energy are marked by a blue rectangle and are normally used as base molecules in further rounds, in this case R-group #501 and #51 with binding energy of -12.39 and -12.37 kcal/mol, respectively.

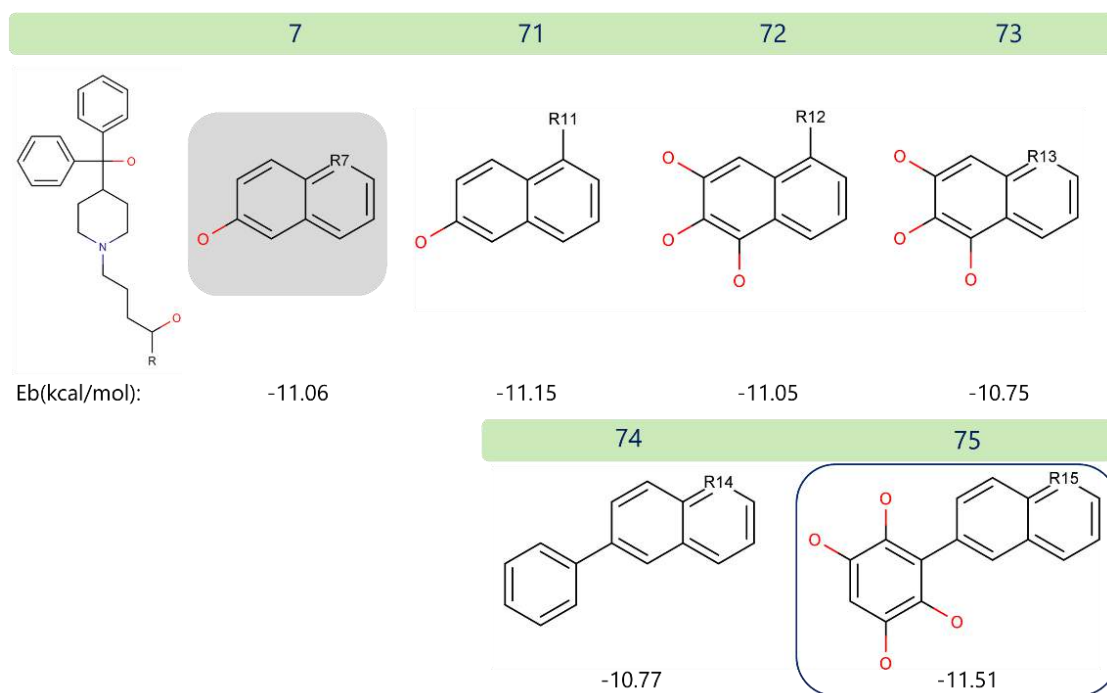


**Figure 54. Terfenadine SAR improvement, round 2.** The starting point molecule, #7 from round 1 is highlighted in grey. Interaction energy in kcal/mol is shown under each molecule. The best substituents in terms of energy are marked by a blue rectangle and are normally used as base molecules in further rounds, in this case R-group #75 with binding energy of -11.51 kcal/mol.

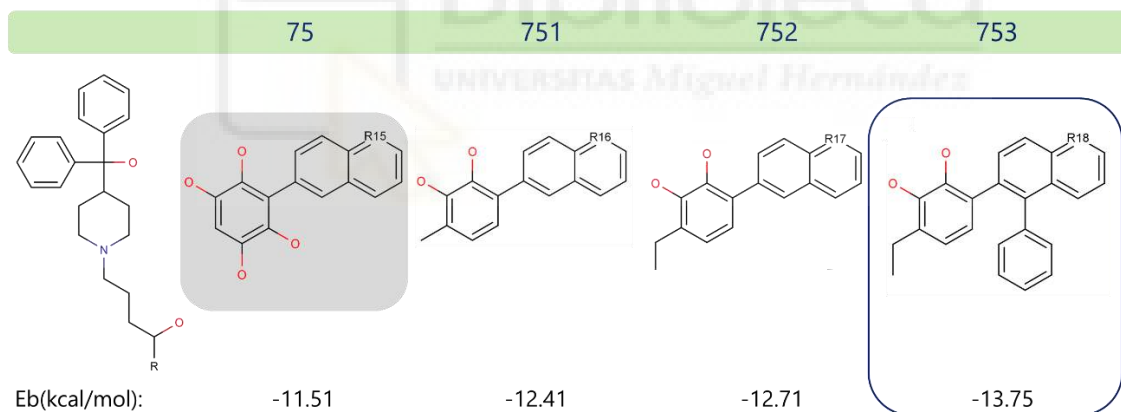


**Figure 55. Terfenadine SAR improvement, round 3.** The starting point molecule, #75 from round 2 is highlighted in grey. Interaction energy in kcal/mol is shown under each molecule. The best substituents in terms of energy are marked by a blue rectangle and are normally used as base molecules in further rounds, in this case R-group #753 with binding energy of -13.75 kcal/mol.

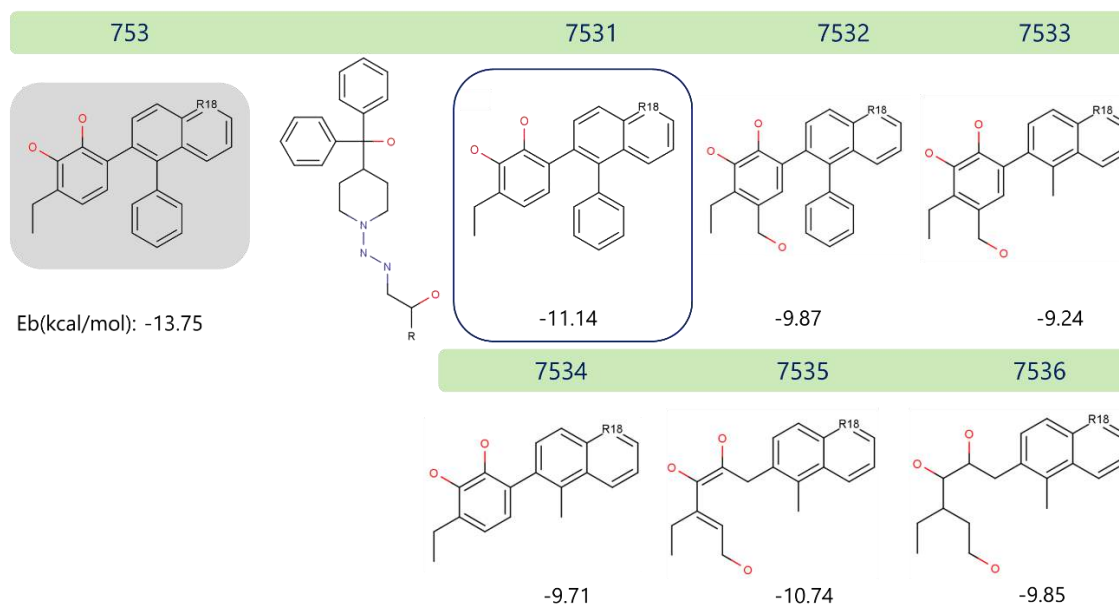


**Figure 56. Terfenadine SAR improvement, round 4.** The base molecule, #753 from round 3 is highlighted in grey. Interaction energy in kcal/mol is shown under each molecule. In order to decrease logP value of molecule #753 two amine groups were introduced in the acyl chain linking piperidine and benzene rings. All resulting molecules present lower interaction energies compared to previous rounds.



## 7. EXPLORING AG1529 EFFECT ON TRP CHANNELS

### 7.1. AG1529 inhibitory activity on recombinant hTRPV1 channel

AG1529 effect was tested on recombinantly expressed hTRPV1 on Hek 293 cells. As Figure 57 B shows, the administration of 1  $\mu\text{M}$  AG1529 blocked almost 60% of capsaicin-elicited inward TRPV1 currents. The  $\text{IC}_{50}$  value revealed from the dose-response curve is  $0.9 \pm 0.5$   $\mu\text{M}$  with a Hill coefficient of  $0.8 \pm 0.4$ . AG1529 water insolubility allowed us to test the compound at 30  $\mu\text{M}$  as the highest concentration, reaching 78% of blockage efficacy. At higher concentrations the final corresponding percentage of DMSO in the working solutions was  $>1\%$  which affected cell viability and activity measurements.

Then, capsaicin potency to activate TRPV1 channel in absence and presence of 1  $\mu\text{M}$  AG1529 was assessed. This AG1529 concentration corresponds to its  $\text{IC}_{50}$  value. As it can be noted on Figure 57 D, capsaicin dose-response shifted to the right in the presence of 1  $\mu\text{M}$  AG1529, to higher agonist concentrations needed to reach a given percentage of TRPV1 activation.  $\text{EC}_{50}$  value of capsaicin suffered a 3-fold increase shifting from  $0.3 \pm 0.1$   $\mu\text{M}$  to  $0.9 \pm 0.1$   $\mu\text{M}$  (unpaired Student's t-test,  $p < 0.0001$ ), while its Hill coefficient suffered a decrease from  $1.3 \pm 0.2$  to  $1.0 \pm 0.1$  (unpaired Student's t-test,  $p < 0.0001$ ). This change in capsaicin  $\text{EC}_{50}$  when activating TRPV1 in the presence of AG1529 relates with a competitive inhibitory mechanism of action.

Reversibility of AG1529 activity was also checked. The protocol to assay this consisted in two capsaicin pulses separated by a washing period. AG1529 was perfused before and during the first capsaicin pulse. As it can be seen on Figure 57 E, two repetitive capsaicin pulses evoked TRPV1 desensitization ( $\text{P2/P1} = 0.81 \pm 0.01$ ) while when AG1529 was applied, second capsaicin response suffered an increment ( $\text{P2/P1} = 1.30 \pm 0.09$ , unpaired Student's t-test,  $p = 0.0027$ ). This evidences that AG1529 blocks capsaicin-evoked TRPV1 current in a reversible manner and that it also partially inhibits capsaicin-induced TRPV1 tachyphylaxis.

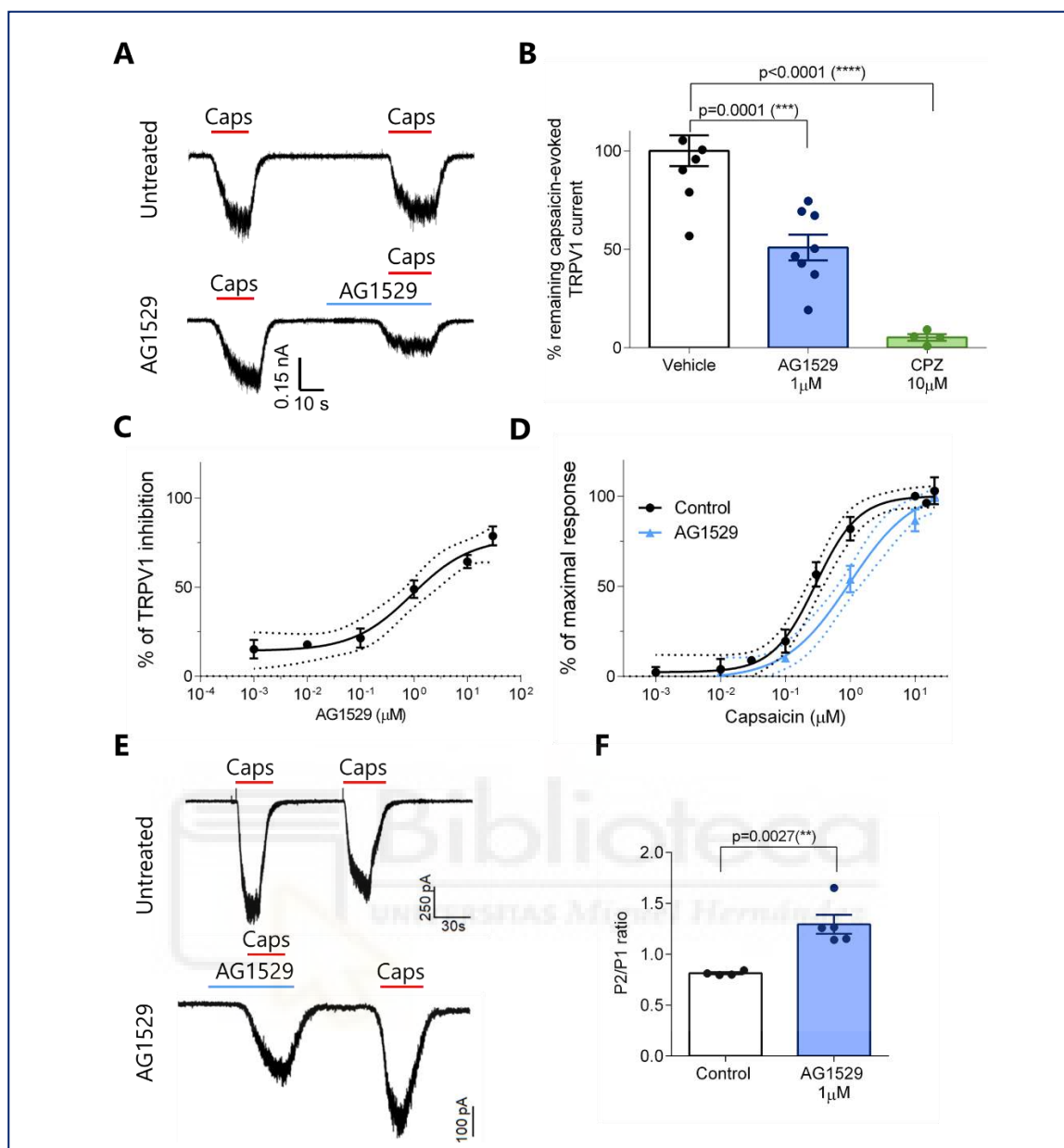


**Figure 57. AG1529 blocks capsaicin-evoked hTRPV1 currents in a reversible manner.** **A)** Representative capsaicin-elicited hTRPV1 current recorded at a holding potential of  $-60$  mV. Untreated or control cells were exposed to two  $500$  nM capsaicin pulses separated by a washing period. AG1529 cells were perfused by  $1$   $\mu$ M AG1529  $30$  s before and during the second capsaicin pulse. Control condition was taken into account to calculate the extend of capsaicin-induced TRPV1 desensitization. **B)** Percentage of remaining capsaicin-elicited TRPV1 current after the application of  $1$   $\mu$ M AG1529 or  $10$   $\mu$ M capsazepine. Data was analysed using One-Way ANOVA ( $F(2,18) = 34.88$ ,  $p < 0.0001$ ) followed by Bonferroni's post hoc test. P-values for statistical difference are indicated. Comparison was made only between vehicle and both antagonists. **C)** Dose-response curve of AG1529.  $IC_{50}$  value was obtained fitting data to a Michaelis-Menten Isotherm.  $IC_{50}$  resulted in  $0.92$  (95% CI,  $0.28$ - $3.01$ )  $\mu$ M and Hill coefficient of  $n_H$   $1.31$  (95% CI,  $0.81$ - $1.82$ ) ( $n=32$ ). **D)** Capsaicin dose response in absence (black) and presence of  $1$   $\mu$ M AG1529 (blue). Data was fitted to a Michaelis-Menten Isotherm. Resulting  $EC_{50}$  value for capsaicin was  $0.29$  (95% CI,  $0.20$ - $0.35$ )  $\mu$ M ( $n=29$ ) with a Hill coefficient of  $1.3$  (95% CI,  $0.9$ - $1.6$ ) while  $EC_{50}$  value in presence of AG1529 was  $0.98$  (95% CI  $0.60$ - $1.13$ )  $\mu$ M ( $n=21$ ) with a Hill coefficient of  $1.0$  (95% CI,  $0.7$ - $1.2$ ). **E)** Representative capsaicin-elicited hTRPV1 current recorded at a holding potential of  $-60$  mV in the absence (Untreated cells) and presence of  $1$   $\mu$ M AG1529 perfused  $30$  s before and during the first capsaicin pulse (AG1529 cells). **F)** P2/P1 ratio of capsaicin pulses for untreated and AG1529 treated cells. Data was analysed using an unpaired Student's t-test. P-value is denoted above bars. All data are expressed as mean  $\pm$  SEM.

## RESULTS

AG1529 effect was explored on affecting other modalities of TRPV1 gating distinct from chemical activation. Figure 58 A represents the effect of AG1529 on voltage-induced TRPV1 activation at room temperature. Voltage stimulation was explored by 20 mV voltage steps from -120 mV to 120 mV. In these conditions TRPV1 channels displayed outward currents from voltages >50 mV. Application of 1  $\mu$ M AG1529 (blue traces) 1 min before registering the steps protocol did not alter significantly voltage gating compared to control (black traces). Current density to voltage relationship (Figure 58 B) and conductance to voltage relationship (Figure 58 C) show a non-significant inhibitory effect of AG1529, hardly perceptible at potentials >100 mV.

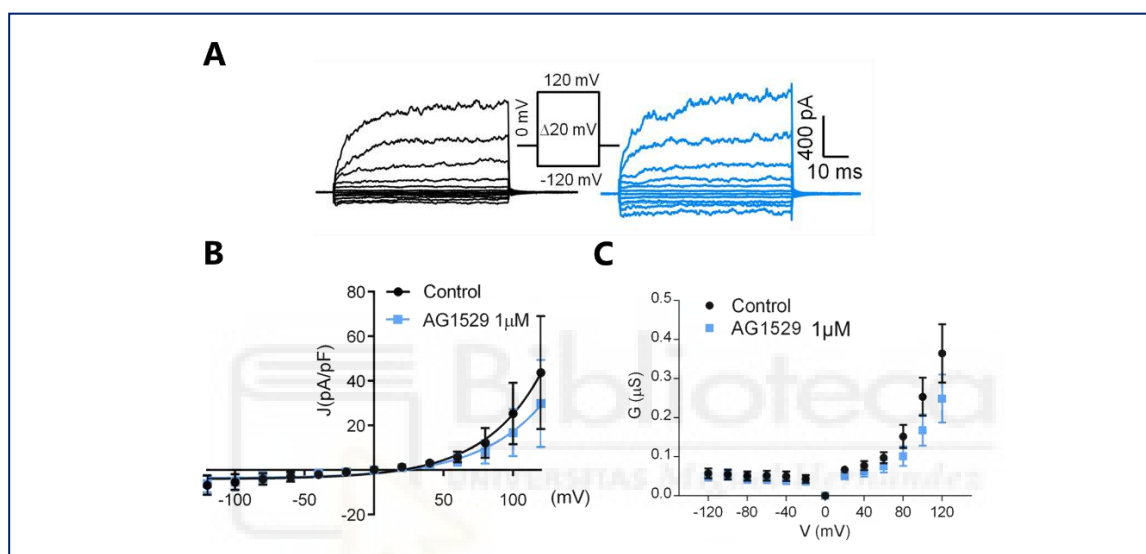


**Figure 58. AG1529 effect on voltage TRPV1 activation.** A) Representative voltage steps protocol from -120 mV to 120 mV in 100 ms steps of 20 mV from a holding potential of 0 mV. In black are shown traces in absence of 1  $\mu$ M AG1529 and in blue, in its presence. B) Current density (pA/pF) to voltage relationship for current in absence (black) and presence (blue) of 1  $\mu$ M AG1529 (n=8). C) Conductance to voltage relationship for currents in absence (black) and presence (blue) of 1  $\mu$ M AG1529.

Also, the effect of AG1529 was evaluated on TRPV1 gating evoked by acidic pH. TRPV1 currents were elicited by the perfusion of extracellular buffer at pH 5.5 in two consecutive pulses separated by a washing period. Two components could be observed in the pH-activated ionic currents, a fast one and a steady one corresponding to ASIC and TRPV1 activation, respectively. Endogenous hASIC channels were blocked with 50  $\mu$ M amiloride (Figure 59 A). 10  $\mu$ M AG1529 blocked nearly 50% of hTRPV1 current evoked by acidic pH while 10  $\mu$ M capsazepine and 1 nM BCTC blocked almost 80% of the current (Figure 59 B) (One-Way ANOVA with Bonferroni's post hoc test;  $F(3,28) = 15.50$ ,  $p < 0.0001$ ;  $p = 0.0013$  AG1529 vs. control;  $p < 0.0001$  CPZ and BCTC vs. control).

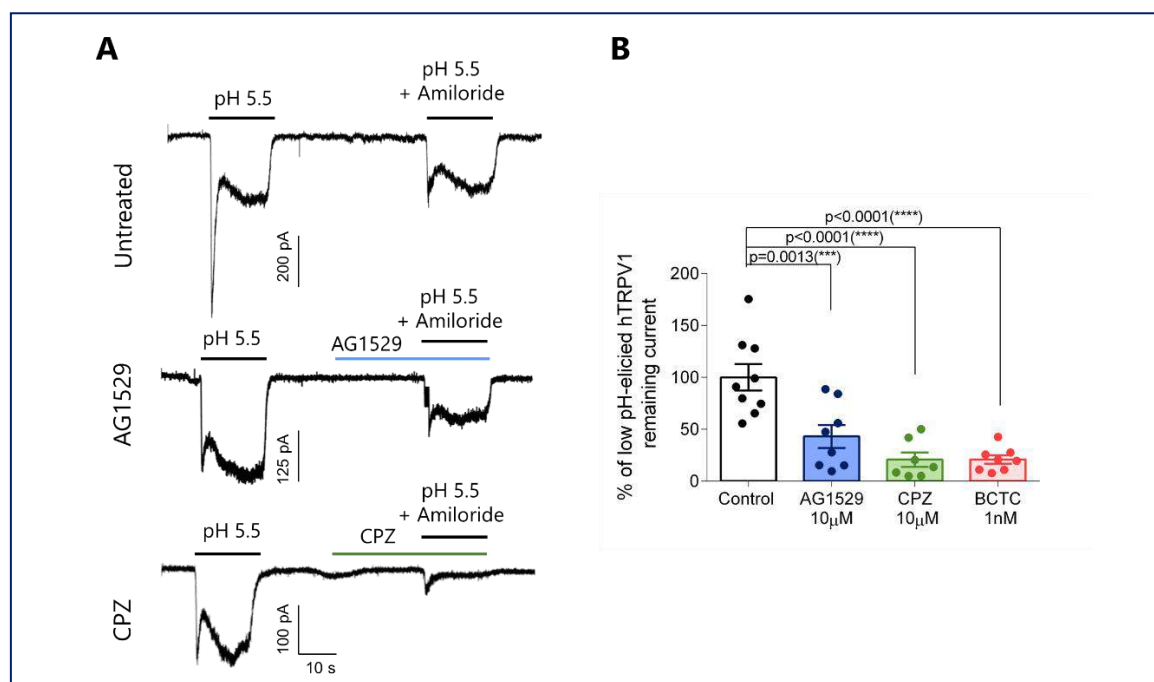


**Figure 59. AG1529 effect on pH-elicited TRPV1 currents.** **A)** Representative acid pH-elicited TRPV1 currents by two pH 5.5 pulses. 50  $\mu$ M amiloride was applied during second acid pH pulse to block endogenous ASIC channels. Cells were recorded at -60 mV of holding potential in absence (Untreated) or presence of compounds (AG1529, CPZ) which were applied 30 s before and during second acid pH pulse. **B)** Normalized pH-elicited TRPV1 remaining inward current in absence (control) or in presence of 10  $\mu$ M AG1529, 10  $\mu$ M capsazepine and 1 nM BCTC. Data was analysed using One-Way ANOVA ( $F(3,28) = 15.5$ ,  $p < 0.0001$ ) followed by Bonferroni's post hoc test. P-values are indicated above bars. All data is expressed as mean  $\pm$  SEM.

Finally, 10  $\mu$ M AG1529 effect was tested on high temperature (43°C)-evoked hTRPV1 currents. Representative ramp curves from -120 to 120 mV elicited at 43°C are shown on Figure 60 A. As it can be seen for control, TRPV1 suffered a desensitization during the second increase in temperature (P2). When capsazepine and AG1529 antagonists were applied before P2, similar recordings to control were obtained. Only BCTC at 1 nM significantly inhibited heat-evoked TRPV1 currents at positive potentials (Figure 60 B) (One-Way ANOVA with Bonferroni's post hoc test;  $F(3,31) = 3.5$ ,  $p = 0.027$ ;  $p = 0.047$  for control vs. BCTC).

These results indicate that AG1529 blocks acidic pH-evoked TRPV1 currents without affecting voltage nor heat-elicited channel responses.

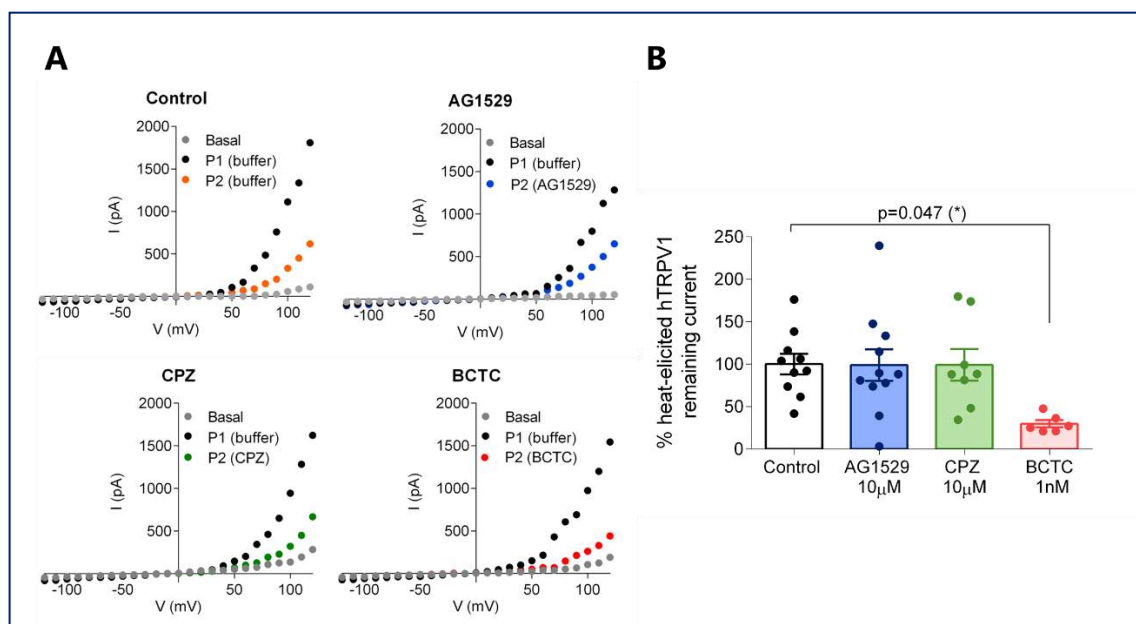


**Figure 60. AG1529 effect on temperature TRPV1 activation.** A) Representative current-voltage relationships of TRPV1 currents at 43°C in the absence (control) and presence of 10 μM AG1529, or 10 μM capsazepine (CPZ) or 1 nM BCTC. Basal stands for ionic current presence at 37°C, P1 and P2, for current evoked at 43°C in absence and in presence of compounds, respectively. Desensitization induced by heat and voltage is shown on control panel. Currents were registered with a voltage ramp protocol from -120 mV to 120 mV in 300 ms. Compounds were applied at 37°C 30 s before P2. B) Percentage of heat-elicited TRPV1 remaining current in absence and presence of compounds and normalized to control. Data was analysed using One-Way ANOVA ( $F(3,31) = 3.5$ ,  $p = 0.027$ ) followed by Bonferroni's post hoc test. P-value for statistical difference is indicated. All data is expressed as mean  $\pm$  SEM.

## 7.2. AG1529 modestly inhibits other thermoTRPs

To further characterize the mechanism of action of AG1529 it was evaluated on other thermoTRPs like TRPM8 and TRPA1. TRPM8 current was evoked by 100 μM menthol applied in two pulses interspersed by a washing period. Compounds were applied 30 s before and during second menthol pulse. As shown on Figure 61, 10 μM AG1529 inhibited nearly 35% of menthol-elicited hTRPM8 current, while the reference TRPM8 blocker AMTB reduced almost completely the channel current at the same concentration (One-Way ANOVA with Bonferroni's post hoc test,  $F(2,32) = 37.57$ ,  $p < 0.0001$ ;  $p = 0.0043$  AG1529 vs. control and  $p < 0.0001$  AMTB vs. control and AG1529). TRPA1 current was elicited by the application of 60 μM AITC following the same protocol as for TRPM8 channel. As it can be seen on Figure 62, 10 μM AG1529 inhibited almost 40% of AITC-evoked TRPA1 inward current, while 5 μM HC030031, a TRPA1 selective inhibitor, blocked completely channel current (One-Way ANOVA with Bonferroni's post hoc test,  $F(2,32) = 15.67$ ,  $p < 0.0001$ ;  $p = 0.0284$  AG1529 vs. control and  $p < 0.0001$  HC030031 vs. control).

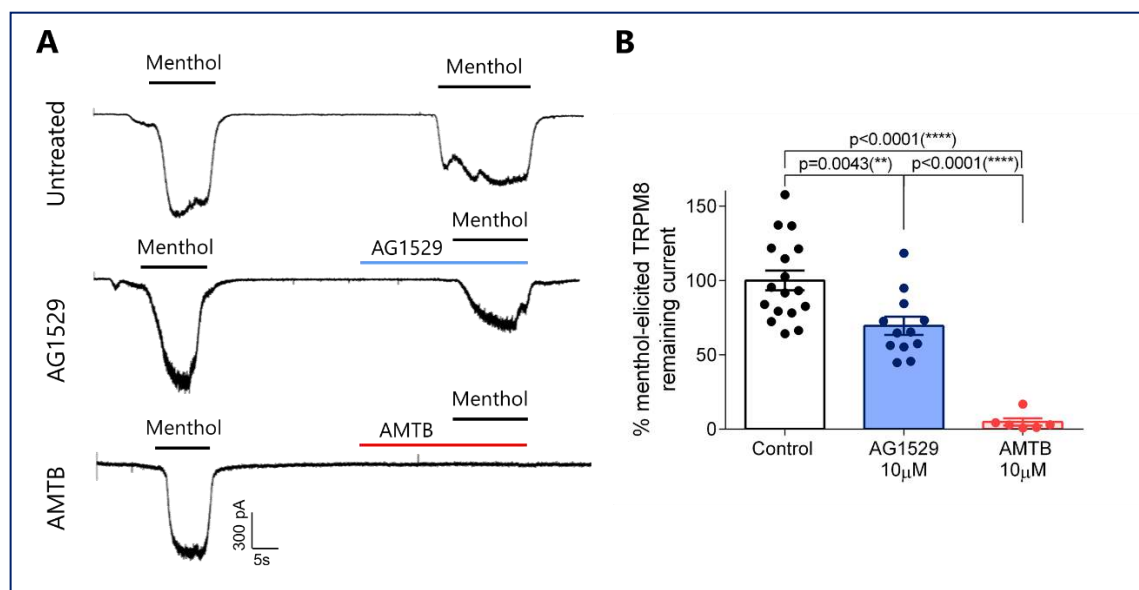


**Figure 61. AG1529 marginal effect on TRPM8.** **A)** Representative menthol-evoked TRPM8 current recorded at a holding potential of  $-60$  mV. Control cells (Untreated) were exposed to two pulses of  $100$   $\mu$ M menthol and were used to check TRPM8 desensitization. AG1529 cells were treated with  $10$   $\mu$ M AG1529  $30$  s before and during second menthol pulse, while AMTB cells were perfused with  $10$   $\mu$ M AMTB during the same time period. **B)** Percentage of menthol-evoked TRPM8 remaining current for control and after application of  $10$   $\mu$ M AG1529 or  $10$   $\mu$ M AMTB. Data was analysed using One-Way ANOVA ( $F(2,32) = 37.57$ ,  $p < 0.0001$ ) with Bonferroni's post hoc test. P-values for statistical difference are denoted above the bars. All data is shown as mean  $\pm$  SEM.

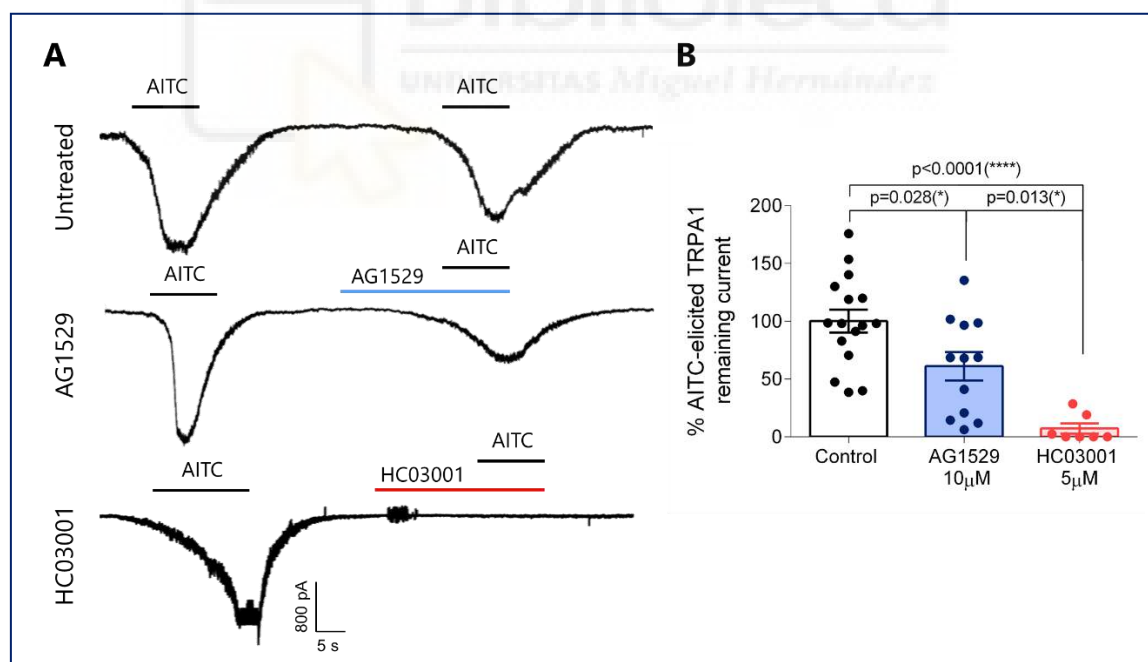


**Figure 62. AG1529 marginal effect on TRPA1.** **A)** Representative AITC-evoked TRPA1 current recorded at a holding potential of  $-60$  mV. Control cells (Untreated) were exposed to two pulses of  $60$   $\mu$ M AITC and were used to check TRPA1 desensitization. AG1529 cells were treated with  $10$   $\mu$ M AG1529  $30$  s before and during second AITC pulse, while HC03001 cells were perfused with  $5$   $\mu$ M HC03001 during the same time period. **B)** Percentage of AITC-evoked TRPA1 remaining current for control and after application of  $10$   $\mu$ M AG1529 or  $5$   $\mu$ M HC03001. Data was analysed using One-Way ANOVA ( $F(2,32) = 15.67$ ,  $p < 0.0001$ ) with Bonferroni's post hoc test. P-values for statistical difference are denoted above the bars. All data is shown as mean  $\pm$  SEM.

## RESULTS

On Figure 63 a comparison between 10  $\mu$ M AG1529 blocking effect on human thermoTRPs is shown. It reveals a significantly lower block of TRPM8 and TRPA1 current compared to TRPV1 (One-Way ANOVA with Bonferroni's post hoc test;  $F(5,63) = 7.63$ ,  $p < 0.0001$ ;  $p = 0.0252$  TRPV1 vs. TRPM8 and  $p = 0.0496$  TRPV1 vs. TRPA1). In summary, AG1529 exerts a preferential but not selective effect on hTRPV1 showing a milder inhibition of hTRPM8 and hTRPA1 channels.

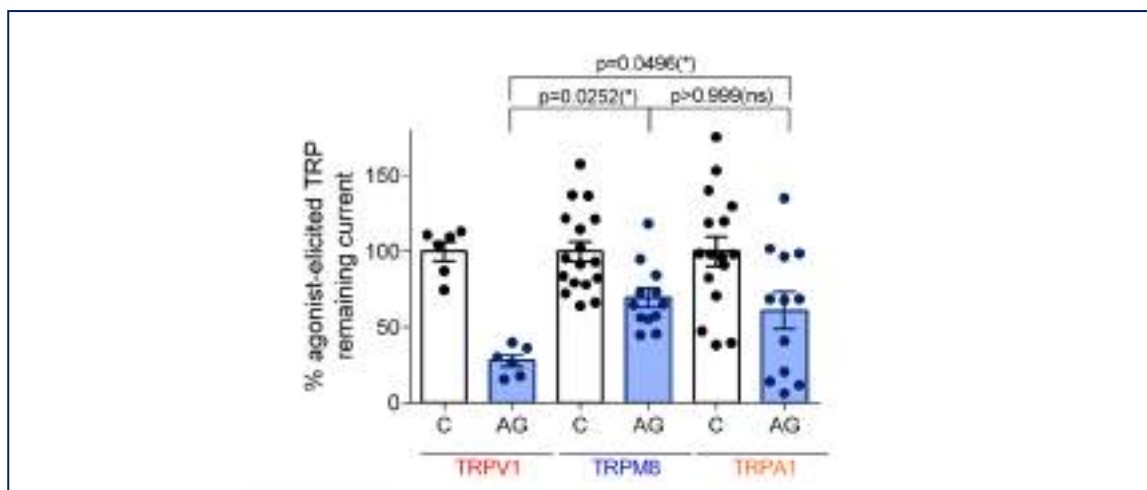


**Figure 63. AG1529 effect comparison between TRP channels.** Percentage of 10  $\mu$ M AG1529 blockade of hTRPV1, hTRPM8 and hTRPA1. In the x-axis labels, C stands for control and AG for AG1529. Data was analysed using One-Way ANOVA ( $F(5,63) = 7.63$ ,  $p < 0.0001$ ) with Bonferroni's multiple comparison post hoc test. P-values are indicated. All data are shown as mean  $\pm$  SEM.

### 7.3. AG1529 inhibitory effect on capsaicin-evoked neuronal firing

Therapeutically useful TRPV1 antagonists should be able to modulate nociceptor excitability, reason why we tested the effect of AG1529 on capsaicin-evoked action potentials on primary cultures of neonatal rat DRG neurons. Action potential bursts were recorded under current-clamp and triggered by the application of 500 nM capsaicin in two consecutive pulses (Figure 64 A-top trace). They were compared with action potential firing after the application during 1 min of 1  $\mu$ M AG1529 before and during second capsaicin pulse (Figure 64 A-bottom trace). A reduction in almost 50% of action potential firing was observed after the application of AG1529 (Figure 64 B) (unpaired Student's t-test,  $p = 0.032$ ).

Putative off-target effect of AG1529 on  $\text{Na}^+$  and  $\text{K}^+$  voltage-gated channels expressed in sensory neurons was studied in voltage-clamp experiments. Representative families of  $\text{Na}^+$  and  $\text{K}^+$  ionic currents evoked by voltage steps of 5 mV from -50 mV to 55 mV in the absence (black) and presence (blue) of 10  $\mu$ M AG1529 are shown on Figure 64

C. Both families of currents seem similar in terms of magnitude and voltage-sensitivity. Current density (Figure 64 D) and conductance (Figure 64 E) to voltage relationships corroborate that AG1529 did not affect Na<sup>+</sup> nor K<sup>+</sup> voltage properties.

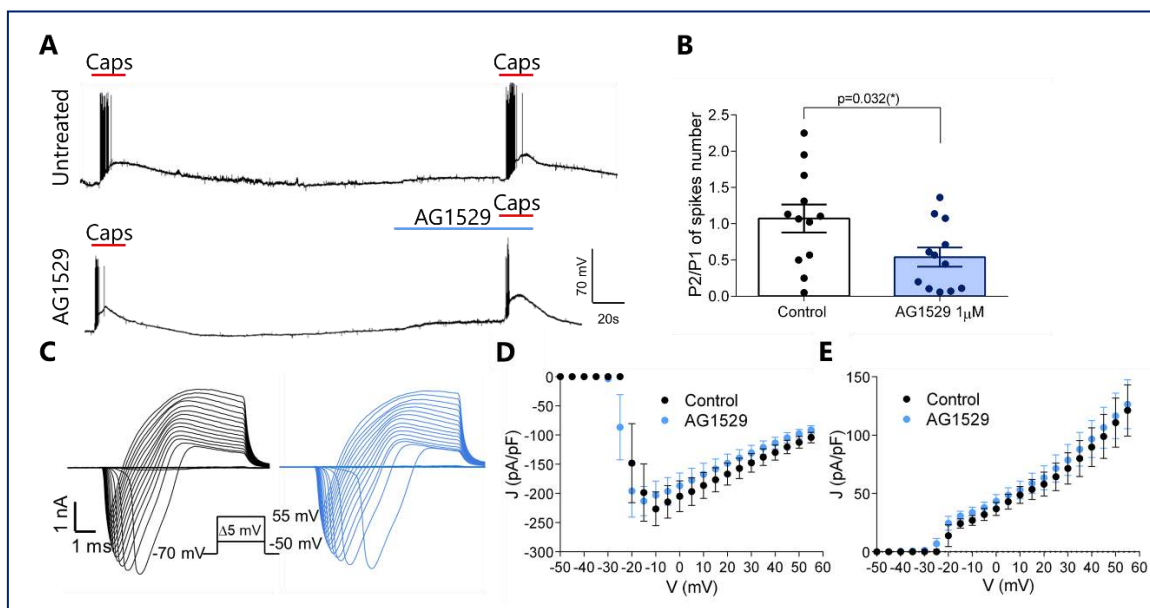


**Figure 64. AG1529 affects capsaicin-elicited DRG neuronal firing.** A) Representative recordings of action potential firing from neonatal rat DRG neurons evoked by the application of 500 nM capsaicin in the absence (Untreated cells) and presence (AG1529 cells) of 1  $\mu$ M AG1529 applied 1 min before and during second capsaicin pulse. B) Ratio P2/P1 of spikes number evoked in untreated or AG1529 perfused cells. Data was statistically analysed using an unpaired Student's t-test. P-value for statistical significance is indicated. C) Representative ionic currents elicited by 5 mV voltage steps of 10 ms from -50 to 55 mV recorded from a holding potential of -70 mV. 1  $\mu$ M AG1529 was applied during 1 min before the recording of the steps protocol (blue). Current density (pA/pF) to voltage relationships for the inward (D) and outward (E) current represented in C. Data is expressed as mean  $\pm$  SEM.

#### 7.4. AG1529 shares the vanilloid TRPV1 binding site

Molecular docking experiments were used in order to support the hypothesis that AG1529 acts as a capsaicin competitive inhibitor of TRPV1. Rat TRPV1 atomic structure in open and closed state with RCSB ID 5IRZ and 3J5P, respectively were used to perform a global blind docking with capsaicin, AG1529 and capsazepine and compare the energetics of compounds binding to capsaicin binding site. No differences in terms of best binding site between open and closed state were observed. From a total of 800 docking runs for each molecule, 116 localized AG1529 into the capsaicin binding site with an energy of  $3.7 \pm 1.3$  kcal/mol, 158 located capsazepine in the same binding site with an energy of  $9.3 \pm 1.1$  kcal/mol and 212 traced capsaicin in its described binding site with an energy of  $6.4 \pm 0.6$  kcal/mol (Figure 65 A). After local docking assays of the compounds into capsaicin binding site were performed, it was found that AG1529 adopted a tail-up,

head-down conformation similar to the one of capsaicin (Figure 65 B and C). AG1529 aliphatic tail interacted with residues L515, F543, M547, T550, N551 and L553 from S3 and S4 segments. Hydrogen bonds between S512 and R557 and the vanillyl head of AG1529 were formed. These polar interactions yield specificity to the interaction.

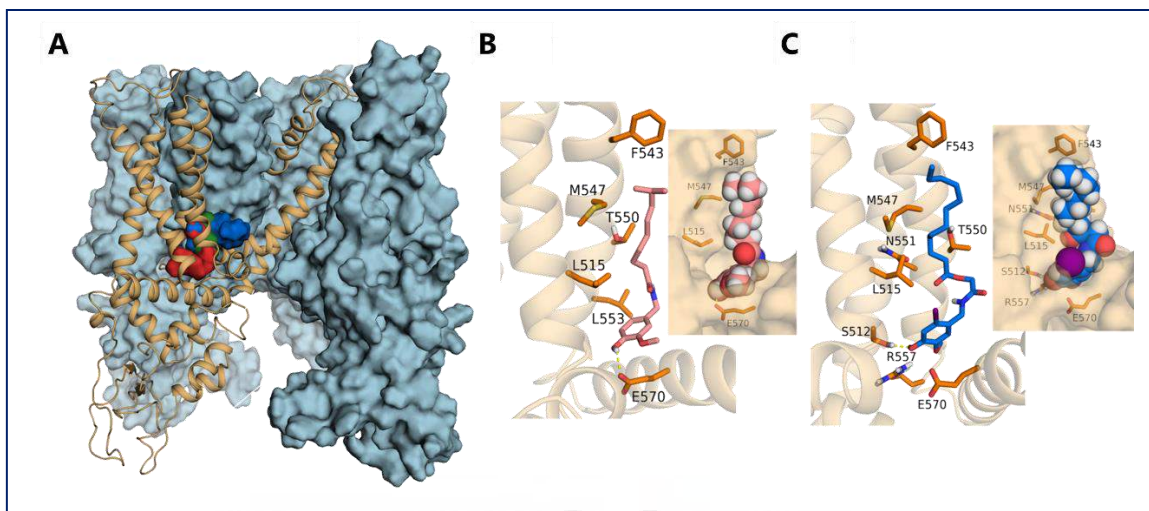


**Figure 65. AG1529 and capsaicin binding sites match each other.** A) Transmembrane view of rat TRPV1 structure showing three subunits as blueish surface and one as orange cartoon. Global blind docking assay localize capsaicin (red surface), capsazepine (green surface) and AG1529 (blue surface) in the capsaicin binding site. B) Local docking assay shows capsaicin (reddish sticks) orientation in its binding site. Hydrophobic interactions between capsaicin tail and residues L515 (S3), F543, M547, T550, N551 and L553 (S4) can be observed. Capsaicin head forms a hydrogen bond with residue E570. In the inset, capsaicin is shown as spheres and TRPV1 as surface in order to imagine better the volume occupied by the compound. C) Local docking assay shows that AG1529 (blue sticks) orientation is similar to capsaicin in its binding site. The same hydrophobic interactions as in the case of capsaicin were observed for AG1529. A hydrogen bond with S512 and R557 was observed. In the inset where AG1529 is shown as spheres and where its iodine group appears in purple, a conformation limitation of AG1529 head can be noticed.

# DISCUSSION



Biblioteca  
UNIVERSITAS Miguel Hernández





Chronic pain is a condition found in numerous pathologies whose treatments are ineffective and linked to important side effects [203]. Modulation of ion channels has constituted for long time a primary way to treat multiple pathologies. K<sub>2</sub>P channels family importance in pain modulation is emerging in the last years as a poorly explored molecular target [97, 210]. Inhibition of TRAAK and other K<sub>2</sub>P channels along with the direct activation or sensitization of pro-algesic TRP channels induces neuronal hyperexcitability typical for inflammatory and neuropathic pain, among others. The co-localization of TRAAK with some thermoTRP channels [70] in sensory neurons could help to manage pain modulation through drug dual action. Thus, activation of TRAAK and inhibition of TRP channels, offers an opportunity which has remained unexplored until now. Although during the last decade a few modulators of TREK subfamily have been described [106, 119, 125, 126, 131, 135, 136], none of them present TRAAK selectivity. Thus, the core motivation of the present thesis is the identification and functional validation of TRAAK selective modulators.

Ion channel activity can be modulated by diverse strategies. The ones contemplated in this work were protein-protein interaction modification and channel's activity modulation by direct binding of ligands. The **first approach** centres in the incidence on cell signalling cascades, modifying protein interactions in which a channel is involved. Regulatory networks rely on **protein-protein interactions** considering them as attractive targets to modulate specific pathways and pathological processes. Targeting protein-protein interfaces for activity modulation has the advantage of normally not interfering with classic binding sites. Protein-protein interactions are difficult to target by small molecules because they should cover large interacting surfaces which are flat, with no grooves or clear binding pockets [250]. In contrast, peptides and peptidomimetics are suitable for addressing against large interface areas in protein interactions. They are attractive due to their synthesis ease and advanced formulation that allows precise key spots identification, post-translational modification and introduction of non-natural amino acids [251]. Peptides are also greatly effective, selective and specific compared to small molecules. Given the advantages provided by peptides to control protein activity, inhibition of protein-TRAAK interaction conformed one strategy to achieve TRAAK modulation. The design of inhibitory peptides for these protein interactions was a key objective. Nevertheless, the lack of protein interactions described for TRAAK and the absence of the entire TRAAK structure in the existing X-ray crystals, greatly diffculted this goal.

Protein-protein interactions in which ion channels participate, normally involve their intracellular domains. TRAAK is provided with a very short N-terminal domain and 133 residues long intracellular C-terminal domain. This last shows a large quantity of proline residues which probably makes it highly loose and difficult to resolve crystallographically. Here, reconstruction of C-terminal domain by homology and *ab initio* modelling was performed. Despite a few on-line servers and *in situ* programmes were used, the lack of reliable homology model to reconstruct the domain hindered the accuracy of the resulting model. The low scoring of the resulting models could derive from the high number of prolines which difficult the adoption of secondary and tertiary protein structures. This could be due to a loose unfolded structure that could adopt different conformations, difficult to predict. If such a model is used in protein docking it would introduce more uncertainties rather than bring solutions.

Due to the difficulties experimented with the prediction of TRAAK C-terminal domain, the use of ADAN database resulted in another possibility to check for protein-protein interactions TRAAK might be involved in. High number of protein-protein interactions take place through SH3 domains [252]. SH3 domains normally bind to ligands with the canonical motifs +xxPxxP or xPxxPx+, where “x” defines any amino acid and “+” a positively charged residue [253]. ADAN database offers the possibility to search for putative binding partners given a query sequence through the calculation of position-specific scoring matrices (PSSM) [238]. It contains a collection of 84 different SH3 domains and by the use of PSSM it is able to predict if some of the present SH3 domains could bind to a provided query sequence. Putative interacting partners seem to be tyrosine kinases, ubiquitinases, oxidases and cytoskeletal remodellers (as the case of  $\beta$ -COP1 [90]). Although these results seem feasible, they should be demonstrated, and a real modulatory effect of these proteins should be described on TRAAK in order to propose the design of interaction disrupting peptides against them. Once the interaction is confirmed experimentally, the SH3-ligand (TRAAK derived) complex could be isolated. Position specific scoring matrices could then be calculated in order to check which amino acids represent key anchor points for the interaction and design peptides which improve this interaction and thus compete with the wild-type sequence found in cells.

A **second strategy** for TRAAK modulation focused on channel's activity regulation by the **direct binding of ligands** to their binding sites, modifying channel's pore and gating. Thus, this second strategy was explored through virtual screening of

diverse libraries on four distinct putative binding sites of TRAAK. The existence of crystal structures incorporating a ligand bound to an active site of its target protein is of great importance when setting virtual screening assays and thus it is a key factor to ensure the success of libraries screening. The only crystal structure incorporating a ligand bound to TRAAK is the one showing a decane molecule just below the pore, which is tough to belong to a membrane lipid [55]. This was the only binding site which suffered no modification and which incorporated a real control ligand whose exact binding pose was already known. ML402 [45] and norfluoxetine [44] binding sites on TREK-1 and TREK-2, respectively, were transferred to TRAAK structure by molecular modelling. The TRAAK models containing ligands ML402 and norfluoxetine were also of high quality since the ligand conformation was maintained although it was necessary to perform minor adjustments on residues' sidechain in the binding sites of TRAAK. TKDC binding site on the extracellular cap of TRAAK [135] incorporates no crystal structure, thus docking assay was performed in order to reproduce the binding site of the molecule. Accordingly, resulting binding energy of virtual screening hit molecules and its comparison with control ligands is an approximation and a deviation from real binding energy could be expected. Global blind docking results using compounds with already known effect on TRAAK converge with ML402, decane and norfluoxetine binding sites, supporting the use of both of them for virtual screening assays.

**Virtual screening** has been used as alternative of high-throughput screening to evaluate the potential of small molecules to interact with a target protein through a putative binding site. Virtual screening needs target and ligands structural information in order to predict the conformation and orientation a ligand adopts in a binding site and estimate the protein-ligand affinity [254]. The most important drawback of this methodology is the reduction of the number of false positives and negatives. The use of various scoring functions tends to reduce false inclusion or exclusion of ligands for *in vitro* testing. Another strategy to tackle this problem is the use of ADME-Tox filters which enable the selection of molecules with a proper pharmacological profile [255]. Finally, the use of artificial intelligence and machine learning to train an algorithm capable to detect a set of putative ligands able to interact with a target protein, using information from already identified protein modulators is gaining importance [256, 257]. Nevertheless, its application in the identification of new TRAAK modulators is impossible given that a large training set of already known TRAAK ligands cannot be constructed.

Libraries selected for virtual screening in this work contained natural compounds, patent free approved drugs, lipids and small peptides. Firstly, natural compounds have constituted an important source of active compounds of drugs [258]. Usually, in this type of libraries, a great chemical structure diversity is found [259]. Natural-product-based drugs include plants, microbes' and animals' compounds and can be synthetic or semi-synthetic [260]. Secondly, given the high economical costs and long development times of drugs, repurposing has become highly attractive. Drug reposition means to identify new uses of already approved drugs. The biggest advantage is the low failure risk due to the already tested drug safety. Sometimes, even formulation development has been completed. Accordingly, this strategy provides substantial preclinical and phase I and II cost savings [261]. On the other hand, the use of small peptides (two, three amino acids long) which mimic functionality and physico-chemical characteristics of small chemical ligands, becomes of great interest given its link to low synthesis costs, low toxicity and tissue accumulation. Finally, lipidic libraries have been selected for screening due to numerous lipidic modulation demonstration over TRAAK [49, 111].

Although a large variety of molecules have been screened against each TRAAK putative binding site, there is a clear preference of already approved molecules as drugs to bind to any of the explored binding pockets. This is foreseeable due to their already improved physico-chemical characteristics, presenting molecular weight, hydrophobicity and chemical groups suitable for drugs. Peptides of two or three amino acids showed the worst interaction energy in general. It is noteworthy to mention also that some ligands resulted in hit compounds for more than one binding site.

Virtual screening resulted in the election of 9 **compounds to be assessed *in vitro***. Half of them resulted to be ineffective while the other half exerted some effect on TRAAK. The lack of effect of pranlukast on TRAAK is supported by the recent publication by Wright PD *et al* [262], where the compound showed a clear agonistic effect on TREK-1 and TREK-2 but not on TRAAK. Compared to basal current, irinotecan seemed to enhance TRAAK activity while pimozide, terfenadine and astemizol reduced it.

**Irinotecan** provoked an increase in TRAAK current which was 50% lower at +120 mV and 50% higher at -120 mV when compared to the effect produced by arachidonic acid at the same concentration. Nevertheless, this increase in inward current is negligible compared to the increase in outward current. Maximal current

increase was reached slower by irinotecan when compared to arachidonic acid at the same concentration which could mean that the exerted effect by irinotecan is indirect or at least that both activators do not share the same activation mechanism or site of action. Irinotecan effect was reversible at 10  $\mu\text{M}$  but not at 100  $\mu\text{M}$ . At this high concentration, irinotecan produces up to 6-fold increase in TRAAK basal current. In a small cell like Hek, a 12 to 20 nA outward  $\text{K}^+$  current is probably not time-sustainable because such a potent opening of TRAAK gradually empties internal  $\text{K}^+$  content of the cell. This has been also observed for TRAAK activation by high concentrations of arachidonic acid [49].

In sensory neurons from neonatal rat DRGs, irinotecan produced no changes in action potential firing threshold or firing frequency. No change in these parameters was either observed after instillation of arachidonic acid. In physiological conditions this could be expected given that a slight activation of TRAAK could be counteracted by other channels which avoid an extreme change of membrane potential to more hyperpolarized values, i.e. HCN channels [263]. On the other hand, test of irinotecan on heterogeneous primary culture of neonatal rat DRG neurons on MEA showed a slight increase in mean spike frequency after its instillation, compared to control. Also, the number of spikes registered only during the application of the compound were in higher amount compared to control and arachidonic acid. MEA results were contrary to what was expected if the compound would act only activating TRAAK. Although not described in literature, irinotecan could target other ion channels directly, such as voltage-dependant  $\text{Na}^+$  or  $\text{K}^+$  channels, or it could insert into cell membrane influencing the behaviour of different mechanosensitive channels. Even so, MEA methodology orchestrates a very complex cellular environment rendering results difficult to interpret with that much unknowns. As mentioned previously, lack of effect of a TRAAK agonist in physiological conditions was expected in patch clamp. For that reason irinotecan was evaluated on *in vitro* neuropathic pain model induced by taxol where a change in the hyperpolarization state after the action potential spike is observed in IB4- neurons. In these cells hyperpolarization state is smaller which turns them more excitable. In this model, irinotecan was able to revert the effect of taxol restoring physiological values of hyperpolarization.

The development of dysarthria, motor aphasia and ataxia in patients with hypokalemia (low extracellular concentration of  $\text{K}^+$ ) during the infusion of irinotecan as chemotherapeutic agent [264-267] could be explained by its probable effect activating

TRAAK. In physiological conditions during mild hypokalemia, cells could counteract it releasing  $K^+$  from intracellular compartments through ion channels like TRAAK which are constitutively in conducting state.  $K^+$  exit would continue until a new equilibrium is reached. Nevertheless, during moderate or severe hypokalemia and in presence of a TRAAK activator,  $K^+$  flow from cell inside to outside could decrease considerably ion intracellular concentration, hyperpolarizing neurons and turning them silent. Removing irinotecan from the equation and restoring normal extracellular concentration of  $K^+$  has been observed to reverse the symptoms.

Regarding **terfenadine** and **astemizol** antagonists assayed on heterologously expressed hTRAAK channel, terfenadine showed higher potency compared to astemizol, although both of them are quite weak inhibitors provoking 20 to 30% blockage of TRAAK current at  $10\mu\text{M}$ . The effect of both is reversible, dose dependent and competitive with arachidonic acid agonism. Patch clamp study on DRGs showed that only terfenadine exerted a notorious effect causing depolarization induced neuronal firing. Both compounds are histamine receptor antagonists with important off-targets. Both produce arrhythmogenic effects due to inhibition of hERG1 channel [268], reason for their initial market withdraw and repositioning as chemotherapeutic drugs against breast [269] and prostate [270] cancer. Moreover, terfenadine has shown inhibition of L-type  $\text{Ca}^{2+}$  channel current, delayed rectifier  $K^+$  channels and time-dependant  $\text{Na}^+$  channels in ventricular myocytes [271, 272]. In addition, recently, it was shown that terfenadine also inhibits Kir2.1 and Kir2.3 channels [273].

Could the depolarization induced neuronal firing be explained by the effect of terfenadine on some of its off-targets? In first place, although the inhibition of hERG1 channel provokes a similar action potential firing, it would be almost exclusive to central nervous system neurons [274]. Despite some authors state there is expression of hERG1 channel in DRG neurons, they are very few, unclear and ambiguous [275, 276]. If hERG1 channel was expressed in DRG neurons, considering the inhibitory effect of astemizol on this channel, an identical depolarization induced firing should have been observed for astemizol and terfenadine. In second place, neither Kir2.1 nor Kir2.3 are expressed in peripheral nervous system [277] and, even if they were, their inhibition would hyperpolarize neurons, decreasing their excitability instead of enhancing it [278]. In third place, terfenadine inhibition of  $\text{Na}^+$  or  $\text{Ca}^{2+}$  currents observed by Ming and Nordin [271] should not produce action potential firing, while inhibition of delayed rectifier  $K^+$  channels should change action potential waveform causing an elongation of

the repolarization state [279]. Furthermore, effect of terfenadine on these last three types of currents has been observed after cells were subjected to longer exposure to the drug (10 min) compared to the present work. All these evidences support the hypothesis that terfenadine is inhibiting TRAAK channel in DRG neurons, or any channel from the TREK subfamily of K<sub>2</sub>P channels.

The presence of **fatty acids** in the tail of the capsaicinoid molecules made us expect they could probably exert some effect on TRAAK. Therefore, a capsaicinoids library designed against TRPV1 was also screened against TKDC, ML402 and norfluoxetine TRAAK binding sites. For this library decane binding site was discarded due to its partial overlap with norfluoxetine active site.

**AG1529** is a compound from a chemical library of capsaicin soft analogues which incorporates a capsaicin-similar head and a lipophilic tail constituted by a C12:0 fatty acid. The implantation of an ester group in this tail makes compounds susceptible to the hydrolysing activity of esterases preventing from their accumulation while their TRPV1 activity is maintained [280]. In order to prove the hypothesis that such a compound could exert a double effect, inhibiting TRPV1 and activating TRAAK through the fatty acid, it was tested on both channels. Although it did not produce any change in TRAAK basal current, possibly because of its saturation, its effect as TRPV1 antagonist at micromolar range made worth its further characterisation. AG1529 reversibly blocked capsaicin-induced TRPV1 current in a preferential manner while it marginally affected pH-elicited TRPV1 gating. The compound did not produce any alteration on voltage- and heat-induced TRPV1 channel activation. This lack of effect on heat-induced TRPV1 current is significant for topical applications where it would not alter dermal temperature sensitivity. AG1529 modestly inhibited hTRPA1 and hTRPM8 channels showing an IC<sub>50</sub> value 10-fold higher for both channels compared to hTRPV1. Conservation of transmembrane binding sites between TRPV1, TRPA1 and TRPM8 has been reported to cause ligand cross-recognition [281-283]. This compound cross-reactivity may be an advantage rather than a disadvantage in complex multifactorial disorders like pain [284-286]. Actually, with our initial hypothesis of double modulation of TRPV1 and TRAAK we were seeking for a cross-reactivity of the compound.

AG1529 is a capsaicin competitive antagonist, demonstrated by the shift of capsaicin EC<sub>50</sub> to higher value. This was supported by *in silico* molecular docking model which located AG1529 and capsaicin in the same binding site. In literature, it has been proposed that TRPV1 opening is induced by capsaicin pull of residue E570 with the

formation of a hydrogen bond which provokes a motion in S6 and the opening of channel's gate [287]. AG1529 incorporates a bulky 2.16Å iodine group on its vanillyl head which endangers compound interaction with residue E570. The presence of the iodine group blocks the head of AG1529 in such an orientation that locks the channel in closed configuration. Finally, AG1529 attenuated primary cultured rat nociceptor firing induced by capsaicin and exerted no effect on Na<sup>+</sup> and K<sup>+</sup> neuronal currents. Although AG1529 exerted no effect on TRAAK, it demonstrated a good inhibitory activity on TRPV1 and it probably could be used in a topical formulation in combination with a TRAAK agonist to treat different types of pain.

Overall, irinotecan appears as top hit compound for more than one TRAAK binding site, including putative agonists and antagonists binding pockets. Pharmacology of TRAAK is poorly explored and further insight into channel modulation is compulsory to better target new compounds against it. Is irinotecan interaction with the ML402 binding site which opens TRAAK pore, or is its probable lipidic membrane penetration which activates this mechanosensor, or maybe is its interaction with the C-terminal domain of TRAAK responsible to finally activate the channel? A more profound effect characterisation of irinotecan, astemizol and terfenadine on TRAAK is needed. Mutagenesis studies could help with the determination of key interacting residues for each binding site. Channel selectivity of tested compounds is also a milestone for an effective channel modulation, although it could not be explored in this work. Structure activity relationship (SAR) of compounds studied here is of great importance to gather not only efficacy and selectivity but also chemical characteristics important for pharmacodynamics, tissular site of action and target pathology to treat. SAR improves molecules interaction characteristics by computational mean, although in this work, chemical group changes were done non-systemically. Compound interactions with its binding site were intended to be improved without increasing excessively its hydrophobicity and keeping physico-chemical characteristics between levels established by Lipinski's Rule. Possibility of cheap purchase or synthesis of resulting molecules should be contemplated. Ideally, molecules should present properties similar to known TRAAK modulators. Nevertheless, in this case, the known channel modulators are very few, thus probably new chemical structures could be now discovered as important for TRAAK activity control. Work developed here sets only the beginning of a pathway which needs a deeper exploration.

# CONCLUSIONS





- Numerous putative TRAAK ligands were found during virtual screening assays set on four TRAAK extracellular and transmembrane binding sites previously determined. *In vitro* testing corroborated four of them, irinotecan, astemizol, terfenadine and pimoziide, modulate TRAAK activity.
- Few presumptive protein TRAAK C-terminal domain interacting partners through SH3 domain were identified.
- Irinotecan enhanced TRAAK mediated whole cell current in recombinant cells in a reversible manner and increased action potential hyperpolarization state in taxol treated IB4- DRG neurons and hyperpolarized cell resting membrane potential.
- Astemizol and terfenadine decreased TRAAK mediated whole cell current in recombinant cells in a reversible manner. Both showed competitiveness with arachidonic acid. Terfenadine decreased neuronal hyperpolarization magnitude after action potential firing and induced a depolarization-evoked action potential firing.
- AG1529 inhibited capsaicin- and pH-elicited TRPV1 current without altering voltage- nor heat-induced channel's gating. AG1529 also moderately blocked TRPM8 and TRPA1 channels and suppressed capsaicin-evoked sensory neuronal firing. The compound exerted no effect on TRAAK.

- Numerosos ligandos putativos de TRAAK fueron identificados durante los ensayos de barrido virtual centrados en cuatro sitios de unión ubicados en los dominios extracelular y transmembrana de TRAAK. Cuatro de dichos ligandos, irinotecan, astemizol, terfenadin y pimozid, demostraron modular la actividad de TRAAK *in vitro*.
- Se identificaron varias proteínas que presuntamente interaccionarían con el dominio C-terminal de TRAAK mediante sus dominios SH3.
- Irinotecan aumentó las corrientes mediadas por TRAAK de forma reversible y acrecentó el estado de hiperpolarización del potencial de acción de reposo celular en neuronas IB4- tratadas con taxol.
- Astemizol y terfenadin disminuyeron las corrientes de célula completa mediadas por TRAAK en células recombinantes de forma reversible. Ambos mostraron competitividad con el ácido araquidónico. Terfenadin redujo la magnitud de hiperpolarización neuronal tras el disparo del potencial de acción e indujo el disparo de potenciales de acción evocados por despolarización.
- AG1529 inhibió la corriente de TRPV1 provocada por capsaicina o pH ácido sin alterar la actividad del canal inducida por voltaje o temperatura. AG1529 bloqueó moderadamente los canales TRPM8 y TRPA1 y reprimió el disparo de potenciales de acción evocadas por capsaicina en neuronas sensoriales. El compuesto no tuvo ningún efecto sobre TRAAK.

# BIBLIOGRAPHY



1. *International Association for the Study of Pain, Pain terms, a current list with definitions and notes on usage*, <https://www.iasp-ain.org/Education/Content.aspx>.
2. Williams, A.C. and K.D. Craig, *Updating the definition of pain*. *Pain*, 2016. **157**(11): p. 2420-2423.
3. Bell, A., *The neurobiology of acute pain*. *Vet J*, 2018. **237**: p. 55-62.
4. Zilliox, L.A., *Neuropathic Pain*. *Continuum (Minneapolis, Minn)*, 2017. **23**(2, Selected Topics in Outpatient Neurology): p. 512-532.
5. Cook, A.D., et al., *Immune Cytokines and Their Receptors in Inflammatory Pain*. *Trends Immunol*, 2018. **39**(3): p. 240-255.
6. Clauw, D.J., *Fibromyalgia: a clinical review*. *JAMA*, 2014. **311**(15): p. 1547-55.
7. Silberstein, S.D., *Migraine pathophysiology and its clinical implications*. *Cephalalgia*, 2004. **24 Suppl 2**: p. 2-7.
8. Moore, C., et al., *Regulation of Pain and Itch by TRP Channels*. *Neurosci Bull*, 2018. **34**(1): p. 120-142.
9. Sherrington, C.S., *Qualitative differences of spinal reflex corresponding with qualitative difference of cutaneous stimulus*. 1903: *Journal of Physiology*. p. 39-46.
10. Sherrington, C.S., *The integrative action of the nervous system*. 1906: Scribner.
11. Abraira, V.E. and D.D. Ginty, *The sensory neurons of touch*. *Neuron*, 2013. **79**(4): p. 618-39.
12. Treede, R.D., R.A. Meyer, and J.N. Campbell, *Myelinated mechanically insensitive afferents from monkey hairy skin: heat-response properties*. *J Neurophysiol*, 1998. **80**(3): p. 1082-93.
13. Snider, W.D. and S.B. McMahon, *Tackling pain at the source: new ideas about nociceptors*. *Neuron*, 1998. **20**(4): p. 629-32.
14. Han, L., et al., *A subpopulation of nociceptors specifically linked to itch*. *Nat Neurosci*, 2013. **16**(2): p. 174-82.
15. REXED, B., *The cytoarchitectonic organization of the spinal cord in the cat*. *J Comp Neurol*, 1952. **96**(3): p. 414-95.
16. Todd, A.J., *Neuronal circuitry for pain processing in the dorsal horn*. *Nat Rev Neurosci*, 2010. **11**(12): p. 823-36.
17. Abraira, V.E., et al., *The Cellular and Synaptic Architecture of the Mechanosensory Dorsal Horn*. *Cell*, 2017. **168**(1-2): p. 295-310.e19.
18. Bezanilla, F., *The action potential: from voltage-gated conductances to molecular structures*. *Biol Res*, 2006. **39**(3): p. 425-35.
19. Yaksh, T.L., et al., *The search for novel analgesics: targets and mechanisms*. *F1000Prime Rep*, 2015. **7**: p. 56.
20. Chiu, I.M., C.A. von Hehn, and C.J. Woolf, *Neurogenic inflammation and the peripheral nervous system in host defense and immunopathology*. *Nat Neurosci*, 2012. **15**(8): p. 1063-7.
21. Gold, M.S. and G.F. Gebhart, *Nociceptor sensitization in pain pathogenesis*. *Nat Med*, 2010. **16**(11): p. 1248-57.
22. Maex, R., *On the Nernst-Planck equation*. *J Integr Neurosci*, 2017. **16**(1): p. 73-91.
23. Tamagawa, H. and K. Ikeda, *Generation of membrane potential beyond the conceptual range of Donnan theory and Goldman-Hodgkin-Katz equation*. *J Biol Phys*, 2017. **43**(3): p. 319-340.
24. Patapoutian, A., S. Tate, and C.J. Woolf, *Transient receptor potential channels: targeting pain at the source*. *Nat Rev Drug Discov*, 2009. **8**(1): p. 55-68.
25. Caterina, M.J. and D. Julius, *The vanilloid receptor: a molecular gateway to the pain pathway*. *Annu Rev Neurosci*, 2001. **24**: p. 487-517.
26. Gamper, N., et al., *Oxidative modification of M-type K(+) channels as a mechanism of cytoprotective neuronal silencing*. *EMBO J*, 2006. **25**(20): p. 4996-5004.

27. Plant, L.D., *A Role for K2P Channels in the Operation of Somatosensory Nociceptors*. *Front Mol Neurosci*, 2012. **5**: p. 21.
28. HODGKIN, A.L. and A.F. HUXLEY, *A quantitative description of membrane current and its application to conduction and excitation in nerve*. *J Physiol*, 1952. **117**(4): p. 500-44.
29. Jones, S.W., *On the resting potential of isolated frog sympathetic neurons*. *Neuron*, 1989. **3**(2): p. 153-61.
30. Goldman, D.E., *POTENTIAL, IMPEDANCE, AND RECTIFICATION IN MEMBRANES*. *J Gen Physiol*, 1943. **27**(1): p. 37-60.
31. Ketchum, K.A., et al., *A new family of outwardly rectifying potassium channel proteins with two pore domains in tandem*. *Nature*, 1995. **376**(6542): p. 690-5.
32. Yu, F.H., et al., *Overview of molecular relationships in the voltage-gated ion channel superfamily*. *Pharmacol Rev*, 2005. **57**(4): p. 387-95.
33. Yellen, G., et al., *Mutations affecting internal TEA blockade identify the probable pore-forming region of a K<sup>+</sup> channel*. *Science*, 1991. **251**(4996): p. 939-42.
34. Goldstein, S.A., et al., *ORK1, a potassium-selective leak channel with two pore domains cloned from Drosophila melanogaster by expression in Saccharomyces cerevisiae*. *Proc Natl Acad Sci U S A*, 1996. **93**(23): p. 13256-61.
35. Goldstein, S.A., et al., *International Union of Pharmacology. LV. Nomenclature and molecular relationships of two-P potassium channels*. *Pharmacol Rev*, 2005. **57**(4): p. 527-40.
36. Niemeyer, M.I., et al., *Gating, Regulation, and Structure in K2P K<sup>+</sup> Channels: In Varietate Concordia?* *Mol Pharmacol*, 2016. **90**(3): p. 309-17.
37. Lopes, C.M., N. Zilberberg, and S.A. Goldstein, *Block of Kcnk3 by protons. Evidence that 2-P-domain potassium channel subunits function as homodimers*. *J Biol Chem*, 2001. **276**(27): p. 24449-52.
38. Kollwe, A., et al., *A structural model for K2P potassium channels based on 23 pairs of interacting sites and continuum electrostatics*. *J Gen Physiol*, 2009. **134**(1): p. 53-68.
39. Suzuki, Y., et al., *Heterodimerization of two pore domain K<sup>+</sup> channel TASK1 and TALK2 in living heterologous expression systems*. *PLoS One*, 2017. **12**(10): p. e0186252.
40. Lengyel, M., G. Czirájk, and P. Enyedi, *Formation of Functional Heterodimers by TREK-1 and TREK-2 Two-pore Domain Potassium Channel Subunits*. *J Biol Chem*, 2016. **291**(26): p. 13649-61.
41. Levitz, J., et al., *Heterodimerization within the TREK channel subfamily produces a diverse family of highly regulated potassium channels*. *Proc Natl Acad Sci U S A*, 2016. **113**(15): p. 4194-9.
42. Miller, A.N. and S.B. Long, *Crystal structure of the human two-pore domain potassium channel K2P1*. *Science*, 2012. **335**(6067): p. 432-6.
43. Brohawn, S.G., J. del Mármol, and R. MacKinnon, *Crystal structure of the human K2P TRAAK, a lipid- and mechano-sensitive K<sup>+</sup> ion channel*. *Science*, 2012. **335**(6067): p. 436-41.
44. Dong, Y.Y., et al., *K2P channel gating mechanisms revealed by structures of TREK-2 and a complex with Prozac*. *Science*, 2015. **347**(6227): p. 1256-9.
45. Lolicato, M., et al., *K<sub>2</sub>P.1 (TREK-1)-activator complexes reveal a cryptic selectivity filter binding site*. *Nature*, 2017. **547**(7663): p. 364-368.
46. Schewe, M., et al., *A Non-canonical Voltage-Sensing Mechanism Controls Gating in K2P K(+) Channels*. *Cell*, 2016. **164**(5): p. 937-49.
47. Lesage, F., et al., *TWIK-1, a ubiquitous human weakly inward rectifying K<sup>+</sup> channel with a novel structure*. *EMBO J*, 1996. **15**(5): p. 1004-11.
48. Fink, M., et al., *Cloning, functional expression and brain localization of a novel unconventional outward rectifier K<sup>+</sup> channel*. *EMBO J*, 1996. **15**(24): p. 6854-62.
49. Fink, M., et al., *A neuronal two P domain K<sup>+</sup> channel stimulated by arachidonic acid and polyunsaturated fatty acids*. *EMBO J*, 1998. **17**(12): p. 3297-308.

50. Bang, H., Y. Kim, and D. Kim, *TREK-2, a new member of the mechanosensitive tandem-pore K<sup>+</sup> channel family*. J Biol Chem, 2000. **275**(23): p. 17412-9.
51. Lesage, F., et al., *Human TREK2, a 2P domain mechano-sensitive K<sup>+</sup> channel with multiple regulations by polyunsaturated fatty acids, lysophospholipids, and Gs, Gi, and Gq protein-coupled receptors*. J Biol Chem, 2000. **275**(37): p. 28398-405.
52. Maingret, F., et al., *Mechano- or acid stimulation, two interactive modes of activation of the TREK-1 potassium channel*. J Biol Chem, 1999. **274**(38): p. 26691-6.
53. Maingret, F., et al., *TRAAK is a mammalian neuronal mechano-gated K<sup>+</sup> channel*. J Biol Chem, 1999. **274**(3): p. 1381-7.
54. Brohawn, S.G., Z. Su, and R. MacKinnon, *Mechanosensitivity is mediated directly by the lipid membrane in TRAAK and TREK1 K<sup>+</sup> channels*. Proc Natl Acad Sci U S A, 2014. **111**(9): p. 3614-9.
55. Brohawn, S.G., E.B. Campbell, and R. MacKinnon, *Physical mechanism for gating and mechanosensitivity of the human TRAAK K<sup>+</sup> channel*. Nature, 2014. **516**(7529): p. 126-30.
56. Medhurst, A.D., et al., *Distribution analysis of human two pore domain potassium channels in tissues of the central nervous system and periphery*. Brain Res Mol Brain Res, 2001. **86**(1-2): p. 101-14.
57. Talley, E.M., et al., *Cns distribution of members of the two-pore-domain (KCNK) potassium channel family*. J Neurosci, 2001. **21**(19): p. 7491-505.
58. Aller, M.I. and W. Wisden, *Changes in expression of some two-pore domain potassium channel genes (KCNK) in selected brain regions of developing mice*. Neuroscience, 2008. **151**(4): p. 1154-72.
59. Gu, W., et al., *Expression pattern and functional characteristics of two novel splice variants of the two-pore-domain potassium channel TREK-2*. J Physiol, 2002. **539**(Pt 3): p. 657-68.
60. Gnatenco, C., et al., *Functional expression of TREK-2 K<sup>+</sup> channel in cultured rat brain astrocytes*. Brain Res, 2002. **931**(1): p. 56-67.
61. Zhou, M., et al., *TWIK-1 and TREK-1 are potassium channels contributing significantly to astrocyte passive conductance in rat hippocampal slices*. J Neurosci, 2009. **29**(26): p. 8551-64.
62. Bearzatto, B., et al., *Axonal transport of TREK and TRAAK potassium channels in rat sciatic nerves*. Neuroreport, 2000. **11**(5): p. 927-30.
63. Kang, D. and D. Kim, *TREK-2 (K2P10.1) and TRESK (K2P18.1) are major background K<sup>+</sup> channels in dorsal root ganglion neurons*. Am J Physiol Cell Physiol, 2006. **291**(1): p. C138-46.
64. Thomas, D., et al., *Alternative translation initiation in rat brain yields K2P2.1 potassium channels permeable to sodium*. Neuron, 2008. **58**(6): p. 859-70.
65. Ozaita, A. and E. Vega-Saenz de Miera, *Cloning of two transcripts, HKT4.1a and HKT4.1b, from the human two-pore K<sup>+</sup> channel gene KCNK4. Chromosomal localization, tissue distribution and functional expression*. Brain Res Mol Brain Res, 2002. **102**(1-2): p. 18-27.
66. Simkin, D., E.J. Cavanaugh, and D. Kim, *Control of the single channel conductance of K2P10.1 (TREK-2) by the amino-terminus: role of alternative translation initiation*. J Physiol, 2008. **586**(23): p. 5651-63.
67. Maingret, F., et al., *TREK-1 is a heat-activated background K(+) channel*. EMBO J, 2000. **19**(11): p. 2483-91.
68. Kang, D., C. Choe, and D. Kim, *Thermosensitivity of the two-pore domain K<sup>+</sup> channels TREK-2 and TRAAK*. J Physiol, 2005. **564**(Pt 1): p. 103-16.
69. Noël, J., et al., *The mechano-activated K<sup>+</sup> channels TRAAK and TREK-1 control both warm and cold perception*. EMBO J, 2009. **28**(9): p. 1308-18.

70. Yamamoto, Y., T. Hatakeyama, and K. Taniguchi, *Immunohistochemical colocalization of TREK-1, TREK-2 and TRAAK with TRP channels in the trigeminal ganglion cells.* *Neurosci Lett*, 2009. **454**(2): p. 129-33.
71. Voets, T., *TRP channels and thermosensation.* *Handb Exp Pharmacol*, 2014. **223**: p. 729-41.
72. Descoeur, J., et al., *Oxaliplatin-induced cold hypersensitivity is due to remodelling of ion channel expression in nociceptors.* *EMBO Mol Med*, 2011. **3**(5): p. 266-78.
73. Pereira, V., et al., *Role of the TREK2 potassium channel in cold and warm thermosensation and in pain perception.* *Pain*, 2014. **155**(12): p. 2534-44.
74. Patel, A.J., et al., *A mammalian two pore domain mechano-gated S-like K<sup>+</sup> channel.* *EMBO J*, 1998. **17**(15): p. 4283-90.
75. Chemin, J., et al., *A phospholipid sensor controls mechanogating of the K<sup>+</sup> channel TREK-1.* *EMBO J*, 2005. **24**(1): p. 44-53.
76. Chemin, J., et al., *Up- and down-regulation of the mechano-gated K(2P) channel TREK-1 by PIP (2) and other membrane phospholipids.* *Pflugers Arch*, 2007. **455**(1): p. 97-103.
77. Lopes, C.M., et al., *PIP2 hydrolysis underlies agonist-induced inhibition and regulates voltage gating of two-pore domain K<sup>+</sup> channels.* *J Physiol*, 2005. **564**(Pt 1): p. 117-29.
78. Sandoz, G., S.C. Bell, and E.Y. Isacoff, *Optical probing of a dynamic membrane interaction that regulates the TREK1 channel.* *Proc Natl Acad Sci U S A*, 2011. **108**(6): p. 2605-10.
79. Honoré, E., et al., *An intracellular proton sensor commands lipid- and mechano-gating of the K(+) channel TREK-1.* *EMBO J*, 2002. **21**(12): p. 2968-76.
80. Sandoz, G., et al., *Extracellular acidification exerts opposite actions on TREK1 and TREK2 potassium channels via a single conserved histidine residue.* *Proc Natl Acad Sci U S A*, 2009. **106**(34): p. 14628-33.
81. Cohen, A., et al., *A novel mechanism for human K2P2.1 channel gating. Facilitation of C-type gating by protonation of extracellular histidine residues.* *J Biol Chem*, 2008. **283**(28): p. 19448-55.
82. Chemin, J., et al., *Mechanisms underlying excitatory effects of group I metabotropic glutamate receptors via inhibition of 2P domain K<sup>+</sup> channels.* *EMBO J*, 2003. **22**(20): p. 5403-11.
83. Murbartián, J., et al., *Sequential phosphorylation mediates receptor- and kinase-induced inhibition of TREK-1 background potassium channels.* *J Biol Chem*, 2005. **280**(34): p. 30175-84.
84. Cain, S.M., et al., *mGlu4 potentiation of K(2P)2.1 is dependant on C-terminal dephosphorylation.* *Mol Cell Neurosci*, 2008. **37**(1): p. 32-9.
85. Enyeart, J.J., et al., *Angiotensin II inhibits bTREK-1 K<sup>+</sup> channels in adrenocortical cells by separate Ca<sup>2+</sup>- and ATP hydrolysis-dependent mechanisms.* *J Biol Chem*, 2005. **280**(35): p. 30814-28.
86. Mathie, A., *Neuronal two-pore-domain potassium channels and their regulation by G protein-coupled receptors.* *J Physiol*, 2007. **578**(Pt 2): p. 377-85.
87. Comoglio, Y., et al., *Phospholipase D2 specifically regulates TREK potassium channels via direct interaction and local production of phosphatidic acid.* *Proc Natl Acad Sci U S A*, 2014. **111**(37): p. 13547-52.
88. Sandoz, G., et al., *AKAP150, a switch to convert mechano-, pH- and arachidonic acid-sensitive TREK K(+) channels into open leak channels.* *EMBO J*, 2006. **25**(24): p. 5864-72.
89. Sandoz, G., et al., *Mtap2 is a constituent of the protein network that regulates twik-related K<sup>+</sup> channel expression and trafficking.* *J Neurosci*, 2008. **28**(34): p. 8545-52.
90. Kim, E., et al., *Enhancement of TREK1 channel surface expression by protein-protein interaction with beta-COP.* *Biochem Biophys Res Commun*, 2010. **395**(2): p. 244-50.

91. Zuzarte, M., et al., *Intracellular traffic of the K<sup>+</sup> channels TASK-1 and TASK-3: role of N- and C-terminal sorting signals and interaction with 14-3-3 proteins*. J Physiol, 2009. **587**(Pt 5): p. 929-52.
92. O'Kelly, I., et al., *Forward transport. 14-3-3 binding overcomes retention in endoplasmic reticulum by dibasic signals*. Cell, 2002. **111**(4): p. 577-88.
93. Mazella, J., et al., *Spadin, a sortilin-derived peptide, targeting rodent TREK-1 channels: a new concept in the antidepressant drug design*. PLoS Biol, 2010. **8**(4): p. e1000355.
94. Harinath, S. and S.K. Sikdar, *Trichloroethanol enhances the activity of recombinant human TREK-1 and TRAAK channels*. Neuropharmacology, 2004. **46**(5): p. 750-60.
95. Soussia, I.B., et al., *Antagonistic Effect of a Cytoplasmic Domain on the Basal Activity of Polymodal Potassium Channels*. Front Mol Neurosci, 2018. **11**: p. 301.
96. Ursell, T., et al., *Role of lipid bilayer mechanics in mechanosensitivity*. 2008, Springer. p. 37-70.
97. Busserolles, J., et al., *Potassium channels in neuropathic pain: advances, challenges, and emerging ideas*. Pain, 2016. **157 Suppl 1**: p. S7-14.
98. Mathie, A. and E.L. Veale, *Two-pore domain potassium channels: potential therapeutic targets for the treatment of pain*. Pflugers Arch, 2015. **467**(5): p. 931-43.
99. Li, X.Y. and H. Toyoda, *Role of leak potassium channels in pain signaling*. Brain Res Bull, 2015. **119**(Pt A): p. 73-9.
100. Kindler, C.H. and C.S. Yost, *Two-pore domain potassium channels: new sites of local anesthetic action and toxicity*. Reg Anesth Pain Med, 2005. **30**(3): p. 260-74.
101. Patel, A.J., et al., *Inhalational anesthetics activate two-pore-domain background K<sup>+</sup> channels*. Nat Neurosci, 1999. **2**(5): p. 422-6.
102. Punke, M.A., et al., *Inhibition of human TREK-1 channels by bupivacaine*. Anesth Analg, 2003. **96**(6): p. 1665-73, table of contents.
103. Nayak, T.K., et al., *Inhibition of human two-pore domain K<sup>+</sup> channel TREK1 by local anesthetic lidocaine: negative cooperativity and half-of-sites saturation kinetics*. Mol Pharmacol, 2009. **76**(4): p. 903-17.
104. Kennard, L.E., et al., *Inhibition of the human two-pore domain potassium channel, TREK-1, by fluoxetine and its metabolite norfluoxetine*. Br J Pharmacol, 2005. **144**(6): p. 821-9.
105. Cadaveira-Mosquera, A., et al., *Activation of TREK currents by the neuroprotective agent riluzole in mouse sympathetic neurons*. J Neurosci, 2011. **31**(4): p. 1375-85.
106. Meadows, H.J., et al., *The neuroprotective agent sipatrigine (BW619C89) potently inhibits the human tandem pore-domain K<sup>+</sup> channels TREK-1 and TRAAK*. Brain Res, 2001. **892**(1): p. 94-101.
107. Lacomblez, L., et al., *Dose-ranging study of riluzole in amyotrophic lateral sclerosis. Amyotrophic Lateral Sclerosis/Riluzole Study Group II*. Lancet, 1996. **347**(9013): p. 1425-31.
108. Noël, J., G. Sandoz, and F. Lesage, *Molecular regulations governing TREK and TRAAK channel functions*. Channels (Austin), 2011. **5**(5): p. 402-9.
109. Meves, H., *Arachidonic acid and ion channels: an update*. Br J Pharmacol, 2008. **155**(1): p. 4-16.
110. Park, K.A. and M.R. Vasko, *Lipid mediators of sensitivity in sensory neurons*. Trends Pharmacol Sci, 2005. **26**(11): p. 571-7.
111. Maingret, F., et al., *Lysophospholipids open the two-pore domain mechano-gated K<sup>+</sup> channels TREK-1 and TRAAK*. J Biol Chem, 2000. **275**(14): p. 10128-33.
112. Kieffer, B.L. and C. Gavériaux-Ruff, *Exploring the opioid system by gene knockout*. Prog Neurobiol, 2002. **66**(5): p. 285-306.
113. Matthes, H.W., et al., *Loss of morphine-induced analgesia, reward effect and withdrawal symptoms in mice lacking the mu-opioid-receptor gene*. Nature, 1996. **383**(6603): p. 819-23.

114. Devilliers, M., et al., *Activation of TREK-1 by morphine results in analgesia without adverse side effects*. Nat Commun, 2013. **4**: p. 2941.
115. Bedson, J., et al., *Risk of adverse events in patients prescribed long-term opioids: A cohort study in the UK Clinical Practice Research Datalink*. Eur J Pain, 2019. **23**(5): p. 908-922.
116. Kendall, S.E., et al., *The cognitive effects of opioids in chronic non-cancer pain*. Pain, 2010. **150**(2): p. 225-30.
117. André, T., et al., *Oxaliplatin, fluorouracil, and leucovorin as adjuvant treatment for colon cancer*. N Engl J Med, 2004. **350**(23): p. 2343-51.
118. Beijers, A.J., et al., *Peripheral neuropathy in colorectal cancer survivors: the influence of oxaliplatin administration. Results from the population-based PROFILES registry*. Acta Oncol, 2015. **54**(4): p. 463-9.
119. Duprat, F., et al., *The neuroprotective agent riluzole activates the two P domain K(+) channels TREK-1 and TRAAK*. Mol Pharmacol, 2000. **57**(5): p. 906-12.
120. Poupon, L., et al., *Targeting the TREK-1 potassium channel via riluzole to eliminate the neuropathic and depressive-like effects of oxaliplatin*. Neuropharmacology, 2018. **140**: p. 43-61.
121. Hama, A. and J. Sagen, *Antinociceptive effect of riluzole in rats with neuropathic spinal cord injury pain*. J Neurotrauma, 2011. **28**(1): p. 127-34.
122. Moon, E.S., et al., *Riluzole attenuates neuropathic pain and enhances functional recovery in a rodent model of cervical spondylotic myelopathy*. Neurobiol Dis, 2014. **62**: p. 394-406.
123. Wangemann, P., et al., *Cl(-)-channel blockers in the thick ascending limb of the loop of Henle. Structure activity relationship*. Pflugers Arch, 1986. **407 Suppl 2**: p. S128-41.
124. Rae, J.L. and G. Farrugia, *Whole-cell potassium current in rabbit corneal epithelium activated by fenamates*. J Membr Biol, 1992. **129**(1): p. 81-97.
125. Takahira, M., et al., *Fenamates and diltiazem modulate lipid-sensitive mechano-gated 2P domain K(+) channels*. Pflugers Arch, 2005. **451**(3): p. 474-8.
126. Bagriantsev, S.N., et al., *A high-throughput functional screen identifies small molecule regulators of temperature- and mechano-sensitive K2P channels*. ACS Chem Biol, 2013. **8**(8): p. 1841-51.
127. Bagriantsev, S.N., K.A. Clark, and D.L. Minor, *Metabolic and thermal stimuli control K(2P)2.1 (TREK-1) through modular sensory and gating domains*. EMBO J, 2012. **31**(15): p. 3297-308.
128. Bagriantsev, S.N., et al., *Multiple modalities converge on a common gate to control K2P channel function*. EMBO J, 2011. **30**(17): p. 3594-606.
129. Lotshaw, D.P., *Biophysical, pharmacological, and functional characteristics of cloned and native mammalian two-pore domain K+ channels*. Cell Biochem Biophys, 2007. **47**(2): p. 209-56.
130. Veale, E.L., et al., *Influence of the N terminus on the biophysical properties and pharmacology of TREK1 potassium channels*. Mol Pharmacol, 2014. **85**(5): p. 671-81.
131. Pope, L., et al., *Protein and Chemical Determinants of BL-1249 Action and Selectivity for K*. ACS Chem Neurosci, 2018. **9**(12): p. 3153-3165.
132. Decher, N., et al., *Sodium permeable and "hypersensitive" TREK-1 channels cause ventricular tachycardia*. EMBO Mol Med, 2017. **9**(4): p. 403-414.
133. Xie, X.M. and J. Garthwaite, *State-dependent inhibition of Na+ currents by the neuroprotective agent 619C89 in rat hippocampal neurons and in a mammalian cell line expressing rat brain type IIA Na+ channels*. Neuroscience, 1996. **73**(4): p. 951-62.
134. McNaughton, N.C., et al., *Inhibition of recombinant low-voltage-activated Ca(2+) channels by the neuroprotective agent BW619C89 (Sipatrigine)*. Neuropharmacology, 2000. **39**(7): p. 1247-53.

135. Luo, Q., et al., *An allosteric ligand-binding site in the extracellular cap of K2P channels*. Nat Commun, 2017. **8**(1): p. 378.
136. Castellanos, A., et al., *Pyrethroids inhibit K2P channels and activate sensory neurons: basis of insecticide-induced paraesthesias*. Pain, 2018. **159**(1): p. 92-105.
137. Minke, B., *Drosophila mutant with a transducer defect*. Biophys Struct Mech, 1977. **3**(1): p. 59-64.
138. Wes, P.D., et al., *TRPC1, a human homolog of a Drosophila store-operated channel*. Proc Natl Acad Sci U S A, 1995. **92**(21): p. 9652-6.
139. Zhu, X., et al., *Molecular cloning of a widely expressed human homologue for the Drosophila trp gene*. FEBS Lett, 1995. **373**(3): p. 193-8.
140. Montell, C., L. Birnbaumer, and V. Flockerzi, *The TRP channels, a remarkably functional family*. Cell, 2002. **108**(5): p. 595-8.
141. Li, H., *TRP Channel Classification*. Adv Exp Med Biol, 2017. **976**: p. 1-8.
142. Latorre, R., C. Zaelzer, and S. Brauchi, *Structure-functional intimacies of transient receptor potential channels*. Q Rev Biophys, 2009. **42**(3): p. 201-46.
143. Harteneck, C., C. Klose, and D. Krautwurst, *Synthetic modulators of TRP channel activity*. Adv Exp Med Biol, 2011. **704**: p. 87-106.
144. Vetter, I. and R.J. Lewis, *Natural product ligands of TRP channels*. Adv Exp Med Biol, 2011. **704**: p. 41-85.
145. Ciardo, M.G. and A. Ferrer-Montiel, *Lipids as central modulators of sensory TRP channels*. Biochim Biophys Acta Biomembr, 2017. **1859**(9 Pt B): p. 1615-1628.
146. Castillo, K., et al., *Thermally activated TRP channels: molecular sensors for temperature detection*. Phys Biol, 2018. **15**(2): p. 021001.
147. Nilius, B., et al., *Gating of TRP channels: a voltage connection?* J Physiol, 2005. **567**(Pt 1): p. 35-44.
148. Liu, C. and C. Montell, *Forcing open TRP channels: Mechanical gating as a unifying activation mechanism*. Biochem Biophys Res Commun, 2015. **460**(1): p. 22-5.
149. Voets, T., et al., *Sensing with TRP channels*. Nat Chem Biol, 2005. **1**(2): p. 85-92.
150. Julius, D., *TRP channels and pain*. Annu Rev Cell Dev Biol, 2013. **29**: p. 355-84.
151. Wetsel, W.C., *Sensing hot and cold with TRP channels*. Int J Hyperthermia, 2011. **27**(4): p. 388-98.
152. Jardín, I., et al., *TRPs in Pain Sensation*. Front Physiol, 2017. **8**: p. 392.
153. Cao, E., et al., *TRPV1 structures in distinct conformations reveal activation mechanisms*. Nature, 2013. **504**(7478): p. 113-8.
154. Schumacher, M.A. and H. Eilers, *TRPV1 splice variants: structure and function*. Front Biosci (Landmark Ed), 2010. **15**: p. 872-82.
155. Zhang, F., et al., *Heat activation is intrinsic to the pore domain of TRPV1*. Proc Natl Acad Sci U S A, 2018. **115**(2): p. E317-E324.
156. Tominaga, M., et al., *The cloned capsaicin receptor integrates multiple pain-producing stimuli*. Neuron, 1998. **21**(3): p. 531-43.
157. Caterina, M.J., et al., *The capsaicin receptor: a heat-activated ion channel in the pain pathway*. Nature, 1997. **389**(6653): p. 816-24.
158. Vigna, S.R., et al., *Leukotriene B4 mediates inflammation via TRPV1 in duct obstruction-induced pancreatitis in rats*. Pancreas, 2011. **40**(5): p. 708-14.
159. Starkus, J., et al., *Diverse TRPV1 responses to cannabinoids*. Channels (Austin), 2019. **13**(1): p. 172-191.
160. Kissin, I. and A. Szallasi, *Therapeutic targeting of TRPV1 by resiniferatoxin, from preclinical studies to clinical trials*. Curr Top Med Chem, 2011. **11**(17): p. 2159-70.
161. Bevan, S., et al., *Capsazepine: a competitive antagonist of the sensory neurone excitant capsaicin*. Br J Pharmacol, 1992. **107**(2): p. 544-52.
162. Pomonis, J.D., et al., *N-(4-Tertiarybutylphenyl)-4-(3-cholorphyridin-2-yl)tetrahydropyrazine -1(2H)-carbox-amide (BCTC), a novel, orally effective vanilloid*

- receptor 1 antagonist with analgesic properties: II. *in vivo* characterization in rat models of inflammatory and neuropathic pain. *J Pharmacol Exp Ther*, 2003. **306**(1): p. 387-93.
163. Ma, L., et al., *Nicotinic acid activates the capsaicin receptor TRPV1: Potential mechanism for cutaneous flushing*. *Arterioscler Thromb Vasc Biol*, 2014. **34**(6): p. 1272-80.
164. Maurer, K., et al., *Acetylsalicylic acid enhances tachyphylaxis of repetitive capsaicin responses in TRPV1-GFP expressing HEK293 cells*. *Neurosci Lett*, 2014. **563**: p. 101-6.
165. Andrei, S.R., et al., *TRPA1 is functionally co-expressed with TRPV1 in cardiac muscle: Co-localization at z-discs, costameres and intercalated discs*. *Channels (Austin)*, 2016. **10**(5): p. 395-409.
166. Cortright, D.N., et al., *The tissue distribution and functional characterization of human VR1*. *Biochem Biophys Res Commun*, 2001. **281**(5): p. 1183-9.
167. De Logu, F., et al., *TRP functions in the broncho-pulmonary system*. *Semin Immunopathol*, 2016. **38**(3): p. 321-9.
168. Rychkov, G.Y. and G.J. Barritt, *Expression and function of TRP channels in liver cells*. *Adv Exp Med Biol*, 2011. **704**: p. 667-86.
169. Ständer, S., et al., *Expression of vanilloid receptor subtype 1 in cutaneous sensory nerve fibers, mast cells, and epithelial cells of appendage structures*. *Exp Dermatol*, 2004. **13**(3): p. 129-39.
170. Liao, M., et al., *Structure of the TRPV1 ion channel determined by electron cryo-microscopy*. *Nature*, 2013. **504**(7478): p. 107-12.
171. Boukalova, S., et al., *Conserved residues within the putative S4-S5 region serve distinct functions among thermosensitive vanilloid transient receptor potential (TRPV) channels*. *J Biol Chem*, 2010. **285**(53): p. 41455-62.
172. Gao, Y., et al., *TRPV1 structures in nanodiscs reveal mechanisms of ligand and lipid action*. *Nature*, 2016. **534**(7607): p. 347-51.
173. Darré, L. and C. Domene, *Binding of Capsaicin to the TRPV1 Ion Channel*. *Mol Pharm*, 2015. **12**(12): p. 4454-65.
174. Rohács, T., et al., *PI(4,5)P2 regulates the activation and desensitization of TRPM8 channels through the TRP domain*. *Nat Neurosci*, 2005. **8**(5): p. 626-34.
175. Prescott, E.D. and D. Julius, *A modular PIP2 binding site as a determinant of capsaicin receptor sensitivity*. *Science*, 2003. **300**(5623): p. 1284-8.
176. Cao, E., et al., *TRPV1 channels are intrinsically heat sensitive and negatively regulated by phosphoinositide lipids*. *Neuron*, 2013. **77**(4): p. 667-79.
177. Holzer, P., *Acid-sensitive ion channels and receptors*. *Handb Exp Pharmacol*, 2009(194): p. 283-332.
178. Jordt, S.E., M. Tominaga, and D. Julius, *Acid potentiation of the capsaicin receptor determined by a key extracellular site*. *Proc Natl Acad Sci U S A*, 2000. **97**(14): p. 8134-9.
179. Ryu, S., et al., *Uncoupling proton activation of vanilloid receptor TRPV1*. *J Neurosci*, 2007. **27**(47): p. 12797-807.
180. Lukacs, V., et al., *Dual regulation of TRPV1 by phosphoinositides*. *J Neurosci*, 2007. **27**(26): p. 7070-80.
181. Karashima, Y., et al., *Modulation of the transient receptor potential channel TRPA1 by phosphatidylinositol 4,5-bisphosphate manipulators*. *Pflugers Arch*, 2008. **457**(1): p. 77-89.
182. Kweon, H.J., et al., *Differential regulation of proton-sensitive ion channels by phospholipids: a comparative study between ASICs and TRPV1*. *PLoS One*, 2015. **10**(3): p. e0122014.

183. Xie, C. and D.H. Wang, *Inhibition of renin release by arachidonic acid metabolites, 12(s)-HPETE and 12-HETE: role of TRPV1 channels*. *Endocrinology*, 2011. **152**(10): p. 3811-9.
184. Gregus, A.M., et al., *Systematic analysis of rat 12/15-lipoxygenase enzymes reveals critical role for spinal eLOX3 hepoxilin synthase activity in inflammatory hyperalgesia*. *FASEB J*, 2013. **27**(5): p. 1939-49.
185. Hwang, S.W., et al., *Direct activation of capsaicin receptors by products of lipoxygenases: endogenous capsaicin-like substances*. *Proc Natl Acad Sci U S A*, 2000. **97**(11): p. 6155-60.
186. Yin, S., et al., *Retinoids activate the irritant receptor TRPV1 and produce sensory hypersensitivity*. *J Clin Invest*, 2013. **123**(9): p. 3941-51.
187. Nieto-Posadas, A., et al., *Lysophosphatidic acid directly activates TRPV1 through a C-terminal binding site*. *Nat Chem Biol*, 2011. **8**(1): p. 78-85.
188. Sisignano, M., et al., *TRP-channels as key integrators of lipid pathways in nociceptive neurons*. *Prog Lipid Res*, 2014. **53**: p. 93-107.
189. Rains, C. and H.M. Bryson, *Topical capsaicin. A review of its pharmacological properties and therapeutic potential in post-herpetic neuralgia, diabetic neuropathy and osteoarthritis*. *Drugs Aging*, 1995. **7**(4): p. 317-28.
190. Andersen, H.H., L. Arendt-Nielsen, and J. Elberling, *Topical capsaicin 8% for the treatment of neuropathic itch conditions*. *Clin Exp Dermatol*, 2017. **42**(5): p. 596-598.
191. Szallasi, A. and P.M. Blumberg, *Vanilloid (Capsaicin) receptors and mechanisms*. *Pharmacol Rev*, 1999. **51**(2): p. 159-212.
192. Wang, Y.Y., et al., *In vitro and in vivo evaluations of topically applied capsaicin and nonivamide from hydrogels*. *Int J Pharm*, 2001. **224**(1-2): p. 89-104.
193. Bode, A.M. and Z. Dong, *The two faces of capsaicin*. *Cancer Res*, 2011. **71**(8): p. 2809-14.
194. Jones, V.M., K.A. Moore, and D.M. Peterson, *Capsaicin 8% topical patch (Qutenza)--a review of the evidence*. *J Pain Palliat Care Pharmacother*, 2011. **25**(1): p. 32-41.
195. Brown, D.C., *Resiniferatoxin: The Evolution of the "Molecular Scalpel" for Chronic Pain Relief*. *Pharmaceuticals (Basel)*, 2016. **9**(3).
196. Frank, J.A., et al., *Photoswitchable fatty acids enable optical control of TRPV1*. *Nat Commun*, 2015. **6**: p. 7118.
197. Szallasi, A., et al., *The vanilloid receptor TRPV1: 10 years from channel cloning to antagonist proof-of-concept*. *Nat Rev Drug Discov*, 2007. **6**(5): p. 357-72.
198. Szallasi, A. and G. Appendino, *Vanilloid receptor TRPV1 antagonists as the next generation of painkillers. Are we putting the cart before the horse?* *J Med Chem*, 2004. **47**(11): p. 2717-23.
199. Gavva, N.R., et al., *Pharmacological blockade of the vanilloid receptor TRPV1 elicits marked hyperthermia in humans*. *Pain*, 2008. **136**(1-2): p. 202-10.
200. Li, S., et al., *TRPV1-antagonist AMG9810 promotes mouse skin tumorigenesis through EGFR/Akt signaling*. *Carcinogenesis*, 2011. **32**(5): p. 779-85.
201. van Hecke, O., N. Torrance, and B.H. Smith, *Chronic pain epidemiology and its clinical relevance*. *Br J Anaesth*, 2013. **111**(1): p. 13-8.
202. Wertli, M.M. and J. Steurer, *Pain medications for acute and chronic low back pain*. *Internist (Berl)*, 2018. **59**(11): p. 1214-1223.
203. McCarthy, M., *Opioids should be last resort to treat chronic pain, says draft CDC guideline*. *BMJ*, 2015. **351**: p. h6905.
204. Fallon, M.T., *Neuropathic pain in cancer*. *Br J Anaesth*, 2013. **111**(1): p. 105-11.
205. Park, S.B., et al., *Chemotherapy-induced peripheral neurotoxicity: a critical analysis*. *CA Cancer J Clin*, 2013. **63**(6): p. 419-37.
206. Carozzi, V.A., A. Canta, and A. Chiorazzi, *Chemotherapy-induced peripheral neuropathy: What do we know about mechanisms?* *Neurosci Lett*, 2015. **596**: p. 90-107.

207. Meacham, K., et al., *Neuropathic Pain: Central vs. Peripheral Mechanisms*. *Curr Pain Headache Rep*, 2017. **21**(6): p. 28.
208. Du, X. and N. Gamper, *Potassium channels in peripheral pain pathways: expression, function and therapeutic potential*. *Curr Neuropharmacol*, 2013. **11**(6): p. 621-40.
209. Verma, P., et al., *Examining Sodium and Potassium Channel Conductances Involved in Hyperexcitability of Chemotherapy-Induced Peripheral Neuropathy: A Mathematical and Cell Culture-Based Study*. *Front Comput Neurosci*, 2020. **14**: p. 564980.
210. Tsantoulas, C. and S.B. McMahon, *Opening paths to novel analgesics: the role of potassium channels in chronic pain*. *Trends Neurosci*, 2014. **37**(3): p. 146-58.
211. Shi, D.N., et al., *MiR-183-5p Alleviates Chronic Constriction Injury-Induced Neuropathic Pain Through Inhibition of TREK-1*. *Neurochem Res*, 2018. **43**(6): p. 1143-1149.
212. Cohen, A., et al., *Pain-associated signals, acidosis and lysophosphatidic acid, modulate the neuronal K(2P)2.1 channel*. *Mol Cell Neurosci*, 2009. **40**(3): p. 382-9.
213. Morris, G.M., R. Huey, and A.J. Olson, *Using AutoDock for ligand-receptor docking*. *Curr Protoc Bioinformatics*, 2008. **Chapter 8**: p. Unit 8.14.
214. Krieger, E. and G. Vriend, *YASARA View - molecular graphics for all devices - from smartphones to workstations*. *Bioinformatics*, 2014. **30**(20): p. 2981-2.
215. Duan, Y., et al., *A point-charge force field for molecular mechanics simulations of proteins based on condensed-phase quantum mechanical calculations*. *J Comput Chem*, 2003. **24**(16): p. 1999-2012.
216. Konagurthu, A.S., et al., *MUSTANG: a multiple structural alignment algorithm*. *Proteins*, 2006. **64**(3): p. 559-74.
217. Neudert, G. and G. Klebe, *DSX: a knowledge-based scoring function for the assessment of protein-ligand complexes*. *J Chem Inf Model*, 2011. **51**(10): p. 2731-45.
218. Wang, R., L. Lai, and S. Wang, *Further development and validation of empirical scoring functions for structure-based binding affinity prediction*. *J Comput Aided Mol Des*, 2002. **16**(1): p. 11-26.
219. Sterling, T. and J.J. Irwin, *ZINC 15--Ligand Discovery for Everyone*. *J Chem Inf Model*, 2015. **55**(11): p. 2324-37.
220. Fahy, E., et al., *LIPID MAPS online tools for lipid research*. *Nucleic Acids Res*, 2007. **35**(Web Server issue): p. W606-12.
221. Altschul, S.F., *A protein alignment scoring system sensitive at all evolutionary distances*. *J Mol Evol*, 1993. **36**(3): p. 290-300.
222. Altschul, S.F., et al., *Basic local alignment search tool*. *J Mol Biol*, 1990. **215**(3): p. 403-10.
223. Altschul, S.F., et al., *Gapped BLAST and PSI-BLAST: a new generation of protein database search programs*. *Nucleic Acids Res*, 1997. **25**(17): p. 3389-402.
224. Qiu, J. and R. Elber, *SSALN: an alignment algorithm using structure-dependent substitution matrices and gap penalties learned from structurally aligned protein pairs*. *Proteins*, 2006. **62**(4): p. 881-91.
225. Hooft, R.W., et al., *Errors in protein structures*. *Nature*, 1996. **381**(6580): p. 272.
226. Hooft, R.W., et al., *The PDBFINDER database: a summary of PDB, DSSP and HSSP information with added value*. *Comput Appl Biosci*, 1996. **12**(6): p. 525-9.
227. Krieger, E., et al., *Improving physical realism, stereochemistry, and side-chain accuracy in homology modeling: Four approaches that performed well in CASP8*. *Proteins*, 2009. **77 Suppl 9**: p. 114-22.
228. Biasini, M., et al., *SWISS-MODEL: modelling protein tertiary and quaternary structure using evolutionary information*. *Nucleic Acids Res*, 2014. **42**(Web Server issue): p. W252-8.
229. Waterhouse, A., et al., *SWISS-MODEL: homology modelling of protein structures and complexes*. *Nucleic Acids Res*, 2018. **46**(W1): p. W296-W303.

230. Huang, T.T., et al., *(PS)2: protein structure prediction server version 3.0*. Nucleic Acids Res, 2015. **43**(W1): p. W338-42.
231. Chen, C.C., J.K. Hwang, and J.M. Yang, *(PS)2: protein structure prediction server*. Nucleic Acids Res, 2006. **34**(Web Server issue): p. W152-7.
232. Kelley, L.A., et al., *The Phyre2 web portal for protein modeling, prediction and analysis*. Nat Protoc, 2015. **10**(6): p. 845-58.
233. Zhang, Y., *I-TASSER server for protein 3D structure prediction*. BMC Bioinformatics, 2008. **9**: p. 40.
234. Baek, M., et al., *GalaxyHomomer: a web server for protein homo-oligomer structure prediction from a monomer sequence or structure*. Nucleic Acids Res, 2017. **45**(W1): p. W320-W324.
235. Chou, P.Y. and G.D. Fasman, *Prediction of protein conformation*. Biochemistry, 1974. **13**(2): p. 222-45.
236. Chou, P.Y. and G.D. Fasman, *Conformational parameters for amino acids in helical, beta-sheet, and random coil regions calculated from proteins*. Biochemistry, 1974. **13**(2): p. 211-22.
237. Kouza, M., et al., *The GOR Method of Protein Secondary Structure Prediction and Its Application as a Protein Aggregation Prediction Tool*. Methods Mol Biol, 2017. **1484**: p. 7-24.
238. Encinar, J.A., et al., *ADAN: a database for prediction of protein-protein interaction of modular domains mediated by linear motifs*. Bioinformatics, 2009. **25**(18): p. 2418-24.
239. Schymkowitz, J., et al., *The FoldX web server: an online force field*. Nucleic Acids Res, 2005. **33**(Web Server issue): p. W382-8.
240. Devesa, I., et al.,  *$\alpha$ CGRP is essential for algescic exocytotic mobilization of TRPV1 channels in peptidergic nociceptors*. Proc Natl Acad Sci U S A, 2014. **111**(51): p. 18345-50.
241. Mathivanan, S., et al., *Bradykinin Induces TRPV1 Exocytotic Recruitment in Peptidergic Nociceptors*. Front Pharmacol, 2016. **7**: p. 178.
242. Gunthorpe, M.J., et al., *Characterisation of a human acid-sensing ion channel (hASIC1a) endogenously expressed in HEK293 cells*. Pflugers Arch, 2001. **442**(5): p. 668-74.
243. Jiang, B., et al., *Endogenous Kv channels in human embryonic kidney (HEK-293) cells*. Mol Cell Biochem, 2002. **238**(1-2): p. 69-79.
244. Florian, L., M. François, and L. Michel, *Cloning and expression of human TRAAK, a polyunsaturated fatty acids-activated and mechano-sensitive K<sup>+</sup> channel*. 2000: FEBS Letters. p. 137-140.
245. Ertl, P., B. Rohde, and P. Selzer, *Fast calculation of molecular polar surface area as a sum of fragment-based contributions and its application to the prediction of drug transport properties*. J Med Chem, 2000. **43**(20): p. 3714-7.
246. Daina, A., O. Michielin, and V. Zoete, *iLOGP: a simple, robust, and efficient description of n-octanol/water partition coefficient for drug design using the GB/SA approach*. J Chem Inf Model, 2014. **54**(12): p. 3284-301.
247. Delaney, J.S., *ESOL: estimating aqueous solubility directly from molecular structure*. J Chem Inf Comput Sci, 2004. **44**(3): p. 1000-5.
248. Macpherson, L.J., et al., *Noxious compounds activate TRPA1 ion channels through covalent modification of cysteines*. Nature, 2007. **445**(7127): p. 541-5.
249. Lipinski, C.A., et al., *Experimental and computational approaches to estimate solubility and permeability in drug discovery and development settings*. Adv Drug Deliv Rev, 2001. **46**(1-3): p. 3-26.
250. Fletcher, S. and A.D. Hamilton, *Targeting protein-protein interactions by rational design: mimicry of protein surfaces*. J R Soc Interface, 2006. **3**(7): p. 215-33.

251. Patel, L.N., J.L. Zaro, and W.C. Shen, *Cell penetrating peptides: intracellular pathways and pharmaceutical perspectives*. Pharm Res, 2007. **24**(11): p. 1977-92.
252. Kurochkina, N. and U. Guha, *SH3 domains: modules of protein-protein interactions*. Biophys Rev, 2013. **5**(1): p. 29-39.
253. Saksela, K. and P. Permi, *SH3 domain ligand binding: What's the consensus and where's the specificity?* FEBS Lett, 2012. **586**(17): p. 2609-14.
254. Śledź, P. and A. Cafilisch, *Protein structure-based drug design: from docking to molecular dynamics*. Curr Opin Struct Biol, 2018. **48**: p. 93-102.
255. Vlieghe, P., et al., *Synthetic therapeutic peptides: science and market*. Drug Discov Today, 2010. **15**(1-2): p. 40-56.
256. Zhong, F., et al., *Artificial intelligence in drug design*. Sci China Life Sci, 2018. **61**(10): p. 1191-1204.
257. Fernández-Ballester, G., A. Fernández-Carvajal, and A. Ferrer-Montiel, *Targeting thermoTRP ion channels*. Expert Opin Ther Targets, 2020. **24**(11): p. 1079-1097.
258. Harvey, A.L., *Natural products in drug discovery*. Drug Discov Today, 2008. **13**(19-20): p. 894-901.
259. Ganesan, A., *The impact of natural products upon modern drug discovery*. Curr Opin Chem Biol, 2008. **12**(3): p. 306-17.
260. Newman, D.J. and G.M. Cragg, *Natural products as sources of new drugs over the last 25 years*. J Nat Prod, 2007. **70**(3): p. 461-77.
261. Pushpakom, S., et al., *Drug repurposing: progress, challenges and recommendations*. Nat Rev Drug Discov, 2019. **18**(1): p. 41-58.
262. Wright, P.D., et al., *Pranlukast is a novel small molecule activator of the two-pore domain potassium channel TREK2*. Biochem Biophys Res Commun, 2019. **520**(1): p. 35-40.
263. Kase, D. and K. Imoto, *The Role of HCN Channels on Membrane Excitability in the Nervous System*. J Signal Transduct, 2012. **2012**: p. 619747.
264. Shaikh, A., et al., *Acquired Fanconi syndrome after treatment with capecitabine, irinotecan, and bevacizumab*. Ann Pharmacother, 2009. **43**(7): p. 1370-3.
265. Chandar, M. and R. de Wilton Marsh, *Severe Generalized Weakness, Paralysis, and Aphasia following Administration of Irinotecan and Oxaliplatin during FOLFIRINOX Chemotherapy*. Case Rep Oncol, 2015. **8**(1): p. 138-41.
266. Baz, D.V., J.S. Bofill, and J.A. Nogueira, *Irinotecan-induced dysarthria*. J Natl Cancer Inst, 2001. **93**(18): p. 1419-20.
267. De Marco, S., et al., *Irinotecan chemotherapy associated with transient dysarthria and aphasia*. Ann Oncol, 2004. **15**(7): p. 1147-8.
268. Suessbrich, H., et al., *Blockade of HERG channels expressed in Xenopus oocytes by the histamine receptor antagonists terfenadine and astemizole*. FEBS Lett, 1996. **385**(1-2): p. 77-80.
269. Shah, R.R. and P.D. Stonier, *Repurposing old drugs in oncology: Opportunities with clinical and regulatory challenges ahead*. J Clin Pharm Ther, 2019. **44**(1): p. 6-22.
270. Wang, W.T., et al., *Terfenadine induces anti-proliferative and apoptotic activities in human hormone-refractory prostate cancer through histamine receptor-independent Mcl-1 cleavage and Bak up-regulation*. Naunyn Schmiedebergs Arch Pharmacol, 2014. **387**(1): p. 33-45.
271. Ming, Z. and C. Nordin, *Terfenadine blocks time-dependent Ca<sup>2+</sup>, Na<sup>+</sup>, and K<sup>+</sup> channels in guinea pig ventricular myocytes*. J Cardiovasc Pharmacol, 1995. **26**(5): p. 761-9.
272. Liu, S., R.B. Melchert, and R.H. Kennedy, *Inhibition of L-type Ca<sup>2+</sup> channel current in rat ventricular myocytes by terfenadine*. Circ Res, 1997. **81**(2): p. 202-10.
273. Delgado-Ramírez, M., et al., *Inhibitory effect of terfenadine on Kir2.1 and Kir2.3 channels*. Acta Pharm, 2021. **71**(2): p. 317-324.
274. Bauer, C.K. and J.R. Schwarz, *Ether-à-go-go K*. J Physiol, 2018. **596**(5): p. 769-783.

275. Babcock, J.J. and M. Li, *hERG channel function: beyond long QT*. Acta Pharmacol Sin, 2013. **34**(3): p. 329-35.
276. Faravelli, L., et al., *A HERG-like K<sup>+</sup> channel in rat F-11 DRG cell line: pharmacological identification and biophysical characterization*. J Physiol, 1996. **496** ( Pt 1): p. 13-23.
277. Ma, C., et al., *Expression of inwardly rectifying potassium channels by an inducible adenoviral vector reduced the neuronal hyperexcitability and hyperalgesia produced by chronic compression of the spinal ganglion*. Mol Pain, 2010. **6**: p. 65.
278. Hibino, H., et al., *Inwardly rectifying potassium channels: their structure, function, and physiological roles*. Physiol Rev, 2010. **90**(1): p. 291-366.
279. Chen, L., K.J. Sampson, and R.S. Kass, *Cardiac Delayed Rectifier Potassium Channels in Health and Disease*. Card Electrophysiol Clin, 2016. **8**(2): p. 307-22.
280. Serafini, M., et al., *Targeting Transient Receptor Potential Vanilloid 1 (TRPV1) Channel Softly: The Discovery of Passerini Adducts as a Topical Treatment for Inflammatory Skin Disorders*. J Med Chem, 2018. **61**(10): p. 4436-4455.
281. Shintaku, K., et al., *Activation of transient receptor potential A1 by a non-pungent capsaicin-like compound, capsiate*. Br J Pharmacol, 2012. **165**(5): p. 1476-86.
282. Macpherson, L.J., et al., *More than cool: promiscuous relationships of menthol and other sensory compounds*. Mol Cell Neurosci, 2006. **32**(4): p. 335-43.
283. Selescu, T., et al., *Camphor activates and sensitizes transient receptor potential melastatin 8 (TRPM8) to cooling and icilin*. Chem Senses, 2013. **38**(7): p. 563-75.
284. Giorgi, S., et al., *Is TRPA1 burning down TRPV1 as druggable target for the treatment of chronic pain?* Int J Mol Sci, 2019. **20**(12).
285. Eid, S.R., et al., *HC-030031, a TRPA1 selective antagonist, attenuates inflammatory- and neuropathy-induced mechanical hypersensitivity*. Mol Pain, 2008. **4**: p. 48.
286. Demartini, C., et al., *Antagonism of Transient Receptor Potential Ankyrin Type-1 Channels as a Potential Target for the Treatment of Trigeminal Neuropathic Pain: Study in an Animal Model*. Int J Mol Sci, 2018. **19**(11).
287. Yang, F., et al., *Structural mechanism underlying capsaicin binding and activation of the TRPV1 ion channel*. Nat Chem Biol, 2015. **11**(7): p. 518-524.

## AGRADECIMIENTOS

Todos los caminos tienen un principio y un final. Estar escribiendo estas palabras significa que he llegado al final de un ciclo y al principio de otro. Durante estos años he aprendido mucho sobre ciencia, pero también he abierto mi mente a nuevos horizontes y me he conocido mejor a mí misma. Ha sido un camino largo y difícil, y estar aquí y ahora ha sido posible gracias a muchas personas.

En primer lugar, quisiera agradecer a mis directores de tesis Dr. Gregorio Fernández Ballester y Dra. Isabel Devesa Giner por haberme brindado la oportunidad de realizar este trabajo con ellos y aprender de ellos, de haber confiado en mí, haber apostado por mí y por su constante apoyo, ánimo, comprensión e invitación a seguir creciendo.

En segundo lugar, quiero dar las gracias al Dr. Antonio Ferrer Montiel y Dra. Asia Fernández Carvajal por haber compartido tantísima sabiduría, por sus constantes consejos y la ayuda prestada todos estos años.

Gracias al Dr. Pierluigi Valente por haberme ofrecido la oportunidad de conocer Italia y la electrofisiología.

Estoy segura de que este periodo hubiese sido mucho más duro sin el apoyo constante de mis compañeros de laboratorio o incluso amigos. Sin duda, el padel, las cañas post-partido o los tardeos pre-Covid en vuestra compañía, se echarán de menos.

Laura ... nunca sospeché que la bajita, morenita de la 2ª promoción de Biotecnología a la que solo conocía de cara iba a pasar tantas horas conmigo, convirtiendo el “despachito” en mi segunda casa, donde poder llorar las penas y celebrar las glorias. Gracias por haberme escuchado innumerables veces, gracias por tus consejos de hermana mayor, gracias por tu ayuda constante, gracias por las risas, gracias por todo.

Ali, aunque llegaste un poco más tarde, te hiciste un hueco enseguida con tu alegría, sonrisa eterna e inocencia propia de una niña.

Gracias también a ti Simo y a ti David A.. Los desayunos en el “García” y los tapeos en el “Niza” no se olvidarán.

Sara, tampoco me olvido de ti.

Gema y Cloti, siempre he estado muy a gusto con vosotras, ¡sois unos amores!

José, Jorge, David C., Eva, gracias por todo.

La otra parte de la familia, Nuria, Vero, Moni, Tania, María José, Ana S., Ana E., gracias por haberme adoptado.

A los antiguos ferrerines que ya no estáis y con los que coincidí fugazmente, Roberto de la Torre, Sakthi, Maria Grazia y Maite, gracias.

Clara, gracias por tu apoyo al inicio de este camino.

Gracias también a la familia Warriors, soltar las tensiones del día a día entre risas, al lado de grandes compañeros y aprendiendo de ti Sifu, es siempre un placer y un honor.

Damián, estas palabras no compensan ni por asomo mi agradecimiento hacia ti, por todo tu amor, apoyo y comprensión durante estos años. Podría escribir otra tesis con todo lo que me has enseñado. Solo puedo dar las gracias al Universo, al destino o lo que sea, llámalo "X" por haberte puesto en mi camino en ese momento tan decisivo.

И на последно място, но не за това по-маловажно, ви благодаря на вас, мамо и татко. Тези последни редове са за вас, за да завършите този цикъл, така както го започнахте, защото без вас аз нямаше да стоя тук където съм сега. Благодаря ви за годините на подкрепа и разбиране. Обичам ви.



# ANNEX





OPEN

## A capsaicinoid-based soft drug, AG1529, for attenuating TRPV1-mediated histaminergic and inflammatory sensory neuron excitability

Magdalena Nikolaeva-Koleva<sup>1,2,6</sup>, Laura Butron<sup>1,6</sup>, Sara González-Rodríguez<sup>1,5</sup>, Isabel Devesa<sup>2</sup>, Pierluigi Valente<sup>3</sup>, Marta Serafini<sup>4</sup>, Armando A. Genazzani<sup>4</sup>, Tracey Pirali<sup>4</sup>, Gregorio Fernández Ballester<sup>1</sup>, Asia Fernández-Carvajal<sup>1</sup> & Antonio Ferrer-Montiel<sup>1</sup>✉

TRPV1, a member of the transient receptor potential (TRP) family, is a nonselective calcium permeable ion channel gated by physical and chemical stimuli. In the skin, TRPV1 plays an important role in neurogenic inflammation, pain and pruritus associated to many dermatological diseases. Consequently, TRPV1 modulators could represent pharmacological tools to respond to important patient needs that still represent an unmet medical demand. Previously, we reported the design of capsaicinoid-based molecules that undergo dermal deactivation (soft drugs), thus preventing their long-term dermal accumulation. Here, we investigated the pharmacological properties of the lead antagonist, 2-((4-hydroxy-2-iodo-5-methoxybenzyl) amino)-2-oxoethyl dodecanoate (AG1529), on heterologously expressed human TRPV1 (hTRPV1), on nociceptor excitability and on an in vivo model of acute pruritus. We report that AG1529 competitively blocked capsaicin-evoked activation of hTRPV1 with micromolar potency, moderately affected pH-induced gating, and did not alter voltage- and heat-mediated responses. AG1529 displays modest receptor selectivity as it mildly blocked recombinant hTRPA1 and hTRPM8 channels. In primary cultures of rat dorsal root ganglion (DRG) neurons, AG1529 potently reduced capsaicin-evoked neuronal firing. AG1529 exhibited lower potency on pH-evoked TRPV1 firing, and TRPA1-elicited nociceptor excitability. Furthermore, AG1529 abolished histaminergic and inflammation mediated TRPV1 sensitization in primary cultures of DRG neurons. Noteworthy, dermal wiping of AG1529, either in an acetone-based formulation or in an anhydrous ointment, dose-dependently attenuated acute histaminergic itch in a rodent model. This cutaneous anti-pruritic effect was devoid of the normal nocifensive action evoked by the burning sensation of capsaicin. Taken together, these preclinical results unveil the mode of action of AG1529 on TRPV1 channels and substantiate the tenet that this capsaicinoid-based soft drug is a promising candidate for drug development as a topical anti-pruritic and anti-inflammatory medication.

Transient receptor potential vanilloid channel (TRPV1) is a thermally activated ion channel that plays a pivotal role in thermosensation, particularly in the detection of environmental noxious temperatures ( $> 42\text{ }^{\circ}\text{C}$ )<sup>1,2</sup>. Apart from heat, TRPV1 channels are also activated by molecules containing a vanilloid group, endovanilloid/endo-cannabinoid molecules such as anandamide, extracellular acidic pH and voltage depolarization<sup>3–9</sup>. Although TRPV1 is highly expressed in the neuronal system, it is also widely present in the skin, mainly in the peripheral terminals of nociceptors, keratinocytes, sebocytes and immune cells<sup>10–15</sup>. Cutaneous TRPV1 channels have been

<sup>1</sup>Instituto de Investigación, Desarrollo e Innovación en Biotecnología Sanitaria de Elche (IDiBE), Universitas Miguel Hernández, 03202 Elche, Spain. <sup>2</sup>AntalGenics SL, Ed. Quorum III, UMH Scientific Park, 03202 Elche, Spain. <sup>3</sup>Department of Experimental Medicine, Section of Physiology, University of Genova, Viale Benedetto XV 3, 16132 Genoa, Italy. <sup>4</sup>Dipartimento Di Scienze del Farmaco, Università Degli Studi del Piemonte Orientale, 28100 Novara, Italy. <sup>5</sup>Present address: Laboratorio de Farmacología, Facultad de Medicina, Instituto Universitario de Oncología del Principado de Asturias (IUOPA), Universidad de Oviedo, 33006 Oviedo, Spain. <sup>6</sup>These authors contributed equally: Magdalena Nikolaeva-Koleva and Laura Butron. ✉email: aferrer@umh.es

primarily involved in temperature sensing, modulating skin barrier function, and in neurogenic inflammation, pain and pruritus<sup>13,16</sup>.

Notably, cutaneous TRPV1 channels are end targets for inflammatory and pruritogenic agents<sup>17–19</sup>. These agents activate intracellular signalling pathways that converge onto TRPV1, increasing its gating<sup>20</sup> and/or promoting the surface expression of channels<sup>21</sup>. Algescically-sensitized TRPV1 channels notably increase the excitability of nociceptors that lead to pain and pruritic signals<sup>22</sup>. Consequently, cumulative evidence indicates that the TRPV1 channel is a valid pharmacological target to treat peripheral inflammatory pain as well as pruritus<sup>23</sup>. Indeed, the desensitizing action of capsaicin on TRPV1 has been long used clinically to treat cutaneous inflammatory conditions, including inflammation, pain and pruritus<sup>24</sup>. However, despite its good therapeutic action, the burning sensation associated to capsaicin, due to its agonistic activity, decreases patient adherence to the treatment. In addition, some reports suggest that its long-term dermal accumulation due to its poor elimination may induce dermal carcinogenesis that could be potentiated by UV exposure<sup>25,26</sup>. Thus, there is a need to develop TRPV1 modulators that, by preserving the therapeutic efficacy of the vanilloid molecule, eliminate the burning sensation and do not accumulate in the skin. Accordingly, several potent TRPV1 antagonists have been developed in recent years and tested in animal models and clinical trials<sup>27</sup>. Unfortunately, hyperthermia, due to the systemic absorption of the antagonists, has prevented many of these compounds to reaching the clinic<sup>28</sup>. Nonetheless, there are modulators, such as N-[(1R)-1-[3,5-difluoro-4-[(methylsulfonyl)amino]phenyl]ethyl]-3-[2-propyl-6-(trifluoromethyl)-3-pyridinyl]-, (2E)- (PAC-14028, Asivatrep), that have shown anti-inflammatory and anti-pruritic activities in phase II clinical trials, displaying an acceptable pharmacological profile<sup>29,30</sup>.

To increase the armamentarium of TRPV1 antagonists with enhanced therapeutic index, we previously introduced the concept of soft drugs to the capsaicinoid family, i.e. drugs that suffer dermal and systemic deactivation after exerting their activity<sup>31</sup>. Thus, capsaicinoid-based soft drugs do not show any increased risk associated with skin accumulation and any side effect related to systemic exposure. We designed TRPV1 antagonists that blocked the rodent TRPV1 with micromolar potency and were sensitive to deactivation by dermal esterases<sup>31</sup>. Our capsaicinoid antagonists preserve the pharmacological scaffold of the vanilloid group, but are devoid of the burning sensation associated with capsaicin. Compound AG1529 was selected as a promising candidate for further development due to its *in vivo* therapeutic activity in animal models of inflammatory pain and pruritus<sup>31</sup>. Here, we further characterize the activity of AG1529 and show that this capsaicinoid blocks the human TRPV1 ortholog (hTRPV1) with micromolar potency. Our data suggest that AG1529 acts as a competitive capsaicin antagonist. This compound modestly blocks pH-evoked hTRPV1 gating but not voltage and temperature activation. It shows modest receptor selectivity as it moderately blocks recombinant hTRPA1 and hTRPM8 channels. Furthermore, AG1529 reduces capsaicin-induced sensory neuron excitability, and attenuates histamine- and inflammatory-sensitization of TRPV1 in primary DRG cultures. Notably, a dermal formulation of AG1529 reduces the itch produced by local injection of histamine in rats. Taken together, our preclinical results suggest that AG1529 is a good candidate for development as an anti-inflammatory and anti-pruritic drug associated to cutaneous disorders.

## Results

**AG1529 reversibly blocks hTRPV1 with micromolar potency.** To assess the therapeutic potential of AG1529, we tested its inhibitory activity on recombinantly expressed hTRPV1. As depicted in Fig. 1A, capsaicin-evoked inward currents were reduced  $\geq 60\%$  by the concomitant administration of  $1\ \mu\text{M}$  AG1529 to HEK293 cells expressing hTRPV1. A dose–response curve revealed an  $\text{IC}_{50}$  of  $0.9 \pm 0.5\ \mu\text{M}$  ( $n = 32$ ) and a Hill coefficient  $n_{\text{H}} = 0.8 \pm 0.4$  for AG1529 blocking hTRPV1 channel activity (Fig. 1B). Note that we could only reach 78% blockade efficacy due to the water insolubility of AG1529 at  $> 30\ \mu\text{M}$ . Higher compound concentrations required the use of high DMSO ( $> 1\%$ ) that affected the activity measurements.

We next analyzed the effect of AG1529 on the capsaicin potency activating hTRPV1 channels. For this experiment, we compared the capsaicin potency activating hTRPV1 in the absence and presence of  $1\ \mu\text{M}$  of AG1529 that corresponds to its  $\text{IC}_{50}$  value. At this AG1529 concentration, sufficient capsaicin-evoked current remains to be reliably quantified. Figure 1C shows that the capsaicin dose–response for hTRPV1 activation was significantly right-shifted to higher agonist concentrations in the presence of  $1\ \mu\text{M}$  AG1529 without affecting the capsaicin efficacy. Fitting the experimental data to a Michaelis–Menten isotherm curve revealed a shift of the vanilloid  $\text{EC}_{50}$  from  $0.28 \pm 0.03\ \mu\text{M}$  to  $0.9 \pm 0.1\ \mu\text{M}$  (i.e. threefold increase,  $p < 0.0001$ , unpaired, two-tail, t-Student,  $n = 29$ ), and a decrease of the agonist Hill coefficient ( $n_{\text{H}}$ ) from  $1.3 \pm 0.2$  to  $1.0 \pm 0.1$ ,  $p < 0.0001$ , unpaired, two-tail t-Student). This displacement of the capsaicin potency ( $\text{EC}_{50}$ ) activating TRPV1 to a higher vanilloid concentration in the presence of AG1529 is consistent with a competitive inhibitory mechanism.

To further evaluate the activity of AG1529, we next investigated if its TRPV1 inhibitory activity was reversible. For this experiment, we used a paradigm consisting on two capsaicin pulses interspersed by a washing period (Fig. 1D). We quantified the ratio P2/P1 as an indicator of capsaicin response recovery. Compound AG1529 at  $1\ \mu\text{M}$  was perfused during the first agonist pulse to block 50% of the ionic current (Fig. 1D, bottom panel). As depicted in panel D (top traces), repeated application of capsaicin desensitized hTRPV1 channels, as evidenced by the lower percentage of current activated by the second (P2) capsaicin pulse (Fig. 1E, P2/P1 =  $0.81 \pm 0.01$ ,  $n = 4$ ). In contrast, the same paradigm applied to cells that were exposed to  $1\ \mu\text{M}$  AG1529 during the first capsaicin pulse, resulted in an increment of the second capsaicin response (Fig. 1D, bottom trace; and Fig. 1E; P2/P1 =  $1.30 \pm 0.09$  ( $n = 5$ ),  $p = 0.0027$ , AG1529 vs. control, unpaired, two-tail, t-student). These data are consistent with: (i) a reversible blockade of hTRPV1 by AG1529; and, (ii) a partial inhibition of capsaicin-induced TRPV1 tachyphylaxis by AG1529. Taken together, these findings indicate that AG1529 is a reversible blocker, and further suggest that it acts as a competitive capsaicin antagonist of hTRPV1.

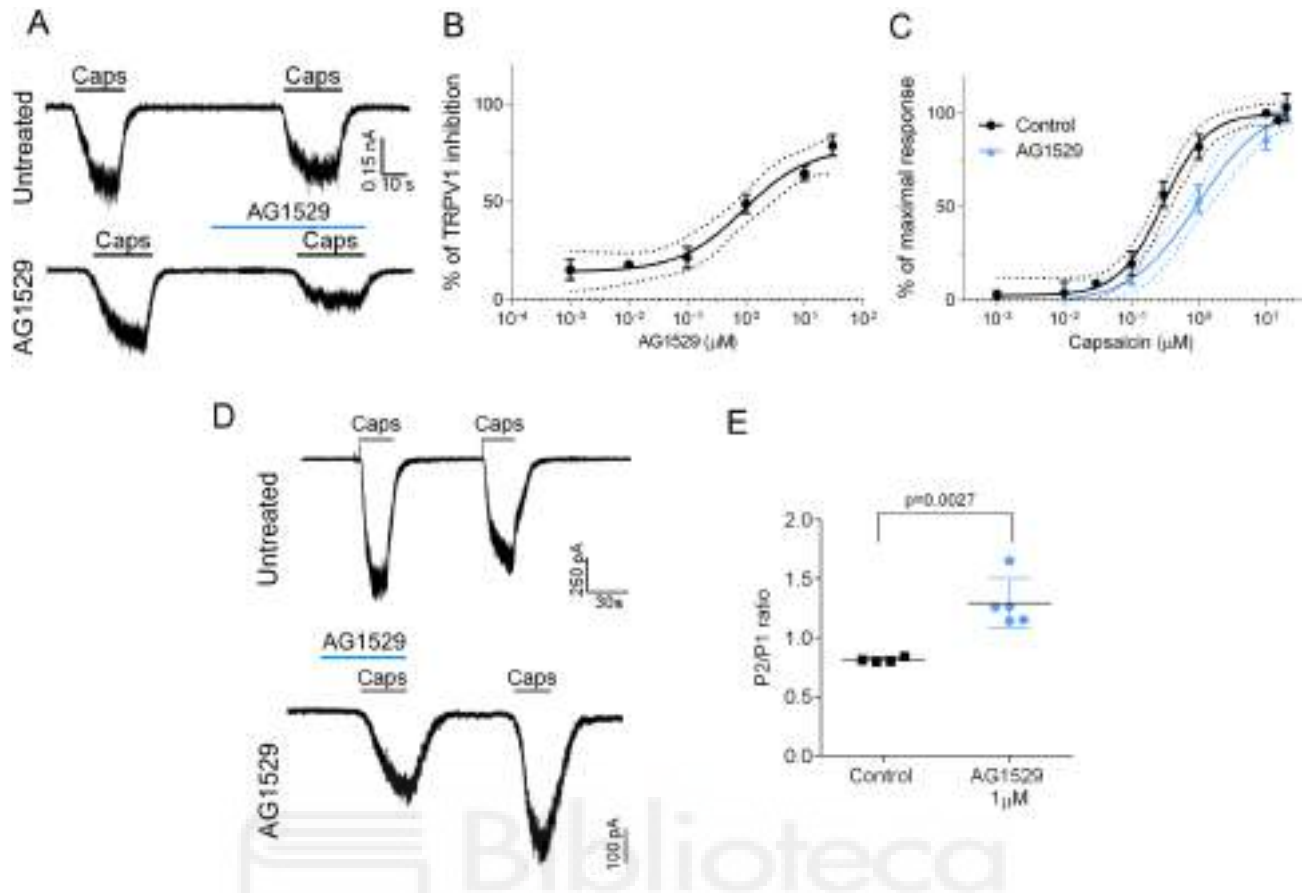


**Figure 1.** AG1529 reversibly blocks capsaicin activation of hTRPV1. Electrophysiological evaluation of AG1529 on heterologously expressed hTRPV1 channel. **(A)** Representative capsaicin-evoked hTRPV1 current recorded at a holding potential of  $-60$  mV for: (i) control condition (Untreated cells), where cells were exposed to two capsaicin pulses ( $0.5$   $\mu\text{M}$ ), interspersed by a washing period; and, (ii) Treated condition (AG1529 cells), where cells were exposed to a capsaicin pulse ( $0.5$   $\mu\text{M}$ ), and after a washing period, cells were exposed to  $1$   $\mu\text{M}$  AG1529 for  $30$  s before the second  $0.5$   $\mu\text{M}$  capsaicin pulse. The percentage of TRPV1 inhibition was calculated as: (% inhibition) =  $[1 - \{(I_{\text{cap1}} - I_{\text{cap2}})_{\text{AG1529}} / (I_{\text{cap1}} - I_{\text{cap2}})_{\text{Control}}\}] \times 100$ ;  $(I_{\text{cap1}} - I_{\text{cap2}})_{\text{Control}}$  accounts for the extend of TRPV1-induced desensitization by capsaicin (control). **(B)** Dose-response curve of AG1529 were fitted to a Michaelis–Menten Isotherm. The best fit provided an  $\text{IC}_{50}$  value of  $0.92$  (95% CI  $0.28$ – $3.01$ )  $\mu\text{M}$  and Hill coefficient of  $n_{\text{H}}$   $1.31$  (95% CI  $0.81$ – $1.82$ ) ( $n = 32$ ). **(C)** Capsaicin dose response in the absence (black) and presence of AG1549 (blue). Data were fitted to a Michaelis–Menten Isotherm. The best fitted values for capsaicin  $\text{EC}_{50}$  value was  $0.29$  (95% CI  $0.20$ – $0.35$ )  $\mu\text{M}$  ( $n = 29$ ) in the absence of  $1$   $\mu\text{M}$  AG1529 and  $0.98$  (95% CI  $0.6$ – $1.13$ )  $\mu\text{M}$  in its presence (blue curve,  $n = 21$ ). Hill coefficient in the absence of AG1529 was  $1.3$  ( $0.9$ – $1.6$ ) and in its presence was  $1.00$  (95% CI  $0.7$ – $1.2$ ). **(D)** Representative repetitive capsaicin-elicited hTRPV1 currents recordings at  $-60$  mV holding potential in the absence (Untreated cells) and presence of  $1$   $\mu\text{M}$  AG1529 before the first vanilloid pulse (AG1529). **(E)** P2/P1 ratio denoting TRPV1 current evoked by each  $0.5$   $\mu\text{M}$  capsaicin pulse, normalized to first vanilloid pulse, in the absence (control,  $n = 4$ ) and the presence of  $1$   $\mu\text{M}$  AG1529 ( $n = 5$ ) before the first capsaicin pulse. Horizontal lines denote the duration of compound pulse. All data are expressed as mean  $\pm$  SEM. Data was analysed using an unpaired, two-tail Student's t-test. p-value is indicated.

**AG1529 modestly affects other modalities of hTRPV1 gating.** Next, we investigated whether AG1529 also inhibited hTRPV1 activity triggered by other activating stimuli, such as voltage, temperature ( $43$   $^{\circ}\text{C}$ ) and acidic pH (pH  $5.5$ ). Figure 2A illustrates the effect of AG1529 on voltage-induced activation of hTRPV1 gating at  $22$   $^{\circ}\text{C}$ . Although at room temperature TRPV1 channels display a low sensitivity to voltage stimulation, they can be opened at depolarized voltages  $\geq 50$  mV (Fig. 2A), giving rise to outward currents. Voltage gating of hTRPV1 was not significantly altered by the presence of  $1$   $\mu\text{M}$  AG1529 (Fig. 2B). The current density-to-voltage relationship depicts a non-significant inhibitory effect, barely discernible at potentials  $> 100$  mV (Fig. 2B). A conductance-to-voltage relationship further indicates a lack of effect of AG1529 on hTRPV1 voltage-evoked currents (Fig. 2C).

To study the effect on temperature activation, we recorded I–V curves at  $43$   $^{\circ}\text{C}$  in the absence and presence of  $10$   $\mu\text{M}$  AG1529. We increased the compound concentration considering the lack of effect seen at  $1$   $\mu\text{M}$ . As controls, we used the well-known TRPV1 antagonists *N*-[2-(4-Chlorophenyl)ethyl]-7,8-dihydroxy-1,3,4,5-tetrahydro-2*H*-2-benzazepine-2-carbothioamide (Capsazepine (CPZ),  $10$   $\mu\text{M}$ ) and 4-(3-Chloro-2-pyridinyl)-*N*-[4-(1,1-dimethylethyl)phenyl]-1-piperazinecarboxamide (BCTC,  $1$  nM). Representatives ramps of currents

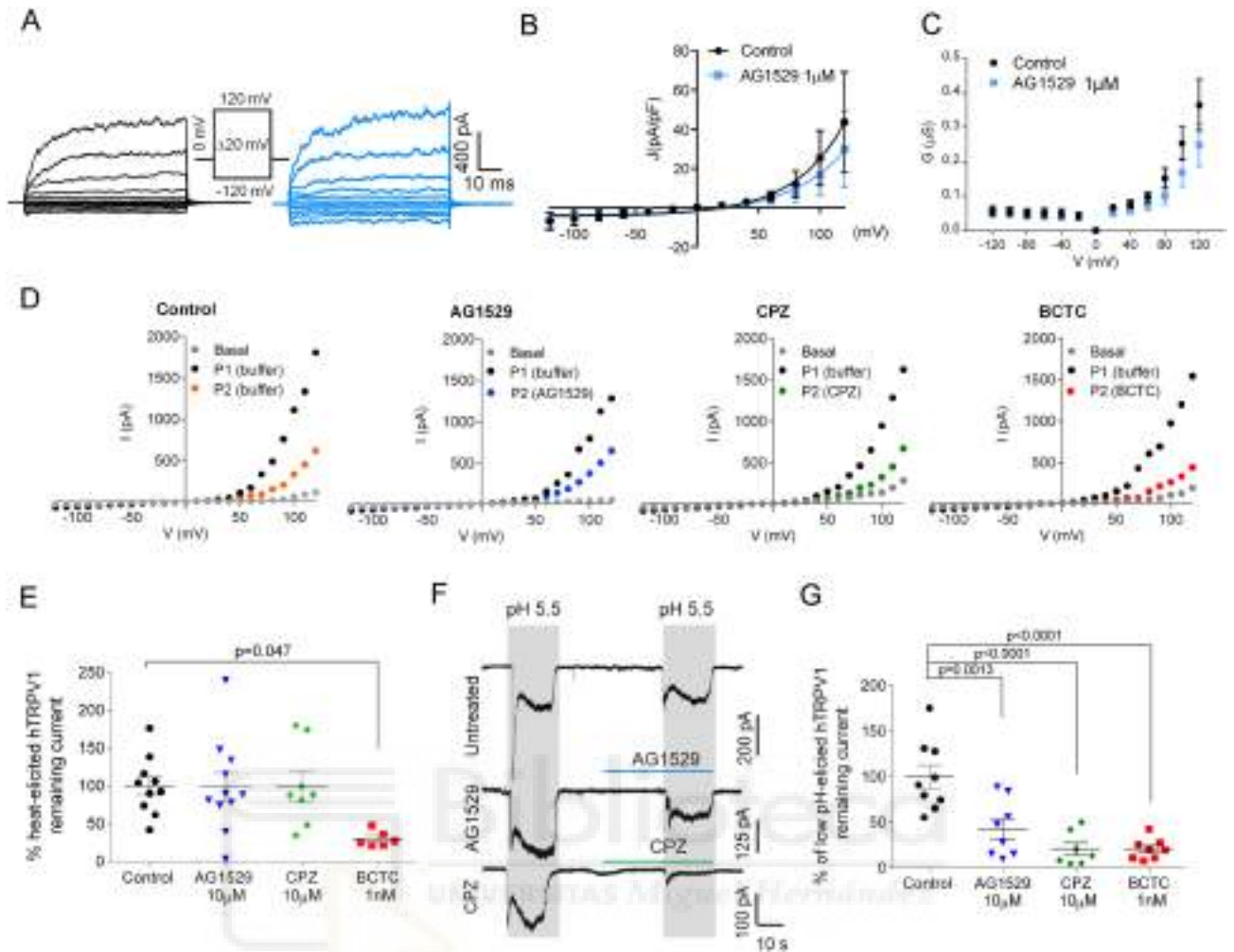


**Figure 2.** AG1529 modestly affects pH, voltage and heat activation. (A) Representative hTRPV1 current recordings elicited by voltage steps protocol from  $-120$  mV to  $120$  mV in  $100$  ms steps of  $20$  mV from a holding potential of  $0$  mV. Black traces represent currents evoked in the absence of AG1529, and blue traces in the presence of  $1 \mu\text{M}$  AG1529. (B) Current density to voltage relationship for ionic currents in the absence ( $n = 8$ ) and presence of the antagonist ( $n = 8$ ). (C) Conductance to voltage relationship for the ionic currents in the absence and presence of the antagonist. Conductance values were estimated from the current density values, using as  $V_x$  the x-intercept of the ionic current. (D) Representative I-V relationships of hTRPV1 ionic currents at  $43^\circ\text{C}$  in the absence (control) and presence of  $10 \mu\text{M}$  AG1529 ( $n = 11$ ) or  $10 \mu\text{M}$  capsazepine (CPZ,  $n = 7$ ) or  $1$  nM BCTC ( $n = 6$ ). Basal, denotes the ionic currents activated at  $37^\circ\text{C}$ ; P1 and P2, the ionic currents evoked at  $43^\circ\text{C}$  in the absence and presence of the compounds, respectively. For control conditions, P2 was evoked in the absence of compounds (buffer) denoting the desensitization induced by heat and voltage. Ionic currents were recorded with a voltage ramp protocol from  $-120$  mV to  $120$  mV in  $300$  ms. Compounds were applied at  $34^\circ\text{C}$  during  $30$  s before the second temperature increase to  $43^\circ\text{C}$ . (E) Normalized voltage-evoked ionic current at  $43^\circ\text{C}$  and  $+120$  mV, in the absence (control) and presence of the antagonists. Remaining TRPV1 current after P2 (desensitization) was used for normalization. Data are expressed as mean  $\pm$  SEM, and were analysed using the One-Way Anova ( $F(3,31) = 3.5$ ,  $p = 0.0269$ ) followed by the Bonferroni's post-hoc test, p-value for statistical difference is indicated. (F) Representative acid pH-elicited hTRPV1 ionic currents evoked by two pH  $5.5$  pulses in control cells (Untreated), and cells exposed to  $10 \mu\text{M}$  AG1529 (AG1529) or  $10 \mu\text{M}$  capsazepine (CPZ) for  $30$  s before the second pH pulse. Amiloride ( $50 \mu\text{M}$ ) was used in all buffers to block endogenous ASIC channels expressed by cells. Currents were elicited at a holding  $V = -60$  mV. (G) Normalized hTRPV1 pH-evoked inward currents elicited for control ( $n = 9$ ),  $10 \mu\text{M}$  AG1529 ( $n = 8$ ),  $10 \mu\text{M}$  capsazepine ( $n = 7$ ) and  $1$  nM BCTC ( $n = 8$ ). Normalized responses were estimated as  $(I_{\text{pH}2}/I_{\text{pH}1}) \times 100$ . Grey rectangles denote the duration of the pH pulses and horizontal lines the duration of the antagonists pulses. All data are expressed as mean  $\pm$  SEM. Data were analysed using the One-Way Anova ( $F(3,28) = 15.5$ ,  $p < 0.0001$ ) followed by the Bonferroni's post-hoc test, p-values for statistical difference are indicated.

evoked at 43 °C are shown in Fig. 2D. As seen, in control cells voltage ramps activated large ionic outward currents (P1) that partially desensitized when a second ramp was recorded 30 s later (P2). Similar recordings were obtained when the antagonists were present during the second voltage ramp (Fig. 2D). Quantitation of the ionic current evoked at 43 °C and +120 mV in the absence and presence of the compounds reveals that only BCTC at 1 nM significantly blocked the evoked currents (Fig. 2E,  $F(3,31) = 3.5$ ,  $p = 0.027$ , and  $p = 0.0473$  for control vs. BCTC, Bonferroni's post-hoc test). Note that AG1529 and capsazepine were both inactive.

Last, we evaluated whether AG1529 affected hTRPV1 gating evoked by acidic extracellular pH. For this experiment, we elicited ionic currents in hTRPV1-HEK293 cells with two pulses of extracellular buffer at pH 5.5, interspersed by a washing step (Fig. 2F). pH-activated ionic currents displayed a fast inactivating component due to activation of ASIC channels, followed by a stationary phase that corresponds to hTRPV1 responses (Fig. 2F). The fast component was blocked by 50  $\mu\text{M}$  amiloride (Fig. 2F). Figure 2F shows that AG1529 and capsazepine significantly reduced the pH-gated ionic currents. Quantitation of this inhibitory activity reveals that 10  $\mu\text{M}$  AG1529 reduced by 50% pH-activated ionic currents, akin to 10  $\mu\text{M}$  capsazepine and 1 nM BCTC (Fig. 2G,  $F(3,28) = 15.50$ ,  $p < 0.0001$ ;  $p = 0.0013$  AG1529 vs. control; and  $p < 0.0001$  CPZ and BCTC vs. control, Bonferroni's post-hoc test). No statistical differences were observed between the AG1529 and CPZ blocking pH-evoked activity. Thus, our results indicate that AG1529 moderately blocks pH-induced hTRPV1 activity, without significantly affecting voltage- and heat-elicited responses.

**AG1529 moderately modulates TRPM8 and TRPA1 channel activity.** ThermoTRP cross-interaction has been reported for modulators of TRPV1, TRPM8 and TRPA1 channels<sup>32,33</sup>. Consequently, we evaluated the effect of AG1529 on recombinantly expressed hTRPM8 and hTRPA1 channels. As exhibited in Fig. 3A, 10  $\mu\text{M}$  AG1529 reduced menthol-evoked ionic currents, although to a lower extent than the reference TRPM8 blocker *N*-(3-Aminopropyl)-2-[(3-methylphenyl)methoxy]-*N*-(2-thienylmethyl) benzamide hydrochloride (AMTB) at 10  $\mu\text{M}$ . Quantitation of this inhibitory activity shows that AG1529 blocked TRPM8 channel activity by  $\approx 40\%$  (Fig. 3B), which is a significantly lower efficacy than that of AMTB ( $F(2,32) = 37.57$ ,  $p < 0.0001$ , with  $p = 0.0043$  for AG1529 vs control and  $p < 0.00001$  for AG1529 vs AMTB, Bonferroni's post-hoc test).

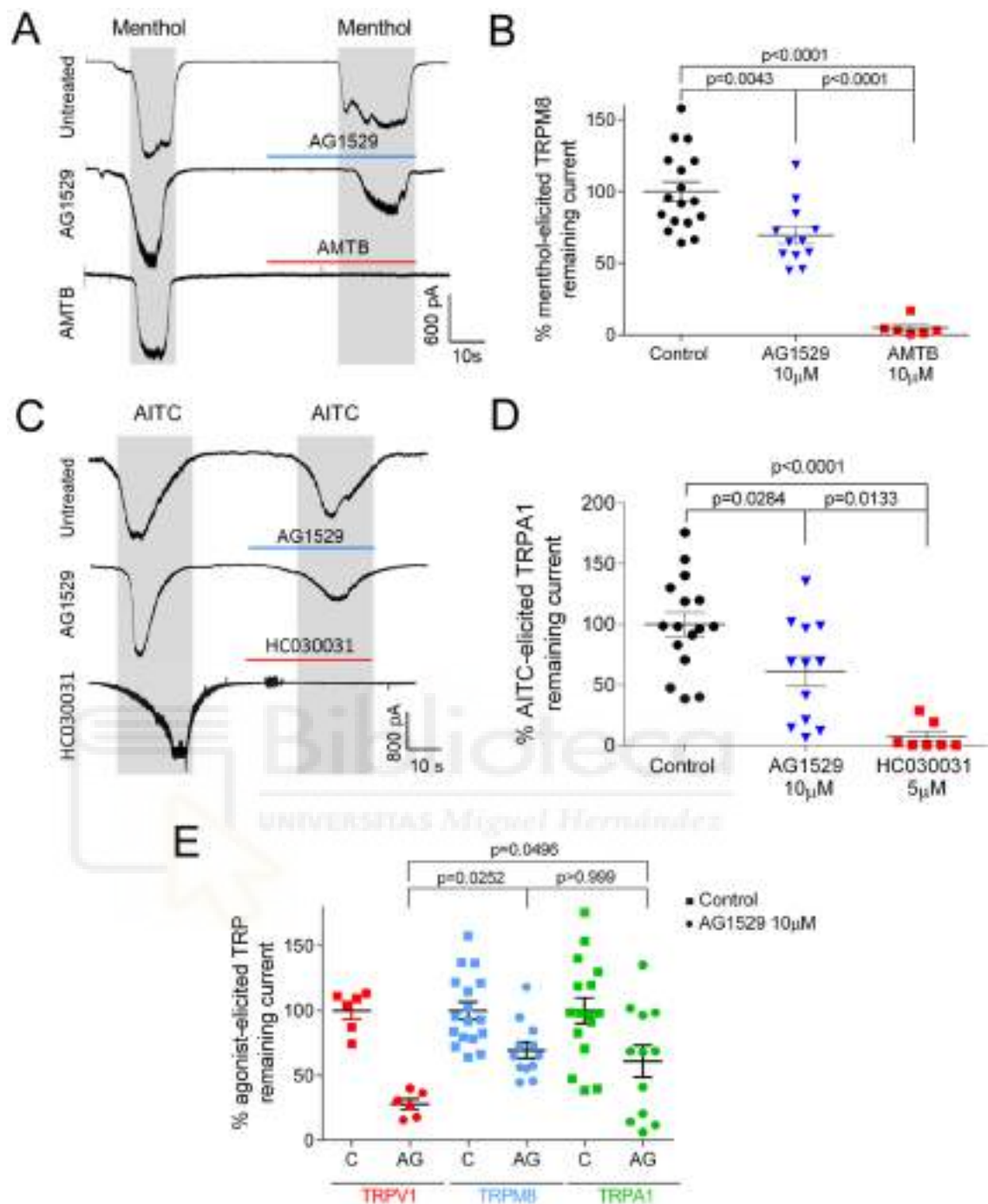
To investigate if AG1529 affected TRPA1-mediated currents, we used allyl isothiocyanate (AITC) as TRPA1 agonist (Fig. 3C). As depicted in Fig. 3C, 10  $\mu\text{M}$  AG1529 inhibited  $\approx 40\%$  of AITC-evoked ionic currents, indicating an effect on hTRPA1 channels (Fig. 3D;  $F(2,32) = 15.67$ ,  $p < 0.0001$ ; control vs. AG1529,  $p = 0.0284$ , Bonferroni's post-hoc test). In contrast, 5  $\mu\text{M}$  of 1,2,3,6-Tetrahydro-1,3-dimethyl-*N*-[4-(1-methylethyl)phenyl]-2,6-dioxo-7H-purine-7-acetamide, 2-(1,3-Dimethyl-2,6-dioxo-1,2,3,6-tetrahydro-7H-purine-7-yl)-*N*-(4-isopropylphenyl)acetamide (HC030031), a reference TRPA1 antagonist, completely abrogated AITC-evoked ionic currents (Fig. 3D; Control vs. HC030031,  $p < 0.0001$ , Bonferroni's post-hoc test). The potency of AG1529 blocking TRPA1 was also significantly lower than that of HC030031 (Fig. 3D; AG1529 vs. HC030031,  $p = 0.0133$ , Bonferroni's post-hoc test).

An statistical comparison of 10  $\mu\text{M}$  AG1529 efficacy blocking the three human thermoTRPs revealed a significantly lower inhibition of TRPM8 and TRPA1 channels as compared with hTRPV1 (Fig. 3E,  $F(2,27) = 4.434$ ,  $p = 0.0216$ ; TRPV1 vs. TRPM8,  $p < 0.0252$  and TRPV1 vs. TRPA1,  $p < 0.0496$ , Bonferroni's multiple comparison post-hoc test). Collectively, these data indicate that AG1529 preferentially, but not selectively, interacts on recombinant hTRPV1 channels, exhibiting a milder inhibitory effect on recombinant hTRPM8 and hTRPA1 channels.

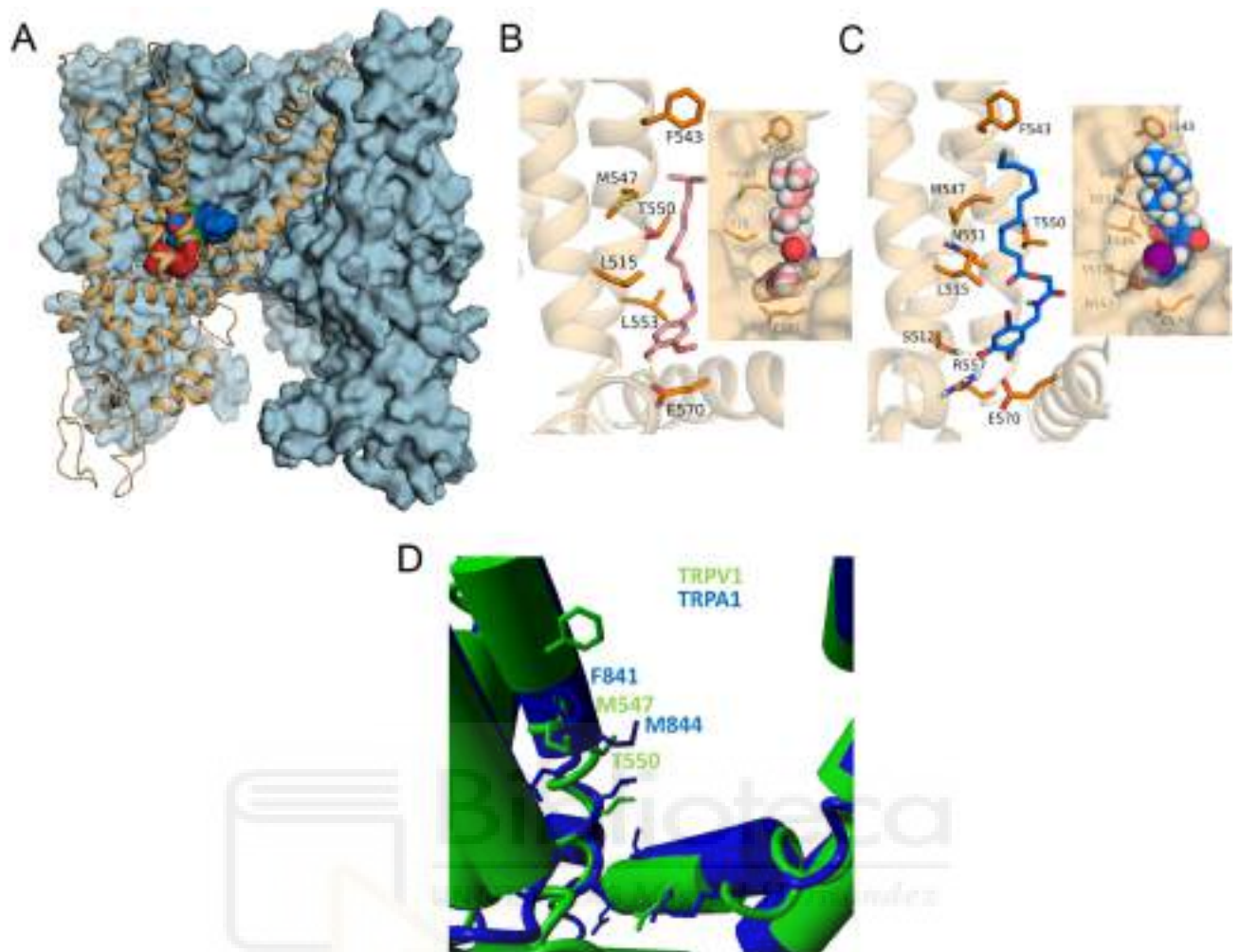
**AG1529 interacts with the vanilloid binding site in TRPV1.** The results on recombinant hTRPV1 suggest that AG1529 may act as a competitive capsaicin antagonist. To further support this tenet, we used molecular modelling to evaluate the putative interaction of AG1529 with the capsaicin binding site in TRPV1 (Fig. 4). We used the TRPV1 atomic structure in its open and closed states and dock AG1529 into the vanilloid binding site to explore the energetics of compound binding and compare it with capsaicin and capsazepine (Fig. 4). The binding energy (mean  $\pm$  SD) of AG1529 was  $3.7 \pm 1.3$  kcal/mol ( $n = 116$  trials), which was comparable to those of capsaicin  $6.4 \pm 0.6$  kcal/mol ( $n = 212$  trials) or capsazepine  $9.3 \pm 1.1$  kcal/mol ( $n = 158$  trials). No differences in terms of best binding site between open and resting states were observed. Inspection of the interactions reveals that, akin to capsaicin, AG1529 may adopt a tail-up, head-down conformation displaying the aliphatic tail Van der Waals interactions with the same key residues, i.e. L515, F543, M547, T550 and L553 in S3 and S4 transmembrane segments. Hydrogen bonds are formed between the vanillyl head and S512 or E570 residues which grant some specificity to the interaction. A similar docking strategy with TRPA1 showed that the equivalent binding pocket is sterically disturbed due to the central orientation of the M844 side chain (M547 in TRPV1; Fig. 4D), affecting the AG1529 binding affinity. This is in accordance with the moderate potency of AG1529 inhibiting TRPA1 activity. Thus, our modelling approach further suggests that AG1529 is a competitive TRPV1 antagonist that binds to the capsaicin binding site to block channel gating.

**AG1529 blocks capsaicin-evoked neuronal firing.** Next, we investigated the effect of AG1529 on capsaicin-evoked action potentials (AP) in primary cultures of rat DRG sensory neurons. Under current-clamp, small sensory neurons exposed to 0.5  $\mu\text{M}$  capsaicin triggered bursts of APs (Fig. 5A, top trace). The ratio of electrical activity evoked by 2 short capsaicin pulses was variable (Fig. 5B), likely reflecting the phenotypic heterogeneity of DRG sensory neurons. Pre-exposure of small sensory neurons under study to 1  $\mu\text{M}$  AG1529 before the second capsaicin pulse produced a reduction in AP firing (Fig. 5A). Evaluation of the AP frequency ratio between the first (P1) and second (P2) capsaicin pulses reveal a significant 50% reduction in AP firing by 1  $\mu\text{M}$  AG1529 (Fig. 5B;  $p = 0.032$ , unpaired, two-tail, *t*-Student,  $n = 12$ ).

To ascertain whether this putative effect on neuronal excitability was due to an off-target blockade of  $\text{Na}^+$  and  $\text{K}^+$  voltage-gated channels, we performed voltage-clamp experiments to investigate whether AG1529 affected



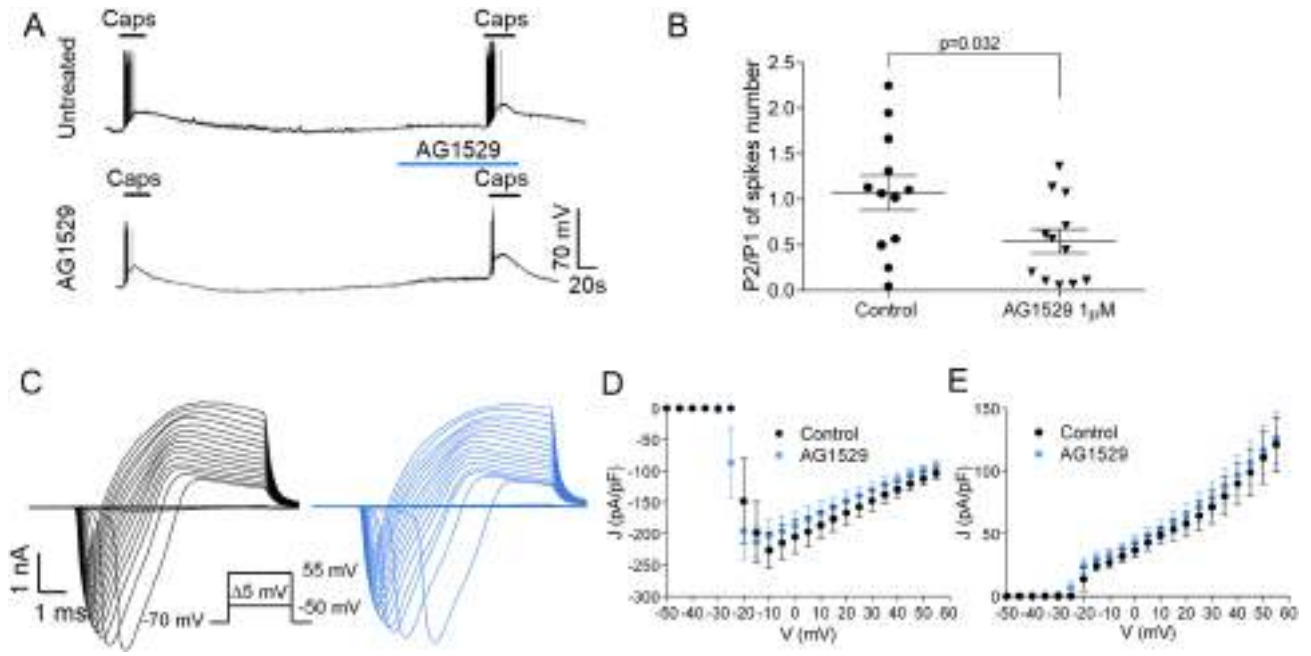
**Figure 3.** AG1529 marginally inhibits TRPM8 and TRPA1 receptors. (A) Representative menthol (100  $\mu\text{M}$ )-elicited hTRPM8 inward currents recorded at a holding potential of  $-60$  mV, for control cells (Untreated) exposed to two menthol pulses; and, for cells treated with 10  $\mu\text{M}$  AG1529 (AG1529) or 10  $\mu\text{M}$  AMTB (AMTB) for 30 s before the second menthol pulse. (B) Percentage of menthol-elicited TRPM8 remaining ionic current with respect to the first menthol pulse. Normalized responses were estimated as  $(I_{\text{Menthol}2}/I_{\text{Menthol}1}) \times 100$ . (C) Representative AITC (60  $\mu\text{M}$ )-elicited hTRPA1 inward currents recorded at a holding potential of  $-60$  mV, for control cells (Untreated) exposed to two AITC pulses; and, for cells treated with 10  $\mu\text{M}$  AG1529 (AG1529) or 5  $\mu\text{M}$  HC030031 (HC030031) for 30 s before the second AITC pulse. (D) Percentage of TRPA1 ionic current with respect to the first AITC pulse. Normalized responses were estimated as  $(I_{\text{AITC}2}/I_{\text{AITC}1}) \times 100$ . Grey rectangles denote the duration of the agonist pulses and horizontal lines the duration of the antagonists pulses. All data are expressed as mean  $\pm$  SEM. (E) Comparison of 10  $\mu\text{M}$  AG1529 blockade of hTRPV1, hTRPM8 and hTRPA1. Data were analysed using the One-Way Anova followed by the Bonferroni's multiple comparison post-hoc test,  $p$ -values for statistical differences are indicated. Detail data of the statistical analysis is described in the main text.



**Figure 4.** AG1529 binds to the capsaicin binding site in TRPV1. **(A)** Transmembrane view of rat TRPV1 structure with three subunits shown as blue surface and one as orange cartoon. For global blind docking assay capsaicin (red surface), capsazepine (green surface) and AG1529 (blue surface) displayed the same binding pocket which corresponds to the capsaicin binding site compressed between helices S3, S4 and the S4–S5 linker. **(B)** Capsaicin (reddish sticks) orientation in its binding site explored through local docking assay. VDW interactions are observed within capsaicin tail and residues L515 (S3), F543, M547, T550 and L553 (S4). Hydrogen bond is formed between capsaicin head and E570 from the S4–S5 linker. In the inset capsaicin is represented as spheres and the receptor as surface. **(C)** AG1529 (blue sticks) adopted the same orientation as capsaicin and displayed the same VDW interactions but formed a hydrogen bond with S512. In the inset AG1529 is represented as spheres, where the purple one stands for iodine group and receptor is shown as surface. It can be observed the conformation limitation the head of AG1529 experiments. **(D)** Structural view of the capsaicin binding pocket of TRPV1 (green) aligned with TRPA1 (blue). Notice that the M844 side chain of TRPA1 is oriented to the central binding cavity sterically perturbing the accessibility of this site to AG1529. Up to 82% of AG1529 docking trials in TRPA1 failed.

these ion channels expressed in the sensory neurons. Figure 5C depicts families of putative Na<sup>+</sup> and K<sup>+</sup> ionic currents evoked by 5 mV voltage steps from -50 mV to 55 mV in the absence (black) and presence of 10 μM AG1529 (blue). As seen, currents in the absence and presence of the antagonist look alike in terms of magnitude and voltage-sensitivity. Current density-to-voltage relationships for both ionic conductances further corroborated that AG1529 did not affect the voltage-activation properties of Na<sup>+</sup> and K<sup>+</sup> conductances (Fig. 5D,E).

**Effect of AG1529 in neuronal electrical activity.** Current-clamp measurements obtained with patch-clamp indicate that AG1529 inhibits capsaicin-evoked AP firing in sensory neurons. To further interrogate AG1529 action on the excitability of DRG neurons, we next used multielectrode arrays (MEA). This technology allows recording bursts of action potentials from neuronal populations that are located near to an electrode, but it cannot differentiate the number of neurons or other cells contributing to it. We used MEA chips having 60 electrodes and monitored the electrical activity at each electrode.



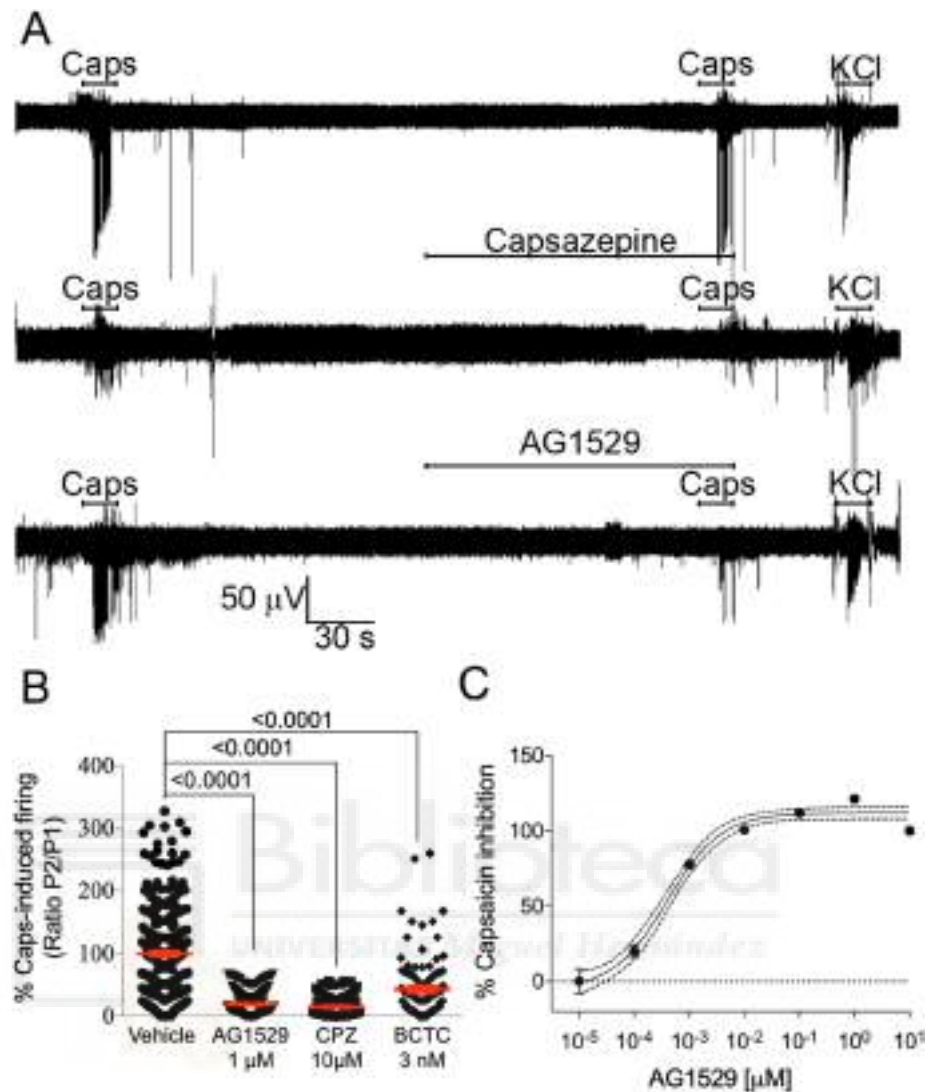
**Figure 5.** AG1529 affects capsaicin-evoked nociceptor firing. (A) Representative recordings of APs firing from DRG neurones elicited by 0.5  $\mu\text{M}$  capsaicin in the absence (Untreated) and presence (AG1529) of 1  $\mu\text{M}$  AG1529. APs were recorded under current clamp mode. Horizontal lines denote the duration of compound pulse. (B) Ratio of second (P2) versus first (P1) peak of APs evoked by capsaicin application in the absence ( $n = 12$ ) and the presence during the P2 of 1  $\mu\text{M}$  AG1529 ( $n = 12$ ). (C) Representative macroscopic ionic currents evoked by a series of depolarizing 5 mV voltage steps of 10 ms, from  $-50$  mV to 55 mV from a holding potential of  $-70$  mV, in the absence (black) and the presence (blue) of 1  $\mu\text{M}$  AG1529. (D) and (E) current density to voltage relationships for the inward and outward currents of panel (C), respectively. All data are expressed as mean  $\pm$  SEM. Data depicted in panel (B) was analysed using an unpaired, two-tail Student's t-test. p-value is indicated.

Figure 6A (top panel) depicts a typical MEA recording from one electrode. The experimental paradigm consisted in applying two 15 s pulses of 0.5  $\mu\text{M}$ , interspersed by a 4.30 min washing step, ending with a 15 s pulse of 40 mM KCl to ensure that the electrical activity near the electrodes was preserved at the end of the protocol. Capsaicin-evoked bursts of neuronal AP firing in  $\approx 70\%$  of the electrodes. Capsaicin-evoked electrical activity was variable as evidenced by the dispersion of the P2/P1 spike frequency ratio (Fig. 6B), likely reflecting the neuronal heterogeneity of the DRG cultures. Vanilloid-induced AP firing was primarily due to TRPV1-mediated neuronal depolarization because capsaicin-evoked neuronal firing of the second pulse was blocked by 10  $\mu\text{M}$  capsazepine or 3 nM BCTC (Fig. 6A, middle panel, and Fig. 6B). Similarly, when 1  $\mu\text{M}$  AG1529 was instilled before the second capsaicin pulse, neuronal firing was significantly reduced (Fig. 6A, lower panel and Fig. 6B;  $F(3,699) = 140.7$ ,  $p < 0.0001$ ;  $p < 0.0001$  for treatments vs. control, Bonferroni's post-hoc test). AG1529 inhibitory activity was dose-dependent, achieving 50% at  $0.39 \pm 0.08$  nM and  $> 98\%$  at 1  $\mu\text{M}$  (Fig. 6C). The Hill coefficient was  $n_H = 0.9 \pm 0.1$ .

AG1529 inhibitory activity of capsaicin-evoked AP firing was attained through inhibition of vanilloid-induced TRPV1 activity, as depolarization-evoked firing triggered by increasing the extracellular KCl to 40 mM was not affected by 1  $\mu\text{M}$  AG1529 (Fig. 7A,B). Nonetheless, it should be stated that a marginal blockade of  $\text{K}^+$  evoked firing activity ( $\approx 25\%$ ) was observed at AG1529 concentrations  $\geq 10$   $\mu\text{M}$ .

Akin to the in vitro assays with recombinant hTRPV1, AG1529 also attenuated pH-induced AP firing of rat DRG neurons, although to a much weaker extent compared to the effect on capsaicin-evoked firing (Fig. 7C,D;  $F(2,275) = 28.15$ ,  $p < 0.0001$ ;  $p < 0.0001$ , AG1529 vs. control and  $p = 0.0025$ , BCTC vs. control, Bonferroni's post-hoc test). It should be considered that pH-induced neuronal excitability may be contributed by both TRPV1 and ASIC channels. Thus, the variable activity recorded in the electrodes that remain insensitive to AG1529 and BCTC (Fig. 7D) may correspond to that triggered by ASIC channels.

We also investigated whether AG1529 affected nociceptor firing evoked by AITC, presumably through activation of TRPA1 channels (Fig. 7E). Indeed, AITC increased AP firing and this effect was sensitive to blockade by HC30031 (Fig. 7E,F). We observed that AG1529 at 1  $\mu\text{M}$  inhibited  $\approx 65\%$  of the AITC-induced neuronal activity (Fig. 7E,F;  $F(2,163) = 14.73$ ,  $p < 0.0001$ ;  $p < 0.0001$ , AG1529 vs. control and  $p = 0.0005$ , HC30031 vs. control, Bonferroni's post-hoc test). This inhibitory activity was similar to that exerted by capsazepine ( $67 \pm 5\%$ ) and BCTC ( $58 \pm 17\%$ ) on AITC evoked nociceptor firing, suggesting a potential cross-talk between TRPV1 and TRPA1 channels that are co-expressed in the same subpopulation of nociceptors, or to the proposed presence of heteromeric channels<sup>34</sup>. A dose response for AG1529 blockade of AITC firing revealed an  $\text{IC}_{50}$  of  $0.3 \pm 0.2$   $\mu\text{M}$  that is 1,000-fold higher than that estimated for capsaicin-evoked nociceptor firing using this methodology. The Hill



**Figure 6.** AG1529 attenuates capsaicin-induced nociceptor excitability. **(A)** Representative MEA recordings showing the capsaicin-evoked AP firing for control (top), 10  $\mu\text{M}$  capsazepine (middle) and 1  $\mu\text{M}$  AG1529 (bottom). Capsaicin (0.5  $\mu\text{M}$ ) was applied in two sequential pulses of 15 s interspersed with a washing period. Compounds were added 2 min before the second capsaicin pulse. The protocol was terminated with a 15 s-pulse of 40 mM KCl to ensure viability of neuronal cultures. **(B)** Normalized capsaicin-induced firing (P2/P1) in the absence (vehicle) and the presence of the antagonists (1  $\mu\text{M}$  AG1529, 10  $\mu\text{M}$  capsazepine, and 3 nM BCTC). **(C)** Dose–response curve of AG1529 blockade of capsaicin-induced AP firing. Data points were fitted to the Michaelis–Menten isotherm, giving an  $\text{IC}_{50}$  value of 0.4 nM (95% CI, 0.3 to 0.6 nM) and an  $n_{\text{H}}$  of 0.88 (95% CI 0.64 to 1.12). The boundary lines denote the interval confidence of the mean values. Data on panel **(B)** were analysed using the One-Way Anova ( $F(3,699) = 140.7$ ,  $p < 0.0001$ ) followed by the Bonferroni’s post-hoc test,  $p$ -values for statistical difference are indicated.  $N$  (independent experiments) = 3, number of electrodes 100–250 per condition).

coefficient  $n_{\text{H}}$  was  $0.8 \pm 0.4$ . Together, these data indicate that AG1529 is a potent inhibitor of vanilloid-induced, TRPV1-mediated nociceptor excitability, and modestly affects that evoked by TRPA1 activation.

#### AG1529 attenuates histamine- and inflammation-induced sensitization of capsaicin-activated sensory neuron firing.

We next investigated whether AG1529 could attenuate the potentiation of TRPV1 activity by histamine and an inflammatory soup. For this task, we desensitized TRPV1 with two pulses of 0.5  $\mu\text{M}$  capsaicin (P1, P2) and evaluated the effect of the pro-algesic agents on neuronal firing activity evoked by a third vanilloid pulse (P3) (Fig. 8A,B). Histamine and the inflammatory soup were instilled between P2 and P3 for 5 min (Fig. 8A,B). As illustrated in Fig. 8A,B, repeated application of capsaicin-evoked neuronal firing produced some desensitization. Exposure of DRG neurons on MEA chips to 50  $\mu\text{M}$  histamine for 5 min between P2 and P3 capsaicin pulses overcome capsaicin-induced desensitization and produced an increment of the vanilloid-evoked nociceptor firing, consistent with a sensitizing action by histamine (Fig. 8A,C). Histamine-induced

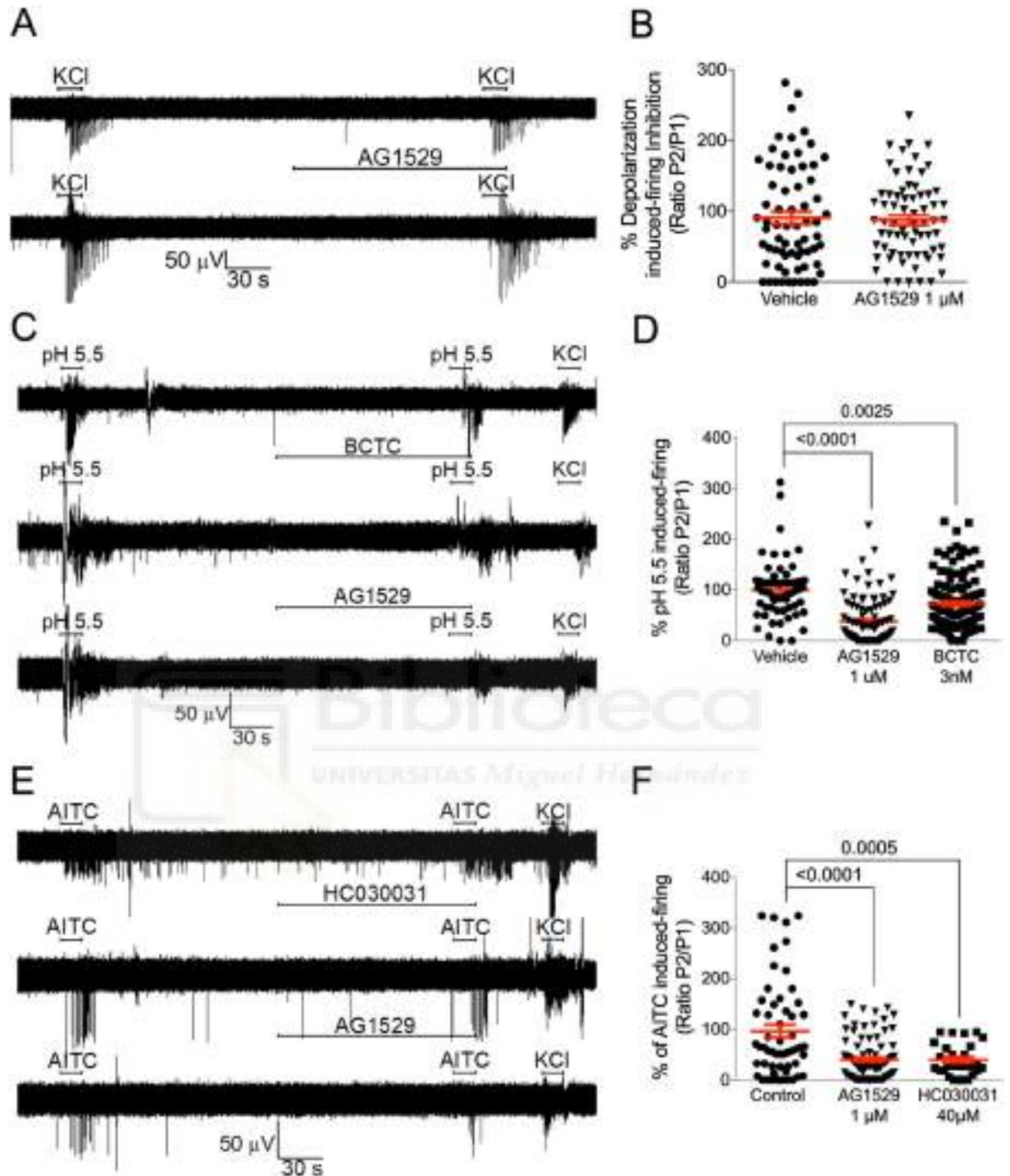


**Figure 7.** AG1529 effect on voltage, pH and AITC-evoked nociceptor excitability. (A) Representative MEA recordings of extracellular  $K^+$  (40 mM KCl)-induced nociceptor firing of APs in the absence and presence of 1  $\mu$ M AG1529, applied 2 min before the second extracellular  $K^+$  pulse. (B) Normalized extracellular  $K^+$ -induced neuronal firing of the second pulse in the absence and presence of AG1529. (C) Representative MEA recordings of acid pH (5.5)-induced nociceptor firing of APs in the absence and presence of 1  $\mu$ M AG1529, applied 2 min before the second acidic stimulus. (D) Normalized pH-induced neuronal firing of the second pulse in the absence and presence of AG1529. Data were analysed using the One-Way Anova ( $F(2,275) = 28.15$ ,  $p < 0.0001$ ). (E) Representative MEA recordings of AITC (50  $\mu$ M)-induced nociceptor firing of APs in the absence and presence of 1  $\mu$ M AG1529, applied 2 min before the second AITC pulse. (F) Normalized AITC-induced neuronal firing of the second pulse in the absence and presence of 1  $\mu$ M AG1529. Data were analysed using the One-Way Anova ( $F(2,163) = 14.73$ ,  $p < 0.0001$  for panel (D) followed by the Bonferroni's post hoc test, p-values for statistical difference are indicated. N (independent experiments) = 3, number of electrodes = 50–130 per condition.

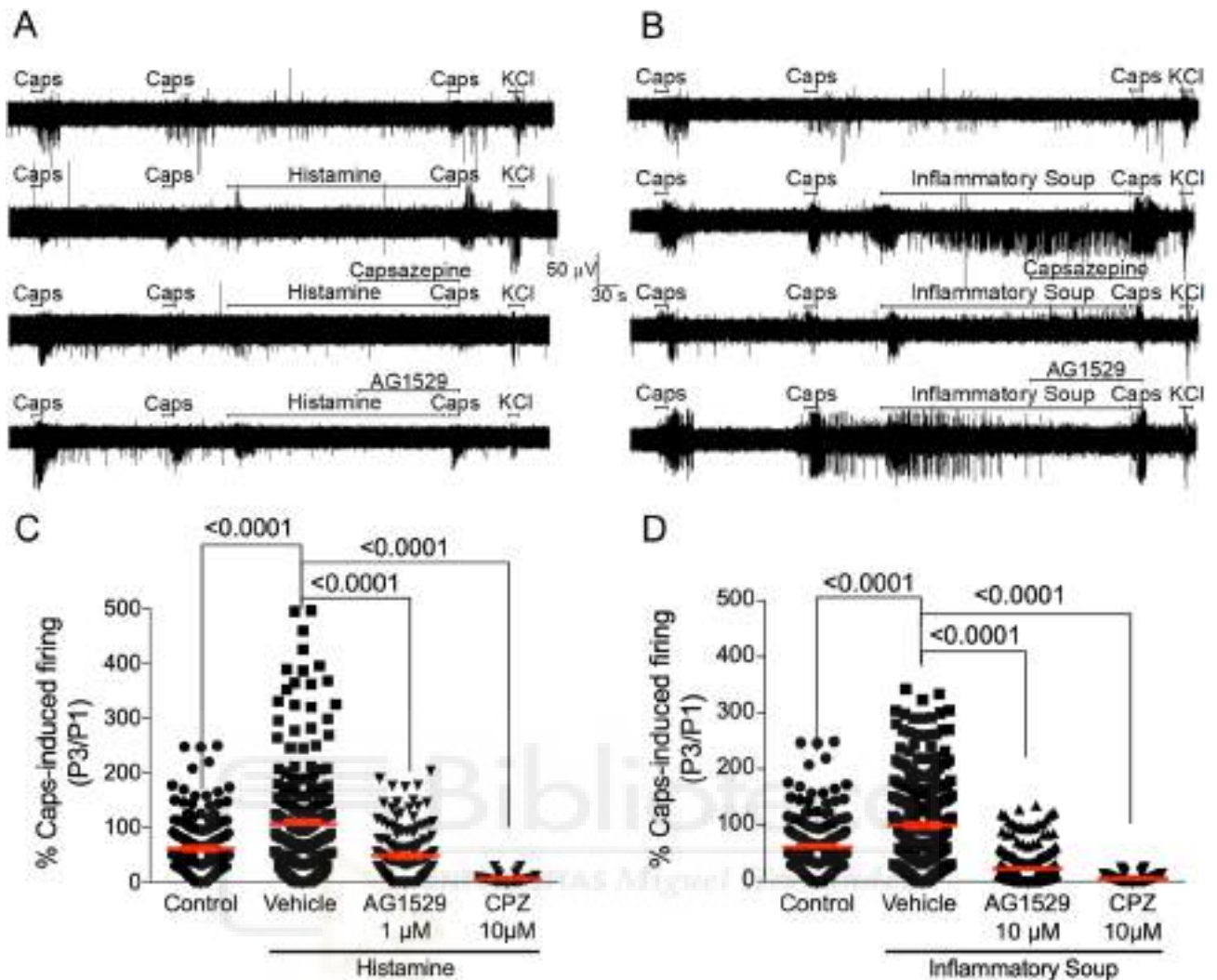


**Figure 8.** AG1529 reduces algesically-sensitized capsaicin-induced nociceptor excitability. (A) Representative MEA recordings of capsaicin-evoked APs and its sensitization by instillation of 50  $\mu$ M histamine 2 min before the third capsaicin pulse, along with the effect of 10  $\mu$ M capsazepine or 1  $\mu$ M AG1529 added 2 min before the third capsaicin pulse (P3). (B) Similar protocol that in (A) but sensitization was triggered by an inflammatory soup containing 50  $\mu$ M histamine, 1  $\mu$ M bradykinin and 10  $\mu$ M ATP. (C,D) Normalized capsaicin-induced firing of the third pulse (P3) with respect to the first one (P1) for the different treatments. Data are expressed as mean  $\pm$  SEM, and analysed using the One-Way Anova ( $F(3,553)=28.28$ ,  $p<0.0001$  for panel (C); and  $F(3,794)=144.5$ ,  $p<0.0001$  for panel (D)) followed by the Bonferroni's post-hoc test, p-values for statistical difference are indicated. N (independent experiments)=3, n° of electrodes=50–200). Data of vehicle without histamine or inflammatory soup were obtained in independent experiment, N=3 and number of electrodes 120.

potentiation of capsaicin firing was inhibited by 10  $\mu$ M capsazepine perfused 2 min before P3 (Fig. 8A,C). These results indicate that histamine signaling was primarily mediated by TRPV1 channels. Notably, AG1529 was also very effective blocking histamine-induced sensitization of TRPV1 in DRG cultures (Fig. 8A). At 1  $\mu$ M, AG1529 reduced by >60% the histamine sensitized capsaicin-induced AP firing (Fig. 8C,  $F(3,553)=28.28$ ,  $p<0.0001$ ;  $p<0.0001$  treatments vs. vehicle, Bonferroni's post-hoc test).

We also tested the activity of compound AG1529 on capsaicin responses sensitized by an inflammatory soup containing 50  $\mu$ M histamine, 1  $\mu$ M bradykinin and 10  $\mu$ M ATP. As expected, instillation of this inflammatory soup for 5 min between P2 and P3 capsaicin pulses abrogated the vanilloid-induced sensitization and promoted a notable potentiation of capsaicin evoked neuronal firing (Fig. 8B,D). Inflammatory potentiation of capsaicin responses was blocked by capsazepine (Fig. 8B,D). Akin to capsazepine, 10  $\mu$ M AG1529 administered 2 min before and during the third capsaicin pulse significantly reduced the vanilloid sensitized AP firing (Fig. 8D;  $F(3,794)=144.5$ ;  $p<0.0001$ ;  $p<0.0001$ , treatments vs. vehicle, Bonferroni's post-hoc test), thus attenuating the inflammatory potentiation of TRPV1 in DRG neurons. Collectively, these results substantiate an anti-pruritic and anti-inflammatory activity of AG1529 by modulating TRPV1 activity in sensory neurons.

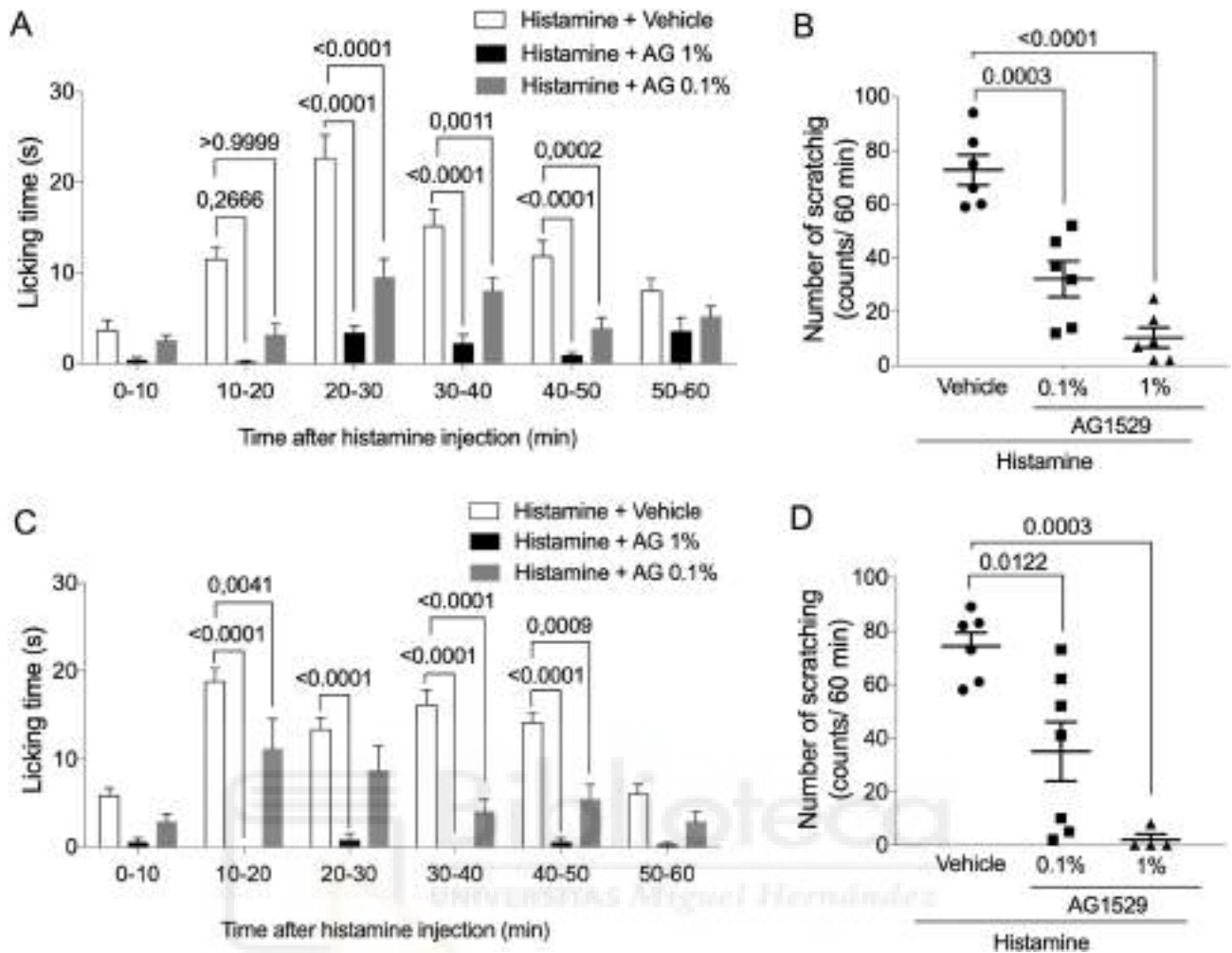


**Figure 9.** Topical application of AG1529 inhibits histamine-evoked pruritus. Effect of AG1529 (0.1 and 1%) dissolved in acetone (A,B) or formulated in a dermal ointment (C,D) on the scratching behavior of rats locally injected with histamine in the back of the neck. Animals were injected with 100  $\mu$ l of a solution at 1 mg/ml of histamine. AG1529 in acetone was wiped in 1 cm<sup>2</sup> area, 30 min before the histamine instillation. Ointment containing AG1529 was applied topically twice/day for 3 days with a spatula in a 1 cm<sup>2</sup> shaved area in the back of the neck. Data are expressed as mean  $\pm$  SEM, n = 6 animals per group. Data were analysed using the One-way Anova followed by the Bonferroni's post-hoc test, p-values for statistical difference are indicated. Detail data of the statistical analysis is described in the main text.

**Topically applied AG1529 reduces histamine-induced pruritus.** Our *in vitro* findings, using histamine and an inflammatory soup containing the pruritogenic agent (Fig. 8), alongside with the previously reported *in vivo* antinociceptive activity of AG1529 when administered systemically (*i.v.*) or locally (intraplantar)<sup>31</sup>, prompted us to question whether dermal application of AG1529 could have therapeutic value. For this experiment, we designed two formulations that are compatible with the low water solubility of AG1529. Firstly, we dissolved the compound in acetone and directly wiped the skin of the animals before local administration of histamine. To monitor the licking activity as a function of time, the 60 min observation period was binned in 10 min intervals (Fig. 9A). As depicted, pruritic activity of histamine was very evident from 10 to 50 min after administration. AG1529 at 0.1% and 1% significantly attenuated the licking time during the entire time interval. Furthermore, AG1529 wiped on the skin reduced the total number of scratches provoked by histamine in a dose dependent manner (Fig. 9B;  $F(2,15) = 33.35$ ,  $p < 0.0001$ ;  $p = 0.0003$ , 0.1% vs vehicle;  $p < 0.0001$ , 1% vs vehicle; and,  $p = 0.0395$ , 0.1% vs 1%, Bonferroni's post-hoc test), indicating that dermal application of the product exerted an anti-pruritic effect.

To further substantiate the translational clinical potential of AG1529, we formulated the compound in an anhydrous ointment and tested its therapeutic efficacy in the rat model of acute histaminergic pruritus. To ensure the skin permeation of the compound, we rubbed the AG1529 ointment previously to the administration of histamine. Dermal application of the AG1529 ointment did not produce any nocifensive response of the rats, substantiating that AG1529 does not produce the burning sensation characteristic of capsaicin. As depicted in Fig. 9C,D, animals pre-treated with the ointment base (vehicle) exhibited a high number of scratches provoked by the pruritogenic agent. In marked contrast, application of the ointment containing AG1529 significantly

attenuated the scratching behavior (Fig. 9C,D), with full abrogation at 1% of AG1529 (Fig. 9D;  $F(2,14) = 15.28$ ;  $p = 0.0003$ ;  $p < 0.0122$ , 0.1% vs vehicle;  $p = 0.0003$ , 1% vs vehicle, Bonferroni's post-hoc test). Therefore, these results signal to dermal formulations containing AG1529 as potential therapeutics for treating pruritus.

## Discussion

TRPV1 is a therapeutic target for modulating nociceptive signaling, including pain and itch. A major effort has been devoted to design therapeutically useful antagonists for the treatment of chronic pain and pruritus. However, most of the highly potent antagonists developed have failed in clinical trials because of unwanted side-effects, primarily hyperthermia<sup>35</sup>. In contrast, the desensitizing action of capsaicin is widely used in the clinic for the treatment of chronic pain and pruritus, but with poor patient adherence due to the burning sensation and the potential carcinogenesis because of its poor skin elimination<sup>36</sup>. Thus, there is interest in developing capsaicin-like molecules devoid of the flaming sensation while preserving the therapeutic action. Previously, we reported the design of soft drugs based on the capsaicinoid scaffold as TRPV1 antagonists that neither show the burning nocifensive response in animals, nor alter the body temperature<sup>31</sup>. Soft drugs are a kind of compounds that are metabolically deactivated by dermal and plasma esterases to inert metabolites, preventing their tissue accumulation and favoring their body elimination<sup>31</sup>. Here, we characterized the effect of soft compound AG1529 on hTRPV1 activity to evaluate its potential clinical translation. In addition, we also assessed the possible therapeutic use of AG1529 as a dermal anti-pruritic drug. We show that AG1529 is a hTRPV1 antagonist that reversibly blocks the channel with micromolar potency. This activity was modestly receptor selective as AG1529 also inhibited hTRPA1 and hTRPM8 receptors, although with lower potency than hTRPV1. Noteworthy, we found that AG1529 preferentially inhibited capsaicin-evoked TRPV1 gating, marginally affected pH-mediated channel activation, and it did not alter voltage- and heat-induced gating. Note that the modest inhibition of pH-evoked TRPV1 responses, and lack of effect on TRPV1 thermal activation may underlie the non-hyperthermic *in vivo* activity of AG1529<sup>31</sup>. Furthermore, the lack of effect on heat-evoked gating suggests that AG1529 may not alter cutaneous temperature sensitivity, which is pivotal for the topical therapeutic application of the compound. Thus, AG1529 is a hTRPV1 antagonist exhibiting *in vitro* functional properties with a potential clinical translation.

Our functional *in vitro* data support the tenet that AG1529 acts as a capsaicin competitive antagonist. Firstly, it displaced the capsaicin  $EC_{50}$  towards a higher value; and, secondly, it attenuated capsaicin-induced desensitization of hTRPV1. A molecular model further substantiated this mechanism of action showing that AG1529 binds with high theoretical energy to the capsaicin binding site in the receptor. Considering this molecular model, it is tempting to use it for hypothesizing a mechanism for the inhibitory activity of AG1529. It has been proposed that capsaicin induces TRPV1 gate opening by pulling of E570 through hydrogen bond formation with the residue which causes the final motion of S6 leading to gate opening<sup>37</sup>. The presence of an iodine group in the vanillyl head of AG1529 appears responsible for the competitive antagonism of AG1529. Indeed, the interaction of the compound with residue E570 seems compromised by the bulky 2.16 Å iodine group that limits the capacity of AG1529 to adopt a head orientation akin to capsaicin (Fig. 4). Note that the orientation driven by the Iodine in the vanilloid group probably induces an electrostatic repulsion with Glu-570 in the S4-S5 loop thus relocating the vanilloid group close to S3. This configuration, along with the lack of interaction with the S4-S5 loop seems to lock the channel in the closed configuration. In support of this hypothesis, elimination of the Iodine from the vanillyl group brings closer the vanilloid group to Glu-570 in the S4-S5 loop, consistent with the agonist activity displayed by this capsaicinoid molecule<sup>31</sup>. Ongoing structure–function studies in our laboratory are testing this model for the interaction of AG1529 with TRPV1.

For therapeutic use is essential that TRPV1 antagonists are capable of modulating nociceptor excitability, particularly under pro-algesic/inflammatory conditions. Our studies reveal that AG1529 effectively attenuates capsaicin-induced nociceptor firing in single sensory neurons and neuronal networks. It is intriguing that the AG1529 potency blocking capsaicin-evoked electrical activity in neuronal networks seeded in MEA chips was notably higher than that inhibiting hTRPV1-mediated ionic currents in recombinant HEK293 cells. This discrepancy does not appear related a different sensitivity of the human and rat orthologs as they are blocked with similar  $IC_{50}$  values (hTRPV1,  $1.2 \pm 0.1 \mu\text{M}$  ( $n = 16$ ) and rTRPV1,  $0.9 \pm 0.2 \mu\text{M}$  ( $n = 13$ ), determined by  $\text{Ca}^{2+}$  microfluorography). Notably, a similar increase in blocking potency of AG1529 was obtained on AITC-evoked electrical activity in neuronal networks. We do not have a solid explanation for the magnitude of these differences in potency recorded by both techniques. One possibility is that it could be contributed by the different cellular environments (recombinant vs neuronal), and/or that the MEA mean electrical activity reflects the electrical activity evoked by the heterogeneous diversity of sensory neurons near an electrode. In contrast, patch-clamp measures individual cells in homogeneous cell populations. Nonetheless, we cannot discard that the higher blocking potency of AG1529 in primary cultures of nociceptors may be also due to off-target actions of the compound that affect the firing of action potentials. In this regard, we observed that  $10 \mu\text{M}$  AG1529 reduced the electrical activity evoked by 40 mM KCl (data not shown). Thus, additional studies are needed to investigate the actions of AG1529 in neuronal excitability to unveil potential off-targets effects in its neuronal activity. It should be noted that apart from the quantitative differences, data obtained in recombinant cells are fairly reproduced in the DRG cultures.

We also found that AG1529 display an inhibitory activity on TRPM8 and TRPA1 channels, although with lower potency. Ligand cross-recognition between these receptors has been reported, and it appears that it could be due to conservation of transmembrane binding pockets capable to accommodate these molecules<sup>32,33,38</sup>. Our results with AG1529 further support this tenet. It is also interesting the activity on TRPA1 as the presence of heteromeric TRPV1-TRPA1 receptors has been reported in sensory neurons<sup>34,39</sup>. It is worth noticing that this inhibitory action on TRPA1 activity may underlie the attenuation of histaminergic and non-histaminergic pruritus exhibited by AG1529, as pruritus is a very complex, multifactorial sensory process involving the contribution

of both TRPV1 and TRPA1 channels<sup>40</sup>. Accordingly, our findings suggest that compound cross-reactivity among thermoTRPs may have a therapeutic advantage in multifactorial disorders such as pain and pruritus compared to highly selective antagonists acting on one target.

A salient contribution of our findings is that AG1529 potently reduced the potentiation of capsaicin-evoked neuronal firing provoked by a pro-inflammatory soup containing bradykinin, ATP and histamine, as well as by histamine alone. This result substantiates a therapeutic potential of AG1529 for attenuating that neurogenic inflammation underlying cutaneous diseases, as well as algescic and pruritogenic conditions that increase sensory neuron excitability. Thus, we evaluated the efficacy of a dermal AG1529 application, considering that soft drugs are designed to be metabolically deactivated in plasma upon exerting their therapeutic action<sup>31</sup>. We found that topically applied AG1529, formulated in a pharmaceutical ointment, remarkably reduced acute histaminergic itch at therapeutic doses (< 1%). These findings complement previous results showing that intraplantar administration of AG1529 diminished both histaminergic and non-histaminergic pruritus<sup>31</sup>. Nonetheless, the full therapeutic potential of AG1529 needs to be addressed in chronic models of pruritus exhibiting a multifactorial etiology that leads to excitation of peripheral nociceptor terminals encoding the pruritogenic signal.

In conclusion, our *in vitro* preclinical results imply that AG1529, akin to PAC14028<sup>41,42</sup>, may be a valuable drug candidate for the treatment of the itching symptoms of dermatological diseases such as dermatitis or psoriasis, along with cutaneous inflammation. AG1529 is a TRPV1 antagonist that does not produce hyperthermia and its deactivation by cutaneous esterases prevents its long accumulation in the skin thus reducing any adverse long-term effect<sup>31</sup>. Furthermore, this capsaicinoid should not alter cutaneous thermal sensitivity as it does not affect heat-evoked TRPV1 gating. Noteworthy, dermal application of the pharmaceutical ointment did not produce a nocifensive or irritating response in the animals, nor any apparent erythema-like cutaneous effect on the shaved back neck skin upon repetitive applications for 3 days suggesting a suitable cutaneous safety for this capsaicinoid. As a result, AG1529 is currently in regulated pre-clinical safety studies, anticipating its potential clinical development for topical treatment of psoriatic pruritus.

## Methods

**Animal experimentation.** All procedures were approved by the Institutional Animal and Ethical Committee of the University Miguel Hernández de Elche, in accordance with the guidelines of the Economic European Community, the National Institutes of Health, and the Committee for Research and Ethical Issues of the International Association for the Study of Pain. Animals were kept in a controlled environment (21–23 °C, 12 h light/dark cycle), and had food and water available *ad libitum*. Neonatal Wistar rats were purchased from UMH in house bred stock (originally from Harlan Laboratories). Adult Wistar rats (100–125 g) were purchased from Harlan Laboratories, Netherlands.

**Primary cultures of DRG nociceptors.** Neonatal dorsal root ganglia (DRGs) from Wistar rats (3–5 days-old) were isolated and digested with 0.25% (w/v) collagenase (type IA) in DMEM GlutaMax with 1% (v/v) penicillin/streptomycin (P/S) solution for 1 h (37 °C, 5% CO<sub>2</sub>, ThermoScientific incubator) as previously described<sup>43,44</sup>. After digestion, DRGs were mechanically dissociated. Single cell suspension was passed through a 100 µm cell strainer and washed with DMEM GlutaMax with 10% (v/v) fetal bovine serum (FBS) and 1% (v/v) P/S. Cells were seeded in a drop on microelectrode array chambers previously coated with poly-L-lysine (8.3 µg/mL) and laminin (5 µg/mL). After 1 h, medium was replaced with DMEM GlutaMax, 10% (v/v) FBS and 1% (v/v) P/S, supplemented with mouse 2.5S NGF 50 ng/mL and 1.25 µg/mL cytosine arabinoside (37 °C, 5% CO<sub>2</sub>). All experiments were performed after 48 h cell seeding. All cell culture procedures were performed in a laminar flow cabinet (Model Telstar AV-100).

**Microelectrode array measurements.** Extracellular recordings were performed using multiple electrode planar arrays of 60-electrode thin MEA chips, with 30 µm diameter electrodes and 200 µm inter-electrode spacing with an integrated reference electrode (Multichannel Systems GmbH)<sup>44</sup>. The electrical activity of primary sensory neurons was recorded by the MEA1060 System (Multi Channel Systems GmbH1) and MC\_Rack software version 4.3.0. Measurement of neuronal firing activity was performed by two different protocols. In the first one, two short 15 s-applications (defined as P1 and P2, respectively) of the stimulus (Capsaicin, AITC, KCl or acidic pH) using continuous perfusion system (2 mL/min) were applied. Between each stimulus cells were washed with external solution for 4 min and 30 s. Treated cells were perfused with AG1529 (obtained from Anta-IGenics), capsazepine, BCTC, (Sigma Aldrich), or HC030031 (Sigma Aldrich), 2 min before and together with P2. In the second one, as a TRPV1-sensitization protocol, neuronal firing was evoked by three short 15 s applications (defined as P1, P2 and P3, respectively) of 0.5 µM capsaicin using continuous perfusion system. Between P1 and P2, cells were washed with external solution for 2 min and 30 s. Between P2 and P3, after washing for 1 min and 30 s with external solution, cells were treated with 50 µM histamine or an inflammatory soup (50 µM Histamine, 1 µM bradykinin, 10 µM ATP) for 5 min. At the end of each protocol 40 mM KCl was applied to confirm appropriate cell culture excitability and viability. All measurements were performed at ~34.5 °C (Multi-channel Systems Temperature Controller).

**Microelectrode array analysis.** Data were analyzed using MC\_RACK spike sorter with a sample rate of 25 kHz and Butterworth high-pass 2nd order filter applied with 200 Hz cutoff. An evoked spike was defined when the amplitude of the neuronal electrical activity was established by automatic threshold estimation at –5.0 µV Std. Dev. Spiking activity was measured in a temporal interval of 60 s, starting right after instillation of the activating stimuli. Electrodes not displaying electrical activity in the first capsaicin pulse were discarded. The recorded signals were then processed to extract mean spike frequency for each pulse (P1–P3). Then, the ratio

P2/P1 or P3/P1 (as indicated) of mean spike frequency was calculated and normalized to vehicle for comparing the different conditions used.

**Patch-clamp recordings from recombinant cells.** Whole-cell patch-clamp recordings were made on HEK 293 LTV cell line cultured in DMEM GlutaMAX supplemented with 10% (v/v) fetal bovine serum and 1% penicillin/streptomycin solution, transiently co-transfected with YFP and hTRPV1 or hTRPM8 or hTRPA1 encoding plasmids using Lipofectamine 3000 (Invitrogen) following manufacturer instructions. Transfected cells were registered 2 days after transfection, seeded on 12 mm Ø glass coverslips treated with poly-L-lysine solution (Sigma Aldrich). Intracellular pipette solution contained in mM: 150 NaCl, 3 MgCl<sub>2</sub>, 5 EGTA and 10 HEPES, pH 7.2 with CsOH. Extracellular physiological solution contained (in mM): 150 NaCl, 6 CsCl, 1 MgCl<sub>2</sub>, 1.5 CaCl<sub>2</sub>, 10 glucose and 10 HEPES, pH 7.4 with NaOH. For extracellular acidic solution 10 mM HEPES was substituted with 10 mM MES remaining the rest of components equal to the physiological solution and adjusting to pH 5.5. All measurements were performed at room temperature except heat-evoked TRPV1 activity recordings. Whole-cell experiments were conducted using an EPC-10 amplifier (HEKA Elektronik) with Patchmaster software. Patch pipettes, prepared from thin-wall borosilicate capillary glass tubing were pulled with a horizontal flaming/brown Micropipette puller Model P-97 from Sutter Instrument. to a final resistance of 2–8 MΩ when filled with internal solution. Recordings were acquired at 10 kHz and low-pass filtered at 3 kHz. Recordings with leak currents > 200 pA or series resistance > 20 MΩ were discarded.

In voltage-clamp recordings, cells were maintained at a constant potential and application of distinct modulators was performed. Total currents were always normalized to the first current peak evoked by a stimulus. AG1529 effect on TRPV1 voltage dependence was studied in a voltage step protocol from –120 mV to 120 mV using 100 ms steps of 20 mV from a holding potential at 0 mV. Leak currents were not subtracted. Conductance was calculated with equation:

$$G = \frac{J}{(V - V_r)}$$

where G is channel conductance, J is the current density (nA/pF), V<sub>r</sub> (mV) is the reversal potential and V (mV) is the applied voltage.

Heat-elicited TRPV1 currents were evoked by increasing of external bath temperature to 43 °C with a heatable perfusion cannula PH01 programmed with the temperature controller TC02 from Multi Channel Systems MCS GmbH. Ionic currents were recorded with a voltage ramp protocol from –120 mV to 120 mV in 300 ms. The protocol to evaluate TRPV1 heat-evoked gating inhibition by AG1529 consisted in: (i) record the ionic activity of the channel at 37 °C using the voltage ramp protocol (basal activity); (ii) increase the external bath temperature up to 43 °C and record the channel activity using the voltage ramp protocol (P1); (iii) decrease the temperature until 37 °C and perfuse AG1529 (10 μM), capsazepine (10 μM) or BCTC (1 nM) for 30 s; and, (iv) rise the temperature to 43 °C; and record the ionic currents with the voltage ramp protocol (P2). Basal current (37 °C) was subtracted from the current evoked at 43 °C. The mean P2/P1 ratio for control was used for normalizing the ionic current at 120 mV for all treatments.

To monitor AG1529 (10 μM) effect on pH-evoked TRPV1 currents, ASIC channels activated by acidic pH present in HEK 293 LTV cell line were blocked with 50 μM Amiloride<sup>45</sup>. Currents were evoked at –60 mV with a pulse of buffer at pH 5.5. The activity of AG1529 was compared to that of capsazepine (10 μM) and BCTC (1 nM).

For capsaicin dose–response relationships, responses were normalized with respect to that evoked in the absence of channel blockers. Capsaicin dose–response curves were fitted to the Michaelis–Menten Isotherm:

$$\frac{I}{I_{\max}} = \frac{1}{\left(\frac{1 + [\text{capsaicin}]}{EC_{50}}\right)^{n_H}}$$

where, EC<sub>50</sub> denotes the concentration of capsaicin needed to activate half of the maximal response, and n<sub>H</sub> denotes the Hill coefficient, which is an estimate of the number of vanilloid binding sites. Dose–response curves for blockade activity were fitted to the Michaelis–Menten Isotherm:

$$\frac{I}{I_{\max}} = \frac{1}{\left(\frac{1 + [\text{blocker}]}{IC_{50}}\right)^{n_H}}$$

where IC<sub>50</sub> denotes the concentration of channel blocker that inhibits half of the response obtained in its absence (I<sub>max</sub>). Experimental data were fitted to the Hill equation with a nonlinear least-square regression algorithm with the Prism7 software package.

**Patch-clamp recordings from DRG nociceptors.** Whole-cell patch-clamp recordings from sensory DRG neurons from neonatal Wistar rats were carried out 2 days after seeding on 12 mm Ø glass coverslips treated with poly-L-lysine solution and Laminin (Sigma Aldrich). Intracellular pipette solution contained (in mM): 4 NaCl, 126 K gluconate, 0.02 CaCl<sub>2</sub>, 1 MgSO<sub>4</sub>, 5 HEPES, 15 glucose, 3 ATP, 0.1 GTP and 5 EGTA, pH 7.2 with KOH. Extracellular solution contained (in mM): 140 NaCl, 4 KCl, 2 CaCl<sub>2</sub>, 2 MgCl<sub>2</sub>, 10 HEPES, 5 glucose and 20 mannitol, pH 7.4 with NaOH.

Current-clamp recordings of APs generated by the application of two pulses of 500 nM capsaicin in a time interval of 5 min and a 1 min perfusion of 1 μM AG1529 before the second capsaicin pulse, during the injection of a constant depolarizing current that maintained the membrane potential at –70 mV were used to calculate

P2/P1 ratio of AP generation. Data was acquired at a sampling rate of 100  $\mu$ s and low-pass filtered at 3 KHZ. Cell that did not responded to the first pulse of capsaicin were discarded.

Voltage-gated DRG neuron currents were evoked by stepping from  $-50$  to  $55$  mV for  $10$  ms with  $5$  mV increments with  $2$  s interpulse intervals. Inward and outward current densities (nA/pF) were obtained by dividing the peak inward and outward current, respectively, by the cell capacitance. Neurons were voltage-clamped at  $-70$  mV. AG1529 ( $1$   $\mu$ M) was perfused during  $2$  min before recording the step protocol.

**In vivo model of pruritus.** AG1529 ( $0.1$  and  $1\%$  w/v) dissolved in acetone was applied topically ( $100$   $\mu$ L) with a syringe  $30$  min before histamine injection in a  $1$   $\text{cm}^2$  area in the back of the neck. Control animals were treated with  $100$   $\mu$ L acetone. AG1529 ointment formulation ( $0.1$  and  $1\%$  w/w) or placebo cream ( $8\%$  glyceryl behenate,  $8\%$  glyceryl stearate,  $4\%$  hydrogenated castor oil  $5\%$  diethylene glycol monoethyl ether,  $0.1\%$  alpha-tocopherol,  $75\%$  caprylic/capric triglyceride) was applied topically twice/day for  $3$  days with a spatula in a  $1$   $\text{cm}^2$  shaved area in the back of the neck. Control animals were treated with placebo cream. Histamine solution ( $1$  mg/ml in saline) was injected subcutaneously in a volume of  $100$   $\mu$ L into the shaved area,  $30$  min after application of AG1529 dissolved in acetone or on day  $4$  after first AG1529 cream administration. Scratching behavior was observed during  $60$  min after histamine injection. The number of scratching bouts (counts of scratching/ $60$  min), defined as the action of scratching the affected area, was measured from the start of the first scratching movement.

**Virtual docking assays.** Rat TRPV1 crystal structure in open ( $3.3$   $\text{\AA}$  resolution, pdb code: 5irz) and closed ( $3.3$   $\text{\AA}$  resolution, pdb code: 3j5p) states were obtained, human TRPA1 ( $2.9$   $\text{\AA}$  resolution, pdb code: 6PQO) from the Research Collaboratory for Structural Bioinformatics (RCSB) Protein Data Bank (PDB) (<https://www.rcsb.org>). The structure of AG1529 was drawn and transformed into 3D structure with Marvin Sketch from ChemAxon (<https://chemaxon.com/>). Capsaicin (PubChem ID: 1548943) and capsaizepine (PubChem ID: 2733484) structures were obtained from the National Center for Biotechnology Information (NCBI) PubChem database (<http://www.ncbi.nlm.nih.gov/pccompound>). The global docking procedure was accomplished with AutoDock  $4^{46}$  implemented in Yasara<sup>47</sup>, in which a total of  $800$  flexible docking runs were set and clustered around the putative binding sites. The program then performed a simulated annealing optimization of the complexes, which moved the structure to a nearby stable energy minimum, by using the implemented Assisted Model Building with Energy Refinement (AMBER03) force field<sup>48</sup>. The Yasara pH command was set to  $7.0$ , to ensure that molecules preserve their pH dependency of bond orders and protonation patterns. The best binding energy complex in each cluster was stored, analyzed, and used to select the best orientation of the interacting partners. The more positive the interaction energy, the more favorable the interaction is. To further explore the best binding site for each molecule a focalized docking assay with a total of  $150$  flexible dockings was performed in a limited area of  $22:30:25$   $\text{\AA}$  (x:y:z) around the capsaicin binding site centered in the global docking conformation that adopted each molecule in this particular site. Figures were drawn with open source PyMol (The PyMOL Molecular Graphics System, Version 1.8 Schrödinger, LLC, at <http://www.pymol.org/>).

**Statistical analysis.** All data are expressed as mean  $\pm$  SEM. The number of replicates is indicated in the figure legends. In vitro data were statistically analyzed using One-Way ANOVA followed by the Bonferroni post-hoc test of multiple comparison as indicated, or unpaired, two-tail Student t-test for some experiments also indicated. For One-Way ANOVA we report the F (DFn, DFd) and the P value, along with the p values derived from the Bonferroni post-hoc test. p-value for all the analyzes was set at  $0.05$ , and the value obtained is reported. For in vivo experiments, the number of animals used was  $n = 4-7$  as indicated.

Received: 10 January 2020; Accepted: 17 December 2020

© The Author(s) 2020

## References

- Caterina, M. J. *et al.* The capsaicin receptor: A heat-activated ion channel in the pain pathway. *Nature* **389**, 816–824. <https://doi.org/10.1038/39807> (1997).
- Voets, T. *et al.* The principle of temperature-dependent gating in cold- and heat-sensitive TRP channels. *Nature* **430**, 748–754. <https://doi.org/10.1038/nature02732> (2004).
- Oh, U., Hwang, S. W. & Kim, D. Capsaicin activates a nonselective cation channel in cultured neonatal rat dorsal root ganglion neurons. *J. Neurosci.* **16**, 1659–1667 (1996).
- Tominaga, M. *et al.* The cloned capsaicin receptor integrates multiple pain-producing stimuli. *Neuron* **21**, 531–543. [https://doi.org/10.1016/s0896-6273\(00\)80564-4](https://doi.org/10.1016/s0896-6273(00)80564-4) (1998).
- Zhu, M. X. Understanding the role of voltage gating of polymodal TRP channels. *J. Physiol.* **585**, 321–322. <https://doi.org/10.1113/jphysiol.2007.147082> (2007).
- Devesa, I. & Ferrer-Montiel, A. Neurotrophins, endocannabinoids and thermo-transient receptor potential: A threesome in pain signalling. *Eur. J. Neurosci.* **39**, 353–362. <https://doi.org/10.1111/ejn.12455> (2014).
- McPartland, J. M., Glass, M. & Pertwee, R. G. Meta-analysis of cannabinoid ligand binding affinity and receptor distribution: Interspecies differences. *Br. J. Pharmacol.* **152**, 583–593. <https://doi.org/10.1038/sj.bjp.0707399> (2007).
- Lam, P. M., McDonald, J. & Lambert, D. G. Characterization and comparison of recombinant human and rat TRPV1 receptors: Effects of exo- and endocannabinoids. *Br. J. Anaesth.* **94**, 649–656. <https://doi.org/10.1093/bja/aei098> (2005).
- Petrosino, S. *et al.* The anti-inflammatory mediator palmitoylethanolamide enhances the levels of 2-arachidonoyl-glycerol and potentiates its actions at TRPV1 cation channels. *Br. J. Pharmacol.* **173**, 1154–1162. <https://doi.org/10.1111/bph.13084> (2016).
- Tóth, A. *et al.* Expression and distribution of vanilloid receptor 1 (TRPV1) in the adult rat brain. *Brain Res. Mol. Brain Res.* **135**, 162–168. <https://doi.org/10.1016/j.molbrainres.2004.12.003> (2005).
- Stock, K. *et al.* The capsaicin receptor TRPV1 as a novel modulator of neural precursor cell proliferation. *Stem Cells* **32**, 3183–3195. <https://doi.org/10.1002/stem.1805> (2014).

12. Ramírez-Barrantes, R. *et al.* Perspectives of TRPV1 function on the neurogenesis and neural plasticity. *Neural Plast.* **2016**, 1568145. <https://doi.org/10.1155/2016/1568145> (2016).
13. Inoue, K., Koizumi, S., Fuziwara, S., Denda, S. & Denda, M. Functional vanilloid receptors in cultured normal human epidermal keratinocytes. *Biochem. Biophys. Res. Commun.* **291**, 124–129. <https://doi.org/10.1006/bbr.2002.6393> (2002).
14. Tóth, B. I., Oláh, A., Szöllösi, A. G. & Bíró, T. TRP channels in the skin. *Br. J. Pharmacol.* **171**, 2568–2581. <https://doi.org/10.1111/bph.12569> (2014).
15. Bertin, S. *et al.* The ion channel TRPV1 regulates the activation and proinflammatory properties of CD4<sup>+</sup> T cells. *Nat. Immunol.* **15**, 1055–1063. <https://doi.org/10.1038/ni.3009> (2014).
16. Denda, M., Sokabe, T., Fukumi-Tominaga, T. & Tominaga, M. Effects of skin surface temperature on epidermal permeability barrier homeostasis. *J. Invest. Dermatol.* **127**, 654–659. <https://doi.org/10.1038/sj.jid.5700590> (2007).
17. Shim, W. S. *et al.* TRPV1 mediates histamine-induced itching via the activation of phospholipase A2 and 12-lipoxygenase. *J. Neurosci.* **27**, 2331–2337. <https://doi.org/10.1523/JNEUROSCI.4643-06.2007> (2007).
18. Tominaga, M. *Molecular Sensors for Cardiovascular Homeostasis* (Springer, Boston, 2007).
19. Katanosaka, K. *et al.* Contribution of TRPV1 to the bradykinin-evoked nociceptive behavior and excitation of cutaneous sensory neurons. *Neurosci. Res.* **62**, 168–175. <https://doi.org/10.1016/j.neures.2008.08.004> (2008).
20. Sugiura, T., Tominaga, M., Katsuya, H. & Mizumura, K. Bradykinin lowers the threshold temperature for heat activation of vanilloid receptor 1. *J. Neurophysiol.* **88**, 544–548. <https://doi.org/10.1152/jn.2002.88.1.544> (2002).
21. Camprubi-Robles, M., Planells-Cases, R. & Ferrer-Montiel, A. Differential contribution of SNARE-dependent exocytosis to inflammatory potentiation of TRPV1 in nociceptors. *FASEB J.* **23**, 3722–3733. <https://doi.org/10.1096/fj.09-134346> (2009).
22. Gouin, O. *et al.* TRPV1 and TRPA1 in cutaneous neurogenic and chronic inflammation: Pro-inflammatory response induced by their activation and their sensitization. *Protein Cell.* **8**, 644–661. <https://doi.org/10.1007/s13238-017-0395-5> (2017).
23. Moore, C., Gupta, R., Jordt, S. E., Chen, Y. & Liedtke, W. B. Regulation of pain and itch by TRP channels. *Neurosci. Bull.* **34**, 120–142. <https://doi.org/10.1007/s12264-017-0200-8> (2018).
24. Papoiu, A. D. & Yosipovitch, G. Topical capsaicin. The fire of a “hot” medicine is reignited. *Expert Opin. Pharmacother.* **11**, 1359–1371. <https://doi.org/10.1517/14656566.2010.481670> (2010).
25. Liu, Z. *et al.* Cancer-promoting effect of capsaicin on DMBA/TPA-induced skin tumorigenesis by modulating inflammation, Erk and p38 in mice. *Food Chem. Toxicol.* **81**, 1–8. <https://doi.org/10.1016/j.fct.2015.04.002> (2015).
26. Li, S. *et al.* TRPV1-antagonist AMG9810 promotes mouse skin tumorigenesis through EGFR/Akt signaling. *Carcinogenesis* **32**, 779–785. <https://doi.org/10.1093/carcin/bgr037> (2011).
27. Lee, Y. *et al.* Transient receptor potential vanilloid type 1 antagonists: A patent review (2011–2014). *Expert Opin. Ther. Pat.* **25**, 291–318. <https://doi.org/10.1517/13543776.2015.1008449> (2015).
28. Gavva, N. R. *et al.* Pharmacological blockade of the vanilloid receptor TRPV1 elicits marked hyperthermia in humans. *Pain* **136**, 202–210. <https://doi.org/10.1016/j.pain.2008.01.024> (2008).
29. Lee, Y. W. *et al.* Efficacy and safety of PAC-14028 cream—a novel, topical, nonsteroidal, selective TRPV1 antagonist in patients with mild-to-moderate atopic dermatitis: A phase IIb randomized trial. *Br. J. Dermatol.* **180**, 1030–1038. <https://doi.org/10.1111/bjd.17455> (2019).
30. Song, P. I. & Armstrong, C. A. Novel therapeutic approach with PAC-14028 cream, a TRPV1 antagonist, for patients with mild-to-moderate atopic dermatitis. *Br. J. Dermatol.* **180**, 971–972. <https://doi.org/10.1111/bjd.17777> (2019).
31. Serafini, M. *et al.* Targeting transient receptor potential vanilloid 1 (TRPV1) channel softly: The discovery of passerini adducts as a topical treatment for inflammatory skin disorders. *J. Med. Chem.* **61**, 4436–4455. <https://doi.org/10.1021/acs.jmedchem.8b00109> (2018).
32. Kistner, K. *et al.* Systemic desensitization through TRPA1 channels by capsazepine and mustard oil—a novel strategy against inflammation and pain. *Sci. Rep.* **6**, 28621. <https://doi.org/10.1038/srep28621> (2016).
33. Behrendt, H. J., Germann, T., Gillen, C., Hatt, H. & Jostock, R. Characterization of the mouse cold-menthol receptor TRPM8 and vanilloid receptor type-1 VR1 using a fluorometric imaging plate reader (FLIPR) assay. *Br. J. Pharmacol.* **141**, 737–745. <https://doi.org/10.1038/sj.bjp.0705652> (2004).
34. Fischer, M. J. *et al.* Direct evidence for functional TRPV1/TRPA1 heteromers. *Pflugers Arch.* **466**, 2229–2241. <https://doi.org/10.1007/s00424-014-1497-z> (2014).
35. Gavva, N. R. *et al.* The vanilloid receptor TRPV1 is tonically activated in vivo and involved in body temperature regulation. *J. Neurosci.* **27**, 3366–3374. <https://doi.org/10.1523/JNEUROSCI.4833-06.2007> (2007).
36. Georgescu, S. R. *et al.* Capsaicin: Friend or foe in skin cancer and other related malignancies?. *Nutrients* <https://doi.org/10.3390/nu9121365> (2017).
37. Yang, F. *et al.* Structural mechanism underlying capsaicin binding and activation of the TRPV1 ion channel. *Nat. Chem. Biol.* **11**, 518–524. <https://doi.org/10.1038/nchembio.1835> (2015).
38. Shintaku, K. *et al.* Activation of transient receptor potential A1 by a non-pungent capsaicin-like compound, capsiate. *Br. J. Pharmacol.* **165**, 1476–1486. <https://doi.org/10.1111/j.1476-5381.2011.01634.x> (2012).
39. Patil, M. J. *et al.* Sensitization of small-diameter sensory neurons is controlled by TRPV1 and TRPA1 association. *FASEB J.* **34**, 287–302. <https://doi.org/10.1096/fj.201902026R> (2020).
40. Ru, F. *et al.* Mechanisms of pruritogen-induced activation of itch nerves in isolated mouse skin. *J. Physiol.* **595**, 3651–3666. <https://doi.org/10.1113/jp273795> (2017).
41. Lim, K. M. & Park, Y. H. Development of PAC-14028, a novel transient receptor potential vanilloid type 1 (TRPV1) channel antagonist as a new drug for refractory skin diseases. *Arch. Pharm. Res.* **35**, 393–396. <https://doi.org/10.1007/s12272-012-0321-6> (2012).
42. Yun, J. W. *et al.* Antipruritic effects of TRPV1 antagonist in murine atopic dermatitis and itching models. *J. Invest. Dermatol.* **131**, 1576–1579. <https://doi.org/10.1038/jid.2011.87> (2011).
43. Devesa, I. *et al.* αCGRP is essential for algescic exocytotic mobilization of TRPV1 channels in peptidergic nociceptors. *Proc. Natl. Acad. Sci. U.S.A.* **111**, 18345–18350. <https://doi.org/10.1073/pnas.1420252111> (2014).
44. Mathivanan, S., Devesa, I., Changeux, J. P. & Ferrer-Montiel, A. Bradykinin induces TRPV1 exocytotic recruitment in peptidergic nociceptors. *Front. Pharmacol.* **7**, 178. <https://doi.org/10.3389/fphar.2016.00178> (2016).
45. Gunthorpe, M. J., Smith, G. D., Davis, J. B. & Randall, A. D. Characterisation of a human acid-sensing ion channel (hASIC1a) endogenously expressed in HEK293 cells. *Pflugers Arch.* **442**, 668–674. <https://doi.org/10.1007/s004240100584> (2001).
46. Morris, G. M., Huey, R. & Olson, A. J. Using AutoDock for ligand-receptor docking. *Curr. Protoc. Bioinform.* <https://doi.org/10.1002/0471250953.bi0814s24> (2008).
47. Krieger, E. & Vriend, G. YASARA view—molecular graphics for all devices—from smartphones to workstations. *Bioinformatics* **30**, 2981–2982. <https://doi.org/10.1093/bioinformatics/btu426> (2014).
48. Duan, Y. *et al.* A point-charge force field for molecular mechanics simulations of proteins based on condensed-phase quantum mechanical calculations. *J. Comput. Chem.* **24**, 1999–2012. <https://doi.org/10.1002/jcc.10349> (2003).

## Acknowledgements

This study was funded by Grants from AEI (MICIU) RTI2018-097189-B-C21 (to AFM and AFC), RTC-2017-6507-1 (to AFM and ID), with FEDER funds from EU “*Una manera de hacer Europa*” and a Grant from the UMH, PAR2019 (to AFM). MG is a recipient of an Industrial doctorate fellowship (DI-16-08303, MICIU), and LB is a recipient of a technician training program fellowship (PTA2017-14381-I, MICIU).

## Authors contribution

M.N.K. performed the patch-clamp experiments, the docking and prepared the figures; L.B. performed the MEA experiments and prepared the figures; S.G.R. contributed to the in vivo testing and prepared the figures; I.D. provided the compound and contributed to the in vivo experiments and revised the manuscript; P.V. contributed to the patch clamp experiments; M.S., A.A.G. and T.P. contributed to the synthesis and chemical characterization of AG1529 and revised the manuscript; G.F.B. supervised the docking experiments; A.F.C. supervised the electrophysiological, the in vivo experiments and revised the manuscript; A.F.M. supervised the project and data, and wrote the manuscript. All authors reviewed the manuscript.

## Competing interests

AFC, GFB and AFM are founders and shareholders of AntalGenics. ID is an employee of AntalGenics. AFM, AFC, TP and AAG are inventors of the patent protecting compound AG1529. AAG has waived his rights to benefit from the exploitation of the results towards pharmaceutical products. The other authors declare no conflict of interest.

## Additional information

**Correspondence** and requests for materials should be addressed to A.F.-M.

**Reprints and permissions information** is available at [www.nature.com/reprints](http://www.nature.com/reprints).

**Publisher’s note** Springer Nature remains neutral with regard to jurisdictional claims in published maps and institutional affiliations.



**Open Access** This article is licensed under a Creative Commons Attribution 4.0 International License, which permits use, sharing, adaptation, distribution and reproduction in any medium or format, as long as you give appropriate credit to the original author(s) and the source, provide a link to the Creative Commons licence, and indicate if changes were made. The images or other third party material in this article are included in the article’s Creative Commons licence, unless indicated otherwise in a credit line to the material. If material is not included in the article’s Creative Commons licence and your intended use is not permitted by statutory regulation or exceeds the permitted use, you will need to obtain permission directly from the copyright holder. To view a copy of this licence, visit <http://creativecommons.org/licenses/by/4.0/>.

© The Author(s) 2021